

Contents

Articles

³⁶ Cl/Cl Accelerator-Mass-Spectrometry Standards: Verification of Their Serial-Dilution-Solution Preparations by Radioactivity Measurements	R. Collé and Joylene W. L. Thomas	653
Pressure-Volume-Temperature Relations in Liquid and Solid Tritium	E. R. Grilly	679
Filter Transmittance Measurements in the Infrared	A. L. Migdall, A. Frenkel, and D. E. Kelleher	691
On Two Numerical Techniques for Light Scattering by Dielectric Agglomerated Structures	Akhlesh Lakhtakia and George W. Mulholland	699
Wavelengths and Energy Levels of Neutral Kr ⁸⁴ and Level Shifts in All Kr Even Isotopes	Victor Kaufman	717

Conference Reports

Third International Conference on Chemical Kinetics Reactions in Gas and Condensed Media	Robert E. Huie	725
Data Administration Management Association Symposium	Judith Newton	729
SUBJECT INDEX TO VOLUME 98		759
AUTHOR INDEX TO VOLUME 98		763

News Briefs

GENERAL DEVELOPMENTS	733
Agencies Target Help for Pollution Prevention NIST, Alaska Evaluate Impact of Burning Oil Spills New Lab Focuses on Novel Machine-Tool Designs	
Software Designed to Save Energy and Dollars Ceramic "Chefs" Fine-Tune Recipes with New Oven No "Second Guessing" with NIST Time Services Guide February Meeting to Feature 1993 Baldrige Winners	734

Two Companies Receive 1993 Baldrige Award New Dental Material Contains No Mercury Technology Centers to Host SBA Experts Panel to Address Open Systems Compatibility	735
New Standard Randomly Chooses Computer Passwords Twenty-Nine Grants Announced for ATP Fourth Round Laser Light Used to Focus Atoms on Surfaces “Electromagnetic Bottle” Traps Ions for Study	736
1994 Baldrige Criteria Focus on Business Planning 1994 NIUF Meeting Dates Announced New Device Improves Mammography Imaging Software Helps Predict, Solve Moisture Problems	737
New “One-Stop” Industry Guide to NIST Available Measuring Energy Flows in a Super-Cold Refrigerator NIUF Group Studies ISDN Wiring Installation EM Materials Measurements Focus of New Report	738
Atomic Clock, Wear-Resistant Alloy Receive Honor Interagency Committee on Standards Policy ISO 9000 Clearinghouse Patent Issued on Sensor to Detect and Classify Submicrometer Particles Method Developed for Characterizing Planar Transmission Lines Formed on Lossy Substrates	739
NIST Images Magnetic Recording Head with New Magnetic-Force Microscope NIST-Led IEEE Working Group Recognized for Development of Surge Voltage Document NIST’s Light Scattering Taxonomy Highlighted in <i>Applied Optics Journal</i>	740
NIST CMM Test Device Commercialized Ultrathin Film SnO ₂ Gas Sensors New Collisional Process Responsible for Radiation Damage in Compounds	741
Eighth National Synchrotron Radiation Instrumentation Conference Convened at NIST Gaithersburg Campus Development of Tunable, Pulsed Solid-State Lasers in the Visible CRADA with AISI for On-Line Magnetic Monitoring of Steel	742
Measurements for Ceramic Powder Processing Combustion Study of Siloxane through CRADA with Industry NIST Researchers Lead Earthquake Investigation to Japan Smoke Yield Measurements Made during International Offshore Experiment	743
New Publication Focuses on Security Issues in Database Language SQL Report Presents Proceedings of Workshop on the Security of National Computer Networks NIST Releases Software for Economic Analysis Workshop for Industry	744
Second-Generation NIST Thin-Film Multijunction Thermal Converters Demonstrate Practicality of Approach Device Simulations Made Possible by NIST Models Speed Utilization of New Power Semiconductor Devices	745
Commercial Semiconductor Test Equipment Based on Standards Resulting from NIST Work NIST Develops Electronic Police Radar Calibrator Model Developed to Evaluate Shielding Effectiveness of Aircraft Skin Structure	746

Results of Indo-U.S. Collaborative Program on Integrated Optics Disseminated through Workshop	747
NIST Works with Machine Tool Builder to Improve High-Speed Linear Motion Performance	
Topography of Multilayer X-Ray Mirror	
Defects Identified in Prototype Advanced Memory Chip	
Frobisher Iron Bloom Studied to Establish Provenance	748
Two New NIST Precision Measurement Grants Awarded for FY 94	
Counting Single Atomic Layers During the Growth of Thin Films	
NIST Assists Manufacturers of Color Displays	749
Powerful Optically Pumped Far-Infrared Laser Line Discovered	
First International Comparison of Phase-Noise-Measurement Systems	
NIST Establishes Two-Way, Time-Coordination Link to Europe	750
Cold Neutron Reflectometer Commissioned	
Software Evaluation Agreement Signed	
Company Signs CRADA Investigating Fracture in Engineering Polymers	751
NIST and NCMS Sign Cooperative Agreement to Develop Lead-Free Solders	
New Techniques Used for Siting Smoke Detectors	
New Fire Suppressants Recommended for In-Flight Protection of Aircraft	
BACnet Produces Positive Reaction from Industry	752
Computer Security Conference Attracts Large Turnout	
Raster Graphics Validation Test Service Initiated	
New Publication Focuses on Information Retrieval Techniques	
Security of Electronic Documents Subject of NIST Report	
Digital Signature Certificate Management Workshop Results Published	753
NIST Critical Stability Constants of Metal Complexes Database Released	
NIST First-Time Measurements Help Manufacturer Design Improved Portable X-Ray Units	
Locating Images Projected by Integrated-Circuit Manufacturing Tools to Nanometer-Level Accuracy	
NIST Transmission Line Measurement Method Demonstrated for High-Permittivity Materials	754
NIST Demonstrates Capability for High-Frequency Surface Resistivity Measurements of High-Temperature-Superconductor Films	
New Method To Detect Highly Excited Atomic States	
NIST Researchers Document Thermal Aging of Foam Insulation	755
ISDN Federal Information Processing Standard (FIPS) Approved	
New Report Focuses on Emerging Features for Geographic Information Systems (GIS) Applications in Database Language Structured Query Language (SQL)	
NIST Makes POSIX Conformance Test Suite Available Electronically	
STANDARD REFERENCE MATERIALS	755
Standard Reference Material 1746—Silver Freezing-Point Standard	
Standard Reference Material 1978—Particle Size Distribution Standard	756
Standard Reference Materials 2590—2591 Josephson Array Voltage Standards	
Standard Reference Material 2137—Boron Implant in Silicon Standard for Calibration of Concentration in a Depth Profile	
<i>Calendar</i>	757

³⁶Cl/Cl Accelerator-Mass-Spectrometry Standards: Verification of Their Serial-Dilution-Solution Preparations by Radioactivity Measurements

Volume 98

Number 6

November–December 1993

R. Collé and Joylene W. L. Thomas

National Institute of Standards and Technology,
Gaithersburg, MD 20899-0001

A consortium of accelerator-mass-spectrometry (AMS) laboratories recently prepared a series of ³⁶Cl/Cl isotopic ratio AMS standards by an eight-step serial gravimetric dilution scheme. Of the resulting nine solutions, only the latter six could be assayed by AMS to confirm the gravimetric dilution factors. This paper provides the results of relative radioactivity measurements on the first four solutions to verify the first three dilution factors. The fourth solution was the only dilution capable of being directly measured by both AMS and radionuclidic metrology of ³⁶Cl, and therefore its assay by radioactivity counting was deemed of considerable importance. Assays were performed by 4πβ⁻ liquid scintillation (LS) counting of gravimetric aliquots of the solutions, with confirmatory measurements by 2πβ⁻ gas-flow proportional counting of gravimetrically-prepared solid sources. The radioactivity measurements on the fourth solution were complex and difficult because of the conflicting combination of a low activity concentration (0.036 Bq·g⁻¹) and high salt content

(146 mg NaCl per g of solution). These conditions necessitated independent studies of the ³⁶Cl LS efficiency as a function of NaCl loading in the LS cocktails and of the feasibility of LS counting of precipitated samples, both of which are also reported here. The results of the radioactivity measurements confirmed the dilution factors for the first three solutions to absolute differences of about 1%, and that for the fourth solution to about 1% to 2%. The overall uncertainties for these verification measurements, at a relative three standard deviation uncertainty interval, were of comparable magnitude, i.e., in the range of ±1% to ±2% for the first three solutions and roughly ±3% for the fourth solution.

Key words: accelerator mass spectrometry (AMS); beta counting; chlorine-36; liquid scintillation (LS); measurements; proportional counting; radioactivity; standards.

Accepted: September 20, 1993

Contents

1. Introduction and Overview	654	2.1.3 LS Efficiency of Precipitated Samples	660
2. Measurement Methods, Results, and Discussion	655	2.1.4 LS Counting of Solution D	665
2.1 Liquid Scintillation Measurements	655	2.2 Proportional Counting Measurements ..	669
2.1.1 LS Efficiency as a Function of NaCl Loading	656	3. Summary and Concluding Notes	675
2.1.2 LS Counting of Solutions A, B, and C	657	4. References	677

1. Introduction and Overview

Measurements of ^{36}Cl by accelerator mass spectrometry (AMS) significantly contribute to research in a variety of disciplines within the geologic, hydrospheric, atmospheric and cosmic sciences [1], and references therein, as well as in other applied areas. For example, such AMS measurements recently were used to evaluate the neutron exposure dosimetry models for the Hiroshima and Nagasaki atomic bombings [2].

The importance of these measurements demands the availability of reliable and accurate $^{36}\text{Cl}/\text{Cl}$ isotopic standards both for calibrations between laboratories and for internal controls within a laboratory.

A series of $^{36}\text{Cl}/\text{Cl}$ AMS standards were recently developed and prepared by a consortium of AMS laboratories [1]. The six AMS standards consist of solutions containing 145.6 mg NaCl per g of solution and have atom ratios of 3.254×10^{-10} , 5.003×10^{-11} , 1.000×10^{-11} , 5.000×10^{-12} , 1.600×10^{-12} , and 5.000×10^{-13} . The solutions were prepared by serial gravimetric dilutions of a ^{36}Cl solution standard, viz., National Institute of Standards and Technology (NIST) Standard Reference Material SRM 4943. The gravimetric dilution factors were estimated to have uncertainties of less than $\pm 1\%$ in terms of a relative standard deviation. The dilutions were performed at the University of California at San Diego (UCSD), and were subsequently checked in three separate experimental trial runs using the University of Rochester AMS facility. In each case, the absolute percent difference in the measured $^{36}\text{Cl}/\text{Cl}$ atom ratio compared to the expected atom ratio, based on gravimetric dilution factors, was better than 2%. The measured atom ratios for the new AMS standards were also

in excellent agreement with older UCSD $^{36}\text{Cl}/\text{Cl}$ standards [1].

In preparing the six new AMS standards, the original stock solution (NIST SRM 4943) underwent an eight-step serial dilution. For additional details, refer to Fig. 1 in [1]. The results of the first three dilutions are summarized in Table 1 where solution A is the SRM stock solution, solution B is a dilution of A, solution C is a dilution of B, and solution D is a dilution of C. Solution D is the first aforementioned AMS standard, and was further used in five dilutions to prepare the remaining five AMS standards. It is the AMS standard of largest $^{36}\text{Cl}/\text{Cl}$ atom ratio and the least dilution capable of being directly measured by AMS.

The experimental design and plan for the preparation of the AMS standards originally envisaged having NIST perform relative radioactivity measurements on the four solutions of Table 1 to verify the first three gravimetric dilution factors [1]. This paper provides the results of these verification measurements.

Measurements of solutions A, B, and C by $4\pi\beta^-$ liquid scintillation (LS) counting techniques to within uncertainties of $\pm 1\%$ to $\pm 2\%$ at a relative three standard deviation uncertainty interval appeared to be straightforward. The measurement of solution D, however, required more laborious and heroic efforts. Inasmuch as solution D was the only dilution of the series capable of being directly measured by both AMS and radioactivity counting, the expense of considerable effort in trying to assay it with comparable accuracy, if possible, was deemed to be a worthwhile enterprise.

The measurement of solution D by LS counting was problematic because of the combination of a relatively low activity concentration (approximately $0.036 \text{ Bq} \cdot \text{g}^{-1}$) in conjunction with a relatively high

Table 1. Reported compositions of the serial dilution solutions used to prepare the $^{36}\text{Cl}/\text{Cl}$ AMS standards

Solution identity	Isotopic ratio $^{36}\text{Cl}/\text{Cl}$	NaCl concentration ($\text{mg} \cdot \text{g}^{-1}$)	^{36}Cl activity concentration ($\text{Bq} \cdot \text{g}^{-1}$)	Gravimetric dilution factors for ^{36}Cl
A ^a	$7 (10^{-2})^b$	0.02 ^b	10950.	
B	$1.059 (10^{-6})$	144.0	114.6	A/B = 95.55
C	$1.825 (10^{-8})$	145.5	1.997	B/C = 57.39 A/C = 5483.
D	$3.245 (10^{-10})$	145.6	0.03551	C/D = 56.24 B/D = 3227. A/D = 308400.

^a NIST SRM 4943.

^b Nominal values.

NaCl concentration (146 mg NaCl per g of solution). The low activity concentration required loading LS cocktails with sample sizes as large as possible to enhance the net counting rates above background. Even with a high ^{36}Cl LS detection efficiency of nearly 99%, the net LS count rate per g of solution D was expected to be only about 3% of background. Hence, even a 5 g LS counting sample would result in a net rate of around 15% of background. In addition, it was subsequently discovered that the dissolved NaCl in these salt solutions (at 146 mg NaCl g^{-1}) began to precipitate out of cocktails prepared with even less than 0.4 g of sample and 15 g of conventional, commercially-available scintillation fluids known to have high salt loading capacities. Even increasing the aqueous phase content in the LS cocktails (with blank water) to 10% only allowed sample aliquots of about 0.75 g (i.e., 110 mg NaCl) before salt precipitates began to form. With any further increases in aqueous phase content, in which the cocktails went from clear solutions to translucent and opaque counting gels, the NaCl solubility in the cocktails actually decreased with increasing water content. At the same time, the effects of such large NaCl loadings on the LS efficiency for ^{36}Cl were largely unknown. Therefore, prior to initiating the intended verification measurements of the AMS standard serial dilutions, it was necessary to conduct several preliminary investigations of the ^{36}Cl LS efficiency as a function of NaCl cocktail loading and of the feasibility of LS counting of precipitated samples. This paper then also provides the results of those studies.

Lastly, this paper describes the attempts that were made to perform confirmatory measurements by low-background, $2\pi\beta^-$ flow-proportional counting of evaporated solid sources prepared from the AMS standard solutions. From the onset, it was considered that these solid source measurements would at best only serve as less accurate, but independent confirmations of the LS results. As for the LS measurements, the β^- proportional counting was similarly problematic for solution D because of the rather massive NaCl concentration. The source preparation requirements and attendant restrictions for the two cases were, in fact, comparative. The evaporated counting sources had to be optimized between using large aliquots to increase the net β^- count rates and small aliquots to decrease self-absorption and scattering β^- count rate losses.

It should be noted, for completeness, that other ^{36}Cl radioactivity assay techniques were also considered. No others within the capability of the NIST

Radioactivity Group, however, appeared feasible. The most viable alternative candidate was by direct Cerenkov counting of the solutions, but it too appeared to be impracticable. The ^{36}Cl β^- spectrum is insufficiently energetic (maximum $E_{\beta^-} = 709.3$ keV; average $E_{\beta^-} = 251.2$ keV) to produce a large Cerenkov radiation yield. It was estimated that the ^{36}Cl detection efficiency by Cerenkov counting was likely to be less than 3% to 5% under even the most optimum sample conditions [3]. All photon spectrometry techniques also had to be excluded since ^{36}Cl primarily decays directly to the ground state of ^{36}Ar (98.1% β^-) with weak electron-capture (1.9% EC) and β^+ -decay (0.0017%) branches to the ground state of ^{36}S without the emission of any gamma rays [4]. The x rays accompanying the EC decay and the 511 keV annihilation radiation from β^+ decay interactions are insubstantial for assaying purposes at the desired $\pm 1\%$ to $\pm 2\%$ relative three standard deviation uncertainty interval.

2. Measurement Methods, Results, and Discussion

2.1 Liquid Scintillation Measurements

In assaying the four solutions under test (Table 1), the LS counting sources, in all cases, consisted of an appropriate aliquot of one of the solutions and approximately 15.1 g of Beckman¹ "Ready Safe," a polyaryllalkane (i.e., an alkylated biphenyl)-surfactant-based scintillation cocktail, contained within nominal 22 mL, glass LS vials. The cocktail was selected in part because of its reported high holding capacity for aqueous salt solutions [5], as well as being environmentally safe (i.e., non-toxic, non-flammable, and bio-degradable). Some of the sources also contained respective proportions of a blank doubly-distilled water solution and a carefully prepared blank NaCl solution having a concentration of 145 mg NaCl per g of solution. The blank water and NaCl solutions were used to vary the NaCl content in some of the counting sources, to match sample compositions (and hence sample quenching) for the different sources prepared from the four solutions, and to prepare matched blanks of nearly identical composition for background subtractions.

¹ Certain commercial equipment, instruments, or materials are identified in this paper to specify adequately the experimental procedure. Such identification does not imply recommendation or endorsement by the National Institute of Standards and Technology, nor does it imply that the materials or equipment identified are necessarily the best available for the purpose.

All of the sample aliquots used to prepare the counting sources were determined gravimetrically with an estimated uncertainty, corresponding to an assumed standard deviation, of $\pm 10 \mu\text{g}$ to $\pm 30 \mu\text{g}$. For sample aliquots ranging from about 30 mg to 60 mg for solution A to greater than 5 g for solution D, the relative standard uncertainties in the sample mass measurements thus are about 0.05% to less than 0.001% in general, and about 0.1% in worst cases, after appropriate gravimetric measurement air-buoyancy corrections, and considering the internal balance-weight uncertainties, and typical mass measurement precision.

The sources were measured in two LS counting systems: (1) a Beckman LS7800 model LS counter equipped with two Hamamatsu R331-05 photomultiplier tubes operating in a coincidence mode, a logarithmic pulse amplifier coupled to an analog-to-digital converter (ADC) for spectral pulse-height analysis, and an external ^{137}Cs source for Compton-edge (Horrocks number) quench monitoring [6]; and (2) a Packard Tri-Carb 2500TR LS analyzer employing two matched high performance photomultiplier tubes also operating in coincidence, but with linear amplification for ADC pulse-height spectral analysis, and with an external ^{133}Ba source that provided an instrument-provided, "transformed Spectral Index of the External Standard (*tSIE*)," quench indicating parameter [7].

Based on theoretical modelling predictions using the CIEMAT/NIST ^3H efficiency tracing method calculations [8–10], the LS counting efficiency for ^{36}Cl in unquenched samples was expected to be about 98% to 99%. This overall efficiency results from a nearly 100% efficiency for the 0.981 β^- -decay branch and with a reasonably high (perhaps 25% to 75%) efficiency for the 0.019 electron capture (EC) branch. Refer to Table 2.

Table 2. Expected ^{36}Cl LS efficiency for unquenched samples

		Assumed ^{36}Cl $4\pi\beta^-$ LS efficiency ^a		
		1.000	0.995	0.990
Assumed ^{36}Cl 4π EC LS Efficiency ^b	0.75	0.995	0.990	0.985 ^c
	0.50	0.991	0.986 ^c	0.981
	0.25	0.986 ^c	0.981	0.976

^a For 98.1% β^- (maximum $E_{\beta^-} = 709.3$ keV; average $E_{\beta^-} = 251.2$ keV).

^b For 1.9% EC.

^c Observed in least quenched samples; $\epsilon_{\text{tot}} = 0.985$ to 0.987.

The LS efficiency, as well as cocktail stability, for samples quenched with large quantities of NaCl was however unknown, and required a preliminary study.

2.1.1 LS Efficiency as a Function of NaCl Loading To investigate the effect of NaCl loading on the ^{36}Cl LS counting efficiency, a series of counting sources with varying NaCl content were prepared with known amounts of ^{36}Cl activity from NIST SRM 4943 (solution A) and with the blank water and NaCl solutions (see Table 3). Each of eleven sources contained from about 20 mg to 65 mg of solution A (about 220 Bq to 720 Bq). The first two sources (SA1 and SA2 in Table 3) contained no additional blank solutions, and hence had minimal NaCl (≤ 0.01 mg) and very low total aqueous content ($< 0.3\%$ water by mass). The next two (SA3 and SA4) were prepared with about 1.2 g and 1.5 g of blank water to a nominal 9% to 10% aqueous content. These two also had minimal NaCl. The next seven (SA5 through SA11) were prepared with varying combinations of blank water and NaCl solutions to give increasing NaCl contents (from about 45 mg to 230 mg NaCl) and with a nearly constant 9% to 10% total aqueous content. The samples with NaCl content up to about 110 mg were clear. The next two (SA8 and SA9) appeared clear at first, but upon settling for a few days began to exhibit a trace of salt precipitates. The last two samples (SA10 and SA11) had large salt precipitates.

Each of the samples along with matched blanks for each sample composition were measured four times over two days with the Beckman LS counter. The counting results are summarized in Table 3 in terms of the calculated ^{36}Cl LS efficiency (mean of the four measurements), the relative standard deviation of the mean s_m , and the average Horrocks number for each sample. The Horrocks number ($H\#$) is a quench indicating parameter that is based on the downward spectrum shift of the Compton edge of an external ^{137}Cs standard with increasing sample quenching. The parameter corresponds to the spectral channel number shift between the sample and an unquenched blank sample.

As indicated in Table 3, for the first two samples (SA1 and SA2) containing minimal NaCl and less than 0.3% water, the quench parameter was about $H\# = 65$ and the efficiency was approximately 0.986 for the mean of the two. With increasing water content to about 9% to 10% (samples SA3 and SA4), $H\#$ increased to approximately 95 with a

Table 3. LS counting efficiency for ^{36}Cl as a function of NaCl sample loading

Sample identity	LS Sample composition ^a				LS Counting results		
	Aqueous mass percent ^b	NaCl mass (mg)	^{36}Cl activity (Bq)	Appearance	Average $H\#^c$	Efficiency	s_m (%) ^d
SA1	0.22	(e)	355.8	clear	64	0.9870	0.047
SA2	0.29	(e)	477.9	clear	65	0.9850	0.027
SA3	9.09	(e)	223.2	clear	94	0.9856	0.084
SA4	9.41	(e)	715.3	clear	95	0.9776	0.039
SA5	9.86	44.59	354.8	clear	96	0.9871	0.067
SA6	10.5	49.58	561.8	clear	97	0.9846	0.039
SA7	9.58	109.0	362.5	clear	94	0.9845	0.049
SA8	9.15	143.3	467.9	ppt. (trace)	85	0.9833	0.079
SA9	9.26	146.5	447.6	ppt. (trace)	85	0.9813	0.059
SA10	9.13	212.6	521.7	ppt.	72	0.9311	0.037
SA11	9.57	227.0	303.9	ppt.	72	0.9507	0.15

^a In approximately 15.06 g scintillator fluid.

^b $[m_{\text{water}}/(m_{\text{water}} + m_{\text{scin}})] 100$.

^c Horrocks number (see text).

^d Relative standard deviation of the mean in percent for four measurements on each sample. The total statistical (Poisson) counting precision in terms of a relative standard deviation was about 0.05% for each sample.

^e Minimal; approximately ≤ 0.01 mg NaCl.

small or almost negligible change in efficiency (mean = 0.982). With increasing NaCl content from the minimal quantities up to about 110 mg (samples SA3 through SA7), the values of $H\#$ remained at about 95 and the efficiencies were virtually identical. With further increases in NaCl content in which precipitates formed in the counting sources (samples SA8 through SA11), the efficiencies began to slightly decrease. At the same time, the measurement precision on these precipitated samples considerably worsened as evidenced by the large differences in efficiency for samples of very similar composition and by the much larger values of s_m for measurements on even the same samples. The apparent irregularities in the efficiencies as a function of this NaCl loading in precipitated samples will be discussed at length in Sec. 2.1.3. Interestingly, the quench parameters for these samples actually decreased (from $H\# = 95$ to $H\# = 72$) with increasing NaCl and increasing precipitation in the samples. It is conjectured that this effect arose because with the increasing precipitation of the salt out of the cocktail mix, the scintillator phase itself became more transparent and contained less of the NaCl to quench the samples. The most surprising overall result however was the relatively high efficiency values (>95%) that were obtained with these large NaCl loadings and moreover that they were obtained even in samples with substantial precipitate formations.

Spectra for these various samples as a function of NaCl loading are discussed in Sec. 2.1.3.

The results of this investigation (Table 3) clearly established the bounds for the composition of LS counting sources that would not result in the formation of precipitates and that would provide reasonably low quenching and high detection efficiency with good measurement precision. The experimental design for the assays of solutions A, B, and C were based on these results. The low activity concentration for solution D, as described in the Introduction (Sec. 1), precluded a similarly based assay procedure.

2.1.2 LS Counting of Solutions A, B, and C

Three LS counting sources were prepared for each of the solutions A, B, and C such that each source contained approximately 110 mg NaCl and 9% water in 15 g of scintillator (see Table 4). The sources were prepared with varying aliquots of the solutions (ranging from 32 mg to 43 mg for A; 260 mg to 720 mg for B; and about 750 mg for C) and with appropriate quantities of the blank water and blank NaCl solutions. These nine sources (along with three others prepared earlier; namely SA1, SA2, and SA7) and matched counting blanks of nearly identical sample composition were measured five times on both the Beckman and the Packard LS counting systems.

The counting results are tabulated in Tables 4 and 5, respectively. The tables provide the mean counting rates per unit mass of solution for each

Table 4. LS results for solutions A, B, C obtained with Beckman LS 7800 counter

Solution	Sample identity	LS Sample composition ^a			LS Counting results for ³⁶ Cl				
		Aqueous mass percent ^b	NaCl mass (mg)	Mean rate (cps · g ⁻¹)	s_m^c (%)	s_p^d (%)	Average $H\#^e$	Efficiency	Activity concentration (Bq · g ⁻¹)
A	SA1 ^f	0.22	g	10800	0.038	0.036	60	0.9863	(10950) ^h
	SA2 ^f	0.29	g	10788	0.020	0.031	61	0.9852	(10950)
	SA7 ^f	9.58	109.	10799	0.032	0.035	92	0.9862	(10950)
	A1	9.29	111.	10800	0.037	0.036	94	0.9863	(10950)
	A2	9.43	109.	10770	0.012	0.031	95	0.9836	(10950)
	A3	9.55	113.	10774	0.035	0.031	95	0.9839	(10950)
B	B1	8.96	105.	113.09	0.15	0.13	94	(0.985) ^h	115.6
	B2	9.12	110.	113.23	0.11	0.090	93	(0.985)	115.0
	B3	8.90	104.	113.07	0.052	0.075	91	(0.985)	114.8
C	C1	9.12	110.	1.9399	0.524	0.85	91	(0.985)	1.969
	C2	9.11	110.	1.9551	0.463	0.85	91	(0.985)	1.985
	C3	9.04	108.	1.9607	1.639	0.86	91	(0.985)	1.991

^a In approximately 15.05 g scintillator fluid.

^b $[m_{\text{water}}/(m_{\text{water}} + m_{\text{scin}})] 100$.

^c Relative standard deviation of the mean in percent for five measurements on each sample.

^d Relative standard deviation in percent for the total statistical (Poisson) counting precision.

^e Horrocks number (see text).

^f Previous samples of Table 2.

^g Minimal; approximately ≤ 0.01 mg NaCl.

^h Values in parentheses are either the known activity concentration for solution A used to calculate the counting efficiencies or are the assumed efficiencies used to calculate the activity concentrations for solutions B and C.

Table 5. LS counting results for solutions A, B, C obtained with Packard 2500 TR counter

Solution	Sample identity ^a	LS Counting results for ³⁶ Cl					Activity concentration (Bq · g ⁻¹)
		Mean rate (cps · g ⁻¹)	s_m (%) ^b	s_p (%) ^c	Average $tSIE$	Efficiency	
A	SA1	10810	0.040	0.036	578	0.9872	(10950)
	SA2	10810	0.041	0.031	571	0.9872	(10950)
	SA7	10803	0.038	0.035	439	0.9866	(10950)
	A1	10825	0.031	0.036	437	0.9886	(10950)
	A2	10789	0.035	0.031	436	0.9853	(10950)
	A3	10802	0.025	0.031	431	0.9865	(10950)
B	B1	113.06	0.13	0.13	440	(0.987) ^e	114.5
	B2	113.34	0.092	0.089	439	(0.987)	114.8
	B3	113.33	0.082	0.075	444	(0.987)	114.8
C	C1	1.9382	0.56	0.82	441	(0.987)	1.964
	C2	1.9487	0.52	0.82	439	(0.987)	1.974
	C3	1.9611	0.38	0.82	441	(0.987)	1.987

^a See Table 3 for LS sample composition.

^b Relative standard deviation of the mean in percent for five measurements on each sample.

^c Relative standard deviation in percent for the total statistical (Poisson) counting precision.

^d Transformed spectral index of the external standard (see text).

^e Values in parentheses are either the known activity concentration for solution A used to calculate the counting efficiencies or are the assumed efficiencies used to calculate the activity concentrations for solutions B and C.

source, computed statistics for the measurement precision, sample quenching parameters, derived or assumed LS counting efficiencies, and the resultant activity concentrations.

The Horrocks number $H\#$ was described previously. The Packard system's quench indicating parameter $tSIE$ is based on a mathematical analysis of the Compton spectrum and consists of a decreasing relative quenching scale in which unquenched samples correspond to $tSIE = 1000$.

The quench parameters $H\#$ (for the Beckman LS system) and $tSIE$ (for the Packard) scale proportionally and are closely matched in all cases, excepting those for samples SA1 and SA2 which contained less water and which were recounted only for comparative purposes. The measurement precision both in terms of the relative standard deviation of the mean for the five measurements (s_m) and in terms of the relative standard deviation for the assumed Poisson-distributed total statistical "counting error" (s_p)² varied appropriately with the respective activity concentrations in the three solutions. The activity concentrations in units of $Bq \cdot g^{-1}$ for solutions B and C were derived from the mean LS counting efficiencies for each counting system which were in turn obtained from the mean count rate concentrations for similarly matched samples and the known activity concentration of solution A (see Tables 4 and 5). Alternatively, as provided in Table 6, ratios of the mean counting rate concentrations for the various solution pairs A/B, A/C, and B/C can be directly compared to the reported gravimetric dilution factors.

The measurement uncertainties for these determinations are summarized in Table 7. The uncertainty analysis procedures used here follow the normal conventions of the NIST Radioactivity Group which for the most part are compatible with those adopted by the principal international metrology standardization bodies [11]. All individual uncertainty components are expressed in terms of estimated (experimental) standard deviations (or standard deviations of the mean where appropriate) or quantities assumed to correspond to standard deviations, irrespective of the method used to evaluate their magnitude. A combined or propagated uncertainty is expressed as an estimated standard deviation which is equal to the positive square root of the total variance obtained by summing all variance and covariance components, however evaluated, using the law of propagation of uncertainty for the specific mathematical function given by the model of the measurement procedure. By convention in this laboratory, the combined uncertainty is expanded by a factor of 3 to obtain an "overall" or expanded uncertainty which is assumed to provide an uncertainty interval having a high level of confidence of roughly 95% to 99%.

The results of these LS determinations for solutions A, B, and C were also subjected to extensive statistical tests on subsets of the data across a variety of variables: sample preparation order, sample composition, sample masses, sample replicates for a given solution, the timing and sequence of the LS measurements, and the LS measurement system used. These included χ^2 -tests of the homogeneity in

Table 6. Comparison of reported to measured dilution factors for solutions A, B, and C

Solution pairs	Ratios of averaged LS results			Reported gravimetric dilution factor (R) ^c	R/R_{LS}
	With Beckman counter ^a	With Packard counter ^b	Both Counters (R_{LS})		
A/B	95.37	95.43	95.39	95.55	1.002
A/C	5527.	5544.	5535.	5483.	0.991
B/C	57.96	58.09	58.03	57.39	0.989

^a See Table 4.

^b See Table 5.

^c See Table 1.

² The total "counting error" devolves from the assumption that the radioactive decay process is Poisson distributed and that its variance (N) is equal to the mean number of total observed counts (N). Here, the combined s_p is expressed as a relative standard deviation in percent and is merely given by $100\sqrt{N_S + N_B}/(N_S - N_B)$ where N_S is the total number of counts summed over all replicate measurements on a sample and N_B is the respective total number of background counts.

subsets of the observed sample variances (across the variables), F-tests of the homogeneity in the various subset sample means, t-tests of differences between the various means, and tests of possible correlations and biases using analysis of variance (ANOVA) techniques with sequential two-way classifications of the variables. None of the tests indi-

Table 7. Uncertainty analysis for the measured dilution factors for solutions A, B, and C

Solution pair	LS counter	LS Measurement precision (%) ^a	Combined uncertainty, u (%) ^b	Overall uncertainty, $3u$ (%) ^c
A/B	Beckman	0.062	0.33	1.0
	Packard	0.058	0.33	1.0
B/C	Beckman	0.56	0.64	1.9
	Packard	0.27	0.41	1.2
A/C	Beckman	0.55	0.64	1.9
	Packard	0.26	0.41	1.2

^a Corresponds to the combined relative standard deviation of the mean in percent for the precision in the LS counting rate concentration ratios. See Tables 4 and 5.

^b Includes uncertainties due to the LS measurements (0.05% to 0.1%), and differences or mismatch in LS efficiency due to differences in sample composition, quenching, and cocktail stability.

^c Corresponds to three times the combined uncertainty u which is assumed to provide an uncertainty interval having a high level of confidence of roughly 95% to 99%.

cated any statistically significant differences in any of the tested subset sample means or sample variances. The agreement in the results between the two LS counting systems as provided in Tables 4, 5, and 6 are representative.

The summarized results of these tables clearly verify and confirm the activity concentrations for solutions B and C, relative to solution A, to absolute differences of better than 1%; and they comparably verify and confirm the dilution factors for the A/B, A/C, and B/C solution pairs. The overall LS measurement uncertainties, at a three standard deviation uncertainty interval, as given in Table 7, are also of a comparable $\pm 1\%$ magnitude and are less than $\pm 2\%$ in worst cases.

2.1.3 LS Efficiency of Precipitated Samples

To investigate the feasibility of assaying solution D with precipitated LS samples, a series of precipitated-sample LS counting sources with increasing NaCl content were prepared as summarized in Table 8. The samples were prepared with about 15.1 g of scintillator and with known gravimetrically-determined aliquots of solution A (about 0.08 g to 0.1 g) and with varying blank water and blank NaCl solutions to vary the total NaCl loading. A similar set of blanks with closely matched sample compositions were also prepared for use in making background subtractions. All of the samples had a visible precipitate. The samples ranged from approximately 110 mg NaCl in 5.2% water with a very small salt precipitate that barely covered the bottom of the LS vial to 800 mg NaCl in 27% water with a massive salt precipitate that filled nearly one

third of the LS vial's volume. These loadings would correspond to solution D aliquots ranging from 0.75 g to 5.5 g. Recalling the discussion in the Introduction (Sec. 1), it was desirable to try to maximize the sample size to maximize the net LS count rates above background.

Table 8 also contains LS counting results on these samples for two experimental trials. Both trials were based on five measurements of each sample over about 2 d with the Beckman LS system. These initial results are tabulated in terms of the mean ³⁶Cl efficiency for the five measurements and the average $H\#$ quench parameter for each sample. The general trends indicated increasing sample quenching and decreasing efficiency with increasing NaCl content. The measurement precision however within the five measurements for a given sample was somewhat greater than typical LS measurement precision. It was also apparent that the efficiency as a function of total NaCl loading was not very systematic or regular (e.g., not exhibiting a monotonical functionality between the efficiency and NaCl content) particularly for samples greater than 650 mg NaCl. Subsequent measurements also revealed that the efficiency was a slowly varying function of the settling time. The efficiency, ϵ , as a function of NaCl mass, m , for three settling conditions are shown in Fig. 1: (a) are the data of Table 8 following about 2 d to 4 d of settling; (b) contains the results obtained after about 14 d to 16 d of settling; and (c) are the results for samples after undergoing centrifuging. The latter measurements were made since it seemed intuitive that

Table 8. LS counting efficiency for ^{36}Cl in precipitated samples.

Sample identity	LS Sample composition ^a			LS Counting results					
	Aqueous ^b mass percent	NaCl mass (mg)	^{36}Cl activity (Bq)	First trial ^c			Second trial ^d		
				Mean efficiency	s_m^e (%)	$H\#^f$	Mean efficiency	s_m^e (%)	$H\#^f$
T1	5.20	109.	901.6	0.953	0.14	75	0.964	0.14	62
T2	9.61	219.	1141.	0.949	0.086	78	0.953	0.11	65
T3	14.7	363.	1220.	0.929	0.14	78	0.951	0.046	68
T4	17.0	436.	1117.	0.923	0.068	77	0.946	0.062	68
T5	19.4	514.	1084.	0.916	0.12	78	0.935	0.10	70
T6	21.3	583.	874.8	0.900	0.031	80	0.931	0.070	71
T7	23.3	656.	1107.	0.895	0.097	80	0.926	0.060	73
T8a	24.1	684.	1024.	0.878	0.14	81	0.922	0.070	74
T8b	24.1	687.	909.0	0.889	0.16	82	0.922	0.16	75
T9a	25.2	729.	914.5	0.890	0.083	81	0.918	0.037	76
T9b	25.2	728.	947.9	0.860	0.10	85	0.924	0.088	76
T10a	25.9	757.	941.7	0.877	0.090	86	0.919	0.094	78
T10b	25.9	757.	868.6	0.906	0.11	82	0.921	0.15	80
T11	27.0	800.	970.2	0.878	0.12	87	0.916	0.070	81

^a In approximately 15.17 g scintillator fluid. All samples had visible precipitates in the cocktail.

^b $[m_{\text{water}}/(m_{\text{water}} + m_{\text{scin}})] 100$.

^c Obtained after 2 to 4 d of settling. Refer to text.

^d Obtained after the samples were centrifuged. Refer to text.

^e Relative standard deviation of the mean in percent for five measurements on each sample. The total statistical (Poisson) counting precision in terms of a relative standard deviation was less than 0.01% for each sample.

^f Average Horrocks number (see text).

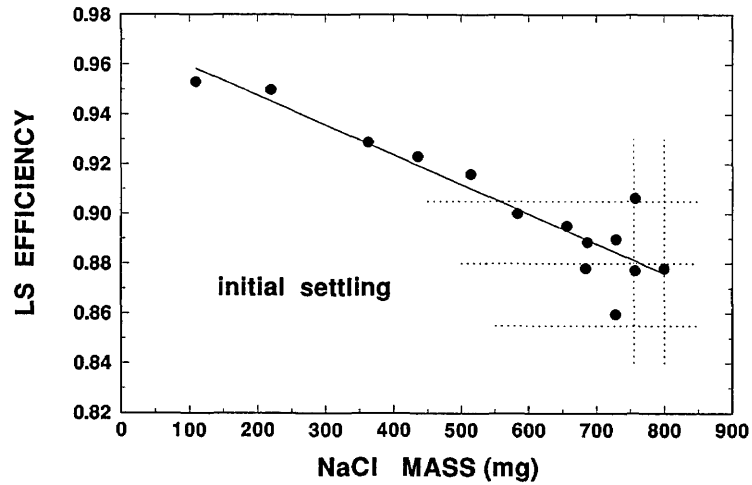
centrifuged samples might approximate a steady-state settling condition. This intuition was proved to be mistaken.

All of the efficiency values of Fig. 1 are based on five replicate measurements with the Beckman system. As mentioned, the internal measurement precision within five measurements for a given sample was poor, with values of s_m ranging from typical LS measurement precision to over 1% in some cases. This can be compared (Table 3, for example) to previously observed values of s_m for unprecipitated LS samples, in which s_m is typically better than 0.05% for a similar number of measurements. The irregularity in the efficiency as a function of NaCl mass is also readily observed in Fig. 1. The lines in each of the graphs of Fig. 1 correspond to χ^2 -minimized linear regressions fitted to the data, and even the slopes $d\epsilon/dm$ for the three settling conditions are substantially different. The fits are not intended to imply a theoretical significance, but were only made for comparison purposes. The three fitted slopes in Fig. 1 are $d\epsilon/dm = -0.119 \text{ g}^{-1}$, -0.079 g^{-1} , and -0.070 g^{-1} , respectively, and have efficiency intercepts (extrapolated to zero NaCl mass) of $\epsilon_0 = 0.972$, 0.958 , and 0.972 . It must be emphasized however that all of these efficiency

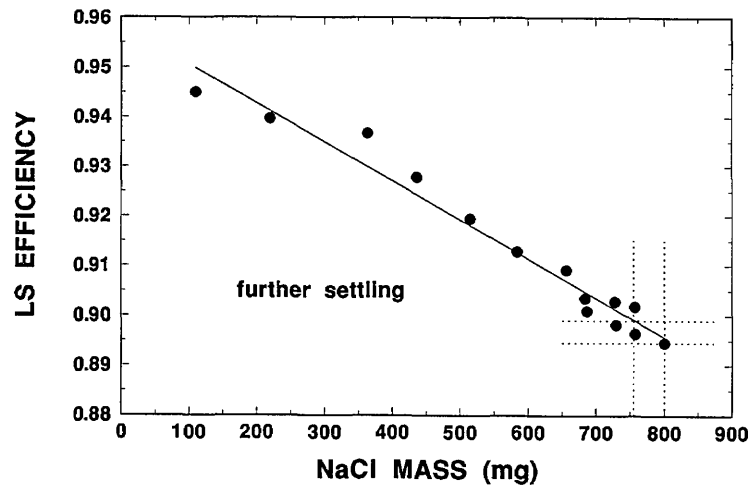
measurements were very temporal and dependent on the settling time for the samples.

Extensive subsequent measurements on these precipitated samples with settling times extending to over 102 d revealed additional unusual and inexplicable behavior. Figure 2 shows the efficiency ϵ as a function of settling time t for two sources containing 219 mg and 757 mg NaCl, displayed over two time scales: (a) from 0 d to 5 d and (b) from 0 d to 30 d. The observed wide variations in the efficiency for near replicate measurements with only small changes in settling time will be addressed below.

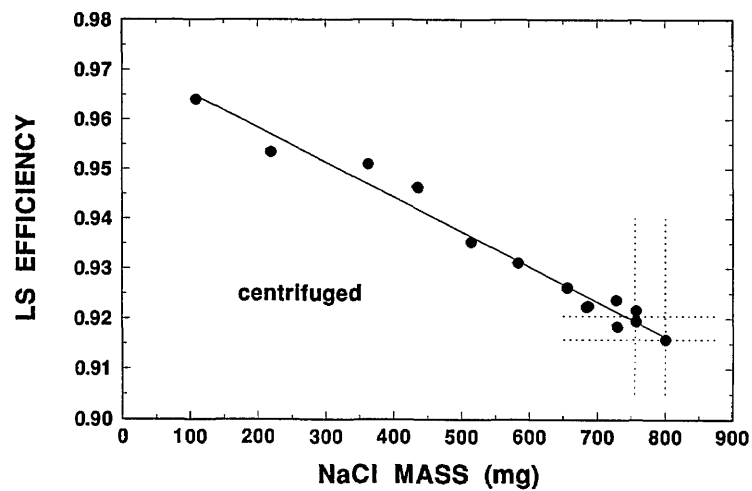
The more massive 757 mg NaCl source had an initially lower efficiency, as might be expected. For both sources, one can observe an abrupt decrease in efficiency of about 1% in 1 d (i.e., $d\epsilon/dt = 0.01 \text{ d}^{-1}$). This rate of change gradually decreased over the next several days until the two slopes for the efficiency became somewhat constant (over the interval from about 5 d to 30 d) at about $d\epsilon/dt = -0.0017 \text{ d}^{-1}$ for the 219 mg source and $d\epsilon/dt = -0.0026 \text{ d}^{-1}$ for the 757 mg source. The less massive source not only had a smaller slope, but its transitory inflection point from its initial $d\epsilon/dt = 0.01 \text{ d}^{-1}$ slope occurred earlier. These effects



a



b



c

Fig. 1. ^{36}Cl LS efficiency as a function of total NaCl loading in precipitated-sample cocktails for three settling conditions: (a) "initial" after 2 d to 4 d; (b) "further" settling after 14 d to 16 d; and (c) for "centrifuged" samples.

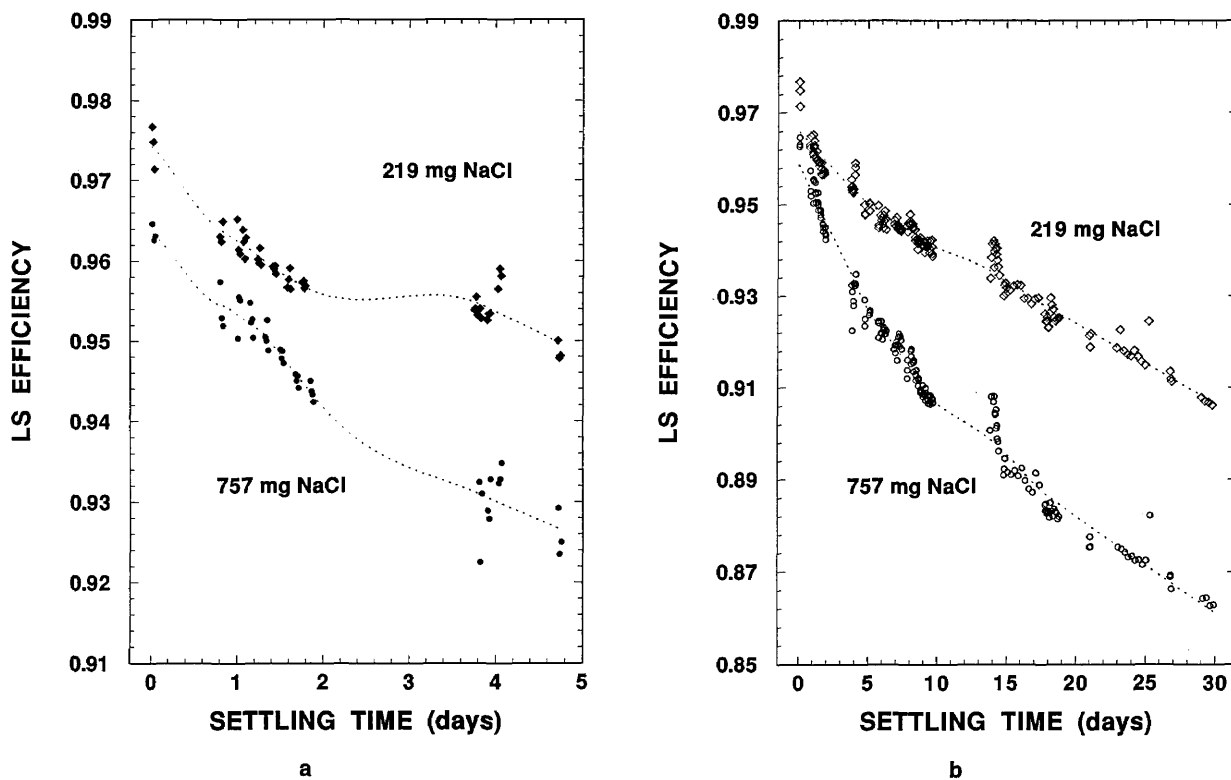


Fig. 2. ^{36}Cl LS efficiency as a function of settling time for two precipitated-sample cocktails containing 219 mg and 757 mg NaCl. Measurements data for settling times (a) up to 5 d, and (b) up to 30 d. The dotted curves have no significance and are only meant to guide the eye.

may be explainable in terms of the more massive source having a larger precipitate that settled more rapidly. The apparent nearly linear decreases in efficiency became even more constant after about 15 d of settling, although it now appeared that the more massive 757 mg source had a $d\epsilon/dt$ slope less than that for the 219 mg source. The efficiency data for settling times in the interval from 15 to 60 d are shown in Fig. 3, and demonstrate the near linearity in this region. Linear regressions (shown as dotted lines in Fig. 3) provided fitted slopes of $d\epsilon/dt = -0.00173 \text{ d}^{-1}$ and -0.00141 d^{-1} .

One may note that the efficiencies obtained with the centrifuged samples [Table 8 and Fig. 1(c)] corresponded to efficiencies that were also obtained after about 6 d or 7 d of settling.

Up to this time, $t \leq 60$ d, except for the reversal in the relative magnitudes of the slopes for the two sources, the efficiency settling data seemed reasonably consistent and intuitively explainable.

After settling times greater than about 60 d, however, the efficiency data for both the 219 mg and 757 mg NaCl sources (see Fig. 4) had abrupt and very rapid decreases. The less massive 219 mg source began to change at around 65 d to 70 d, and

its efficiency dropped to nearly 60% within the next 30 d; whereas the more massive 757 mg source did not exhibit this change until about 75 d to 80 d, but then underwent an even more rapid efficiency drop to less than 55% within the next 20 d. This unexpected and inexplicable behavior precluded hopes of ever finding a steady-state efficiency condition for counting the precipitated-sample sources.

The quite noticeable wide fluctuations and variations in the efficiency versus settling time data (Figs. 2–4) were also disconcerting and disappointing. The cause of this substantial irreproducibility was initially unknown. Replicate and sequential measurements on the same sample often exhibited greater efficiency variations than efficiency values obtained at much later settling times. These variations could be as great as several percent. Similarly, the measured efficiencies on a given sample could on occasion even exhibit increases as a function of increasing settling time. This irreproducibility was eventually attributed to partial stirrings of the settled precipitates when the counting sources moved up and down on the elevator of the automatic sample changer for the LS counting system.

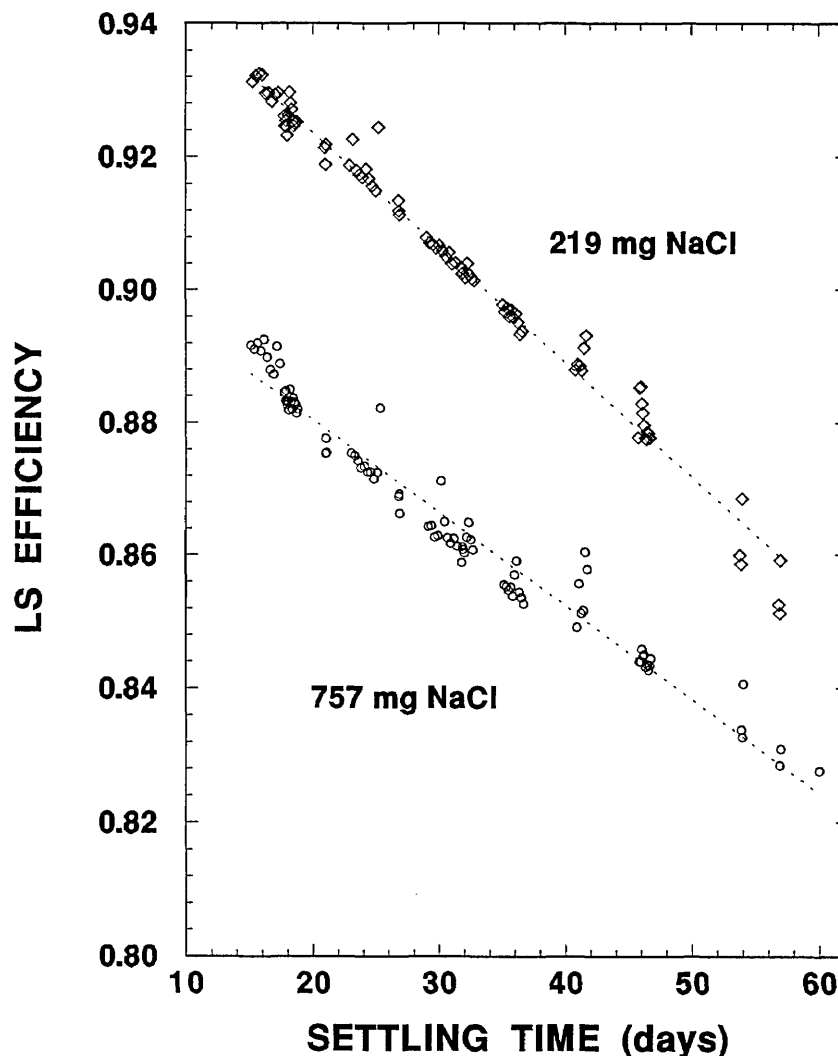


Fig. 3. ^{36}Cl LS efficiency data for the two precipitated samples for settling times between 15 d and 60 d. The dotted lines are χ^2 -minimized linear regressions.

Therefore, the best one might hope for in attempting to assay solution D was to try to make relative measurements against solution A for closely matched precipitated samples (i.e., in terms of their total NaCl loading) and as a function of matched settling times.

Comparison of the ^{36}Cl LS spectra for different NaCl loadings in both clear and precipitated-sample sources are also informative. Figure 5 contains four typical spectra under four widely differing conditions. The spectra, obtained with the Packard LS system, are presented in terms of the measured efficiency per channel for samples containing known quantities of ^{36}Cl as a function of the channel number. The channel numbers are directly proportional to β^- energies. The first spectrum, for sample SA1 (see Table 3), is that with least

quenching. This sample was a clear solution containing ≈ 0.02 mg NaCl and about 0.22% water, and had an efficiency of 0.986. The spectral shape has the overall, general appearance of that expected for an undistorted ^{36}Cl beta-ray spectrum (having a single, non-unique second forbidden β^- -transition) [12]. The second spectrum, for sample SA7, is only modestly quenched from that of first, although the sample contains 109 mg NaCl and 9.9% water. The total efficiency, summed over all channels for this sample, is still 0.986, but the spectral shifts to lower energies are quite evident. Other spectra for samples of composition intermediate between the above two also exhibit these very gradual shifts between the extremes of the above two spectra. With any further increases in the NaCl content in the samples to the point at which precip-

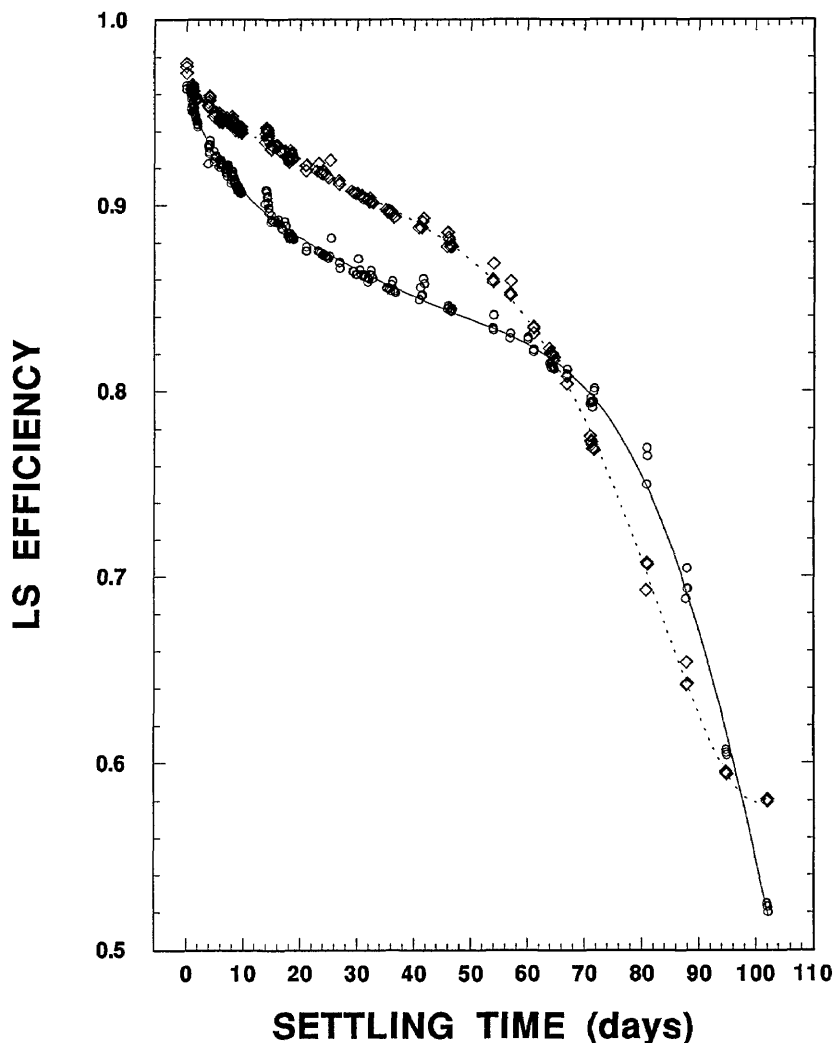


Fig. 4. ^{36}Cl LS efficiency data for the two precipitated samples for settling times up to 102 d. The dotted curve is that for the 219 mg NaCl sample; the solid curve for the 757 mg NaCl sample. Refer to the text for discussion.

itates begin to form, the spectral shapes change dramatically. The spectrum for precipitated sample SA11 (containing 227 mg NaCl and 9.6% water) in Fig. 5 shows this dramatic change. The doubling of the NaCl content in this sample from that of the last spectrum resulted in a drastically compressed spectral shape. The total efficiency was still quite large at about 95%, but a substantial fraction of this efficiency derived from detected events at energies corresponding to channel numbers of less than 100. The final spectrum in Fig. 5 for sample T10b (see Table 8) shows the continuing spectral shifts to lower energies and to lower total efficiencies with increasing NaCl content in precipitated samples. Other spectra (not shown) for precipitated samples as a function of settling time exhibit identical effects.

2.1.4 LS Counting of Solution D Two LS counting sources containing gravimetrically-determined aliquots of solution D were prepared to conduct the assay. The samples, labelled D1 and D2, contained 5.2075 g and 5.5432 g of solution D in 15.160 g and 15.439 g of scintillator, respectively. Both samples contained massive precipitates; and their total loadings corresponded to 755 mg NaCl and 34.4% water for D1, and 804 mg NaCl and 35.9% water for D2

The samples were measured relative to matched precipitated samples of solution A, and with corresponding matched blanks, on the Beckman LS system. The samples were matched in terms of total NaCl mass and the approximate water content (mass percent) in each cocktail. Each experimental trial consisted of 8 to 15 replicate measurement

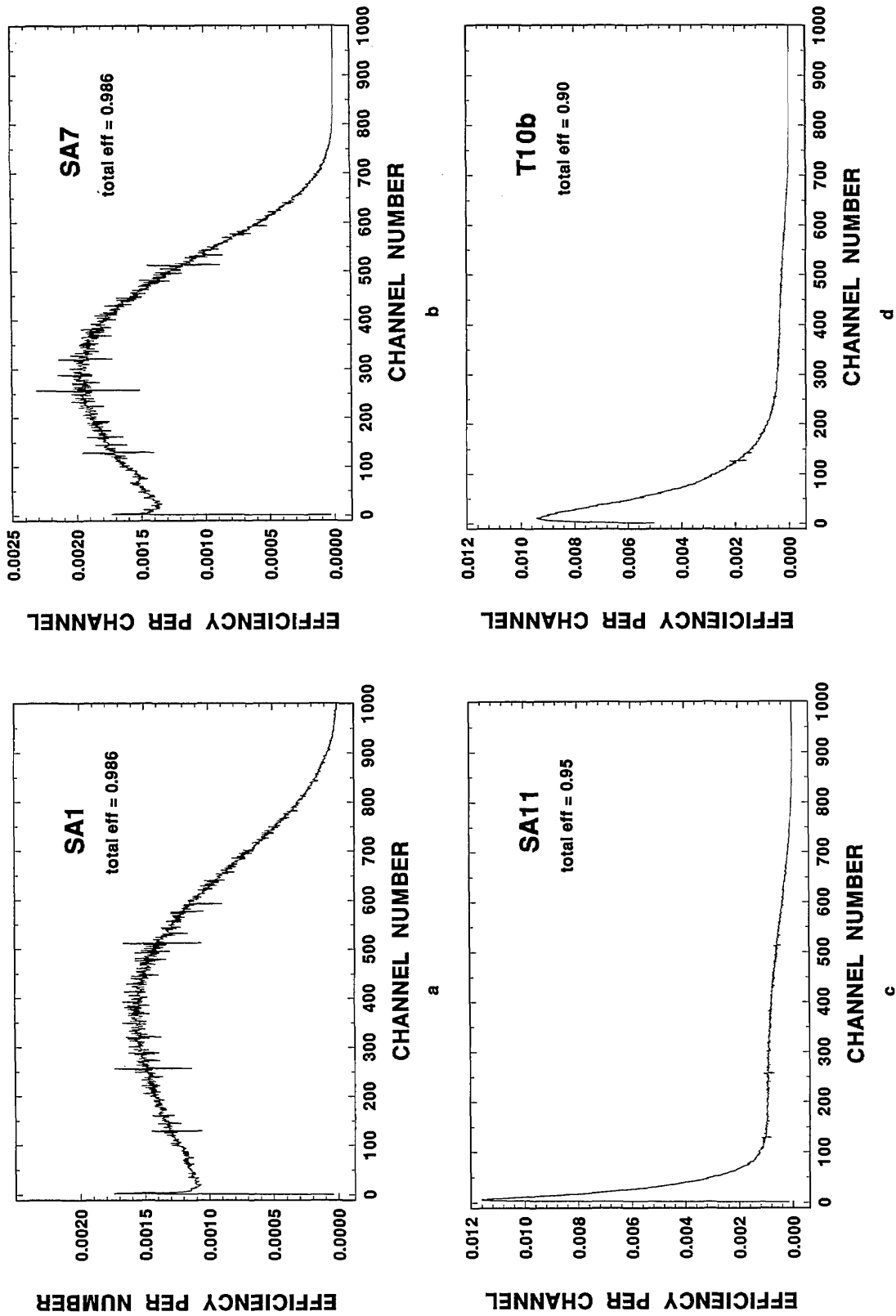


Fig. 5. Typical ^{36}Cl LS spectra of cocktails loaded with varying NaCl content: (a) SA1, a clear sample containing ≈ 0.02 mg NaCl in 0.22% water; (b) SA7, a clear sample containing 111 mg NaCl in 9.3% water; (c) SA11, a precipitated sample containing 227 mg NaCl in 9.6% water; and (d) T10b, a precipitated sample containing 757 mg NaCl in 26% water. Refer to the text and tables for typical quench parameters and efficiencies under these conditions.

cycles. Each cycle consisted of sequential measurements of a solution D sample (either D1 or D2), a matched blank for background subtraction, and matched solution A samples. The three sample types (D, blank, and A) were measured alternately in order to closely match settling times between samples. Counting times for the measurement of each sample ranged from 6,000 s to 18,000 s. The total counting time on each sample for a given trial (i.e., 8 cycles to 15 cycles) therefore ranged from 60,000 s to 180,000 s. Such long counting time intervals were required because of the low total counting rates for the solution D samples.

Five such closely matched trials on each solution D sample (D1 and D2) were performed, and the results are summarized in Table 9. For each trial, the table provides the mean count rate concentration ($\text{cps} \cdot \text{g}^{-1}$) obtained by averaging the individual background-corrected count rates obtained from the n measurement cycles, the calculated relative

standard deviation of the mean s_m for the measurement set, and the total statistical (Poisson) counting precision, in terms of a relative standard deviation s_p , calculated from the total number of sample and background counts obtained in the n measurement cycles. As indicated, the magnitude of both the s_m and s_p precision estimators are substantial, typically ranging from 2% to 4%. This appreciable imprecision is due in part to the large measurement variations obtained with precipitated samples as discussed previously in Sec. 2.1.3, and in part to the large statistical "counting error" for these low level samples. The net sample count rate was typically only about 15% of background. For example, the first row entry for sample D1 in Table 9 had an average background count rate of 1.071 cps ($s_m = 0.59\%$), gross counting rates ranging from 1.196 cps to 1.263 cps, and hence net rates of about 0.125 cps to 0.192 cps for the sample (with a mean of 0.157 cps and $s_m = 4.4\%$).

Table 9. LS counting results for precipitated samples of solution D as a function of settling time

LS Sample	Sample settling conditions	LS Counting results				Assumed efficiency ^c	³⁶ Cl Activity concentration ($\text{Bq} \cdot \text{g}^{-1}$) ^d	Ratio reported to measured value ^e
		Mean rate ($\text{cps} \cdot \text{g}^{-1}$)	s_m^a (%)	n^a	s_p^b (%)			
D1	Initial (2 d–4 d)	0.03016	4.4	9	4.2	0.88 (0.025)	0.03427	1.036
	Centrifuged	0.03332	2.4	8	4.0	0.921 (0.002)	0.03618	0.982
	Further (14 d–16 d)	0.03244	2.2	15	3.0	0.899 (0.003)	0.03608	0.984
	After 21 d–33 d	0.03105	2.8	10	3.6	0.866 (0.002)	0.03586	0.990
	After 58 d–61 d	0.02988	2.3	9	3.8	0.832 (0.002)	0.03591	0.988
D2	Initial (2 d–4 d)	0.03029	3.6	10	3.7	0.88 (0.025)	0.03442	1.032
	Centrifuged	0.03417	3.8	8	3.7	0.916 (0.002)	0.03730	0.952
	Further (14 d–16 d)	0.03383	1.9	14	2.8	0.895 (0.003)	0.03780	0.939
	After 21 d–23 d	0.03080	2.9	10	3.6	0.863 (0.002)	0.03569	0.995
	After 58 d–61 d	0.02886	2.4	8	3.8	0.828 (0.002)	0.03485	1.019

^a Relative standard deviation of the mean in percent for the tabulated number of measurements, n .

^b The total statistical (Poisson) counting precision in terms of a relative standard deviation in percent, obtained in the n measurements. Refer to earlier footnote.

^c The ³⁶Cl efficiency obtained from samples of solution A with matched composition and counted after comparable settling times. Values in parentheses are estimated standard deviations for the tabulated efficiencies.

^d Obtained from the LS mean count rate and the assumed ³⁶Cl efficiency.

^e For a reported value of 0.03551 $\text{Bq} \cdot \text{g}^{-1}$. See Table 1.

The assumed efficiencies in Table 9 were obtained from averaging the LS results for the solution A samples across all matched measurements within an n -measurement cycle trial. The ^{36}Cl activity concentration in samples D1 and D2 were then calculated from the similarly averaged D1 and D2 mean count rate concentrations and these efficiency values. The data were also analyzed by calculating the individual D to A ratio for each adjacent measurement pair within a cycle, and then averaging the resulting n measurement ^{36}Cl activity concentrations. The results of the two calculational approaches were invariant within statistical precision. The uncertainties in the efficiencies determined in this way were estimated to be $\pm 2\%$ to $\pm 3\%$ at an assumed one standard deviation uncertainty interval. This estimation may be better appreciated by examination of the settling data of Fig. 1. The vertical dotted lines at around 750 mg and 800 mg NaCl correspond to the NaCl content in samples D1 and D2. The three dotted horizontal lines in Fig. 1(a) represent best estimates of the mean efficiency (0.88), and the lower and upper bounds on the uncertainty interval which corresponds to 0.88 ± 0.025 . Estimates of the assumed efficiency means are similarly illustrated in Figs. 1(b) and 1(c). These uncertainty estimates however do not directly address possible additional uncertainty components due to sample composition mismatching differences.

It should also be mentioned that the timings of the matched measurement trials (data of Table 9) were in part selected to correspond to settling times having a fairly systematic regularity, such as the near linear region exhibited in Fig. 3.

The last column of Table 9 compares the ten independently-determined values of the solution D activity concentration to that reported for the AMS standard (compare Table 1). These activity concentration ratios are also equivalent, however, to ratios of the reported to measured D/A dilution factors. Table 10 summarizes these comparison ratios in terms of several computed statistical estimators. It is evident that there are no substantial differences between the grand means for sample D1, D2, and both samples. Because of this, as well as the large number of replications and sampling combinations that comprise these grand means, it is reasonable to conclude that the additional uncertainties due to possible sample composition mismatches for these precipitated samples were not dominant, and that they did not introduce a significant bias error. There are also no significant differences in the three averaging methods used to calculate the grand means. These summarized results (Table 10) clearly confirm the solution D activity concentration relative to that of solution A (or equivalently the D/A dilution factor) to an absolute difference of roughly 1%, and to better than 2% in worst cases. The uncertainty in these comparisons, mainly on consideration of the values of s_m and s_p , are roughly $\pm 3\%$ at a relative three standard deviation uncertainty interval. All other possible contributing uncertainty components, e.g., those due to radioactive decay corrections, background subtraction corrections, dead time counting corrections, timing measurements, gravimetric determinations, LS cocktail stability, or efficiency mismatches arising from sample composition and quenching differences are either embodied in the overall uncertainty estimate or are negligible.

Table 10. Statistical summary of the LS counting results for solution D

Computed statistic ^a	Sample D1	Sample D2	Both samples
Grand mean (unweighted)	0.996	0.987	0.992
s_m (%) ^b for grand mean	1.0	1.1	1.0
Number of individual means in grand mean	5	5	10
s_p (%) ^c for grand mean	1.6	1.5	1.1
Grand mean (weighted by number of measurements in each individual mean)	0.995	0.984	0.989
Grand mean (weighted by $1/s_m^2$ in each individual mean)	0.989	0.979	0.984

^a Based on the data of Table 9.

^b Relative standard deviation of the mean expressed in percent.

^c Total statistical (Poisson) counting precision in terms of a relative standard deviation in percent obtained over all measurements. Refer to earlier footnote.

2.2 Proportional Counting Measurements

An additional sequence of assay measurements of solutions A, B, C, and D were performed by low-background $2\pi\beta^-$ gas-flow proportional counting of solid sources. It was known *a priori* that their results were likely to be less accurate than those obtained by LS counting; and therefore, they were only intended to serve as secondary, confirmatory measurements. In addition, these solid source measurements were in large part designed to serve as an experimental backup for the assay of solution D, and were initiated before it was known whether LS counting of solution D was feasible.

The counting sources were prepared by dispensing gravimetrically-determined aliquots of the solutions and, in some cases, appropriate quantities of the NaCl blank solution onto source mounts which consisted of circular disks of 39 mm diameter ion exchange papers that were fixed onto larger 52 mm diameter stainless steel planchet inserts. The dispensed solutions were subsequently evaporated to dryness in air, and the mounts were then covered and sealed with a mylar film having a surface density of $1.75 \text{ mg} \cdot \text{cm}^{-2}$. The ion exchange paper used for the source mounts was a Reeve Angel Amberlite, grade SB-2, filter matrix containing IRA-400 resin in Cl^- form which is a strong-base-type anion exchanger.

Two sources for each solution were prepared as summarized in Table 11. For solutions A and B, the order of dispensing the active and blank solutions was reversed in preparing each of their two sources. For the first sources (either A1 or B1), the

blank solution was dispensed first and followed by the addition of the active (either A or B) solution; whereas for the second source (either A2 or B2), the active solution was dispensed first and followed by the blank solution. They were prepared in this way so that any possible differences in the β^- self absorption due to the addition of the blank solution could be accounted for. The sources for solutions C and D were prepared with undiluted aliquots of the solutions.

The evaporated sources were visibly irregular in the distribution and thickness of the NaCl crystals. The average NaCl-crystal surface densities for the sources ranged from about $10 \text{ mg} \cdot \text{cm}^{-2}$ to $13 \text{ mg} \cdot \text{cm}^{-2}$. Although undesirable from a β^- counting perspective, the use of such thick self-absorbing sources was necessitated by the low activity concentration for solution D that required the use of large sample aliquots. In order to make relative measurements, the sources for solutions A, B, and C were matched to those for solution D.

The $2\pi\beta^-$ measurements of the solid sources were performed with a Berthold LB-770 11-channel low-level planchet counting system. The system comprises ten separate gas-flow proportional counter tubes that allow the simultaneous measurement of ten 60 mm diameter sample planchets, and a common guard counter tube, located above the ten measuring counter tubes, that acts as an anticoincidence shield to achieve low backgrounds. The counting gas was a "P-10" argon-methane (90:10) mixture. The counters are housed in a 10 cm lead shield for additional external radiation shielding.

Table 11. Composition of the evaporated solid sources of solutions A, B, C, and D used for the $2\pi\beta^-$ gas-flow-proportional counting measurements

Solution	Source identity	Mass of active solution (g)	Mass of blank NaCl solution (g)	Total mass of NaCl (mg)	Approximate ^{36}Cl activity (Bq) ^a
A	A1	0.033517	0.85851	124.5	370
	A2	0.046795	1.0955	158.9	510
B	B1	0.42990	0.42070	123.3	49
	B2	0.39177	0.40158	115.0	45
C	C1	0.84273		122.2	1.7
	C2	0.87004		126.2	1.7
D	D1	0.79823		115.7	0.03
	D2	0.88431		128.2	0.03
Blank	b		0.85921	124.6	

^a Based on the reported activity concentrations given in Table 1.

Typical background count rates for the ten counters range from about 0.2 to 0.9 counts per minute when operated on the high voltage beta plateau. In comparison, the large flat guard counter has a background rate of about 650 counts per minute. Counter tubes located at the ends of the housing have the larger backgrounds because of less lead and anticoincidence shielding. Therefore, the center or middle counters were chosen for measurement of the lower level sources.

The background considerations were critically important. Assuming even an idealized 2π detection efficiency of 0.5 with no self-absorption losses, a 0.03 Bq solution D source would provide a net count rate of only about 0.9 cpm. Hence, the background count rates for even the lowest-background counters (i.e., 0.2 cpm) made substantial contributions to the gross count rates for the solution D sources and needed to be determined very precisely.

The crossover of stray and scattered radiation to the counters from adjacent source positions was reported by the manufacturer to be approximately 0.002% for a pure beta (^{90}Sr - ^{90}Y) source and less than 0.1% for a beta-gamma (^{137}Cs) source. Somewhat larger stray factors were observed with the ^{36}Cl (a nearly pure beta emitter) solution A sources used in this work. The largest factor, for one of the end counter tubes with an adjacent source, was 0.3%. The factors for middle or center counters, again with adjacent sources, were nearly an order of magnitude less.

Detection efficiency variations between the ten counters were too large to rely on the use of an average efficiency. The observed efficiency variations for ^{36}Cl between the six lowest-background counters ranged from 1% to 6% based on measurements of one source across the counters. The apparent detection efficiencies for the sources were in the range of 0.33 to 0.40. Figure 6 illustrates the observed efficiencies, and the β^- self absorption in the solid sources for the six sources of solutions A, B, and C as measured in two of the counters. The reported activity concentrations for solutions A, B, and C (Table 1) were assumed in deriving these apparent efficiencies. Excepting the most massive source (A2), the variations in efficiency (within a given counter) for the other more closely matched sources were, of course, much smaller. The apparent efficiency variations between these other five sources, mainly due to differences in the source β^- self absorption, were about $\pm 2\%$ to $\pm 3\%$ as indicated in the data of Fig. 6. These observed dispersions however also include contributions from the

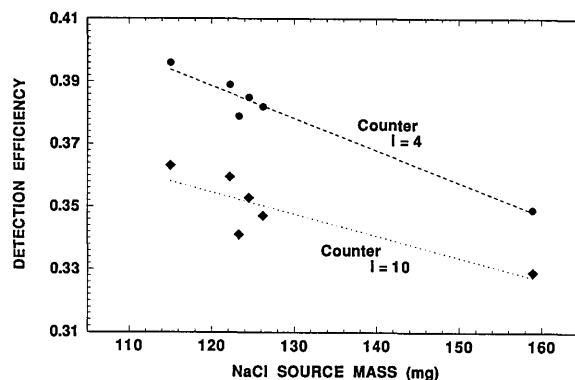


Fig. 6. Apparent $2\pi\beta^-$ gas-flow proportional counting detection efficiency for two counters obtained with the solid sources of solutions A, B, and C assuming the reported (Table 1) ^{36}Cl activity concentrations.

statistical counting imprecision and differences arising from source positioning and placement in the counters.

Dead-time count rate losses were fairly negligible for any of the sources. The electronic pulse resolving times for the proportional counters were of the order of $\tau = 10 \mu\text{s}$, thereby giving dead-time corrections ranging from less than 0.2% for the solution A sources, to less than 0.02% for the solution B sources, to less than 0.001% for the solution C sources, and less than 0.00001% for the solution D sources.

With the above source characteristic, background, detection efficiency, and β^- counting considerations in mind, the experimental design for the measurements was based on the following criteria: (1) a relative measurement between any two sources required that both sources be counted on the same counter to assure equivalent detection efficiencies; (2) the background count rate for that same counter needed to be precisely determined; (3) measurement of several different combinations of the sources for each solution pair were required to account for possible differences in source preparation and β^- self absorption in the sources; (4) the relative determinations for the various solution pairs also needed to be based on measurements in several counters; (5) measurements of different sources and backgrounds on the same counter needed to be interspersed to account for any temporal differences; (6) long counting time intervals, for the backgrounds and low count rate sources, were required to achieve good statistical precision; and (7) a large number of replicate measurements were needed to account for possible differences in positioning the sources in the counters.

The experimental design employed for the measurements is outlined in the matrix of Fig. 7. The matrix provides the locations of the sources alternately counted in the various counters as a function of the measurement sequence. Each measurement cycle j consisted of five to seven replicate measurements where each replicate was of 20 min to 1000 min in duration. Sources for solutions C and D (C1, C2, D1, and D2) were measured interchangeably, as shown, in the lowest-background counters $i = 2, 3, 4, 6, 7,$ and 8 . The shaded elements of the matrix represent background measurements of equal time duration. Counters 5, 9, and 10 were used as controls with solution A and B sources in case any normalizations between measurement cycles were necessary. Counter 1 was used as a background control for all measurement cycles. Measurement of the blank source (b) was interspersed between counters and measurement cycles. The total continuous counting time for all 18 measurement cycles exceeded 25 d of live time (37,000 min) which was conducted over approximately 38 d of real time.

The results of these counting measurements consisted of a huge [18 cycle \times 10 counter \times 5 to 7 measurement] three-dimensional matrix of data which was reduced to derive a substantial number of relative determinations of the activity concentrations, first for the various source pairs, and ultimately for

their respective solution pairs. For example, the results from any one of the counters $j = 2, 3,$ and 4 provide between 10 to 12 independent measurements of C1, D1, and the background (cycles $j = 1$ through 6) as well as five to seven measurements on each of sources A1, A2, B1, and B2 along with an additional two measurements of blank source b and eight measurements of background (cycles 7 through 18). These results not only provide average determinations of the C1/D1 source activity concentration ratio for each of the three counters, but also determinations of the B1/D1, B2/D1, A1/D1, A2/D1, B1/C1, B2/C1, A1/C1, A2/C1, A1/B1, A1/B2, A2/B1, and A2/B2 ratios for each counter. Similarly, the results from any one of the $j = 6, 7,$ and 8 counters provide equally determined ratios for the C2/D2 source pair, and another comparable set of determinations for all the same source pairs listed above. Table 12 summarizes the total number of determinations that were made for all possible combinations of the various source pairs on each counter to provide their respective solution pair ratios. In examining Table 12 it is important to note that, based on the experimental design (Fig. 7), not all source pair ratios for a given counter were determined with equal numbers of measurements for both sources. Table 13 summarizes the total number of measurements made in each counter for each source. In analyzing the data set, the measurement results for a given source pair combination (within a given counter i) was averaged over all appropriate measurement cycles j . Analyses of smaller subsets of the data in terms of calculating the ratios for individual i and j combinations indicated that there were no significant differences with the results obtained by averaging over all cycles. Obviously, this conclusion would equally be valid as long as there were no significant differences in the source count rates between cycles within a given counter. Figure 8 demonstrates the good reproducibility in the relative count rates for four sources and background over three measurement cycles, $j = 1, 2,$ and 3 . The plotted results for three of the sources (B1, A1, and C1) in Fig. 8 were normalized by somewhat arbitrary factors merely to display the results on a similar scale. These illustrated data, obtained over an approximate 11-day interval, are representative and typical.

Detailed results for the determined C/D solution pair ratios are provided in Table 14. These results are based on the C1/D1 (in counters $i = 2, 3,$ and 4) and C2/D2 (in counters $i = 6, 7,$ and 8) source pairs from the first six measurement cycles ($j = 1$ through 6). The results are tabulated in terms of the mean

$i =$	2	3	4	6	7	8	1	5	9	10	$n(j) =$	$t(n) =$
$j = 1$	C1	D1		C2	D2			B1	b	A1	5	1000
2	C1	D1		C2	D2			B1	b	A1	5	1000
3	C1	D1		C2	D2			B1	b	A1	6	1000
4	D1	C1		D2	C2			B1	b	A1	5	1000
5	D1	C1		D2	C2			B1	b	A1	7	1000
6	D1	C1		D2	C2			B1	b	A1	5	1000
7	A1				b	B1		B2		A2	5	100
8	A1				B1	b		B2		A2	5	100
9	b		A1	B1				B2		A2	7	100
10		b	B1	A1				B2		A2	6	100
11		B1		b	A1			B2		A2	5	100
12	B1		b			A1		B2		A2	6	100
13	A2	b				B2		A1		B1	5	20
14	b	A2				B2		A1		B1	5	20
15			A2	B2		b		A1		B1	5	20
16			B2	A2		b		A1		B1	5	20
17			B2	b		A2		A1		B1	5	20
18	B2		b		A2		A1		B1		5	20

i = counter identity number
 j = measurement cycle identity number
 $n(j)$ = number of measurements in cycle
 $t(n)$ = count time (minutes) for each measurement
 shaded areas are background measurements

Fig. 7. Experimental design for the $2\pi\beta^-$ gas-flow proportional counting measurements of evaporated solid sources of solutions A, B, C, and D. The design consists of a matrix of the location and measurement sequence of the counting sources in chamber i for measurement cycle j with n_j replicate measurements, each of counting time duration t_n .

Table 12. Summary of all source pair measurement combinations used in the determinations of their respective solution pair activity concentration ratio (or dilution factors) by $2\pi\beta^-$ gas-flow proportional counting

Solution pair	Total number of determinations	Source pair combinations for measurements made in counter i^a							
		$i=2$	$i=3$	$i=4$	$i=6$	$i=7$	$i=8$	$i=5$	$i=10$
C/D	6	C1/D1	C1/D1	C1/D1	C2/D2	C2/D2	C2/D2		
B/D	12	B1/D1 B2/D1	B1/D1 B2/D1	B1/D1 B2/D1	B1/D2 B2/D2	B1/D2 B2/D2	B1/D2 B2/D2		
A/D	12	A1/D1 A2/D1	A1/D1 A2/D1	A1/D1 A2/D1	A1/D2 A2/D2	A1/D2 A2/D2	A1/D2 A2/D2		
B/C	12	B1/C1 B2/C1	B1/C1 B2/C1	B1/C1 B2/C1	B1/C2 B2/C2	B1/C2 B2/C2	B1/C2 B2/C2		
A/C	12	A1/C1 A2/C1	A1/C1 A2/C1	A1/C1 A2/C1	A1/C2 A2/C2	A1/C2 A2/C2	A1/C2 A2/C2		
A/B	28	A1/B1 A1/B2 A2/B1 A2/B2	A1/B1 A1/B2 A2/B1 A2/B2	A1/B1 A1/B2 A2/B1 A2/B2	A1/B1 A1/B2 A2/B1 A2/B2	A1/B1 A1/B2 A2/B1 A2/B2	A1/B1 A1/B2 A2/B1 A2/B2	A1/B1 A1/B2	A1/B1 A2/B1

^a Refer to Fig. 6.**Table 13.** Summary of the numbers of $2\pi\beta^-$ gas-flow-proportional counting measurements performed on the evaporated solid sources

Source identity ^a	Number of meas. cycles source was measured ^b	Total number of measurements made in counter i for each source ^b									
		$i=2$	$i=3$	$i=4$	$i=6$	$i=7$	$i=8$	$i=1$	$i=5$	$i=9$	$i=10$
bkgnd	18	42	45	40	42	46	43	97		64	
A1	18	5	5	7	6	5	6		30		33
A2	12	5	5	5	5	5	5				34
B1	18	6	5	6	7	5	5		33		30
B2	12	5	5	5	5	5	5		34		
C1	6	10	11	12							
C2	6				10	11	12				
D1	6	12	10	11							
D2	6				12	10	11				
blank	18	12	11	11	10	10	10			33	

^a See Table 11.^b Refer to Fig. 6.

count rate for each source in each detector averaged over all the $n = 10$ to 12 measurements in both counting cycles, and the two precision estimators, s_m and s_p , for each mean. The magnitudes of s_m and s_p clearly indicate the much better precision in the measurement of the solution C sources compared to the solution D or background measurements. The activity concentration ratios (last column of Table 14) were then obtained from the relation

$$R_{C/D} = \frac{(d_C - d_{\text{bkgnd}})/m_C}{(d_D - d_{\text{bkgnd}})/m_D}$$

where d_C and d_D are the mean count rates for the solution C and D sources, d_{bkgnd} is the mean background count rate, and m_C and m_D are the aliquot masses of the C and D solution sources. No dead-time loss corrections were made, nor were any attempts made to try to account for differences in β^- self absorption in the sources. The six determinations (three for the C1/D1 source pair, and three

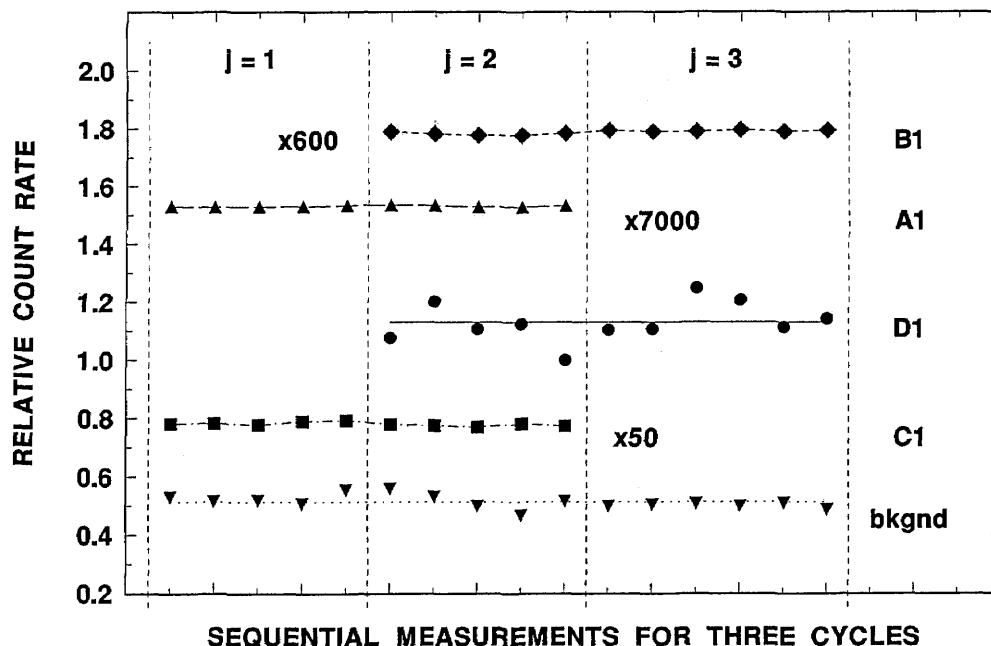


Fig. 8. Typical $2\pi\beta^-$ gas-flow proportional counting measurement results in terms of relative count rates for sequential measurements over three measurement cycles j for five sources: B1 (measured in counter $i=5$); A1 ($i=10$); D1 ($i=4$); C1 ($i=2$); and background ($i=1$).

for C2/D2) have a mean ratio of 52.37 with a standard deviation of the mean of $s_m(n=6)=2.0\%$. There are no significant differences between this mean ratio and the mean obtained from just the C1/D1 source pair values (52.08) or that for the C2/D2 pair values (52.65). Analyses of the mean ratio results across other variables such as by counter number i for a specific source pair and cycle number j , based on t -tests of differences in the various means and on χ^2 - and F -tests of the homogeneity in the various subset sample means and variances, indicated that there were no statistically significant differences in any of the tested subset sample means or variances.

Similar analyses were performed on all the other 76 source pair combinations (see Table 12) to obtain the mean solution pair ratios. For the sake of brevity, the detailed counting result data (analogous to that presented in Table 14) for these are omitted here. A summary of the cumulated mean ratios for all of these determinations are however tabulated in Table 15, which also contains the comparisons to the reported ratios of Table 1. The first row of Table 15, for example, devolves directly from the analyzed results of Table 14. As before, subsets of the mean ratio results across the source, counter number, and measurement cycle variables were tested (t -, χ^2 -, and F -tests, as well as

by sequential 2-variable ANOVA techniques) for differences in subset means and variances. Excepting a difference in ratios obtained with sources A1 and A2, attributed to β^- self absorption differences (see below) in these two sources, all of the other subset sample means and variances were statistically equivalent.

The mean activity concentration ratios or dilution factors for the solution pairs have relative standard deviations of the mean s_m ranging from less than 0.2% for the 28 determinations of the A/B ratio to over 4% for the A/D ratio. As somewhat expected, the s_m values are typically smaller for those solution pairs that are closer in activity concentration (A/B, B/C, and C/D), and increasingly larger for those having greater activity concentration differences (A/C, B/D, and A/D). The very small $s_m=0.17\%$ value for the A/B ratio was also surprising in that there was a statistically significant difference in the A1/A2 source pair ratios across all i and j counter number and measurement cycle variables. The difference was attributed to the difference in β^- self absorption in the more massive A2 source. The average A1/A2 difference observed over all measurements in all seven counters was 4.6%. No attempt was made however to account for this observed absorption difference in the A2 and A1 sources in deriving any of the solution A

Table 14. Gas-flow proportional counting measurement results for the C/D solution pair activity concentration ratio (or dilution factor)

Counter <i>i</i> ^a	Source identity ^b	Mean count rate (cpm)	s_m^c (%)	n^d	s_p^e (%)	Activity concentration ratio for C/D ^f
2	C1	38.967	0.29	10	0.17	51.47
	bkgnd	0.2055	2.9	11	2.2	
	D1	0.9150	1.3	12	1.1	
3	C1	38.639	0.24	11	0.16	53.04
	bkgnd	0.2310	4.3	12	2.1	
	D1	0.9139	2.1	10	1.1	
4	C1	39.072	0.22	12	0.16	51.73
	bkgnd	0.4237	1.0	10	1.6	
	D1	1.1390	1.8	11	0.94	
6	C2	39.969	0.19	10	0.17	48.70
	bkgnd	0.4625	3.7	11	1.5	
	D2	1.2763	4.0	12	0.89	
7	C2	40.492	0.35	11	0.16	52.64
	bkgnd	0.2443	3.4	12	2.1	
	D2	1.0114	2.2	10	1.1	
8	C2	40.224	0.17	12	0.16	56.62
	bkgnd	0.4364	2.1	10	1.4	
	D2	1.1506	1.1	11	0.78	
mean ratio						52.37
n						6
s_m (%)						2.0

^a Refer to Fig. 6.^b See Table 11.^c Relative standard deviation of the mean count rate for n measurements expressed in percent.^d Total number of measurements in mean count rate.^e Total statistical (Poisson) counting precision in terms of a relative standard deviation in percent obtained over all n measurements.^f Refer to discussion in text.**Table 15.** Gas-flow-proportional counting measurement results of all solution pairs and comparisons to the reported gravimetric dilution factors

Solution pair	Mean ratio R_m^a	n^b	s_m^c (%)	Reported ratio R^d	R/R_m
C/D	52.37	6	2.0	56.24	1.074
B/D	2844.	12	2.8	3227.	1.135
A/D	261300.	12	4.1	308400.	1.180
B/C	54.80	12	0.65	57.39	1.047
A/C	5034.	12	1.1	5483.	1.089
A/B	91.87	28	0.17	95.55	1.040

^a Mean activity concentration ratio (or dilution factor) for the solution pair.^b Total number of determinations of the ratio as given in Table 12.^c Relative standard deviation of the mean ratio for n determinations expressed in percent.^d See Table 1.

ratios. That is, the ratios with solution A were derived by averaging the mean count rate concentration ratios over the averages of both the A2 and A1 sources. As stated above, there were no similarly observed statistically significant differences in the results for any of the other solution B, C, or D sources. The invariance in the C1/D1 and C2/D2 means of Table 14, discussed previously, is illustrative.

The comparisons between the reported activity concentration ratios or dilution factors R of Table 1 and the measured ratio R_m ranged from $R/R_m = 1.040$ for A/B to $R/R_m = 1.180$ for A/D. Again, it is perhaps not surprising that the greater differences were obtained for solutions having greater concentration differences (A/C, B/D, and A/D) and less for those having smaller concentration differences.

One of the more surprising, and rather inexplicable, findings is that all of the tabulated solution pair ratios are positively biased, i.e., $R/R_m > 1$. For every tabulated solution pair, the measurement result for the higher activity concentration solution source is always in the denominator of the comparator R/R_m . This might suggest the existence of some type of measurement bias that is systematic with increasing activity concentration, e.g., dead-time losses. The large magnitudes of the effect however would seem to exclude this as a possibility. Another interesting finding was that the differences between R and R_m were strongly correlated

with the measurement precision. Figure 9 shows the correlation plot for the R/R_m difference as a function of the relative standard deviation of the mean s_m . The reduced correlation coefficient is 0.957. This does, in part, imply that the magnitudes in the observed differences between the reported ratios R and the measured values R_m are indeed dependent on the measurement precision. The analyses of the overall uncertainties on these measurements (Table 16) further indicate that the magnitudes of the R/R_m differences can largely be attributed to the measurement uncertainties. Nonetheless, these uncertainty arguments somewhat beg the question of why the apparent differences in R/R_m were all positively biased in all six solution pair cases (Table 15). Any reasonable explanation for this remains unknown.

In conclusion, these $2\pi\beta^-$ gas-flow proportional counting measurements, intended to be secondary, confirmations of the LS results, verified the reported dilution factors to about 4% to 8% for the single-dilution solution pairs (A/B, B/C, and C/D) and to roughly 9% to 18% for the double- and triple-dilutions (A/C, B/D, and A/D solution pairs).

3. Summary and Concluding Notes

The first three dilutions in the eight-step serial gravimetric dilution scheme that was used to prepare a series of $^{36}\text{Cl}/\text{Cl}$ isotopic ratio AMS stan-

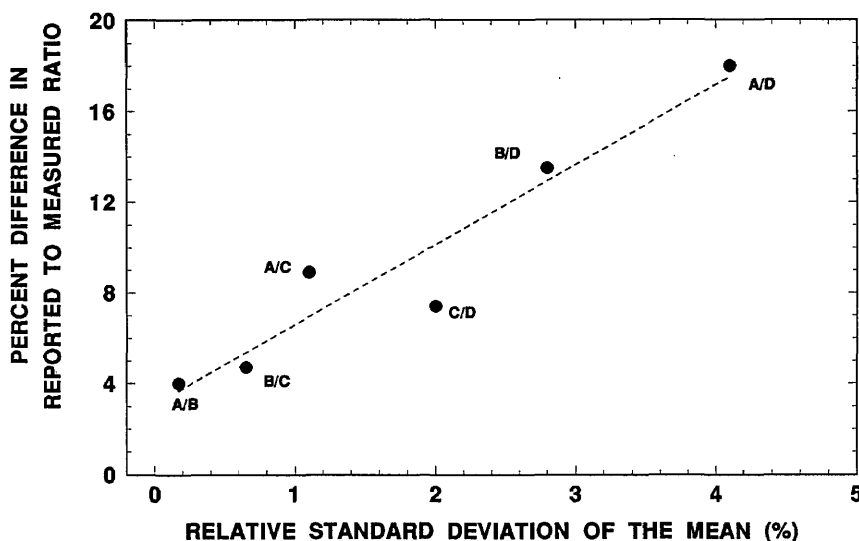


Fig. 9. Correlation between the absolute percent difference in the reported to measured ratios for the various solution pairs and the relative standard deviation of the mean for the measured ratio obtained by $2\pi\beta^-$ gas-flow proportional counting of evaporated solid sources.

Table 16. Uncertainty analyses for the $2\pi\beta^-$ gas-flow-proportional counting measurement of the solution pairs

Uncertainty components and propagated uncertainties	Relative uncertainties in percent for solution pairs					
	A/B	A/C	A/D	B/C	B/D	C/D
Measurement precision, s_m of Table 15	0.17	1.1	4.1	0.65	2.8	2.0
Gravimetric aliquot determinations	0.15	0.15	0.15	0.1	0.1	0.1
Background subtractions	a	a	a	a	a	a
Radioactive decay corrections	a	a	a	a	a	a
Dead-time losses	0.2	0.2	0.2	0.02	0.02	(a)
Source β^- self absorption	2.3–4.6 ^a	2.3–4.6 ^a	2.3–4.6 ^a	1–2. ^a	1–2. ^a	1–2. ^a
Source positioning variations	a	0.2 ^a	0.2 ^a	0.2 ^a	0.2 ^a	0.4 ^a
Combined standard uncertainty, u	2.3–4.6	2.6–4.7	4.7–6.2	1.2–2.1	3.0–3.5	2.3–2.9
$3 u^b$	7–14	8–14	14–19	4–6	9–10	7–9

^a Assumed to be wholly, or in part, embodied in s_m ; or negligible.

^b Corresponds to three times the combined uncertainty u , which is assumed to provide an uncertainty interval having a high level of confidence of roughly 95% to 99%.

dards were verified by the relative radioactivity measurements on four ^{36}Cl solutions described hereinbefore. The results, based on liquid scintillation counting of sample aliquots of the diluting solutions along with confirmatory measurements by gas-flow proportional counting of evaporated solid sources, were treated and discussed *in extenso* and are principally summarized in Tables 6, 10, and 15. In all cases, the reported gravimetric dilution factors were verified to absolute differences of better than 2%.

Beyond the findings of these validation measurements however, the investigations described here were also significant in terms of broadening the applications of several conventional techniques in radionuclidic metrology.

The assay of β^- emitting radionuclides by $4\pi\beta^-$ LS counting, particularly for reasonably energetic nearly pure beta emitters like ^{36}Cl , was previously well known, well documented, and somewhat straightforward. These LS techniques however were mainly employed with homogeneous solution cocktails having only moderate sample quenching. This study demonstrated the potential for LS counting of samples quenched with large quantities

of NaCl. Even for samples loaded with in excess of 100 mg NaCl, the cocktails appeared sufficiently stable, and the LS efficiencies remained surprisingly large at greater than 98%.

The discovery of the feasibility of performing highly-accurate LS measurements of precipitated samples was even more significant. This type of assay procedure is of necessity more complex and demanding. It requires relative measurements of closely matched precipitated samples as a function of matched settling times. Although the measurement precision with these very heterogeneous samples is inherently worse compared to conventional LS counting, it is possible with sufficient measurement trials and replications to achieve overall measurement uncertainties of a few percent.

Similarly, the results of the $2\pi\beta^-$ gas-flow proportional counting measurements clearly demonstrated the potentialities and power of a proficient experimental design even when dealing with an intrinsically inferior measurement method. The large β^- self-absorption losses in the rather thick solid sources and other attendant variabilities in the proportional counting still did not exclude the possibility of performing reasonably accurate assays.

It may be useful, in conclusion, to reconsider the difficult nature of these radioactivity measurements. They required solution assays that were nearly beyond the capability of available methodologies and technology. The solutions contained 145 mg NaCl per gram of solution and had ^{36}Cl activity concentrations ranging from $11 \text{ kBq} \cdot \text{g}^{-1}$ to $0.036 \text{ Bq} \cdot \text{g}^{-1}$, the latter having net counting rates that were only a few percent of typical backgrounds. Yet, the assays were performed with overall measurement uncertainties, corresponding to a relative three standard deviation uncertainty interval, of $\pm 1\%$ to $\pm 3\%$ in general for the LS counting measurements and about $\pm 5\%$ in best cases for the gas-flow proportional counting measurements. If anything then, this work illustrated that even when confronted with a difficult, seemingly impossible measurement task [such as that resulting from the worst conflicting combination of a sample containing a large carrier (e.g., salt) mass and a very low activity concentration], it is often possible to adapt, modify, or extend conventional methodologies to that task. This requires, of course, careful experimental designs and plans, painstaking and exacting metrological practices, and, perhaps most importantly, dogged determination and tenacious perseverance. This paper is no doubt a surprise to those individuals who believed that the assay of solution D by radioactivity measurements was not doable.

Acknowledgments

The authors gratefully acknowledge the contributions of their NIST colleagues: Dr. B. M. Coursey for consultations on LS counting; Dr. K. G. W. Inn for the loan of the flow-proportional counter in the low-level laboratory, instructions on the counter's use, and suggestions on the solid source preparations; Dr. J. M. R. Hutchinson for occasional direction and useful discussions; Mr. D. B. Gołas, Mr. J. Cessna, and Dr. L. L. Lucas for their ever-helpful advice and assistance in all laboratory matters; and Mrs. Gloria Wiersma for her cheerful and as-usual efficient preparation of this manuscript. Lastly but foremost, the senior author heartily thanks and acknowledges Mme. Dr. K. A. Maroufi-Collé and M. Arthur M. Collé for their contributing sacrifices and creative inspirations throughout the course of this work.

4. References

- [1] P. Sharma, P. W. Kubik, U. Fehn, et al., Development of ^{36}Cl Standards for AMS, Nucl. Instr. Meth. Phys. Res. **B52**, 410–415 (1990).
- [2] T. Straume, S. D. Egbert, W. A. Woolson, et al., Neutron Discrepancies in the DS86 Hiroshima Dosimetry System, Health Phys. **63**, 421–426 (1992).
- [3] R. P. Parker and R. H. Elrick, Cerenkov Counting As a Means of Assaying β -Emitting Radionuclides, in E. D. Branscome (ed.), Current Status of Liquid Scintillation Counting, Giunne and Stratton, NY (1970) pp. 110–122.
- [4] C. M. Lederer, V. S. Shirley, et al., Table of Isotopes, 7th ed., Wiley Interscience, NY (1978).
- [5] Beckman Instruments Inc., Technical Note on "Ready Safe" Liquid Scintillation Cocktail, Fullerton, CA, 1991.
- [6] D. L. Horrocks, Applications of Liquid Scintillation Counting, Academic Press, New York (1974) pp. 210–221.
- [7] M. J. Kessler, Liquid Scintillation Analysis, Packard Instrument Co., Meridan, CN, 1989, pp. 3–7 through 3–24.
- [8] A. Grau Molonda and E. Garcia-Torano, Evaluation of Counting Efficiency in Liquid Scintillation Counting of Pure β -Ray Emitters, Int. J. Appl. Radiat. Isotopes **33**, 249–253 (1982).
- [9] B. M. Coursey, W. B. Mann, A. Grau Molonda, E. Garcia-Torano, Standardization of Carbon-14 by $4\pi\gamma$ Liquid Scintillation Efficiency Tracing with Hydrogen-3, Int. J. Appl. Radiat. Isotopes **37**, 403–408 (1986).
- [10] B. M. Coursey, A. Grau Molonda, E. Garcia-Torano, and J. M. Arcos, Standardization of Pure-Beta-Particle-Emitting Radionuclides, Trans. Amer. Nucl. Soc. **50**, 13–15 (1985).
- [11] B. N. Taylor and C. E. Kuyatt, Guidelines for Evaluating and Expressing the Uncertainty of NIST Measurement Results, Natl. Inst. Stand. Technol. Technical Note 1297 (1993).
- [12] J. Mantel, the Beta Ray Spectrum and the Average Beta Energy of Several Isotopes of Interest in Medicine and Biology, Int. J. Appl. Radiat. Isotopes **23**, 407–413 (1972).

About the authors: Dr. R. Collé has been at NIST since 1974 and is a specialist in radionuclidic metrology and standards development. He currently serves as a research chemist in the Radioactivity Group of the NIST Physics Laboratory. Ms. J. W. L. Thomas serves as a research chemist in the Radioactivity Group of the NIST Physics Laboratory. The National Institute of Standards and Technology is an agency of the Technology Administration, U.S. Department of Commerce.

Pressure-Volume-Temperature Relations in Liquid and Solid Tritium

Volume 98

Number 6

November–December 1993

E. R. Grilly

Los Alamos National Laboratory,
Los Alamos, NM 87545

PVT relations in liquid and solid T_2 near the melting curve were measured over 20.5 K–22.1 K and 0 MPa–7 MPa (0 bar–70 bar) with a cell that used diaphragms for pressure and volume variation and measurement. Because of ortho-para self conversion, the melting pressure P_m and the liquid molar volume V_{lm} increased with time. The rates were consistent with a second order reaction similar to that for c the $J = \text{odd}$ concentration:

$$dc/dt = -k_1c^2 + k_2c(1-c),$$

where $k_1 = 6 - 9 \times 10^{-2} \text{h}^{-1}$. By extrapolation, the ortho and para forms dif-

fered by $\Delta P_m \sim 6$ bar and $\Delta V_{lm} \sim 0.5\%$. Measurements of the volume change on melting and the thermal expansion and compressibility for liquid T_2 were consistent with those for H_2 and D_2 . Impurities such as H_2 , HT, DT, and ^3He were removed by a technique using an adsorption column of cold activated alumina. Corrections for ^3He growth during an experiment were adequate except near the triple point.

Key words: deuterium; hydrogen; *PVT* relations; tritium.

Accepted: September 24, 1993

1. Introduction

Basic interest in the hydrogens H_2 , D_2 , and T_2 is notably enhanced by the existence of significant zero-point energy, large relative mass differences, and different ortho-para characteristics. In addition, D_2 and T_2 in the condensed phases are prime candidates as fuels for controlled nuclear fusion.

Although the discoveries of D_2 in 1931 [1] and T_2 in 1934 [2] were close together in time, the pressure-volume-temperature (*PVT*) measurements on T_2 have lagged far behind those on D_2 . Essentially they were the 1951 measurements of vapor pressure [3] and liquid density [4] up to 3 bar¹ and 29

K and the 1956 melting curve determination up to 3100 bar and 60 K [5]. Contributing to the sluggishness of research efforts have been the high cost of T_2 and the difficulties that arise from its radioactivity (2.8 Ci/cm³ STP gas). Health and environment concerns require great care in containing T_2 and definite provisions for accidental release. The continual creation of ^3He from nuclear decay automatically adds a significant impurity. Self-heating demands proper equipment design and/or data corrections. The exchange of tritium with hydrogen in equipment causes physical breakdown of plastics and contamination of the tritium with hydrogen. These problems have affected the accuracy and completeness of the data reported here.

¹ The bar (= 10^5Pa) is used in this paper rather than the pascal in order to facilitate the comparison of the results of this work with the results of previous and similar work. It should be noted that the International Committee for Weights and Measures allows the use of the bar temporarily with the International System of Units.

2. Apparatus and Procedures

The apparatus and procedures were basically those used for similar studies on ^3He [6], ^4He [7], D_2 [8], and H_2 [9]. The experimental cell consisted of three BeCu diaphragms welded at their circumferences and separated by 0.3 mm gaps. The lower gap, connected to a room-temperature He gas handling system via a capillary tube, had its pressure adjusted and measured directly. The upper gap was the T_2 experimental chamber and was connected to the room-temperature T_2 handling system via a low-temperature valve and a capillary tube. The sample pressure was determined from the deflection of the upper diaphragm, measured by electric capacitance. The experimental volume was determined from the pressures in the two gaps, using the calibrations described in Ref. [8].

The T_2 system is shown schematically in Fig. 1. Four stainless steel tanks, each of 1500 cm^3 volume, were used to hold T_2 , either for storage or for transfer to various parts of the system. The T_2 was pumped at low pressure with a rotary vane pump and compressed to 70 bar with a diaphragm compressor. The uranium bed (U), Pd diffuser (Pd), and Al_2O_3 adsorption tube (Al_2O_3) were used for T_2 purification. T_2 gas samples were collected in sample tubes and analyzed by mass spectrometer. Calibration of capacitance versus cell pressure was done with the cell valve (V20) open and the T_2 separated from the oil piston gauge by a differential pressure indicator (DPI). To prevent excessive pressure in the cell upon loss of cooling when V20 was closed, a thermocouple on the cell signaled a motor to open V20, which allowed venting to a

tank via a pressure relief valve (PRV). The plastic material in the cell valve tip and in the stem seals of the manipulative valves was the polyimide Vespel SP 211, which resisted the destructive action of T_2 quite well.

3. Purification

A significant problem in T_2 experiments is the growth of ^3He from radioactive decay at the rate of 0.031% per day. It was anticipated that a $^3\text{He}\text{-T}_2$ mixture would behave like a $^4\text{He}\text{-H}_2$ mixture in solubility and effect on PVT measurements. The ^3He growth during an experiment (at most 76 h long) was not expected to exceed solubility limits. Thus it was felt that the PVT measurements could be adequately corrected for ^3He growth during an experiment but it was mandatory that the experiment start with ^3He -free T_2 . Several methods of removing ^3He were used. Exposure to U at 300 K binds T_2 as UT_3 and allows the unabsorbed ^3He to be pumped away but good removal requires several cycles. A Pd tube diffuser retains all gases except the hydrogens. But these methods are slow and do not remove hydrogen and deuterium, which are initially present or appear in the gas when most materials are exposed to T_2 . Therefore the final process used was desorption from Al_2O_3 , following basically the method of Depatie and Mills [10] for preparation of 99% o- H_2 or p- D_2 . About 32 cm^3 of 2 mm dia. pellets of Al_2O_3 was placed in a 21 cm long stainless steel tube (15.3 mm O.D. and 0.28 mm wall). At the center of this was a stainless steel tube (3.2 mm O.D. and 0.25 mm wall) for with-

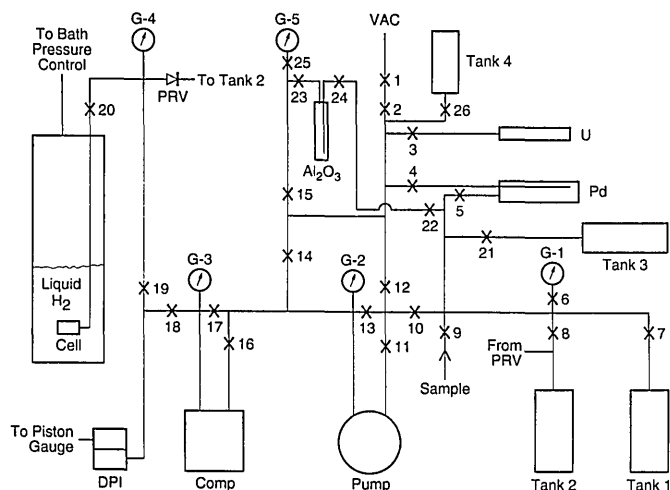


Fig. 1. Schematic of tritium PVT system.

drawing the gas. Prior to use, the Al_2O_3 was evacuated at 140°C for 2 h. The impure gas was added to the Al_2O_3 tube immersed in liquid H_2 until saturation occurred at 87 mbar, after which it was passed through the tube at 87 mbar. The gas entered the top of the Al_2O_3 column and exited from the bottom until the exiting gas composition was the same as that of the entering gas, at which time flow was stopped. Then the liquid H_2 bath was lowered slowly until the effluent gas was almost pure T_2 , after which the gas was collected separately while the adsorption tube warmed to room temperature. A pre- T_2 test on D_2 containing 0.61% HD produced 3500 cm^3 STP D_2 with 0.03% HD. For T_2 initially containing 0.26% H_2 , 1.97% ^3He , 7.34% HT, and 0.49% DT, Table 1 gives the composition of effluent gas samples taken at various points of withdrawal. Collection of the gas after $V=1600\text{ cm}^3$ yielded 1600 cm^3 T_2 containing 0.18% H, 0.10% D, and $< 0.01\%$ ^3He which was enough for a PVT run.

Table 1. Gas composition (%) as a function of effluent volume

$V(\text{cm}^3\text{STP})$	600	900	1200	1600	3200
H_2	3.71	0.080	0.064	0.046	0.028
^3He	0.90	0.010	< 0.01	< 0.01	< 0.01
HT	75.84	5.66	0.36	0.38	0.20
DT	2.50	0.54	0.46	0.36	0.06
T_2	17.05	93.62	99.12	99.21	99.72

4. Ortho-Para Considerations

The equilibrium ortho-para composition in T_2 for various temperatures was calculated by Jones [11] and Gaines, Tsugawa, and Souers [12] and measured by Frauenfelder, Heinrich, and Olin [13]. The Gaines et al. results ($T \leq 22.5\text{ K}$) agreed fairly well with the Jones results, which covered 0 K–175 K. The measurements [13] gave somewhat higher values of c , the $J = \text{odd}$ concentration, which could result from a higher sample temperature than the thermometer reading because of the radioactive heating. The Jones calculation is used as the standard in this paper.

The equilibrium values $c(e)$ versus temperature T for H_2 , D_2 , and T_2 are shown to 100 K in Fig. 2. The normal (n) values (those at $T = 300\text{ K}$) are 0.75 for H_2 and T_2 and 0.33 for D_2 . While $c(e)$ for H_2 and D_2 at 20 K is very small and insensitive to T , $c(e) = 0.34$ for T_2 and increases rapidly with increasing T . Furthermore, the o-p conversion in T_2 is

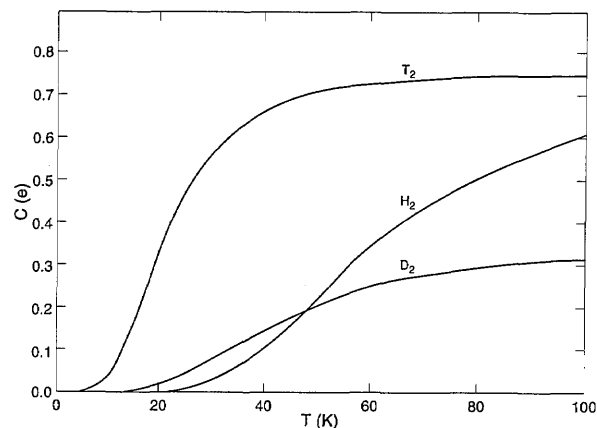


Fig. 2. Concentration of $J = \text{odd}$ states in the hydrogens at equilibrium vs temperature.

much faster than in H_2 under similar conditions. Therefore, it is important to determine c during the PVT measurements on T_2 . The variations of c with time t and vapor pressure were measured and partially reported earlier [14]. There, the values of c were derived from gas thermal conductivity measurements on samples from the condensed phase, thus the rapid back conversion, $p \rightarrow o$, in the gas phase decreased reliability somewhat. The best fits of the data were: for the solid,

$$dc/dt = -kc^2 \quad (1)$$

and for the liquid,

$$dc/dt = -k_1c^2 + k_2c(1-c) \quad (2)$$

where k and k_1 are empirical rate constants and $k_2 = k_1c(e)/(1-c(e))$.

The results on o-p conversion are summarized in Table 2 in several useful forms: (a) r_0 , the conversion rate at zero time; (b) $t_{1/2}$, the time to convert 1/2 way to equilibrium; and (c) k, k_1 , and k_2 , the rate constants. In solid T_2 , the observed $t_{1/2}$ values of 2.0 h, 2.6 h, and 8.1 h at 4.0 K, 15.0 K, and 19.5 K, respectively, are moderately consistent with the NMR results of Gaines et al. [12] and Sater et al. [15] (although the latter found a minimum at 11.4 K) and with 1.5 h at 4 K of Frauenfelder et al. [13] using gas thermal conductivity analysis. However, Albers, Harteck, and Reeves [16] measured 0.28 h at 4 K with gas thermal conductivity. Our observed $t_{1/2} = 8.3\text{ h}$ in liquid at 20.7 K also agrees with the Gaines et al. result. Thus, the conversion rates are about the same in liquid and solid near the triple point (20.6 K), which simplifies interpreting the

Table 2. Ortho→para conversion in T₂ at vapor pressure

Solid			
<i>T</i> (K)	4.0	15.0	19.5
<i>c</i> (e)	0	0.166	0.325
<i>k</i> (h ⁻¹)	0.675	0.321	0.065
<i>r</i> ₀ (%h ⁻¹)	38	18	4
<i>t</i> _{1/2} (h)	2.0	2.6	8.1
Liquid			
<i>T</i> (K)	20.7		24.4
<i>c</i> (e)	0.358		0.460
<i>k</i> ₁ (10 ⁻² h ⁻¹)	8.46		6.32
<i>k</i> ₂ (10 ⁻² h ⁻¹)	4.72		5.40
<i>r</i> ₀ (%h ⁻¹)	3.9		2.5
<i>t</i> _{1/2} (h)	8.3		8.8

PVT measurements on a liquid/solid mixture. The value of $k_1 \sim 8 \times 10^{-2} \text{h}^{-1}$ is eight times the k_1 for H₂ given by Woolley, Scott, and Brickwedde [17].

Vapor pressures of T₂ at a certain *c* value, $P(c)$, and of n-T₂ $P(n)$, were measured simultaneously in a special two-cell system. The differences, $\Delta P = P(c) - P(n)$, are summarized in Table 3. Their behavior follows that of H₂ at similar values of $P(n)$, as in Woolley et al. [17]. For example, extrapolation of the $P(n) = 840$ mbar data to $c = 0$ gives $\Delta P = 29$ mbar for T₂ and $\Delta P = 31$ mbar for H₂.

Table 3. Vapor pressure of T₂ at various ortho values

Phase	<i>P</i> (n) mbar	<i>T</i> K	<i>c</i>	ΔP mbar	$\Delta P/\Delta c$ mbar
liquid	840	24.4	0.66	6.0	67
liquid	840	24.4	0.54	12	57
liquid	840	24.4	0	(29)	(39)
liquid	228	20.7	0.48	4	15
solid	123	10.5	0.33	5.9	14
solid	116	19.4	0.46	4	14

In the *PVT* measurements above vapor pressure, gas thermal conductivity could not be used to determine *c*. Instead, the variations of melting pressure and liquid molar volume with time were used to determine o-p conversion rates. In these measurements, it was assumed that the initial value of *c* was 0.75 because: (1) the purification process left the T₂ sample at $c \sim 0.75$; and (2) the typical 2 h–5 h storage times at 300 K and 1.1 bar in a 1500 cm³ SS tank before condensation promoted conversion to n-T₂.

5. Results

The *PVT* measurements typically began 2 h–3 h after condensation and continued for 50 h–76 h. Usually a single loading of the cell at a given *T* was used to measure compressibility and thermal expansion of liquid and solid, melting pressure, and volume change on melting. The liquid was compressed by a diaphragm until freezing began, which required 2 bar–4 bar overpressure. After the cell pressure stabilized, the compression was slowly continued past completion of freezing, which was indicated by a rapid rise in pressure.

5.1 Melting Pressures

The melting pressures P_m discussed here were the first-freeze values, obtained by extrapolation to zero amount of solid. If the compression was delayed, the increase in P_m with time was attributed to o-p conversion and ³He growth. The o-p change seemed to follow Eq. (2) where $c = 0.75 - \Delta P_m/q$, $\Delta P_m = P_m(c) - P_m(c = 0.75)$, $q = \Delta P_m/(0.75 - c)$, and k_1 and q are constant at constant *T*. Measurements of P_m for ⁴He-H₂ mixtures made up in the gas phase showed the regular effects of a slightly soluble gas and agreed fairly well with results of Berezhnyak and Sheinina [18]. The mixture P_m increased 3 bar–4 bar per 1% of ⁴He over the P_m range of 0 bar–70 bar. Since ³He formation in T₂ is $1.29 \times 10^{-3}\%$ per hour, it was expected that ³He dissolved in condensed T₂ would increase P_m by 3.7 mbar–5.0 mbar h⁻¹, which would necessitate small corrections. If saturation were exceeded, the ³He would probably act as an ideal gas, i.e., *V* varies as P^{-1} . Thus, the correction would be 60 mbar h⁻¹ at the lowest P_m (2.4 bar at 20.55 K), and 3.4 mbar h⁻¹ at the highest P_m (70 bar). The ³He growth in 76 h (the longest time after purification) is 0.098% whereas the ⁴He-H₂ measurements in this cell and in Ref. [18] gave 0.16% ⁴He as the solubility limit at 2.4 bar and 14 K. It follows that ³He would be expected to stay in solution. However, it apparently had left solution at 20.55 K when P_m and liquid compressibility β_1 were measured. Here the measured “ P_m ” was 2.4 bar, whereas linear extrapolation from higher *T* gave $P_m = 0$. If the excess pressure all came from ideal gas ³He the solubility would be 0.046% ³He. Sherman (R. H. Sherman, personal communication) measured 0.077%, which would result in 0.098–0.077 = 0.021% ³He as gas at 0.97 bar, which would yield 1.4 bar as the real P_m . For this sample, the measured β_1 was 10 times “normal,” i.e., values

for T_2 aged 2 h–4 h. Furthermore, T_2 with 52 h–70 h ^3He growth at 20.60 K and 20.65 K showed β_1 to be 4–7 times “normal.” These high β_1 values must have been the result of gas in the cell. The ^4He – H_2 mixtures containing up to 1% ^4He , but below saturation, never gave β_1 values greater than 10% above pure H_2 values. This throws suspicion on the high P_m and β_1 results for T_2 .

Taylor [19] summarized some experiments on condensed T_2 in which ^3He had grown beyond the normal solubility limit. In liquid and solid T_2 there was a lack of vapor pressure buildup consistent with the ^3He production rate. In another case, analysis of successive aliquots of gas removed from aged liquid T_2 showed the last liquid was ^3He -rich. Supplementary evidence for ^3He not appearing as gas was provided by electrical conductivity and magnetic susceptibility measurements. The formation of free ^3He was visually observed by Hoffer (J. K. Hoffer, personal communication), who condensed DT near the triple point in a cylindrical cell with sapphire windows at the ends [20]. After 8 d as a liquid, the DT showed no bubbles. (They could not be hidden in the fill tube, for it entered the bottom of the cell.) After a freeze and a melt, the sample showed a bubble at the top of the cell with a volume that was $\sim 1\%$ of the ideal gas volume for 8 d ^3He growth. A second freeze and melt produced the same bubble, which persisted for 3 d. Then, within 12 h the bubble grew to 100% of the calculated volume for 12 d ^3He growth, taking up 20% of the cell volume. During the next three days no change in the bubble was seen, even after a freeze and a melt. The behavior of ^3He grown in condensed T_2 seems to be unpredictable.

For this paper, the P_m measurements were corrected as if the ^3He – T_2 sample formed a solution like ^4He – H_2 . Figure 3 shows $\Delta P_m = P_m(t) - P_m(0)$ at 20.650 K, 21.900 K, and 22.100 K with and without ^3He corrections. If the high rate at 20.65 K was caused by ^3He growth, it seems that a greater correction is needed. In the fit to Eq. (2), q and the initial ΔP_m were varied to get the most consistent k_1 for each run. The results, summarized in Table 4, show the similarities with the time variation of c in liquid at vapor pressure (Table 2). The average value $q = 6.0$ agrees with the H_2 values 5.7–6.4 over 14 K–16 K from: $P_m(p)$ by Youngblood [21]; $P_m(n)$ by Mills and Grilly [5]; and $P_m(p)$ and $P_m(n)$ in the present apparatus.

Regardless of the previous discussion, extrapolation of P_m ($t < 6$ h) to $t = 0$ gave $P_m(n)$. For e- T_2 , values of $P_m(e)$ with ^3He corrections were obtained from q values or $P_m(t \sim 50$ h). Corrections for

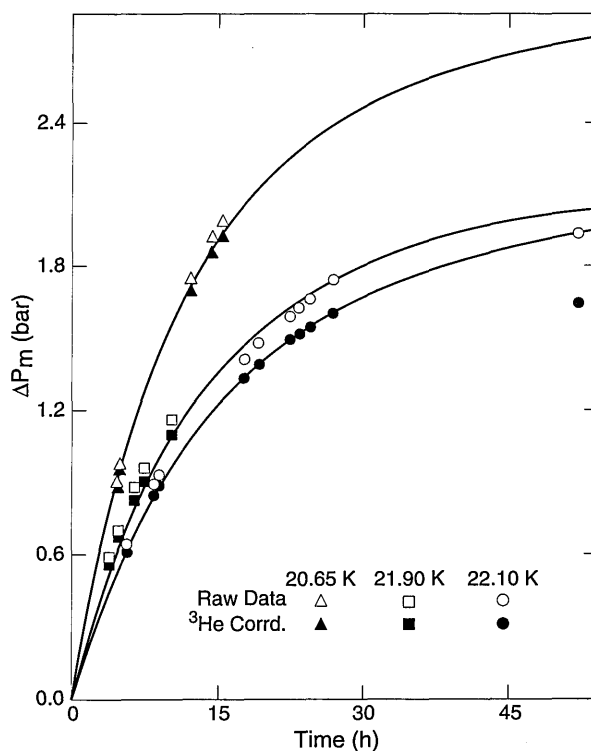


Fig. 3. Tritium melting pressure vs time at several temperatures.

Table 4. Ortho→para conversion in T_2 from melting pressure change. Results in parentheses are from data uncorrected for ^3He

T (K)	20.65	21.90	22.10
P_{m0} (bar)	3.295	58.630	67.906
c (e)	0.358	0.393	0.400
k_1 (10^{-2}h^{-1})	7.90(8.00)	6.58(7.00)	5.46(5.58)
k_2 (10^{-2}h^{-1})	4.41(4.46)	4.26(4.53)	3.64(3.70)
r_0 ($\% \text{h}^{-1}$)	3.62(3.66)	2.90(3.09)	2.39(2.44)
$t_{1/2}$ (h)	8.86(8.74)	9.89(9.30)	11.76(11.54)
q (bar)	7.4(7.6)	6.1(6.2)	6.1(6.5)

0.08%–0.42% H content ($\text{H}_2\% + 1/2\text{HT}\%$) were made at the rate of -1.7 bar per 1% H. The results are summarized in Table 5, illustrated in Fig. 4 for $P_m < 25$ bar, and, over 20.83 K–22.10 K, fit the equations:

$$P_m(n) = 0.22 + 45.92 (T - 20.627) \text{ bar}, \quad (3)$$

$$P_m(e) = 0.22 + 45.27 (T - 20.568) \text{ bar}. \quad (4)$$

The constant 0.22 is the triple point pressure for n- T_2 determined from vapor pressure measurements [3], and it is assumed for e- T_2 as well. The linear P_m – T relation corresponds with the H_2 and D_2 curves. The greater values just above the triple

Table 5. Melting pressure of T₂

T K	H% ^a	P(n) bar	P-P _{eq} bar	c(e)	t ^b h	P(e) ^c bar	P-P _{eq} bar	q bar
20.550	0.13			0.356	71	2.145 ^d		
20.650	0.13	3.295 ^d	+2.02	0.358		(6.196 ^d)	+2.26	7.4
20.700	0.21	4.722 ^d	+1.15	0.359	52	7.053 ^d	+0.86	6.0
20.900	0.08			0.365	42	15.235	-0.01	6.4
21.000	0.08	17.419	+0.07	0.368		(19.864)	+0.09	6.4
21.000	0.21			0.368	68	19.772	0.00	6.2
21.050	0.22	19.632	-0.01	0.370		(22.140)	+0.10	6.6
21.100	0.42	21.968	+0.03	0.371	53	24.469	+0.16	6.6
21.390	0.15	35.198	-0.06	0.379		(37.239)	-0.19	5.5
21.600	0.35	44.660	-0.24	0.385				5.6
21.700	0.10			0.388	56	51.593	+0.12	5.8
21.750	0.25	51.751	-0.04	0.389	58	53.377	-0.35	4.5
21.900	0.10	58.630	-0.05	0.393				6.1
22.100	0.15	67.906	+0.05	0.400		(70.041)	+0.48	6.1
22.100	0.15			0.400	52	69.574	0.00	4.8

^a Corrections to P were made at the rate of -1.7 bar for 1% H.

^b t was the time in the condensed state when P(e) was measured.

^c Values in parentheses are from Eq. (2) fitting.

^d See text for the uncertainty involved.

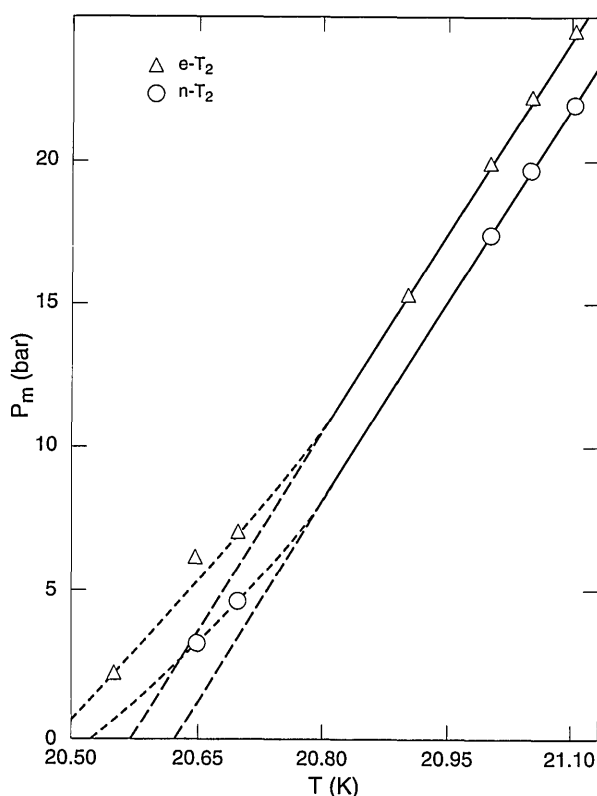


Fig. 4. Tritium melting pressure vs temperature.

point, as shown in Fig. 4, cannot be resolved at present. If Eqs. (3) and (4) held down to the triple point, the T_{ip} values would be 20.627 K for n-T₂

and 20.568 K for e-T₂. The 20.627 K value is close to $T_{ip}(n-T_2) = 20.62$ K, the junction of the liquid and solid vapor pressure equations [3]. Unfortunately, those equations ignored the highest point measured in the solid region, 2.116 bar at 20.547 K. If the liquid and solid curves went through that point, $T_{ip}(n-T_2)$ would be 20.547 K, falling between the possible values from the melting curve, 20.53 K and 20.62 K. The $T_{ip}(e-T_2)$ seems to be in the 20.48 K–20.57 K range. In Table 5, $P - P_{eq}$ is the difference between experimental and equation values of P_m .

The sole previous P_m measurement in the present range was 56.68 bar at 21.826 K for n-T₂ by Mills and Grilly [5], which is 1.48 bar higher than the present result. Of this deviation, 0.76 bar could be from the 0.9% HT impurity in the earlier measurement. Their equation gives values that are lower than the present by 2.5 bar. An equation devised by Goodwin [22] gives values lower than the present by 0.64 bar.

5.2 Volume Change with Time

The increase with time seen in liquid volume V_l at constant T and P ($\sim P_m$) was also attributed to o-p conversion and ³He growth. The data fit Eq. (2) where $c = 0.75 - \Delta V_l/sV_l$, $\Delta V_l = V_l(c) - V_l(c = 0.75)$, and $s = \Delta V_l/(0.75 - c)V_l$ with $k_1 = 7.53 \times 10^{-2} \text{h}^{-1}$ and $s = 5.7 \times 10^{-3}$ for the raw values of $\Delta V_l/V_l$ at 21.00 K ($c(e) = 0.368$) and 14.86 bar. In Fig. 5, the raw data deviate from the dashed equation curve, indicating

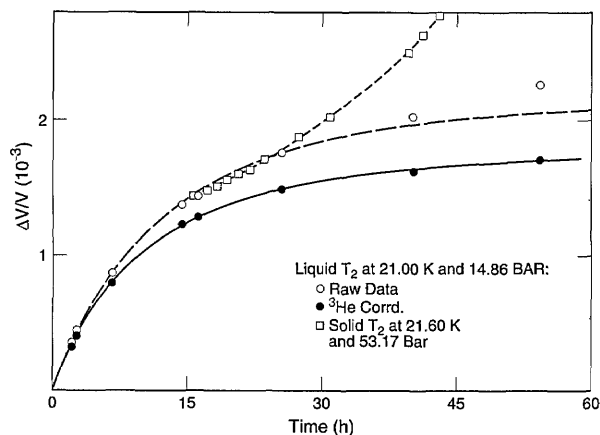


Fig. 5. Relative volume change of T_2 vs time.

that o-p conversion almost stops after 30 h and thereafter V_1 increases mostly from ${}^3\text{He}$ growth. An empirical correction to $\Delta V_1/V_1$, $-1.0 \times 10^{-5} \text{h}^{-1}$, to yield coincidence between the corrected data and the solid equation curve results in $k_1 = 8.98 \times 10^{-2} \text{h}^{-1}$ and $s = 4.6 \times 10^{-3}$. The k_1 values are similar to the results from P_m (Table 4), but the s values are smaller than the values for H_2 : 6.5×10^{-3} by Scott and Brickwedde [23] at vapor pressure; 6.7×10^{-3} by Wallace and Meyer [24] at P_m . Measurements of $\Delta V/V$ vs t on solid T_2 at 21.600 K and 53.17 bar were begun after the sample had been liquid for 6 h and solid for 9.5 h. They were added to the 21.000 K liquid value at $t = 15.5$ h. The results, shown in Fig. 5, follow the liquid curve for 9 h before rising sharply, probably because of breakup of the solid.

5.3 Liquid Thermal Expansion and Compressibility

The thermal expansion coefficient, $\alpha = V^{-1}(\partial V/\partial T)_P$, and the compressibility coefficient, $\beta = -V^{-1}(\partial V/\partial P)_T$, of the liquid were measured directly. All α and $2/3$ of the β measurements were made on essentially e- T_2 . The measurements at $c = 0.6\text{--}0.7$ fit in with the others. They would require a +1.5% correction, at most, for the volume change from o-p conversion during the 5 min measurement, and this is within the scatter of data. The differences in α and β for n- H_2 and e- H_2 were found to be within 2%. Therefore, it is assumed that the T_2 data are independent of c . The α results are given in Fig. 6 as functions of T at various pressures. The dashed curve is through T_m of e- T_2 . The β results are shown in Fig. 7 as functions of P at various temperatures, and the dashed curve is through P_m of e- T_2 .

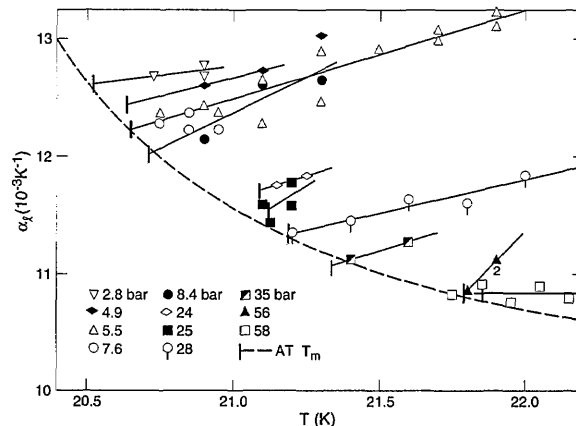


Fig. 6. Thermal expansion of liquid e- T_2 vs temperature at various pressures.

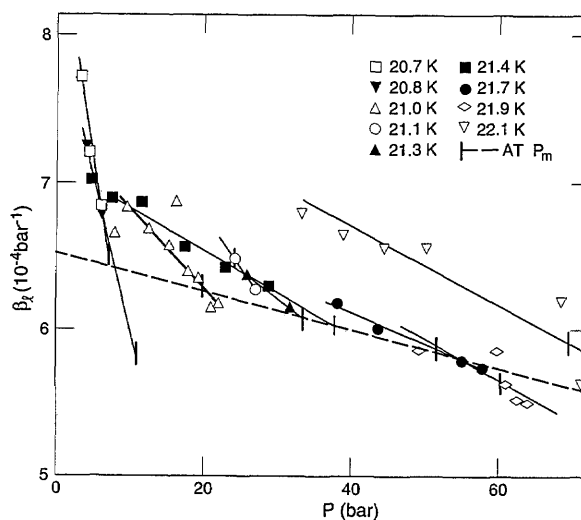


Fig. 7. Compressibility of liquid e- T_2 vs pressure at various temperatures.

There are no other data on α or β for T_2 . Comparison of α for H_2 , D_2 [8] and T_2 is shown in Fig. 8. The three isotopes show similar slopes $(\partial\alpha/\partial T)_P$ and their α values come together with pressure, becoming equal at 57 bar. Figure 9 shows β for the isotopes tending to merge at high pressures.

5.4 Molar Volumes

The molar volume of liquid T_2 along the melting curve V_{lm} was calculated from the measurement at the triple point [4], $22.051 \text{ cm}^3 \text{ mol}^{-1}$ for n- T_2 , and the measured α and β values. This V_{lm} multiplied by the measured $\Delta V_m/V_{lm}$ yielded ΔV_m , the volume change on melting. Finally, the solid molar volume

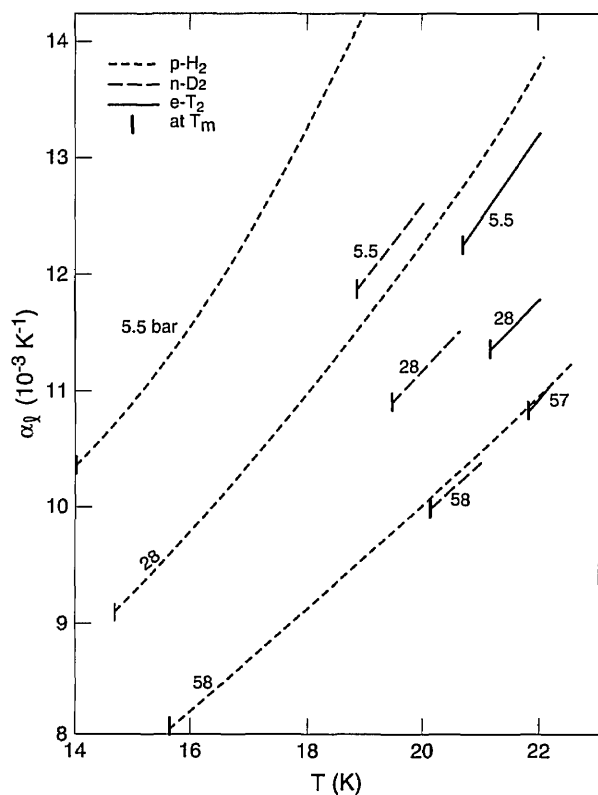


Fig. 8. Liquid thermal expansion of the hydrogens vs temperature at several pressures.

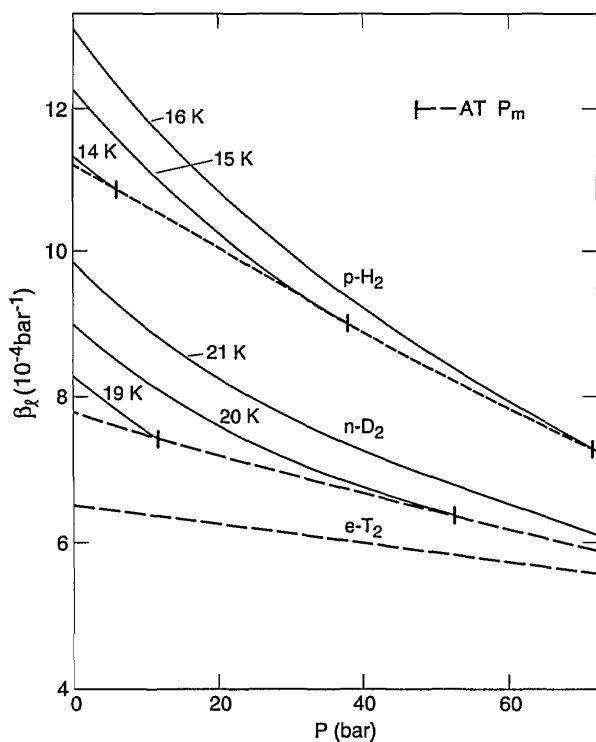


Fig. 9. Liquid compressibility of the hydrogens vs pressure at several temperatures.

V_{sm} was determined from $V_{lm} - \Delta V_m$. Figures 10 and 11 give the results on $\Delta V_m/V_{lm}$ and ΔV_m , respectively, for T_2 , H_2 , and D_2 [8]. Essentially, the $\Delta V_m/V_{lm}$ curves show a parallel displacement for the isotopes while the ΔV_m curves are fairly close together. The results are given in Table 6. All the smoothed PVT values along the melting curve are summarized in Table 7 which should be self-consistent. Here, the V_{lm} and V_{sm} values are for $n\text{-}T_2$, but the values for $e\text{-}T_2$ are only slightly larger. Values of $V_{lm}(e\text{-}T_2) - V_{lm}(n\text{-}T_2)$ were calculated from the $o\text{-}p$ expansion and the $P_m(n\text{-}T_2) \rightarrow P_m(e\text{-}T_2)$ contraction, using the s values in Table 4 and the β values in Table 7. The two effects largely cancel

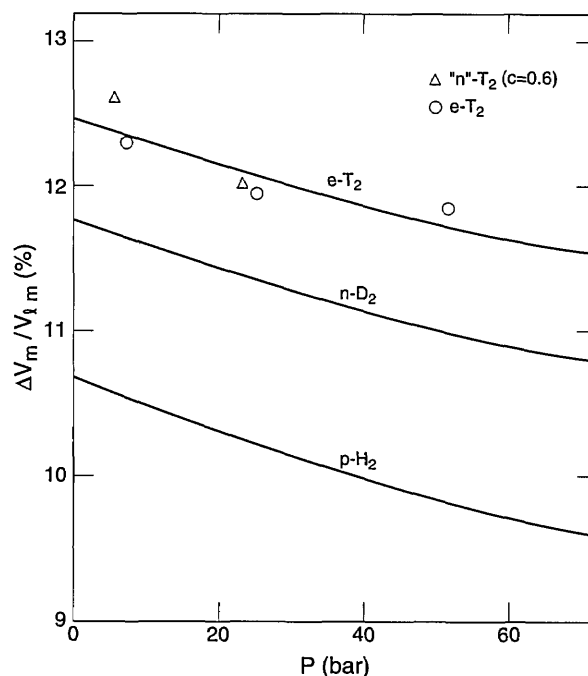


Fig. 10. Relative volume change on melting of the hydrogens.

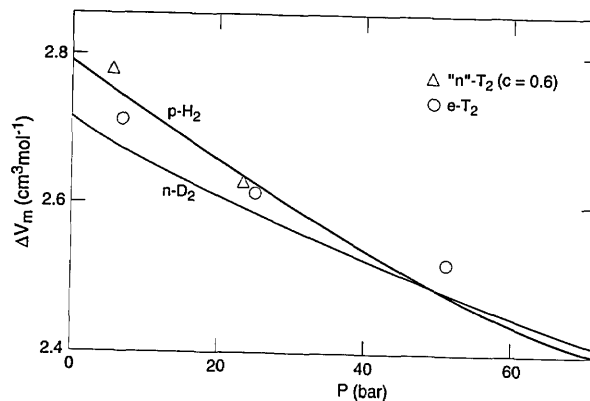


Fig. 11. Volume change on melting of the hydrogens.

Table 6. Volume change on melting of T₂

<i>T</i> K	<i>P_m</i> ^a bar	$\Delta V_m/V_{lm}$ ^a %	<i>V_{lm}</i> cm ³ mol ⁻¹	ΔV_m cm ³ mol ⁻¹	<i>V_{sm}</i> cm ³ mol ⁻¹
n-T ₂					
20.700	4.72	12.62	22.024	2.779	19.245
21.100	22.23	12.02	21.881	2.630	19.251
e-T ₂					
20.700	7.05	12.30	22.026	2.709	19.317
21.100	24.47	11.95	21.883	2.615	19.268
21.700	51.59	11.86	21.659	2.569	19.090

^a Direct measurement.

Table 7. Properties of T₂ along the melting curve

<i>T</i> K	<i>P</i> (n-T ₂) bar	<i>P</i> (e-T ₂) bar	<i>c</i> (e)	α_1 10 ⁻³ K ⁻¹	β_1 10 ⁻⁴ bar ⁻¹	<i>V_l</i> (n-T ₂) cm ³ mol ⁻¹	<i>V_l</i> (e-T ₂) cm ³ mol ⁻¹	$\Delta V_m/V_l$ %	ΔV_m cm ³ mol ⁻¹	<i>V_s</i> (n-T ₂) ^b cm ³ mol ⁻¹
20.535 ^a	0.22	1.80	0.357	12.4	6.85	22.051	22.060	12.40	2.734	19.317
20.700	4.72	7.05	0.359	12.2	6.79	22.024	22.026	12.35	2.720	19.304
20.800	8.30	10.80	0.362	12.0	6.72	21.995	21.997	12.29	2.703	19.292
20.900	12.76	15.24	0.365	11.9	6.65	21.959	21.961	12.22	2.683	19.276
21.000	17.35	19.77	0.368	11.7	6.59	21.920	21.922	12.15	2.663	19.257
21.100	21.94	24.30	0.371	11.6	6.51	21.881	21.883	12.08	2.643	19.238
21.200	26.53	28.87	0.374	11.4	6.45	21.842	21.844	12.01	2.623	19.219
21.300	31.12	33.36	0.377	11.2	6.39	21.804	21.806	11.95	2.606	19.198
21.400	35.72	37.88	0.379	11.1	6.32	21.766	21.768	11.89	2.588	19.178
21.500	40.31	42.41	0.382	11.0	6.24	21.728	21.730	11.83	2.570	19.158
21.600	44.90	46.94	0.385	10.9	6.16	21.691	21.694	11.77	2.553	19.138
21.700	49.49	51.47	0.388	10.9	6.10	21.655	21.659	11.72	2.538	19.117
21.800	54.08	56.00	0.390	10.8	6.04	21.618	21.624	11.67	2.523	19.095
21.900	58.68	60.52	0.393	10.8	5.97	21.582	21.589	11.62	2.508	19.074
22.000	63.27	65.05	0.396	10.7	5.90	21.547	21.555	11.58	2.495	19.052
22.100	67.86	69.57	0.400	10.7	5.82	21.512	21.521	11.54	2.482	19.030

^a See text on the triple point.

^b $V_s(e-T_2) - V_s(n-T_2) = V_l(e-T_2) - V_l(n-T_2)$.

each other, leaving a net difference of only 0.002 cm³mol⁻¹ for the most part, with high values of 0.009 at 20.535 K and 22.1 K. The result is carried over to *V_{sm}* since $\Delta V_m/V_{lm}$ is assumed to be independent of *c*.

The possibility of comparison with other work is small. Hammel [25] predicted $\Delta V_m = 2.66$ cm³mol⁻¹ at the triple point, whereas here we get 2.734. Driessen et al. [26] calculated values of *V_{sm}* that are 0.05 cm³mol⁻¹–0.07 cm³mol⁻¹ lower than ours over 20.535 K–22.1 K range.

5.5 Solid Thermal Expansion and Compressibility

The measurements of α and β for the solid phase gave erratic and probably low values in general.

This behavior can be expected from poor pliability of the solid in the measuring cell, which tends to be worse away from the melting curve [8]. The behavior occurred in all the isotopes, but T₂ has other properties that could influence the measurements: ³He production, internal heating, and solid fracturing. Although the measurements were made on e-T₂ the results can probably be used for any o-p composition.

For each of H₂, D₂, and T₂, α was measured at several pressures as a function of *T*, and each time it increased with *T*. However, α at constant *T* generally decreases with *P*. Thus the extrapolations of α to *T_m* can lead to roughly constant values, which occurs for H₂ and D₂ [8]. However α increases with *T_m* for T₂. Figure 12 illustrates these behaviors,

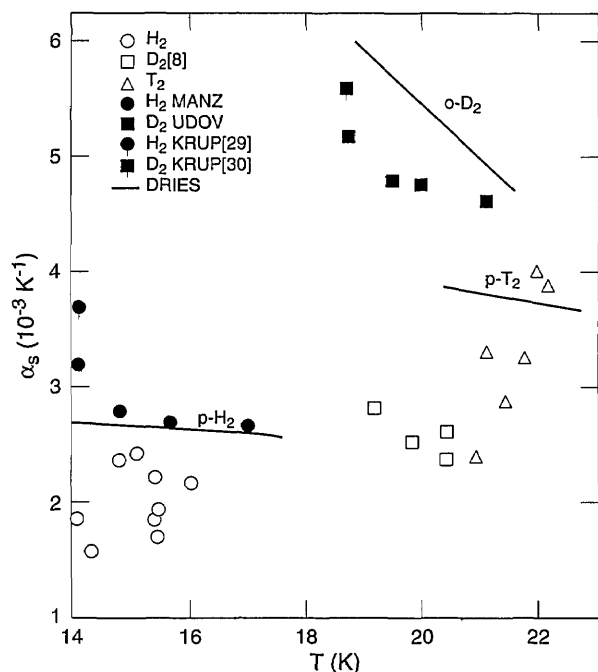


Fig. 12. Solid thermal expansion of the hydrogens along the melting curve. MANZ is Manzhelii et al. [27]; UDOV is Udovidchenko et al. [28]; KRUP [29] is Krupskii et al. [29]; KRUP [30] is Krupskii et al. [30]; DRIES is Driessen et al. [26].

along with the overall increase in α from H_2 to D_2 to T_2 . The results of Driessen et al. [26] are also shown there. They measured the isochores of p- H_2 and o- D_2 up to 2 kbar, between the melting curve and 4.2 K, by use of a cell whose wall deflections were measured with strain gauges. Molar volumes were determined by correlation with data at the melting line and 4.2 K. Isochores were fit by integration of specific heat. The resulting equation of state was used to calculate V , α , and β up to 25 kbar. The derivation of an EOS for p- T_2 was "guided by experimental results for H_2 and D_2 ." Their α results appear to be in rough agreement with ours for H_2 and T_2 but for D_2 they are about twice as great. Densities were derived from dielectric constant measurements on p- H_2 by Manzhelii et al. [27] and on n- D_2 by Udovidchenko et al. [28]. Their α results (good to $\pm 10\%$), shown in Fig. 12, match the Driessen et al. results for H_2 very well and for D_2 within 15%. From x-ray studies of lattice parameters, Krupskii et al. [29,30] derived α for p- H_2 that is 37% higher than the Driessen et al. result and α for o- D_2 that is 8% lower.

The measurements of β as a function of P at several temperatures show a decrease with P . Generally, β increases with T , therefore, the extrapolated values of β to P_m can be almost constant, as

illustrated in Fig. 13. There is also a big decrease in β from H_2 to D_2 to T_2 . The values for H_2 , D_2 [8], and T_2 are about 0.90, 0.55, and 0.77, respectively, of the Driessen et al. [26] results. The measurements of Manzhelii et al. [27] and of Udovidchenko and Manzhelii [31] on β of p- H_2 are 5%–10% greater than those of Driessen et al. [26] while the values of Udovidchenko et al. [28] for n- D_2 are slightly lower. Other measurements on H_2 and D_2 were made at 4.2 K using various direct and indirect techniques. In general, the values are low. In some cases, values of P were not low enough to allow satisfactory extrapolations.

In spite of these discrepancies in α and β results, there is hope for more accurate values for T_2 . Overall, the Driessen et al. [26] results on H_2 and D_2 fit in fairly well with others. It follows that their T_2 results should be credible. For example, the change in V_s along the melting curve between 20.5

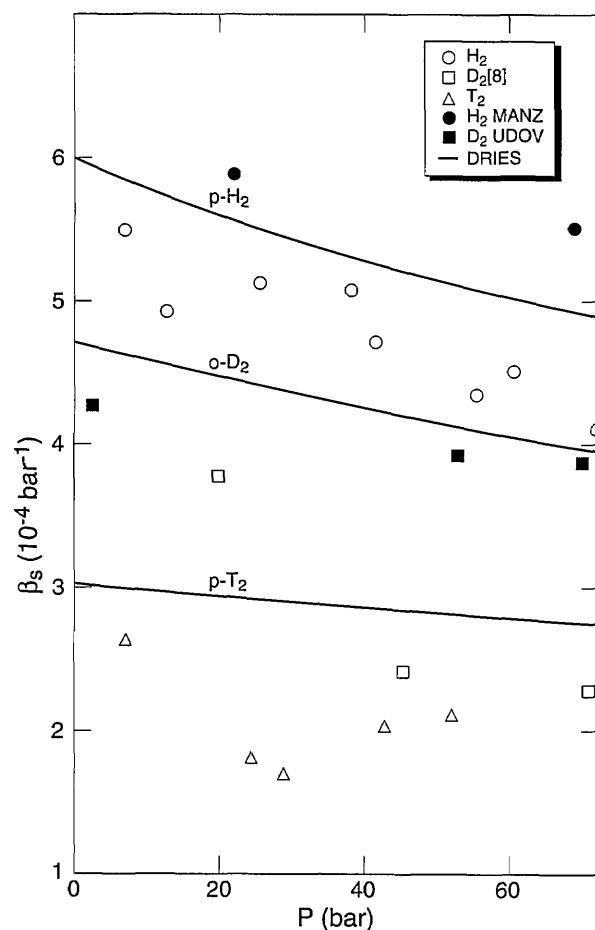


Fig. 13. Solid compressibility of the hydrogens along the melting curve. MANZ is Manzhelii et al. [27,31]; UDOV is Udovidchenko et al. [28]; DRIES is Driessen et al. [26].

K and 22.1 K is calculated from their α and β values to be $0.252 \text{ cm}^3\text{mol}^{-1}$, in reasonable agreement with $\Delta V_s = 0.287$ in Table 7.

In solid H_2 and D_2 , some anomalies in α and β were observed [8] but hardly deserve recognition as phase change effects. There is no point adding to the confusion in this subject [27, 28, 29, 30, 32, 33]. In T_2 , no anomaly was recognized, but observation was very limited.

5.6 Thermal Results

The enthalpy change on melting (heat of fusion) calculated from the Clapeyron equation $\Delta H_m = T\Delta V_m dP_m/dT$, using the present *PVT* measurements on *n-T*₂, is almost constant at 255 Jmol^{-1} in the range 20.9 K–22.1 K or 13 bar–70 bar. However, below 20.9 K the rapid decrease in dP_m/dT lowers it to 144 Jmol^{-1} at T_{ip} . On the other hand, ΔH_m for H_2 and D_2 varies linearly with P_m over 0 bar–70 bar from 117 Jmol^{-1} to 130 Jmol^{-1} for *p-H*₂, according to Dwyer et al. [34], and from 197 to 210 for *n-D*₂ [8]. If we wish to focus more on the similarities of the isotopes, perhaps it would be better to compare the behavior of the entropy change $\Delta S_m = \Delta H_m/T$. This decreases over 13 bar–70 bar by 2% for H_2 and D_2 and by 4% for T_2 .

6. Summary

The *PVT* relations in liquid and solid T_2 were measured near the melting curve over 20.5 K–22.1 K and 0 bar–70 bar. They were compared with measurements on H_2 and D_2 and with calculations on T_2 . Comparison of the three isotopes leads to few surprises. The melting pressure variations with temperature and ortho-para composition are consistent. An exception is the strange behavior of P_m for T_2 in the 0.3 K interval just above the triple point. The o-p conversion in condensed T_2 is faster than in H_2 but slow enough to allow observation of its effect on the *PVT* relations. The liquid and solid molar volumes of the three isotopes are consistent in magnitude and in their variations with o-p composition, pressure, and temperature. Still unresolved is the status of ^3He produced in condensed T_2 .

Acknowledgment

I thank J. K. Hoffer and R. H. Sherman for sharing their observations on ^3He in condensed T_2 .

7. References

- [1] H. C. Urey, F. G. Brickwedde, and G. M. Murphy, *Phys. Rev.* **39**, 164 (1932).
- [2] M. L. E. Oliphant, P. Harteck, and Lord Rutherford, *Proc. Roy. Soc.* **144 A**, 692 (1934).
- [3] E. R. Grilly, *J. Am. Chem. Soc.* **73**, 843 (1951).
- [4] E. R. Grilly, *J. Am. Chem. Soc.* **73**, 5307 (1951).
- [5] R. L. Mills and E. R. Grilly, *Phys. Rev.* **101**, 1246 (1956).
- [6] E. R. Grilly, *J. Low Temp. Phys.* **4**, 615 (1971).
- [7] E. R. Grilly, *J. Low Temp. Phys.* **11**, 33 (1973).
- [8] L. A. Schwalbe and E. R. Grilly, *J. Res. Natl. Bur. Stand. (U.S.)* **89**, 227 (1984).
- [9] L. A. Schwalbe and E. R. Grilly, *J. Res. Natl. Bur. Stand. (U.S.)* **89**, 317 (1984).
- [10] D. A. Depatie and R. L. Mills, *Rev. Sci. Instr.* **39**, 105 (1968).
- [11] W. M. Jones, *J. Chem. Phys.* **16**, 1077 (1948).
- [12] J. R. Gaines, R. T. Tsugawa, and P. C. Souers, *Phys. Rev. Lett.* **42**, 1717 (1979).
- [13] R. Frauenfelder, F. Heinrich, and J. B. Olin, *Helv. Phys. Acta* **38**, 279 (1965).
- [14] E. R. Grilly, *Proceedings of the Third International Conference on Low Temperature Physics and Chemistry, Houston (1953)* p. 66.
- [15] J. D. Sater, J. R. Gaines, E. M. Fearon, P. C. Souers, F. E. McMurphy, and E. R. Mapoles, *Phys. Rev. B* **37**, 1482 (1988).
- [16] E. W. Albers, P. Harteck, and R. R. Reeves, *J. Amer. Chem. Soc.* **86**, 204 (1964).
- [17] H. W. Woolley, R. B. Scott, and F. G. Brickwedde, *J. Res. Natl. Bur. Stand. (U.S.)* **41**, 454 (1948).
- [18] N. G. Bereznyak and A. A. Sheinina, *Fiz. Nizk. Temp.* **7**, 685 (1981). [*Sov. J. Low Temp. Phys.* **7**, 335 (1981)].
- [19] R. D. Taylor, *Proceedings of the 17th International Conference on Low Temperature Physics, Karlsruhe, 1984, part II, Paper EL 10*.
- [20] J. K. Hoffer and L. R. Foreman, *Phys. Rev. Lett.* **60**, 1310 (1988).
- [21] B. A. Youngblood, *J. Chem. Phys.* **48**, 4181 (1968).
- [22] R. D. Goodwin, *Cryogenics* **2** (6) 353 (1962).
- [23] R. B. Scott and F. G. Brickwedde, *J. Res. Natl. Bur. Stand. (U.S.)* **19**, 237 (1937); *J. Chem. Phys.* **5**, 736 (1937).
- [24] B. A. Wallace and H. Meyer, *Proceedings of the 13th International Conference on Low Temperature Physics, Boulder, CO, Vol. 2 (1972)* p. 194.
- [25] E. F. Hammel, *J. Chem. Phys.* **18**, 228 (1950).
- [26] A. Driessen, Thesis, Univ. of Amsterdam (1982); A. Driessen and I. F. Silvera, *J. Low Temp. Phys.* **54**, 565 (1984).
- [27] V. G. Manzhelii, B. G. Udovidchenko, and V. B. Esel'son, *Fiz. Nizk. Temp.* **1**, 799 (1975). [*Sov. J. Low Temp. Phys.* **1**, 384 (1975)]. Also: V. G. Manzhelii, B. G. Udovidchenko, and V. B. Esel'son, *Zh. Eksp. Teor. Pisma* **18**, 30 (1973). [*Sov. Phys.-JETP Letters* **18**, 16 (1973)]. B. G. Udovidchenko, V. G. Manzhelii, and V. B. Esel'son, *Phys. Status Solidi (a)* **19**, K189 (1973).
- [28] B. G. Udovidchenko, V. B. Esel'son, and V. G. Manzhelii, *Fiz. Nizk. Temp.* **10**, 13 (1984). [*Sov. J. Low Temp. Phys.* **10**, 5 (1984)].
- [29] I. N. Krupskii, A. I. Prokhvatilov, and G. N. Shcherbakov, *Fiz. Nizk. Temp.* **9**, 83 (1983). [*Sov. J. Low Temp. Phys.* **9**, 42 (1983)].

- [30] I. N. Krupskii, A. I. Prokhvatilov, and G. N. Shcherbakov, *Fiz. Nizk Temp.* **10**, 5 (1984). [*Sov. J. Low Temp. Phys.* **10**, 1 (1984)].
- [31] B. G. Udovidchenko and V. G. Manzhelii, *J. Low Temp. Phys.* **3**, 429 (1970).
- [32] N. G. Bereznyak and A. A. Sheinina, *Fiz. Nizk Temp.* **6**, 1255 (1980) [*Sov. J. Low Temp. Phys.* **6**, 608 (1980)].
- [33] G. N. Shcherbakov, A. I. Prokhvatilov, and I. N. Krupskii, *Fiz. Nizk Temp.* **11**, 521 (1985). [*Sov. J. Low Temp. Phys.* **11**, 284 (1985)].

About the author: E. R. Grilly is a physicist retired from the Condensed Matter and Thermal Physics Group of Los Alamos National Laboratory, in which this work was done.

Filter Transmittance Measurements in the Infrared

Volume 98

Number 6

November–December 1993

**A. L. Migdall, A. Frenkel, and
D. E. Kelleher**

National Institute of Standards
and Technology,
Gaithersburg, MD 20899-0001

We have set up a novel direct detection system to measure filter transmittances over an attenuation range of at least 5 decades, with relative combined standard uncertainties as low as 0.5% (1σ) per decade, in the $9\ \mu\text{m}$ to $11\ \mu\text{m}$ spectral region. This system, using an apparatus originally designed for a heterodyne measurement of transmittance, achieves higher accuracy at the expense of a reduced dynamic range. This independent measurement of transmittance allows verification of the heterodyne technique. Our system uses a source modulated at 30 MHz and a specially constructed high dynamic range and high accuracy lock-in amplifier capable of operation at the modulation frequency. The high modulation frequency and narrow bandwidth of the

system allow thermal background radiation to be suppressed and high accuracy to be achieved. We correct for the non-ideal natures of the detector and attenuators. In particular, the detector position is scanned to reduce the effect of its spatial nonuniformity and the deflection of the transmitted beam caused by the nonparallel surfaces of the filter. We discuss the sources of systematic errors and the methodology to reduce their contribution.

Key words: attenuators; direct detection; filter transmittance; heterodyne detection; infrared.

Accepted: October 12, 1993

1. Introduction

We have developed a method for accurately measuring a wide range of filter attenuation in the infrared (ir) using a direct detection system. The method makes use of a specially constructed high frequency lock-in amplifier which allows ir attenuation measurements to be tied to a high accuracy radio frequency attenuation standard. We have measured the absolute attenuation of filters at two wavelengths, $10.2\ \mu\text{m}$ and $10.6\ \mu\text{m}$. Subsequent measurements will use an ir Fourier Transform Interferometer to determine the spectral variation of the attenuation of these filters. Ultimately this work will allow the National Institute of Standards and Technology to provide calibrated neutral density filters over a wide range of attenuations.

The measurement scheme described here is a high accuracy direct detection method with a

dynamic range of more than 5 decades. This system was set up to allow independent verification of an even higher dynamic range heterodyne detection scheme described elsewhere [1,2]. The filters measured here, along with the estimated uncertainties, will be used to corroborate the accuracy of the higher dynamic range heterodyne detection scheme.

Accurate methods for measuring filter attenuations are well established in the visible region of the spectrum. This is not the case in the infrared however, where measurements become increasingly difficult, particularly at large attenuations. The problems are associated with both detectors and attenuators. Detectors in the ir generally have inferior spatial uniformity and are linear over restricted dynamic ranges, compared to visible

detectors, while attenuators in the ir are not neutral because bulk materials with spectrally neutral absorption are unavailable. As a result most ir attenuators are reflective coatings on transmitting substrates or bulk absorbing cutoff filters. One disadvantage of reflective attenuators is the interference effect that becomes evident when used with laser sources [3]. This is a particular problem with highly attenuating filters whose optical density ($OD = -\log_{10}T$, where T is the filter transmittance) is difficult to measure with a thermal source. Finally, the temperature dependence of both detectors and filters is generally worse in the ir.

2. Experimental Setup

Our measurement scheme uses a CO₂ laser modulated at 30 MHz, a high frequency detector and lock-in amplifier. The ratio of detected signals with and without the filter in the laser beam is used to determine the filter OD . The high frequency of modulation reduces laser noise common at low frequencies and allows the use of a high accuracy and high dynamic range lock-in amplifier. The narrow bandwidth capability of the lock-in amplifier allows us to neglect the ambient thermal background radiation which peaks in the CO₂ laser wavelength

range. The particular modulation frequency, 30 MHz, was chosen because there exists a radio frequency (rf) attenuation standard at that frequency at NIST. That makes possible a lock-in amplifier system capable of high accuracy amplitude measurement as well as high dynamic range, as opposed to lock-in systems where only dynamic range or frequency selectivity is the goal.

The layout of the experimental setup is shown in Fig. 1. The source is a grating frequency-stabilized CO₂ laser. The frequency of the laser is locked to the center of a line determined by the grating. This stabilizes the laser intensity to better than 0.5% maximum deviation over an hour and to within 4% over a day. After passing through an adjustable attenuator, the output of the CO₂ laser is split into two beams. Each of these beams is sent through an acousto-optic modulator (AOM). One of the AOMs is set to upshift the frequency of the beam passing through it by 40 MHz, while the other AOM upshifts its beam by 70 MHz. These two frequency shifted beams are then recombined and made to pass through a lens, an aperture and the mounted filter before final detection. The combined beams induce a signal at 30 MHz, the difference frequency. The dual beam frequency shifts allow a 30 MHz modulation of the ir signal to

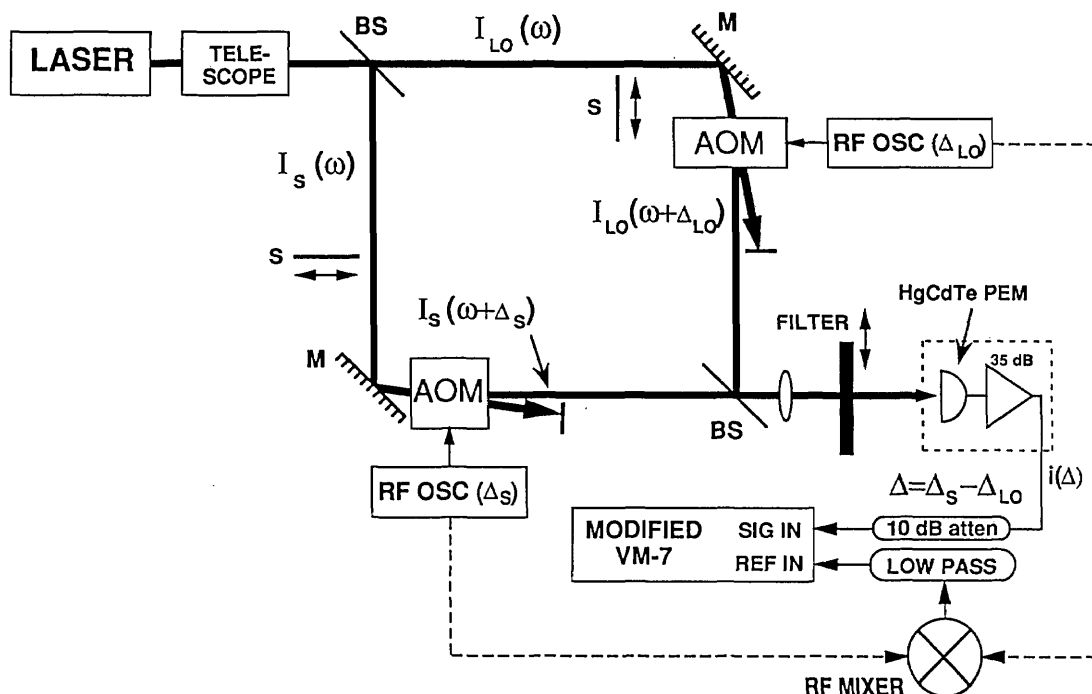


Fig. 1. Experimental setup—mirrors, beamsplitters and shutters are labeled M, BS, and S, respectively.

be generated without requiring a 30 MHz driver for an AOM. This eliminates the need to shield the ir detector from the AOM driver, which uses ~ 10 W of rf power. Shutters are used for baseline subtraction to eliminate the effects of any internal lock-in offsets or any coherent pickup.

The 30 MHz amplitude is measured using a lock-in amplifier based on two custom-modified 30 MHz Weinschel VM-7¹ attenuator and signal calibrators [2,4]. The original instruments were designed for 30 MHz attenuator calibrations. The modifications allow the instrument to function as a true dual phase lock-in amplifier at 30 MHz while retaining the high accuracy of the original instrument.

Our tests on the present form of the modified instrument show a dynamic range of about 180 dB. The manufacturer's specifications for the accuracy of the original instrument were 0.02 dB per 10 dB from 0 dBm to -100 dBm, 0.04 dB per 10 dB from -100 dBm to -110 dBm and 0.12 dB per 10 dB from -110 dBm to -120 dBm. Our own linearity tests of the modified instrument [2] indicate that the standard uncertainty [5] is $\sim 1/3$ of these values.

We use a temperature stabilized photoelectromagnetic (PEM) HgCdTe detector with a 1 mm \times 1 mm active area. The thermal time constant is on the order of minutes, so the thermal regulation cannot respond to rapid effects such as heating by the laser as the filter is moved in and out of the beam. However, as described later, tests of the linearity of the entire system showed that this is not a problem for all but the highest laser powers. The detector is mounted on a two axis motorized positioning stage allowing the detector to be centered with respect to the optical beam. This is important due to detector nonuniformity and deflection of the transmitted beam by filters with nonparallel surfaces. The detector is followed by an rf preamplifier having a gain of 35 dB, and a 10 dB rf attenuator which we found necessary to limit oscillations caused by interaction between the preamplifier and lock-in amplifier.

The filter type itself is crucial to the ultimate accuracy of these measurements. We investigated two types of filters for this project: filters made from a bulk absorbing material and the more usual

reflective coating on a substrate. We discuss later the merits of both filter types and how their characteristics affect the transmittance accuracy.

The absorptive type attenuator samples were made of three different thicknesses of LiF. This material is highly absorbing at wavelengths beyond about 9 μ m. Since the filter absorption is proportional to thickness, special care was taken to make the thicknesses uniform across the samples. We were able to make the samples flat to 10 μ m across the 25 mm samples. The observed deflection of an 633 nm beam through the filter was less than 0.15 mrad. The reflective filters tested were commercially available neutral density filters with metallic films on germanium substrates. Both types of filters were held in a temperature stabilized copper block. Two thermistors were mounted in holes in the block for monitoring and controlling the temperature.

3. Measurement Technique

The measurement procedure was designed to minimize uncertainties due to the nonideal nature of the detectors and filters. Detectors in the ir generally have poor spatial uniformity. The uniformity of the PEM HgCdTe detector used in our work was found to vary by a factor of 3 from the center to the edge, so it is clearly important to recenter a beam that is slightly deflected as it passes through a filter that is not perfectly parallel. To accomplish this, the detector was scanned through a 4 \times 4 x-y grid of 16 points. These scans were taken for both the filter in and filter out positions. To determine the peak signal, or optimal centering, each set of 16 points was fit to a two-dimensional parabolic surface. The transmittance was found from the ratio of the fitted peak signals with the filter in and filter out. Zero levels measured with the shutters closed were subtracted before fitting the data. The ratio of optical beam size to detector diameter was adjusted by moving the detector through the beam focus to minimize the rms deviation between the parabolic fit and the data. This was done to minimize the sensitivity of the measurement to spatial variations of the beam profile and detector uniformity. The optimum was reached when the beam size was on the order of the detector diameter.

For the absorptive type filters this was all that was required to extract an optical density from the data. This advantage in ease of measurement must be weighed against the steep wavelength dependence of the absorption. The reflective type filters however, while spectrally uniform when used with

¹ Certain trade names and company products are mentioned in the text or identified in an illustration in order to adequately specify the experimental procedure and equipment used. In no case does such identification imply recommendation or endorsement by the National Institute of Standards and Technology, nor does it imply that the products are necessarily the best available for the purpose.

broadband sources, require a more complicated measurement procedure. This is because the use of a narrow band light source, such as a laser, with a reflective type attenuator introduces complications that do not occur with a broadband source or bulk absorbing attenuator. To the extent that a filter substrate has flat and parallel surfaces, it will act as a Fabry-Perot etalon. (Producing a filter that is not parallel will reduce this effect, but will also deflect the transmitted beam which causes other complications.) The overall visibility of the resulting fringes varies as the geometric mean of the reflectances of the front and back surfaces. Even if care is taken to put a good antireflection (0.1% reflectivity) coating on the second surface, the geometric mean of the two reflectivities is large enough to produce significant interference effects ($\pm 0.03 OD$). (In addition, the spectral dependence of antireflection coatings can reduce the useful wavelength range of the filter.) This results in a transmittance that varies periodically with laser wavelength. The period of this variation ($\lambda^2/2nL$ where λ is the wavelength, n is the refractive index of the substrate and L is the filter thickness) is about $0.01 \mu\text{m}$ for a 1 mm thick substrate.

To obtain a reflective filter transmittance that can be compared with a transmittance measured using a broadband source, we must average over the variations with laser wavelength. This could be accomplished by scanning the laser wavelength, but our laser is not capable of scanning continuously over a large enough range. We show preliminary results of an alternate method to allow the transmittance variation to be observed without varying the laser wavelength. This is done by using temperature to vary the effective thickness, or optical path length, of the filter. This is possible because the index of refraction of the substrate is temperature dependent. To minimize the temperature variation required, we chose Ge as a substrate material, because its index temperature coefficient is extremely large, $396 \times 10^{-6}/^\circ\text{C}$. With this material, a temperature range of 12°C allows a complete period of the transmittance variation to be mapped.

Since the filter thickness varies across its aperture and the laser beam divergence is not zero, the actual shape of the transmittance variation is the Fabry-Perot function integrated over these variations. For simplicity, we fit the transmittance variation versus temperature to a sine function plus an offset term, $A + B \sin(Ct + D)$, where A , B , C , and D are constants and t is the temperature. The offset term, A , is what we used as the average transmittance. Because the amplitude of the OD

variation was not too large (typically ± 0.01 to ± 0.05), this procedure allows us to extract an average transmittance with reasonable accuracy even though the sinusoidal form is not quite the right shape. The ultimate accuracy of this method will require further investigation.

4. Results

We measured the transmittances of three thicknesses of LiF at two wavelengths, $10.2 \mu\text{m}$ and $10.6 \mu\text{m}$ and at several temperatures. The results measured at a temperature of 29.6°C are shown in Table 1 with the last columns showing the temperature dependence of the attenuation at the two wavelengths.

The combined standard uncertainties of the OD values are mainly dominated by the VM7 measurement uncertainty. The results, as shown in Fig. 2, can be approximated by an overall value of $0.002 OD/OD$ or about 0.5% transmittance uncertainty per decade. The make up of the total combined standard uncertainties of the OD/L values are the quadrature sum of the standard uncertainties of the sample temperature ($\sim 20 \text{ mK}$) and thickness, wavelength (assuming $3 \times 10^{-5} \mu\text{m}$ laser linewidth), statistical and VM7 measurement uncertainties. Of these, sample thickness and the VM7 are the two major sources of uncertainty.

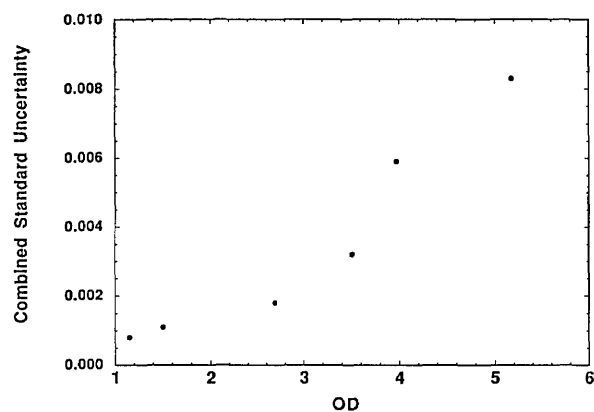


Fig. 2. OD combined standard uncertainty vs OD for the LiF filter measurements.

The thickness uncertainty was dominant for small OD samples, while the VM7 uncertainty was dominant at large OD . The sample thicknesses were measured by the Precision Engineering Division at NIST using an electro-mechanical dual probe comparator referenced to NIST gauge

Table 1. Measured attenuation of LiF filter samples at two wavelengths

Wave-length (μm)	Sample thickness L (mm)	OD	δOD 1σ	OD/L (mm^{-1})	$\delta(OD/L)$ 1σ (mm^{-1})	$OD/(Lt)$ ($\text{mm}^{-1}\text{ }^\circ\text{C}^{-1}$)	$\delta OD/(Lt)$ 1σ ($\text{mm}^{-1}\text{ }^\circ\text{C}^{-1}$)
10.2	0.7068	1.155	0.0008	1.632	0.0048	0.0044	0.0002
	1.6200	2.690	0.0018	1.659	0.0023		
	2.4308	3.971	0.0059	1.633	0.0028		
10.6	0.7068	1.507	0.0011	2.132	0.0062	0.0063	0.0006
	0.6200	3.511	0.0032	2.167	0.0033		
	2.4308	5.175	0.0083	2.129	0.0038		

blocks. The standard uncertainty with which the center thickness could be determined was $0.17\ \mu\text{m}$. The major component of this uncertainty was due to variations of the sample thickness, which were as great as $3.3\ \mu\text{m}$ across the central 50% of the 25 mm filter diameter. Since the optical beam diameter was a few millimeters and the filter position relative to the beam varied somewhat for these measurements, we estimate the standard uncertainty of the thickness to be $\sim 2\ \mu\text{m}$. The values of OD/L are for the bulk sample material with the estimated surface reflectance subtracted off before calculating the attenuation per thickness. The calculated component of optical density due to the reflectance of two surfaces is 0.00158 at $10.2\ \mu\text{m}$ and 0.00068 at $10.6\ \mu\text{m}$ with a standard uncertainty of 0.0002.

These results with LiF filters demonstrate a dynamic range of the technique of over 5 decades. The two different wavelength measurements of OD/L for the 0.7068 mm and 2.4308 mm samples agree to within the uncertainties. The OD/L of the 1.6200 mm sample differs from the other two by amounts well beyond the uncertainties. The ratio of the attenuation per thickness of the 1.6200 mm sample to the average of the other two samples is 1.0163 and 1.0171 at $10.2\ \mu\text{m}$ and $10.6\ \mu\text{m}$, respectively. The consistency of this difference (and the fact that the 0.7068 mm and 2.4308 mm samples were ordered from one source while the 1.6200 mm sample came from another vendor) suggests that it is due to a material variation rather than a measurement uncertainty.

We are able to compare the results here with measurements of LiF using the heterodyne measurement method published earlier [2]. The 1.6200 mm sample measured here, was in fact made from the 2.06 mm sample measured in Ref. [2]. The heterodyne optical density measurement result of $2.120\ \text{mm}^{-1}$ from the 2.06 mm sample was taken at

$10.59\ \mu\text{m}$ and at an estimated temperature of $24.8\ ^\circ\text{C}$. The value obtained here for the 1.6200 mm sample adjusted to $10.59\ \mu\text{m}$ and $24.8\ ^\circ\text{C}$ is $2.1154\ \text{mm}^{-1}$. The difference between these two measurements is about the same as the combined standard uncertainty of the direct measurement. This is reasonable agreement, considering that the heterodyne result was made to test dynamic range rather than accuracy. In particular, the reason for reworking the original 2.06 mm sample was that its optical flatness and parallelism were deficient enough to noticeably deflect and distort a visible laser beam. The effect of this defect on the heterodyne result was not corrected for.

The results here can also be compared with the results of Hohls [6]. By interpolation between stated wavelengths and adjusting for the temperature difference we obtain a value of $1.681\ \text{mm}^{-1}$ and $2.128\ \text{mm}^{-1}$ for $10.2\ \mu\text{m}$ and $10.6\ \mu\text{m}$, respectively. As the estimated combined standard uncertainty of this early data is 5%, these values are in good agreement with our results.

These results, consistent measurements of OD/L for different thicknesses, put an upper limit of $\sim 0.002\ OD/OD$ on any nonlinearity error in the measurement system. In addition, we checked linearity by measuring the OD of a single LiF filter at a range of laser powers. The results (Fig. 3) show the measured OD as a function of signal seen by the lock-in amplifier with filter out of the optical path. These signals correspond to laser powers between about 0.2 mW and 200 mW at the LiF filter. The OD is nearly independent of signal level, except at the high end, where there may be a hint of saturation at about the 0.001 level. All our measurements were taken with lock-in input signals below $-30\ \text{dBm}$.

The measurements using reflective filters were more difficult. Figure 4 shows the OD of a sample filter versus temperature. The variation due to

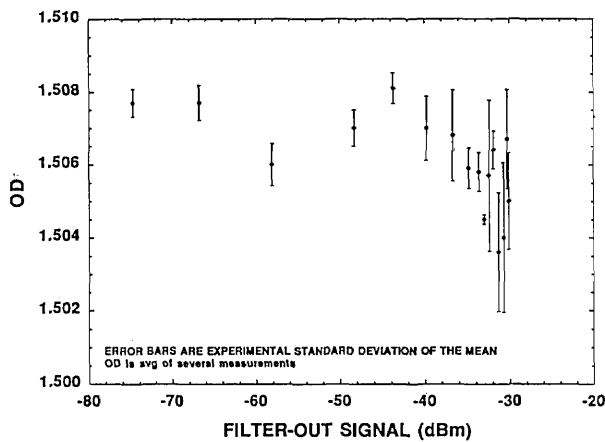


Fig. 3. OD vs signal for LF sample. Demonstrates measurement linearity vs laser power.

interference is clearly visible. The fit function and parameters are also shown. Although the systematic deviation between the fit function and the data is clearly noticeable, we estimate that the offset parameter *A* is determined to within 0.01. The repeatability of these measurement results was significantly better than this fit determination. While this procedure allows the interference effects associated with reflective filters to be observed, it will require

more work to assign a combined standard uncertainty to the measurements. We need to be able to characterize the divergence and uniformity of the laser wavefront as well as the wavefront distortion of the filter itself. For some reflective filters tested, we were able to observe the fringe pattern in the back reflected beam. We saw about 10 straight fringes indicating a wedged filter that did not greatly distort the wavefront.

5. Conclusions

We have demonstrated a direct detection scheme capable of measuring optical densities of filters over a dynamic range of 5 decades. The relative combined standard uncertainty appears to be about 0.002 *OD/OD* as demonstrated using a bulk absorbing material. For reflective type filters, the accuracy with which the high spectral resolution laser measurements can be averaged over to obtain a low resolution (or broadband) result must be studied further. Other future work will include measurements of transmittance at cryogenic temperatures, wide spectral range FTIR measurements of transmittance, development of NIST Standard Reference Material attenuation filters for the ir and measurements of *OD*'s ranging from about 2–10 using the heterodyne detection method.

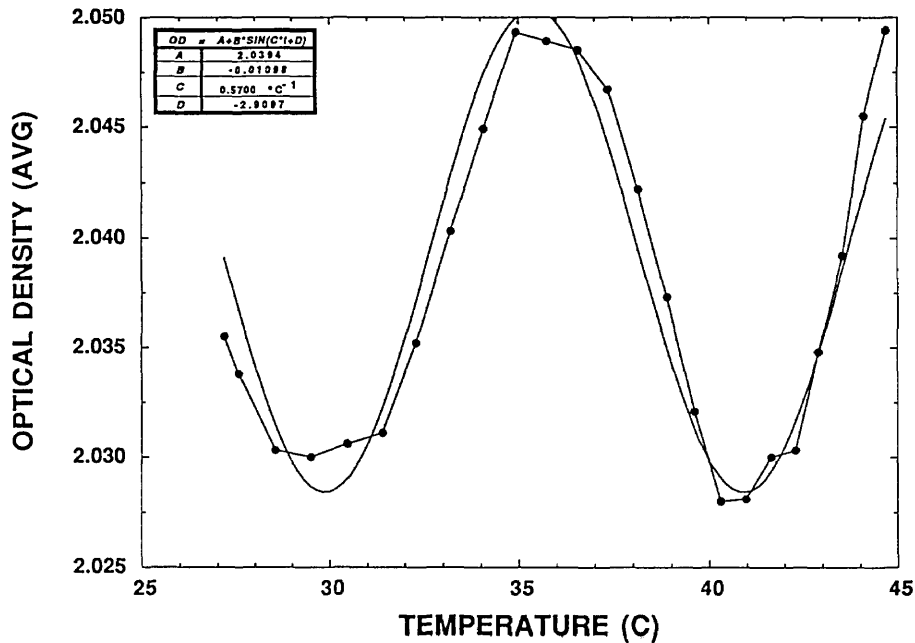


Fig. 4. OD vs temperature and fit for reflective filter.

Acknowledgment

We are grateful to John Stoup of the Precision Engineering Division at NIST for his measurements of the filter thicknesses and Raju Datla for his support and encouragement.

About the authors: *Alan Migdall is a physicist in the NIST Radiometric Physics Division, A. Frenkel is member of technical staff in the NIST Radiometric Physics Division, and D. E. Kelleher is a physicist in the NIST Atomic Physics Division. The National Institute of Standards and Technology is an agency of the Technology Administration, U.S. Department of Commerce.*

6. References

- [1] A. L. Migdall, et. al, Use of Heterodyne Detection to Measure Optical Transmittance Over a Wide Range, *Appl. Opt.* **29**, 5136–5144 (1990).
- [2] A. L. Migdall, B. Roop, and G. J. Xai, Measuring Filter Transmittance using Heterodyne Detection, *Metrologia* **28**, 217–220 (1991).
- [3] L. N. Hadley and D. M. Dennison, Reflection and Transmission Interference Filters. Part I, *J. Opt. Soc. Am.* **37**, 451–465 (1947); L. N. Hadley and D. M. Dennison, Reflection and Transmission Interference Filters. Part II, *J. Opt. Soc. Am.* **38**, 483–496 (1948); J. Holden, Multiple-Beam Interferometry: Intensity Distribution in the Reflected System, *Proc. Phys. Soc.* **62**, 405–417 (1949).
- [4] Lucas Weinschel, P.O. Box 6001, Gaithersburg, MD 20877, USA.
- [5] B. N. Taylor and C. E. Kuyatt, Guidelines for Evaluating and Expressing the Uncertainty of NIST Measurement Results, National Institute of Standards and Technology, Tech. Note 1297 (1993)
- [6] Hohls, Von H. W., *Ann. Phys.* **29** (5), 433–448 (1937).

On Two Numerical Techniques for Light Scattering by Dielectric Agglomerated Structures

Volume 98

Number 6

November–December 1993

Akhlesh Lakhtakia

Department of Engineering Science and Mechanics, Pennsylvania State University, University Park, PA 16802

and

George W. Mulholland

National Institute of Standards and Technology, Gaithersburg, MD 20899-0001

Smoke agglomerates are made of many soot spheres, and their light scattering response is of interest in fire research. The numerical techniques chiefly used for theoretical scattering studies are the method of moments and the coupled dipole moment. The two methods have been obtained in this tutorial paper directly from the monochromatic Maxwell curl equations and shown to be equivalent.

The effects of the finite size of the primary spheres have been numerically delineated.

Key words: agglomerates; coupled dipole method; light scattering; method of moments; smoke.

Accepted: August 13, 1993

Glossary

0	Null vector	${}^{(m)}E_{\text{exc}}(\mathbf{x})$	Electric field intensity exciting the subregion V_m
$\mathbf{0}$	Null dyadic	$E_{\text{exc},m}$	$= {}^{(m)}E_{\text{exc}}(\mathbf{x}_m)$
a	Radius of a spherical subregion	$E_{\text{inc}}(\mathbf{x})$	Incident electric field intensity
$\mathbf{a}, \mathbf{b}, d_1, d_2$	Arbitrary vectors	E_m	Electric field intensity at \mathbf{x}_m
a_m	$(1/2) \times$ maximum linear cross-sectional dimension of the subregion V_m	$E_{\text{sca}}(\mathbf{x})$	Scattered electric field intensity
\mathbf{A}_{km}	Dyadic kernel for the MOM equations	$F_{\text{sca}}(\mathbf{u}_s)$	Far-zone scattering amplitude in the direction \mathbf{u}_s
$\hat{A}_{kk}, \hat{A}'_{kk}$	Self-terms when MOM is used with spherical subregions	$\mathbf{G}(\mathbf{x}, \mathbf{x}')$	Free space dyadic Green's function
b	Side of a cubical subregion	\mathbf{G}_{km}	$= \mathbf{G}(\mathbf{x}_k, \mathbf{x}_m)$
$\mathbf{B}(\mathbf{x})$	Magnetic flux density (weber per square meter)	$\mathbf{H}(\mathbf{x})$	Magnetic field intensity (ampere per meter)
$\mathbf{D}(\mathbf{x})$	Electric flux density (coulomb per square meter)	$H_{\text{sca}}(\mathbf{x})$	Scattered magnetic field intensity
e_{inc}	Electric field intensity amplitude of an incident plane wave	i	$= (-1)^{1/2}$
$E(\mathbf{x})$	Electric field intensity (volt per meter)	\mathbf{I}	Identity dyadic
		$\mathbf{J}(\mathbf{x})$	Electric current density (ampere per cubic meter)
		\mathbf{J}_m	$= \mathbf{J}(\mathbf{x}_m)$
		$\mathbf{J}_{\text{cond}}(\mathbf{x})$	Conduction current density (ampere per cubic meter)

$J_{\text{pol}}(\mathbf{x})$	Polarization current density (ampere per cubic meter)	μ_0	Permeability of free space ($= 4\pi \times 10^{-7}$ henry per meter)
k_0	Free space wavenumber (inverse meter)	ω	Circular frequency (radian per second)
$\mathbf{L}_m, \mathbf{M}_m, \mathbf{T}_m$	Depolarization dyadics for the three-dimensional subregion V_m	Ω	Solid angle
M	Total number of subregions	τ	Polarizability scalar of a spherical subregion
p_m	Electric dipole moment equivalent to the subregion V_m	τ_m	Polarizability scalar of the m -th spherical subregion
P_{abs}	Time-averaged absorbed power	τ_D	Draine's polarizability scalar of a spherical subregion
P_{sca}	Time-averaged scattered power	τ_{DB}	Dungey-Bohren polarizability scalar of a spherical subregion
P_{ext}	Time-averaged extinguished power	v_m	Volume of the subregion V_m (cubic meter)
\mathbf{Q}_{km}	Dyadic kernel for the CDM equations	$\psi(\beta)$	A Riccati-Bessel function of argument β .
S_m	Closed surface of the three-dimensional subregion V_m	$\zeta(\beta)$	A Riccati-Hankel function of argument β .
t	Time (seconds)		
\mathbf{t}_m	Polarizability dyadic of the subregion V_m		
\mathbf{u}_s	Unit vector denoting direction in the far zone		
\mathbf{u}_{inc}	Unit vector denoting propagation direction of an incident plane wave		
V_{ext}	Three-dimensional region external to the scatterer		
V_{int}	Three-dimensional region occupied by the scatterer		
V_m	Three-dimensional subregion		
\mathbf{x}	Three-dimensional position vector (meter)		
\mathbf{x}_m	Distinguished point inside the subregion V_m		
\mathbf{X}_{km}	$\mathbf{x}_k - \mathbf{x}_m$		
α	Mossotti-Clausius polarizability scalar of a spherical subregion		
α_m	Mossotti-Clausius polarizability scalar of the m -th spherical subregion		
δ_{km}	Kronecker delta		
$\delta(\mathbf{x} - \mathbf{x}')$	Dirac delta		
ϵ_0	Permittivity of free space ($= 8.854 \times 10^{-12}$ farad per meter)		
ϵ_r	Relative permittivity		
$\epsilon_r(\mathbf{x})$	Relative permittivity of dielectric matter occupying V_{int}		
$\epsilon_{r,m}$	Relative permittivity of dielectric matter of the subregion V_m		
η_0	Intrinsic impedance of free space ($= 120\pi$ ohm)		
Λ	$= [(1 - ik_0 a) \exp(ik_0 a) - 1]$		
λ	$=$ Wavelength in free space ($= 2\pi/k_0$)		

1. Introduction

Electromagnetic scattering problems involving complicated geometries are treated numerically nowadays. Apart from some low- or high-frequency methods [1, 2] and the T-matrix method [3], implementation of most numerical techniques entails a partitioning of the region occupied by the scatterer into many subregions. This is generally true whether a differential formulation is used or an integro differential formalism.

The method of moments (MOM) [4–6], as applied to an inhomogeneous dielectric scatterer, is an approach based on the evaluation of an electric field volume integral equation over the region occupied by the scatterer. This region is partitioned into a number of subregions; the electric field in each subregion is represented by a subregional basis function; and the volume integral equation is converted into a set of simultaneous algebraic equations that are solved using standard procedures. The subregions are generally cubes, although the relevant self-terms are usually evaluated as that of equivoluminal spheres.

Whereas the MOM is an *actual field* formalism, the coupled dipole method (CDM) is based on the concept of an *exciting field*. The CDM was formulated intuitively in 1969 by Purcell and Penny-packer [7] for dielectric scatterers, although it had by that time a rich history spanning many decades [8]. Conceived from a microscopic viewpoint, the CDM has only a semi-microscopic basis; indeed,

the operational basis for applying the CDM to boundary value problems is totally macroscopic [9]. Both the MOM and the CDM were recently extended to bianisotropic scatterers and their respective *weak* and *strong* forms were shown to be equivalent [10].

This tutorial paper contains a complete derivation of the MOM and the CDM for the scattering of time-harmonic electromagnetic waves by an inhomogeneous dielectric object possessing an isotropic permittivity, the starting point of the exercise being the monochromatic Maxwell curl equations. A central topic of the paper is the elucidation of the relationship between the MOM, which is widely used in electrical engineering, and the CDM, which is motivated by concepts in atomic physics [7]. Our treatment is directed towards the researcher who is interested in understanding these methods but who may not be a specialist in electromagnetic field theory.

A current topic of considerable interest is light scattering by agglomerated structures made up of individual spheres arranged in a low-density structure. Examples of such structures include smoke agglomerates formed in fires or internal combustion engines; various materials produced in combustion systems including silica and titanium dioxide; and, perhaps, interstellar dust. The earliest relevant analyses [11, 12] of light scattering from smoke were based on the Rayleigh-Debye approximation, in which the field exciting any particular primary sphere is taken to be just the field that is actually incident on the agglomerate. Such a procedure neglects multiple scattering effects, and is acceptable for primary spheres with size parameter (=radius multiplied by the free space wavenumber) less than about 0.2. The typical size parameters for the smoke agglomerates mentioned above lie in the range 0.1 to about 0.25 at visible frequencies.

Both the CDM [13, 14] and the MOM [15, 16] have been applied to compute scattering from smoke agglomerates in the recent past, since neither technique suffers from the limitations of the Rayleigh-Debye approximation. While the MOM and the CDM are expected to give the same results for infinitesimally small size parameters [17], the methods—as ordinarily used—do not yield identical results as the primary sphere size increases [18, 19]. This is because the CDM has been used chiefly in what may be called its *weak* form, while it is the *strong* form of the MOM that is in standard usage [10]. The strong form is valid for larger primary spheres because the effect of the singularity of the

free space dyadic Green's function is better estimated therein than in the weak form. This becomes clearer in the following sections.

2. Volume Integral Equation

As is schematically illustrated in Fig. 1, let all space be divided into two mutually disjoint regions, V_{int} and V_{ext} , that are distinguishable from each other by the occupancy of matter. The region V_{ext} is vacuous; hence,

$$\mathbf{D}(\mathbf{x}) = \epsilon_0 \mathbf{E}(\mathbf{x}); \mathbf{x} \in V_{\text{ext}}, \quad (1a)$$

$$\mathbf{B}(\mathbf{x}) = \mu_0 \mathbf{H}(\mathbf{x}); \mathbf{x} \in V_{\text{ext}}. \quad (1b)$$

The region V_{int} is filled with an isotropic, linear, possibly inhomogeneous, dielectric continuum with frequency dependent $[\exp(-i\omega t)]$ constitutive equations

$$\mathbf{D}(\mathbf{x}) = \epsilon_0 \epsilon_r(\mathbf{x}) \mathbf{E}(\mathbf{x}); \mathbf{x} \in V_{\text{int}}, \quad (2a)$$

$$\mathbf{B}(\mathbf{x}) = \mu_0 \mathbf{H}(\mathbf{x}); \mathbf{x} \in V_{\text{int}}, \quad (2b)$$

where $\epsilon_r(\mathbf{x})$ is the complex relative permittivity scalar. The square root of $\epsilon_r(\mathbf{x})$ is the local complex refractive index, $\text{Imag}[\omega\epsilon_0\epsilon_r(\mathbf{x})]$ is the local conductivity, and ω is the circular frequency.

There is no requirement that V_{int} be a simply-connected convex region. Sharp corners and cusps should be absent, it being preferable that the boundary surface that separates V_{int} from V_{ext} be at least once-differentiable everywhere to enable the unambiguous prescription of a unit normal at every point on it. Furthermore, the maximum linear extent of V_{int} must be bounded so that only the region V_{ext} extends out to infinity in all directions.

The monochromatic Maxwell curl equations, in the absence of any externally impressed sources, are given in V_{ext} as

$$\nabla \times \mathbf{E}(\mathbf{x}) - i\omega\mu_0 \mathbf{H}(\mathbf{x}) = \mathbf{0}; \mathbf{x} \in V_{\text{ext}}, \quad (3a)$$

$$\nabla \times \mathbf{H}(\mathbf{x}) + i\omega\epsilon_0 \mathbf{E}(\mathbf{x}) = \mathbf{0}; \mathbf{x} \in V_{\text{ext}}, \quad (3b)$$

with $\mathbf{0}$ denoting the null vector. Similarly, in V_{int} we have

$$\nabla \times \mathbf{E}(\mathbf{x}) - i\omega\mu_0 \mathbf{H}(\mathbf{x}) = \mathbf{0}; \mathbf{x} \in V_{\text{int}}, \quad (4a)$$

$$\nabla \times \mathbf{H}(\mathbf{x}) + i\omega\epsilon_0 \epsilon_r(\mathbf{x}) \mathbf{E}(\mathbf{x}) = \mathbf{0}; \mathbf{x} \in V_{\text{int}}. \quad (4b)$$

On rewriting Eq. (4b) as

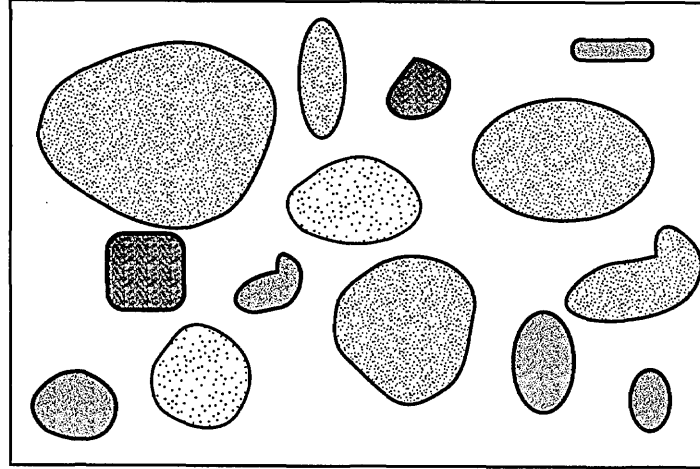


Fig. 1. Schematic of the scattering problem. The unshaded region V_{ext} extends to infinity in all directions, while the shaded regions collectively constitute V_{int} .

$$\begin{aligned} \nabla \times \mathbf{H}(\mathbf{x}) + i\omega\epsilon_0 \mathbf{E}(\mathbf{x}) + i\omega\epsilon_0 [\epsilon_r(\mathbf{x}) - 1] \mathbf{E}(\mathbf{x}) \\ = \mathbf{0}; \mathbf{x} \in V_{int}, \end{aligned} \quad (4c)$$

and comparing it with Eq. (3b), we are able to state the Maxwell curl equations *everywhere* as

$$\nabla \times \mathbf{E}(\mathbf{x}) - i\omega\mu_0 \mathbf{H}(\mathbf{x}) = \mathbf{0}; \mathbf{x} \in V_{int} + V_{ext}, \quad (5a)$$

$$\nabla \times \mathbf{H}(\mathbf{x}) + i\omega\epsilon_0 \mathbf{E}(\mathbf{x}) = \mathbf{J}(\mathbf{x}); \mathbf{x} \in V_{int} + V_{ext}. \quad (5b)$$

In Eq. (5b), the volume electric current density $\mathbf{J}(\mathbf{x}) \equiv \mathbf{0}$ for $\mathbf{x} \in V_{ext}$, but

$$\mathbf{J}(\mathbf{x}) = -i\omega\epsilon_0 [\epsilon_r(\mathbf{x}) - 1] \mathbf{E}(\mathbf{x}); \mathbf{x} \in V_{int}. \quad (5c)$$

In this fashion a volume electric current density has effectively replaced the dielectric matter occupying the region V_{int} [20, Sec. 3–11].

The volume electric current density $\mathbf{J}(\mathbf{x})$ defined by Eq. (5c) is not a fictitious entity in the present context. We must remember that, while the region V_{ext} is vacuous, the region V_{int} is occupied by dielectric matter. The monochromatic polarization current density in this dielectric matter is given by

$$\begin{aligned} \mathbf{J}_{pol}(\mathbf{x}) = -i\omega\epsilon_0 \{ \text{Real} [\epsilon_r(\mathbf{x})] - 1 \} \mathbf{E}(\mathbf{x}); \\ \mathbf{x} \in V_{int}, \end{aligned} \quad (6a)$$

while the conduction current density is given by

$$\mathbf{J}_{cond}(\mathbf{x}) = \omega\epsilon_0 \text{Imag} [\epsilon_r(\mathbf{x})] \mathbf{E}(\mathbf{x}); \mathbf{x} \in V_{int}. \quad (6b)$$

It is now easy to see that

$$\mathbf{J}(\mathbf{x}) = \mathbf{J}_{pol}(\mathbf{x}) + \mathbf{J}_{cond}(\mathbf{x}); \mathbf{x} \in V_{int}, \quad (6c)$$

which implies that $\mathbf{J}(\mathbf{x})$ is not merely a mathematically convenient quantity for dielectric scatterers.

It is enough that we look for the solution of the differential equations (5a,b) in terms of only the electric field, since the magnetic field everywhere may be obtained from Eq. (5a) if the electric field is known everywhere: $\mathbf{H}(\mathbf{x}) = \nabla \times \mathbf{E}(\mathbf{x}) / i\omega\mu_0$. On taking the curl of both sides of Eq. (5a), and then substituting for $\nabla \times \mathbf{H}(\mathbf{x})$ from Eq. (5b) in the result, we get

$$\begin{aligned} \nabla \times \nabla \times \mathbf{E}(\mathbf{x}) - k_0^2 \mathbf{E}(\mathbf{x}) = i\omega\mu_0 \mathbf{J}(\mathbf{x}); \\ \mathbf{x} \in V_{int} + V_{ext}, \end{aligned} \quad (7)$$

where $k_0 = \omega(\mu_0\epsilon_0)^{1/2}$ is the free space wavenumber. We take cognizance of the fact that when $\mathbf{J}(\mathbf{x})$ is set equal to zero everywhere, Eq. (7) reduces to the celebrated vector Helmholtz equation.

As shown in Appendix A, it follows from Eq. (7) that the electric field $\mathbf{E}(\mathbf{x})$ is the solution of the volume integral equation

$$\begin{aligned} \mathbf{E}(\mathbf{x}) - \mathbf{E}_{inc}(\mathbf{x}) = i\omega\mu_0 \iiint_{V_{int}} d^3\mathbf{x}' \\ \{ \mathbf{G}(\mathbf{x}, \mathbf{x}') \cdot \mathbf{J}(\mathbf{x}') \}; \mathbf{x} \in V_{int} + V_{ext}, \end{aligned} \quad (8a)$$

or, equivalently,

$$\begin{aligned} \mathbf{E}(\mathbf{x}) - \mathbf{E}_{inc}(\mathbf{x}) = k_0^2 \iiint_{V_{int}} d^3\mathbf{x}' \{ [\epsilon_r(\mathbf{x}') - 1] \\ \mathbf{G}(\mathbf{x}, \mathbf{x}') \cdot \mathbf{E}(\mathbf{x}') \}; \mathbf{x} \in V_{int} + V_{ext}, \end{aligned} \quad (8b)$$

on using Eq. (5c). Here

$$\mathbf{G}(\mathbf{x}, \mathbf{x}') = [\mathbf{I} + (1/k_0^2)\nabla\nabla][\exp(ik_0|\mathbf{x}-\mathbf{x}'|)/4\pi|\mathbf{x}-\mathbf{x}'|] \quad (8c)$$

is the free space dyadic Green's function and \mathbf{I} is the identity dyadic. The field $\mathbf{E}_{inc}(\mathbf{x})$ is the solution of Eq. (7) when $\mathbf{J}(\mathbf{x}) \equiv \mathbf{0}$ for all $\mathbf{x} \in V_{int} + V_{ext}$, and is the electric field existing in $V_{int} + V_{ext}$ if $\epsilon_r(\mathbf{x}) = 1$ for all $\mathbf{x} \in V_{int}$. The standard radiation conditions are satisfied by the right sides of Eqs. (8a,b) as $k_0|\mathbf{x}| \rightarrow \infty$ [21].

3. Intermediate Remarks

Equation (8a) is utilized in setting up the CDM, while the integral Eq. (8b) is solved in the MOM, and it is this commonality that partially begets the algorithmic equivalence of the two techniques. In setting up the solutions of Eq. (7) in the form of the integral Eqs. (8a,b), we have brought in two significant topics that need some rumination right now: (i) dyadics and (ii) the free space dyadic Green's function.

Dyadics are as American as apple pie, being the brainchildren of Josiah Willard Gibbs. In 1884, Gibbs circulated a pamphlet introducing the concept and nomenclature of dyadics. Mathematics books with dyadic notation were written every so often earlier in this century, but most mathematicians appear to have eventually discarded dyadics in favor of tensors. In electromagnetics, though, dyadic notation has been used with great profit, the books by van Bladel [22], Fedorov [23] and Chen [24] being immensely popular. A short exposition on dyadics was brought out by Lindell [25] in 1981, and is much recommended to the interested reader.

A dyadic serves as a linear mapping from one vector to another vector; thus, a dyadic \mathbf{D} is a mapping from \mathbf{a} to \mathbf{b} given by $\mathbf{b} = \mathbf{D} \cdot \mathbf{a}$. This property leads to the idea of a *dyad* that is *composed* of two vectors, i.e., $\mathbf{D}_{12} = \mathbf{d}_1 \mathbf{d}_2$. It follows that $\mathbf{D}_{12} \cdot \mathbf{a} = \mathbf{d}_1(\mathbf{d}_2 \cdot \mathbf{a})$ and $\mathbf{a} \cdot \mathbf{D}_{12} = (\mathbf{a} \cdot \mathbf{d}_1)\mathbf{d}_2$ are vectors, and $\mathbf{D}_{12} \times \mathbf{a} = \mathbf{d}_1(\mathbf{d}_2 \times \mathbf{a})$ and $\mathbf{a} \times \mathbf{D}_{12} = (\mathbf{a} \times \mathbf{d}_1)\mathbf{d}_2$ are dyads, and the oft-used appellation *bivectors* for dyads appears justified [26]. Because a dyadic can be written as the sum of dyads, the general representation of a dyadic is the sum $\mathbf{D} = \sum_{km} D_{km} \mathbf{d}_k \mathbf{d}_m$ [27].

The identity dyadic \mathbf{I} is such that $\mathbf{D} \cdot \mathbf{I} = \mathbf{D} = \mathbf{I} \cdot \mathbf{D}$, and the null dyadic $\mathbf{0}$ is such that $\mathbf{D} \cdot \mathbf{0} = \mathbf{0} = \mathbf{0} \cdot \mathbf{D}$. The simplest antisymmetric dyadic is $\mathbf{u} \times \mathbf{I}$, where \mathbf{u} is any vector of unit length. Even vector differential operators can be thought of as dyadics; thus, the curl operator is written as $\nabla \times \mathbf{I}$, and the divergence

operator as $\nabla \cdot \mathbf{I}$, in dyadic notation. It is not possible for us to go through all the wonderful properties of dyadics than can be exploited in theoretical electromagnetics research, so we refer the interested reader to the compendiums in the books by Chen [24], van Bladel [22], and Varadan et al. [28]. The main feature of computational significance is that, as dyads are bivectors, all dyadics used in this paper can be thought of as 3×3 matrices.

The second issue concerns the singularity of the dyadic Green's function $\mathbf{G}(\mathbf{x}, \mathbf{x}')$ used in Eqs. (8a,b) and defined in Eq. (8c): the factor $\exp(ik_0|\mathbf{x}-\mathbf{x}'|)/4\pi|\mathbf{x}-\mathbf{x}'|$ goes to infinity as $|\mathbf{x}-\mathbf{x}'| \rightarrow 0$. When evaluating $\mathbf{G}(\mathbf{x}, \mathbf{x}')$, the second derivatives therefore have to be carefully handled. As shown by van Bladel [29], the classical procedure leads one to write

$$\iint \int_V d^3x' \mathbf{G}(\mathbf{x}, \mathbf{x}') \cdot \mathbf{b}(\mathbf{x}') = -(1/3k_0^2) \mathbf{b}(\mathbf{x}) +$$

$$\text{P.V.} \iint \int_V d^3x' \{\mathbf{G}(\mathbf{x}, \mathbf{x}') \cdot \mathbf{b}(\mathbf{x}')\}; \mathbf{x} \in V, \quad (9)$$

where P.V. stands for "principal value." When computing the P.V. integral on the right side of Eq. (9), an infinitesimally small spherical region centered about the point $\mathbf{x}' = \mathbf{x}$ is excluded from the domain of integration. Computing the P.V. integral is not problematic because [30]

$$\mathbf{G}(\mathbf{x}, \mathbf{x}') = [(\mathbf{I} - \mathbf{u}_X \mathbf{u}_X) + (i/k_0|\mathbf{X}|)(1 + i/k_0|\mathbf{X}|)$$

$$(\mathbf{I} - 3 \mathbf{u}_X \mathbf{u}_X)] \{\exp(ik_0|\mathbf{X}|)/4\pi|\mathbf{X}|\}; |\mathbf{X}| \neq 0, \quad (10)$$

is not singular when the source point \mathbf{x}' and the field point \mathbf{x} do not coincide; here $\mathbf{X} = \mathbf{x} - \mathbf{x}'$ and $\mathbf{u}_X = \mathbf{X}/|\mathbf{X}|$. Yaghjian [31] has modified the right side of (9) to an expression wherein the excluded infinitesimal region need not be spherical.

We will use an alternative approach to evaluate the integral (9), as shown in Appendix 2. In this approach [6, 10, 32], the region of integration is split into two regions: one region includes the point $\mathbf{x}' = \mathbf{x}$ in its interior, while the second one is the remainder. Use is made of Gauss' theorem and the Green's function for Poisson's equation to determine this integral. This procedure is attractive as it places very little restrictions on the shape and the size of the region surrounding the point $\mathbf{x}' = \mathbf{x}$.

4. The Method of Moments

The method of moments is a general mathematical procedure for transforming a linear operator equation into a set of simultaneous algebraic

equations, and the interested reader is referred to [4], Chap. 1, for a simple introduction. We are, however, confining ourselves here to the application of MOM to electromagnetic scattering problems.

Although the MOM has grown increasingly sophisticated in the last decade [6, 33], a simple version [5] suffices for the easy conversion of the integral equation (8b) into a set of simultaneous algebraic equations. We begin by partitioning the scatterer region V_{int} into simply connected subregions V_m , $1 \leq m \leq M$, each bounded by a closed surface S_m , so that Eq. (8b) can be transformed to

$$E(\mathbf{x}) = E_{\text{inc}}(\mathbf{x}) + k_0^2 \sum_m \iiint_{V_m} d^3\mathbf{x}' \{[\epsilon_r(\mathbf{x}') - 1] \mathbf{G}(\mathbf{x}, \mathbf{x}') \cdot E(\mathbf{x}')\}, \mathbf{x} \in \sum_m V_m + V_{\text{ext}}. \quad (11)$$

The main features of this partitioning scheme are as follows:

- (i) Each subregion V_m is modeled as being homogeneous such that

$$\epsilon_r(\mathbf{x}) = \epsilon_{r,m}; \mathbf{x} \in V_m. \quad (12)$$

- (ii) The maximum linear cross-sectional extent $2a_m$ of V_m is such that $a_m/\lambda < 0.1$ and $a_m |\epsilon_{r,m} - 1|/\lambda < 0.1$; that is, the dimension a_m is no more than a tenth of the wavelength λ in the exterior region V_{ext} as well as of the wavelength in the subregion V_m .

- (iii) The surface S_m that bounds the subregion V_m is sufficiently smooth so as to be at least once differentiable, which enables the unambiguous prescription of a normal at any point on S_m .

Satisfaction of these three conditions, in practice, means that the union $\sum_m V_m$ of the subregions is only approximately coincident with the scatterer region V_{int} . Condition (i) can lead to an artificial material discontinuity across the interface of two adjacent subregions, therefore the simple MOM algorithm given in this section works best when adjacent subregions do not differ widely in their permittivities. Condition (ii) ensures that the spatial variations of the electromagnetic field inside each subregion are small enough so that each subregion can be thought of as a dipole scatterer [34], though different authors use somewhat different upper bounds on the subregional size [35, 36]. Condition (iii) is mostly ignored by MOM users, their usual practice being to use cubical subregions. Thus, the adequacy and the accuracy of the MOM—and the CDM—results depend in large measure on the adequacy of the partitioning scheme.

Two ancillary aspects of the partitioning scheme need to be stated for the simple MOM algorithm. First, the incident field must have slow enough spatial variations that it may be considered almost spatially constant over any subregion. Second, not only the permittivity but also the actual field is assumed spatially constant in each subregion. Together, these two assumptions constitute a long wavelength approximation [37], whose consequences are exploited in the MOM as well as in the CDM.

Let the volume of V_m be denoted by $v_m = \iiint_{V_m} d^3\mathbf{x}$, and let \mathbf{x}_m denote a distinguished point (such as the centroid) lying inside V_m . On setting $\mathbf{x} = \mathbf{x}_k$ in Eq. (11) we get the relation

$$E(\mathbf{x}_k) - k_0^2 [\epsilon_{r,k} - 1] \iiint_{V_k} d^3\mathbf{x}' \{ \mathbf{G}(\mathbf{x}_k, \mathbf{x}') \cdot E(\mathbf{x}') \} = E_{\text{inc}}(\mathbf{x}_k) + k_0^2 \sum_{m,m \neq k} [\epsilon_{r,m} - 1] \iiint_{V_m} d^3\mathbf{x}' \{ \mathbf{G}(\mathbf{x}_k, \mathbf{x}') \cdot E(\mathbf{x}') \}; 1 \leq k \leq M. \quad (13a)$$

Next, on using the approximation $E(\mathbf{x}) \cong E(\mathbf{x}_m)$ for all $\mathbf{x} \in V_m$ and carrying out the integrations over all subregions, we get

$$E_k - (\epsilon_{r,k} - 1) [k_0^2 \mathbf{M}_k - \mathbf{L}_k] \cdot E_k = E_{\text{inc}}(\mathbf{x}_k) + k_0^2 \sum_{m,m \neq k} \{ v_m [\epsilon_{r,m} - 1] \mathbf{G}(\mathbf{x}_k, \mathbf{x}_m) \cdot E_m \}; 1 \leq k \leq M, \quad (13b)$$

where $E_m \cong E(\mathbf{x}_m)$. In obtaining Eq. (13b) from Eq. (13a), we have accomplished the integration on the subregion V_m , $m \neq k$, very simply by evaluating the specific integrand at \mathbf{x}_m and multiplying it by the volumetric capacity v_m . The integral $\iiint_{V_k} d^3\mathbf{x}' \mathbf{G}(\mathbf{x}_k, \mathbf{x}') \cdot E(\mathbf{x}')$, on the other hand, has been estimated using Eq. (A2-5a).

With the assistance of Eqs. (5c) and (12), we transform Eq. (13b) into $3M$ simultaneous algebraic equations compactly stated in vector dyadic notation as

$$E_{\text{inc}}(\mathbf{x}_k) = \sum_{m \in \{1, 2, \dots, M\}} [\mathbf{A}_{km} \cdot E_m]; 1 \leq k \leq M, \quad (14a)$$

where the $3M$ unknowns are the cartesian components of the fields E_m , $1 \leq m \leq M$. The dyadic kernel used in Eq. (14a) is given as

$$\mathbf{A}_{km} = \mathbf{I} \delta_{km} + (1 - \epsilon_{r,k}) \delta_{km} [k_0^2 \mathbf{M}_k - \mathbf{L}_k] + k_0^2 v_m (1 - \epsilon_{r,m}) (1 - \delta_{km}) \mathbf{G}_{km}, \quad (14b)$$

where δ_{km} is the Kronecker delta and the definition

$$\begin{aligned} \mathbf{G}_{km} = \mathbf{G}(\mathbf{x}_k, \mathbf{x}_m) = & [(1 - X_{km}X_{km}/|X_{km}|^2) + \\ & (i/k_0|X_{km}|)(1 - 3X_{km}X_{km}/|X_{km}|^2) + \\ & (i/k_0|X_{km}|)^2 (1 - 3X_{km}X_{km}/|X_{km}|^2)] \\ & [\exp(ik_0|X_{km}|)/4\pi|X_{km}|]; m \neq k, \end{aligned} \quad (15)$$

follows from Eq. (A2-6a) with $X_{km} = \mathbf{x}_k - \mathbf{x}_m$. In this straightforward and simple version of the MOM, wherein the electric field has been assumed to be piecewise constant over the scatterer region V_{int} , Eq. (14a) has to be solved for the three cartesian components of all E_m for specified $E_{inc}(\mathbf{x})$.

Bearing in mind that all of our dyadics can be easily thought as 3×3 matrices, one can solve Eq. (14a) using a variety of matrix manipulation techniques. The Gauss elimination procedure [38] is simple but places a heavy demand on computer memory. Much less computationally intensive is the conjugate gradient method [39], which is now being heavily employed for MOM calculations [40].

Once all E_m have been thus calculated, the scattered electric field in V_{ext} can be computed as the sum

$$\begin{aligned} E_{sca}(\mathbf{x}) = E(\mathbf{x}) - E_{inc}(\mathbf{x}) = \\ k_0^2 \sum_{m \in \{1,2,\dots,M\}} \{v_m [\epsilon_{r,m} - 1] \mathbf{G}(\mathbf{x}, \mathbf{x}_m) \cdot \mathbf{E}_m\}; \mathbf{x} \in V_{ext}, \end{aligned} \quad (16)$$

which expression follows from Eq. (8b). Now, from Eq. (A2-6a), we have the asymptote [41]

$$\begin{aligned} \text{Tend}_{k_0|\mathbf{x} - \mathbf{x}_m| \rightarrow \infty} \mathbf{G}(\mathbf{x}, \mathbf{x}_m) \cong [1 - (\mathbf{x} - \mathbf{x}_m)(\mathbf{x} - \mathbf{x}_m)/ \\ |\mathbf{x} - \mathbf{x}_m|^2] [\exp(ik_0|\mathbf{x} - \mathbf{x}_m|)/4\pi|\mathbf{x} - \mathbf{x}_m|], \end{aligned} \quad (17a)$$

correct to order $1/|\mathbf{x} - \mathbf{x}_m|$. Since all \mathbf{x}_m are generally distributed around the origin, the further reduction

$$\begin{aligned} \text{Tend}_{k_0|\mathbf{x} - \mathbf{x}_m| \rightarrow \infty} \mathbf{G}(\mathbf{x}, \mathbf{x}_m) \cong [1 - \mathbf{x}\mathbf{x}/|\mathbf{x}|^2] \\ \{\exp(ik_0|\mathbf{x} - \mathbf{x}_m|)/4\pi|\mathbf{x}|\}, \end{aligned} \quad (17b)$$

is reasonable. Finally, making the Fraunhofer approximation [42]

$$\exp(ik_0|\mathbf{x} - \mathbf{x}_m|) \cong \exp[ik_0|\mathbf{x}|] \exp[ik_0\mathbf{x} \cdot \mathbf{x}_m/|\mathbf{x}|] \quad (17c)$$

on the left side of Eq. (17b) yields

$$\begin{aligned} \text{Tend}_{k_0|\mathbf{x} - \mathbf{x}_m| \rightarrow \infty} \mathbf{G}(\mathbf{x}, \mathbf{x}_m) \cong [1 - \mathbf{x}\mathbf{x}/|\mathbf{x}|^2] \exp(ik_0|\mathbf{x}|) \\ \exp(-ik_0\mathbf{x} \cdot \mathbf{x}_m/|\mathbf{x}|)/4\pi|\mathbf{x}|. \end{aligned} \quad (17d)$$

Consequently, the scattered electric field of Eq. (16) has the asymptotic representation

$$\text{Tend}_{k_0r \rightarrow \infty} E_{sca}(\mathbf{x}\mathbf{u}_s) \cong [\exp(ik_0r)/r] F_{sca}(\mathbf{u}_s), \quad (18)$$

in the direction \mathbf{u}_s in the far zone, with the far-zone scattering amplitude defined by

$$F_{sca}(\mathbf{u}_s) = (k_0^2/4\pi) [1 - \mathbf{u}_s\mathbf{u}_s].$$

$$\sum_{m \in \{1,2,\dots,M\}} \{\exp(-ik_0\mathbf{u}_s \cdot \mathbf{x}_m) v_m [\epsilon_{r,m} - 1] \mathbf{E}_m\}, \quad (19)$$

which shows quite clearly that $\mathbf{u}_s \cdot F_{sca}(\mathbf{u}_s) \cong 0$.

5. The Coupled Dipole Method

The heart of the MOM is Eq. (13b) which involves the electric field E_k that is *actually present* at \mathbf{x}_k . However, in the CDM we have to consider the electric field that excites the subregion V_k , each subregion being explicitly modeled as an electric dipole moment. In order to obtain an expression for this exciting field, we return to Eq. (8a), and rewrite it as

$$\begin{aligned} E(\mathbf{x}) - i\omega\mu_0 \iint \int_{V_k} d^3x' \{\mathbf{G}(\mathbf{x}, \mathbf{x}') \cdot \mathbf{J}(\mathbf{x}')\} = \\ E_{inc}(\mathbf{x}) + i\omega\mu_0 \sum_{m, m \neq k} \iint \int_{V_m} d^3x' \{\mathbf{G}(\mathbf{x}, \mathbf{x}') \cdot \mathbf{J}(\mathbf{x}')\}; \\ \mathbf{x} \in \sum_m V_m + V_{ext}, \end{aligned} \quad (20)$$

after partitioning the scatterer region precisely in the same manner as was done for the MOM solution. We know that $E_{inc}(\mathbf{x})$ is the field in the absence of the scatterer and that the quantity

$$i\omega\mu_0 \iint \int_{V_m} d^3x' \{\mathbf{G}(\mathbf{x}, \mathbf{x}') \cdot \mathbf{J}(\mathbf{x}')\}; \mathbf{x} \notin V_m, m \neq k,$$

is an electric field whose source clearly lies in the subregion V_m , $m \neq k$. Thus, the whole of the right side of Eq. (20) is a composite electric field with multiple sources, but none of the sources lies in V_k . This composite electric field

$$\begin{aligned} {}^{(k)}E_{exc}(\mathbf{x}) = E_{inc}(\mathbf{x}) + i\omega\mu_0 \sum_{m, m \neq k} \iint \int_{V_m} d^3x' \\ \{\mathbf{G}(\mathbf{x}, \mathbf{x}') \cdot \mathbf{J}(\mathbf{x}')\}; \mathbf{x} \in V_k, \end{aligned} \quad (21a)$$

can be thought of as the field that excites V_k .

Since the left side of Eq. (20) must be equal to its right side, it follows that

$${}^{(k)}E_{\text{exc}}(\mathbf{x}) = E(\mathbf{x}) - i\omega\mu_0 \iiint_{V_k} d^3x' \{ \mathbf{G}(\mathbf{x}, \mathbf{x}') \cdot \mathbf{J}(\mathbf{x}') \};$$

$$\mathbf{x} \in V_k. \quad (21b)$$

On setting $\mathbf{x} = \mathbf{x}_k$ in Eq. (21b), and completing the volume integration therein using Eq. (A2-5a), we get the expression

$$E_{\text{exc},k} = E_k - i\omega\mu_0 [\mathbf{M}_k - (1/k_0^2)\mathbf{L}_k] \cdot \mathbf{J}_k = E_{\text{exc},k};$$

$$1 \leq k \leq M; \quad (22)$$

here, $\mathbf{J}_k = \mathbf{J}(\mathbf{x}_k)$ and $E_{\text{exc},k} = {}^{(k)}E_{\text{exc}}(\mathbf{x}_k)$. But, by virtue of Eq. (5c) we have

$$\mathbf{J}_k = i\omega\epsilon_0 (1 - \epsilon_{r,k}) E_k; \quad 1 \leq k \leq M, \quad (23a)$$

which means that Eq. (22) reduces to

$$\mathbf{A}_{kk} \cdot E_k = E_{\text{exc},k}; \quad 1 \leq k \leq M, \quad (23b)$$

whence,

$$E_k = \mathbf{A}_{kk}^{-1} \cdot E_{\text{exc},k}; \quad 1 \leq k \leq M, \quad (23c)$$

$$\mathbf{J}_k = i\omega\epsilon_0 (1 - \epsilon_{r,k}) \mathbf{A}_{kk}^{-1} \cdot E_{\text{exc},k}; \quad 1 \leq k \leq M. \quad (23d)$$

Consistent with the long-wavelength approach, in the CDM we think of the equivalent electric dipole moment [9, 10]

$$\mathbf{p}_k = (i/\omega)\mathbf{v}_k \mathbf{J}_k \quad (24a)$$

located at \mathbf{x}_k ; thus,

$$\mathbf{p}_k = \mathbf{t}_k \cdot E_{\text{exc},k}, \quad (24b)$$

after using Eq. (21b), where

$$\mathbf{t}_k = \mathbf{v}_k \epsilon_0 (\epsilon_{r,k} - 1) \mathbf{A}_{kk}^{-1} \quad (24c)$$

is the polarizability dyadic of the dielectric region V_k .

We return to Eq. (21a) at this stage, set $\mathbf{x} = \mathbf{x}_k$ therein, and do the volume integrations; the result is the vector dyadic relation

$$E_{\text{exc},k} = E_{\text{inc}}(\mathbf{x}_k) + i\omega\mu_0 \sum_{m \neq k} \{ \mathbf{v}_m \mathbf{G}_{km} \cdot \mathbf{J}_m \};$$

$$1 \leq k \leq M, \quad (25)$$

in accord with the long-wavelength approximation. With the aid of Eq. (24a), we rewrite Eq. (25) as

$$E_{\text{exc},k} = E_{\text{inc}}(\mathbf{x}_k) + \omega^2\mu_0 \sum_{m \neq k} \{ \mathbf{G}_{km} \cdot \mathbf{p}_m \}, \quad (26a)$$

and the use of Eq. (24b) yields

$$E_{\text{exc},k} = E_{\text{inc}}(\mathbf{x}_k) + \omega^2\mu_0 \sum_{m \neq k} \{ \mathbf{G}_{km} \cdot \mathbf{t}_m \} \cdot E_{\text{exc},m}. \quad (26b)$$

Equation (26b) constitutes the core of the CDM and, for numerical work, is best rewritten as the set of the $3M$ algebraic scalar equations

$$E_{\text{inc}}(\mathbf{x}_k) = \sum_{m \in \{1,2,\dots,M\}} [\mathbf{Q}_{km} \cdot E_{\text{exc},m}]; \quad 1 \leq k \leq M, \quad (27a)$$

for the cartesian components of $E_{\text{exc},m}$, where the dyadic kernel

$$\mathbf{Q}_{km} = \mathbf{I}\delta_{km} - \omega^2\mu_0 \mathbf{G}_{km} \cdot \mathbf{t}_m (1 - \delta_{km}). \quad (27b)$$

The CDM algorithm is structurally just the same as the MOM algorithm, as is easily demonstrated by a comparison of Eqs. (27a,b) with Eqs. (14a,b). Hence, computational techniques for solving Eq. (27a) are the same as for solving Eq. (14a).

Once all $E_{\text{exc},m}$ have been obtained as the solution of Eq. (27a), one can use Eq. (24b) to find all \mathbf{p}_m and ascertain the scattered field as the sum

$$E_{\text{sca}}(\mathbf{x}) = E(\mathbf{x}) - E_{\text{inc}}(\mathbf{x}) =$$

$$\omega^2\mu_0 \sum_{m \in \{1,2,\dots,M\}} \{ \mathbf{G}(\mathbf{x}, \mathbf{x}_m) \cdot \mathbf{p}_m \}; \quad \mathbf{x} \in V_{\text{ext}}, \quad (28)$$

which relation follows from Eq. (8a). Equation (18) still applies for the scattered electric field in the far zone, but the far-zone scattering amplitude is now given by

$$\mathbf{F}_{\text{sca}}(\mathbf{u}_s) = (\omega^2\mu_0/4\pi) [\mathbf{I} - \mathbf{u}_s \mathbf{u}_s] \cdot$$

$$\sum_{m \in \{1,2,\dots,M\}} \{ \exp(-ik_0 \mathbf{u}_s \cdot \mathbf{x}_m) \mathbf{p}_m \}; \quad (29a)$$

equivalently,

$$\mathbf{F}_{\text{sca}}(\mathbf{u}_s) = (\omega^2\mu_0/4\pi) [\mathbf{I} - \mathbf{u}_s \mathbf{u}_s] \cdot$$

$$\sum_{m \in \{1,2,\dots,M\}} \{ \exp(-ik_0 \mathbf{u}_s \cdot \mathbf{x}_m) \mathbf{t}_m \cdot E_{\text{exc},m} \}. \quad (29b)$$

Parenthetically, we remark here that the Rayleigh-Debye approximation for scattering by smoke agglomerates [11, 12] may be obtained by replacing $E_{\text{exc},m}$ in Eq. (29b) by $E_{\text{inc}}(\mathbf{x}_m)$.

6. Scattering and Absorption

The presence of a scatterer has two observable consequences insofar as the conservation of electromagnetic energy is concerned. A portion of the energy radiated by the source of $E_{inc}(x)$ is scattered in all directions by the scatterer. Another portion is absorbed by the scatterer and converted into other forms such as heat. All calculations pertaining to the scattered and the absorbed powers at a given circular frequency ω are made in terms of power averaged over the time period $2\pi/\omega$.

Because $F_{sca}(u_s)$ is of the form $[I - u_s u_s] \cdot b$, it follows that $u_s \cdot F_{sca}(u_s) \equiv 0$, as has been mentioned earlier. By virtue of Eqs. (3a) and (18), we have

$$\begin{aligned} \text{Tend}_{k_0x \rightarrow \infty} H_{sca}(xu_s) &\equiv \\ (1/\eta_0) [\exp(ik_0x)/x] u_s \times F_{sca}(u_s), \end{aligned} \quad (30)$$

where $\eta_0 = (\mu_0/\epsilon_0)^{1/2}$ is the intrinsic impedance of free space. These observations imply that the scattered field in the far zone is Transverse Electro-Magnetic (TEM) in character.

The time-averaged scattered power per unit solid angle in the direction u_s is defined as

$$dP_{sca}(u_s)/d\Omega(u_s) = (1/2)$$

$$\text{Tend}_{k_0x \rightarrow \infty} \text{Real} [x^2 u_s \cdot \{E_{sca}(xu_s) \times H_{sca}^*(xu_s)\}], \quad (31a)$$

with $d\Omega(u_s) \equiv \sin\theta_s d\theta_s d\phi_s$, as is customary in spherical coordinates, and the asterisk denoting the complex conjugate. After putting Eqs. (18) and (30) in Eq. (31a), we obtain

$$dP_{sca}(u_s)/d\Omega(u_s) = (1/2\eta_0) F_{sca}(u_s) \cdot F_{sca}^*(u_s); \quad (31b)$$

consequently, we are able to ascertain the total time-averaged scattered power as the integral

$$\begin{aligned} P_{sca} &= (1/2\eta_0) \int_0^{2\pi} d\phi_s \int_0^\pi d\theta_s \sin\theta_s \\ &F_{sca}(u_s) \cdot F_{sca}^*(u_s). \end{aligned} \quad (31c)$$

Unless the scatterer material is intrinsically lossless, there is absorption of electromagnetic energy in V_{int} . Because the scatterer is simply a dielectric object here, the time-averaged power absorbed in V_{int} may be computed as the volume integral

$$\begin{aligned} P_{abs} &= \text{Real} [(i\omega/2) \iiint_{V_{int}} d^3x E(x) \cdot D^*(x)] \\ &\quad (32a) \end{aligned}$$

from Poynting's theorem for monochromatic fields [24, Chap. 2]. After using Eq. (2a) on the right side of this relation, we get the result

$$P_{abs} = \text{Real} [(i\omega/2)$$

$$\iiint_{V_{int}} d^3x \{\epsilon_0 \epsilon_r^*(x) E(x) \cdot E^*(x)\}]. \quad (32b)$$

Finally, after using Eq. (12) as well as the long-wavelength approximation made heretofore, we are able to reduce this expression to the sum

$$\begin{aligned} P_{abs} &= \text{Real} [(i\omega/2) \iiint_{V_{int}} d^3x \{\epsilon_0 \epsilon_{r,m}^* E_m \cdot E_m^*\}] = \\ &- (\omega/2) \text{Imag} [\sum_m v_m \{\epsilon_0 \epsilon_{r,m}^* E_m \cdot E_m^*\}]. \end{aligned} \quad (33)$$

Because $E_m \cdot E_m^*$ is purely real, no power absorption will take place in V_m if $\epsilon_{r,m}$ is purely real; indeed, $P_{abs} \equiv 0$, provided $\text{Imag} [\epsilon_r(x)] \equiv 0$ for all $x \in V_{int}$.

Insofar as the MOM is concerned, the solution $\{E_m; m = 1, 2, \dots, M\}$ of Eq. (14a) may be directly substituted into Eq. (33) for the computation of P_{abs} . The calculation of P_{abs} in the CDM is only slightly more complicated: the exciting fields $\{E_{exc,m}; m = 1, 2, \dots, M\}$ obtained by solving Eq. (27a) have to be substituted into Eq. (23c) to get $\{E_m; m = 1, 2, \dots, M\}$. Thus, an useful expression for CDM computations is

$$\begin{aligned} P_{abs} &= -(\omega/2) \text{Imag} [\sum_m v_m \{\epsilon_0 \epsilon_{r,m}^* \\ &T_m \cdot E_{exc,m} \cdot T_m^* \cdot E_{exc,m}^*\}], \end{aligned} \quad (34a)$$

where

$$T_m = [I + (1 - \epsilon_{r,m}) (k_0^2 M_m - L_m)]^{-1}. \quad (34b)$$

The total time-averaged power extinguished by the scatterer region is the sum

$$P_{ext} = P_{sca} + P_{abs}. \quad (35)$$

Quite often, one is interested in the extinction of the plane wave

$$E_{inc}(x) = e_{inc} \exp[ik_0 u_{inc} \cdot x], \quad (36a)$$

$$H_{inc}(x) = (1/\eta_0) u_{inc} \times e_{inc} \exp[ik_0 u_{inc} \cdot x], \quad (36b)$$

where e_{inc} carries the units of volts per meter and u_{inc} is a dimensionless unit vector such that $e_{inc} \cdot u_{inc} = 0$. In this case, the total time-averaged

power extinguished by the presence of matter in V_{int} can be estimated using the forward scattering amplitude as [22, Chap. 8]:

$$P_{\text{ext}} = (2\pi/\omega\mu_0) \text{Imag} [e_{\text{inc}}^* \cdot F_{\text{sca}}(\mathbf{u}_{\text{inc}})] . \quad (37)$$

Substitution of Eqs. (29a) and (36a) in this relation gives us

$$P_{\text{ext}} = (\omega/2) \text{Imag} [\sum_m \{E_{\text{inc}}^*(\mathbf{x}_m) \cdot \mathbf{p}_m\}] , \quad (38a)$$

whence,

$$P_{\text{ext}} = (\omega/2) \text{Imag} [\sum_m \{E_{\text{inc}}^*(\mathbf{x}_m) \cdot \mathbf{t}_m \cdot E_{\text{exc},m}\}] \quad (38b)$$

for use with the CDM. The MOM analog of Eq. (38b) is easily obtained by substituting Eq. (23b) therein; ergo,

$$P_{\text{ext}} = (\omega\epsilon_0/2) \text{Imag} [\sum_m \{v_m (\epsilon_{r,m} - 1) E_{\text{inc}}^*(\mathbf{x}_m) \cdot E_m\}] , \quad (38c)$$

for use with the MOM.

7. Spherical and Cubical Subregions

Although spheroidal and ellipsoidal subregions have been used [43, 44], it is commonplace in literature to have cubical or spherical subregions. CDM users are more comfortable with spherical subregions, while MOM users are fond of cubical ones. Cubes and spheres have the same dyadic \mathbf{L} , and in many MOM codes the \mathbf{M} dyadic of a cube is estimated as that of an equi-voluminal sphere; see Appendix C. Without any particular loss of generality therefore, we take the subregions to be spherical and of identical radii in the remainder of this paper.

Let the subregion V_k be the sphere of radius a with its center at \mathbf{x}_k . As a result, the volume $v_k = (4\pi/3)a^3$, the dyadic $\mathbf{L}_k = (1/3)\mathbf{I}$, and the dyadic $\mathbf{M}_k = (2/3k_0^2)[(1 - ik_0a) \exp(ik_0a) - 1]\mathbf{I}$, as shown in Appendix C. Consequently, the MOM dyadic kernel given in Eq. (14b) reduces to

$$\mathbf{A}_{kk} = \mathbf{I} [1 + (1/3)(1 - \epsilon_{r,k})\{2(1 - ik_0a) \exp(ik_0a) - 3\}] , \quad (39a)$$

$$\mathbf{A}_{km} = (4\pi/3) a^3 k_0^2 (1 - \epsilon_{r,m}) \mathbf{G}_{km}; m \neq k . \quad (39b)$$

In the same manner, the CDM dyadic kernel of Eq. (27b) simplifies to

$$\mathbf{Q}_{kk} = \mathbf{I} , \quad (40a)$$

$$\mathbf{Q}_{km} = -\omega^2\mu_0 (4\pi/3)a^3 \epsilon_0(\epsilon_{r,m} - 1)$$

$$[1 + (1/3)(1 - \epsilon_{r,m})\{2(1 - ik_0a)$$

$$\exp(ik_0a) - 3\}]^{-1} \mathbf{G}_{km}; m \neq k . \quad (40b)$$

An analysis of the self-terms is crucial to the understanding of the MOM and the CDM. From Eq. (39a) it follows that the MOM self-term can be broken up as

$$\mathbf{A}_{kk} = \{\mathring{A}_{kk} + \mathring{A}_{kk}\}\mathbf{I} , \quad (41a)$$

where

$$\mathring{A}_{kk} = (\epsilon_{r,k} + 2)/3 , \quad (41b)$$

and

$$\mathring{A}_{kk} = (2/3)(1 - \epsilon_{r,k})[(1 - ik_0a) \exp(ik_0a) - 1] . \quad (41c)$$

Both \mathring{A}_{kk} and \mathring{A}_{kk} should be called self-terms; instead, it seems only \mathring{A}_{kk} has been accorded that honor in some MOM papers, e.g., [16–19, 45].

The CDM self-term is somewhat obscure, being hidden as the polarizability dyadic \mathbf{t}_k of Eq. (24b). In the present instance, the polarizability dyadic reduces to a scalar because the subregion is spherical; hence,

$$\mathbf{t}_k = \mathbf{I} \tau_k , \quad (42a)$$

where

$$\tau_k = \alpha_k / (1 + \mathring{A}_{kk}/\mathring{A}_{kk}) , \quad (42b)$$

and

$$\alpha_k = 4\pi a^3 \epsilon_0(\epsilon_{r,k} - 1)/(\epsilon_{r,k} + 2) \quad (42c)$$

is the Mossotti-Clausius polarizability [46, 47] of the electrically small dielectric sphere.

Let $k_0a \ll 1$ in Eq. (41c) and \mathring{A}_{kk} be evaluated correct to order $k_0^3 a^3$. Then,

$$\tau_k \cong \alpha_k / \{1 - k_0^2(a^{-1} + 2ik_0/3)\alpha_k/4\pi\epsilon_0\} , \quad (43)$$

and we observe that the $(2ik_0^3/3)\alpha_k/4\pi\epsilon_0$ term in the denominator of the right side of Eq. (43) is the radiative reaction term used by Draine [48] in his CDM formulation. More often, \mathring{A}_{kk} is evaluated correct only to the first order in k_0a , leading to

$\tau_k \cong \alpha_k$ [7], and thereby giving rise to the semi-microscopic flavor of this numerical approach [9].

8. Strong and Weak Forms

The various approximations that can be made for the self-terms lead us to the *strong* and the *weak* forms of the MOM and the CDM [10]. In the strong forms (S-CDM & S-MOM), Eq. (A2–5a) is used to estimate the self-term ($m = k$) in Eqs. (13a) and (21b). In the Weak forms (W-CDM & W-MOM), Eq. (A2–7) is used in place of Eq. (A2–5a) for this estimation. For isotropic dielectric scatterers, the W-CDM is exemplified by Purcell and Pennypacker [7] using spherical subregions, and the S-CDM has become recently available [17] for the same problem. The S-MOM has been used for isotropic dielectric scatterers for many years [6, 33], but the idea of W-MOM is of more recent provenance [17].

The W-MOM corresponds exactly to the W-CDM, while the S-MOM corresponds exactly to the S-CDM. When all subregional volumetric capacities are very small, the S-MOM/S-CDM effectively transmutes into the W-MOM/W-CDM. Generally stated, therefore, it can be surmised that the scatterer region V_{int} must be broken up into a larger number of subregions when the W-MOM/W-CDM is used than if the S-MOM/S-CDM is used. Comparison of S-MOM results with the W-CDM results, with identical partitioning of the scatterer region, [e.g., 16, 18, 19], in some instances may be like comparing apples with oranges. The difference between S-CDM/S-MOM and W-CDM/W-MOM is solely due to the inclusion or the exclusion of the dyadic \mathbf{M}_k in the expression for \mathbf{A}_{kk} , therefore computational time is marginally increased and the memory requirement negligibly, when one shifts from W-CDM/W-MOM to S-CDM/S-MOM.

9. Spherical Subregions and Finite-Size Effects

An assessment of the MOM and the CDM for isotropic dielectric scatterers with spherical subregions is now in order. To facilitate such a comparison, we reiterate that

$$\mathbf{A}_{kk} = \{1 + (1 - \epsilon_{r,k})[(2/3)(1 - ik_0a) \exp(ik_0a) - 1]\}, \quad \text{[S-MOM] (44a)}$$

$$\mathbf{A}_{kk} \cong \{(\epsilon_{r,k} + 2)/3\} \mathbf{I}; \quad \text{[W-MOM] (44b)}$$

and correspondingly,

$$\tau_k = (4\pi/3)a^3 \epsilon_0(\epsilon_{r,k} - 1)/\{1 + (1 - \epsilon_{r,k}) [(2/3)(1 - ik_0a) \exp(ik_0a) - 1]\}, \quad \text{[S-CDM] (45a)}$$

$$\tau_k \cong 4\pi a^3 \epsilon_0(\epsilon_{r,k} - 1)/(\epsilon_{r,k} + 2) = \alpha_k. \quad \text{[W-CDM] (45b)}$$

We can evaluate the strong forms vis-a-vis the weak forms through the Taylor expansion of the ratio τ/α about $\epsilon_r = 1$, there being no need for us to continue the subscript k in the remainder of this paper. Using Eqs. (41b), (41c) and (42b), we get the expansion

$$\tau/\alpha = 1 + 2\Lambda[(\epsilon_r - 1)/3] + 2\Lambda(2\Lambda - 1)[(\epsilon_r - 1)/3]^2 + \dots, \quad (46a)$$

where $\Lambda = [(1 - ik_0a) \exp(ik_0a) - 1]$ has been used for convenience; and it becomes clear that the weak forms are poor approximations of the strong forms when the relative permittivity is significantly different from unity.

Likewise, the Maclaurin expansion of τ/α with respect to the size parameter k_0a ,

$$\tau/\alpha = 1 + [(\epsilon_r - 1)/(\epsilon_r + 2)](k_0a)^2 + (2i/3)[(\epsilon_r - 1)/(\epsilon_r + 2)](k_0a)^3 + \dots, \quad (46b)$$

indicates that the weak forms become increasingly inadequate as the size parameter of the subregion increases.

Equations (46a) and (46b) tell us that strong forms incorporate finite-size effects meaningfully, while the weak forms do so trivially. This conclusion is reinforced by Figs. 2–4 that show plots of τ/α versus the normalized radius k_0a of an electrically small sphere for $\epsilon_r = 1.5, 2.5$ and 4.0 . In these figures we have ensured that the maximum value of $k_0a|\epsilon_r|^{1/2}$ is about 0.5. We observe – not surprisingly – that τ is complex while α is purely real for these input parameters. Furthermore, in all three figures the ratio $|\tau/\alpha|$ lies between 1.02 and 1.03 when $k_0a|\epsilon_r|^{1/2} \cong 0.5$; while $\tau/\alpha = 1$ for $k_0a = 0$, of course. Similar conclusions can be drawn from Fig. 5, wherein the calculations of τ/α have been reported for a lossy dielectric sphere with $\epsilon_r = 3.75 + 0.25i$. These figures highlight the understanding on finite-size effects drawn from Eqs. (46a,b), and it follows that coarser partitioning of V_{int} may be acceptable when S-CDM/S-MOM is used than when W-CDM/W-MOM is used. These thoughts can be validated by careful examination of the graphs recently published by Ku [19].

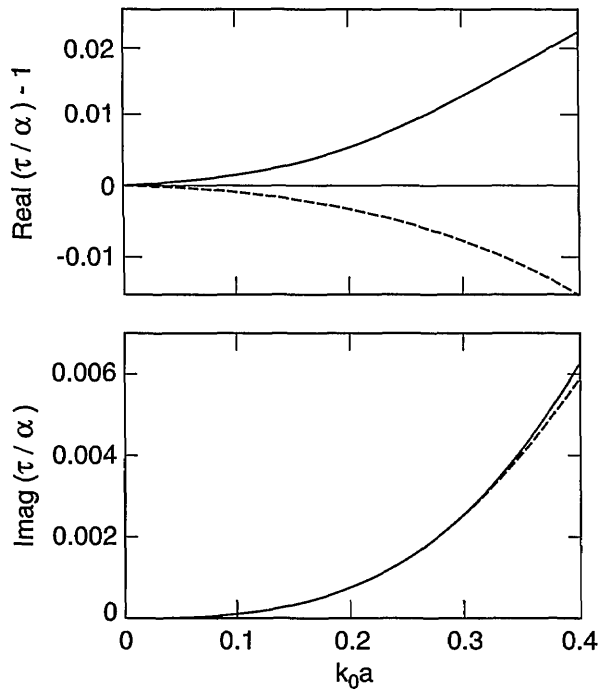


Fig. 2. Functions $[\tau/\alpha - 1]$ (solid lines) and $[\tau_{DB}/\alpha - 1]$ (dashed lines) as functions of the size parameter k_0a of a spherical sub-region whose relative permittivity $\epsilon_r = 1.5$; the Mossotti-Clausius polarizability $\alpha = 4\pi a^3 \epsilon_0(\epsilon_r - 1)/(\epsilon_r + 2)$.

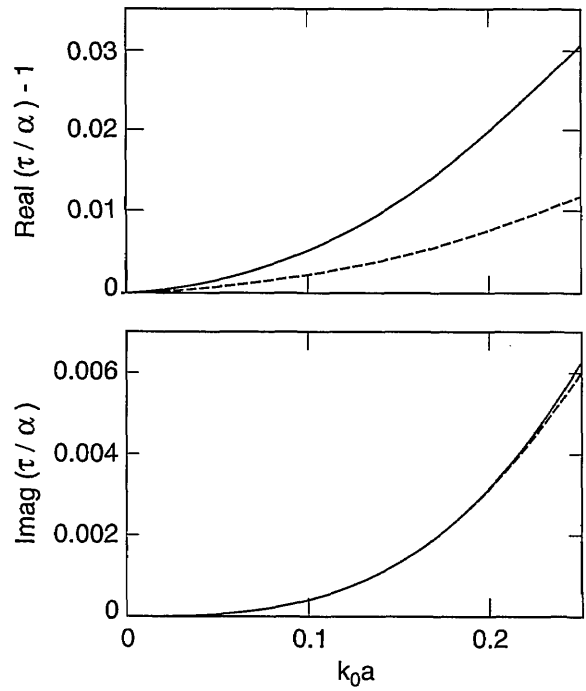


Fig. 4. Same as Fig. 2, but $\epsilon_r = 4.0$.

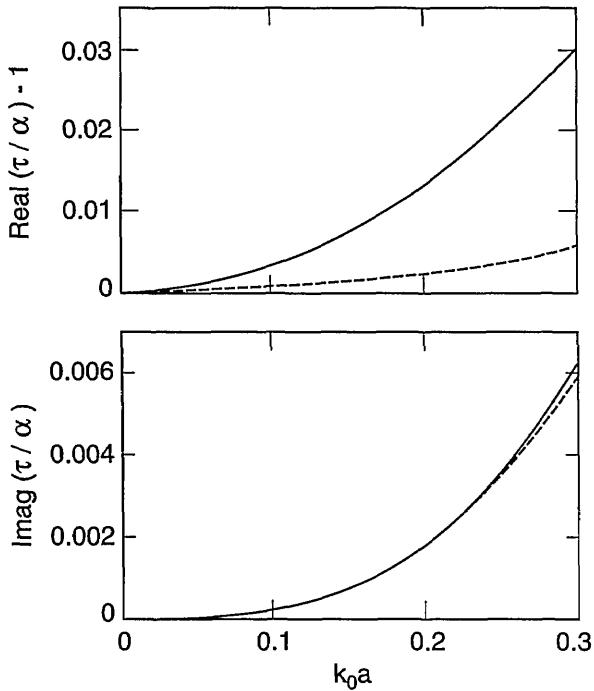


Fig. 3. Same as Fig. 2, but $\epsilon_r = 2.5$.

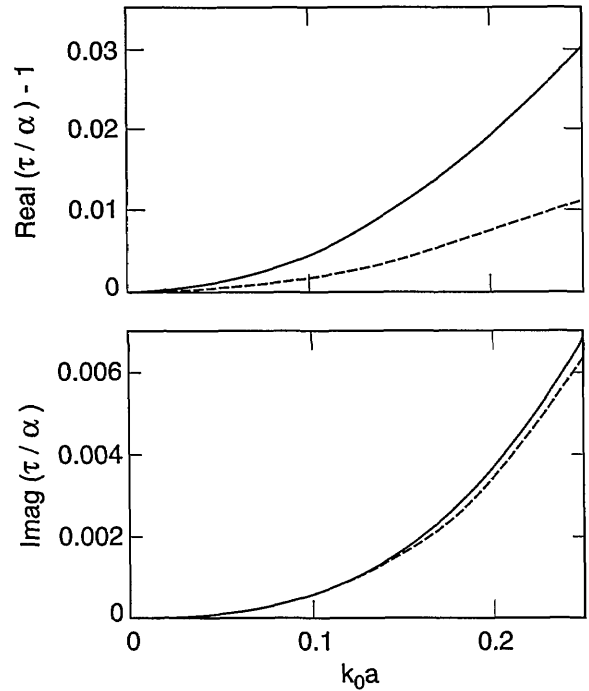


Fig. 5. Same as Fig. 2, but $\epsilon_r = 3.75 + 0.25i$.

The strong forms discussed above are not the only way of introducing finite-size effects, there being at least two more CDM algorithms available for that purpose. As alluded to earlier, Draine [48] replaced the Mossotti-Clausius polarizability by

$$\tau_D = \alpha / \{1 - (i/6\pi\epsilon_0)k_0^3\alpha\}. \quad [\text{D-CDM}] \quad (47)$$

However, τ_D is fully contained in τ , as we have seen in Eq. (43); and τ_D approaches α as the size parameter k_0a becomes vanishingly small.

The second source for the incorporation of finite-size effects has been the Lorentz-Mie-Debye analysis for scattering by a dielectric sphere [46]. The electromagnetic field scattered by any object can be described in terms of a multipole expansion [49]. With inspiration from Doyle [50], Dungey and Bohren [51] introduced finite-size effects in the CDM by using the lowest order Mie coefficient—corresponding to the electric dipole term of the multipole expansion—for the polarizability in place of the Mossotti-Clausius polarizability α . Thus,

$$\tau_{DB} = (i6\pi\epsilon_0/k_0^3)$$

$$\frac{[\epsilon_r^{1/2}\psi(k_0a\epsilon_r^{1/2})\partial\psi(k_0a) - \psi(k_0a)\partial\psi(k_0a\epsilon_r^{1/2})]}{[\epsilon_r^{1/2}\psi(k_0a\epsilon_r^{1/2})\partial\zeta(k_0a) - \zeta(k_0a)\partial\psi(k_0a\epsilon_r^{1/2})]}$$

$$[\text{DB-CDM}] \quad (48)$$

was used in [47], with $\psi(\beta) = \beta^{-1} \sin(\beta) - \cos(\beta)$, $\partial\psi(\beta) = d\psi/d\beta$, $\zeta(\beta) = -(1+i/\beta) \exp(i\beta)$, and $\partial\zeta(\beta) = d\zeta/d\beta$.

Using Eq. (48), it can be shown that τ_{DB} approaches α as the normalized radius k_0a becomes vanishingly small. This is also borne out in Figs. 2–5, wherein the computed values of τ_{DB}/α are compared with those of τ/α as functions of the normalized radius k_0a for $\epsilon_r = 1.5, 2.5, 4.0$ and $3.75 + 0.25i$. The general behavior of τ_{DB} is the same as of τ : (i) τ_{DB} is complex even for purely real ϵ_r , and (ii) the ratio $|\tau_{DB}/\alpha|$ lies between 0.99 and 1.01 when $k_0a|\epsilon_r^{1/2}| \approx 0.5$ in these figures. A more remarkable observation is that $|1 - \tau_{DB}/\alpha| \leq |1 - \tau/\alpha|$; in other words, τ_{DB} is closer to the Mossotti-Clausius polarizability α than τ is.

Draine [48] and Dungey and Bohren [51] concluded from their numerical investigations that D-CDM and DB-CDM, respectively, generally provide scattering results superior to those from W-CDM. This does not come as a surprise because the self-terms in W-CDM (or W-MOM) are

estimated with the least accuracy. On the other hand, although it is difficult to provide general enough conclusions for the adequacy of either D-CDM or DB-CDM vis-a-vis that of the S-CDM/S-MOM, it is safe to state that any claims of superiority—based purely on the estimation of some gross parameter, such as the total scattering cross-section—are debatable. Indeed, the only good way of deciding on the superiority of S-CDM, D-CDM or DB-CDM is by making calculations for the specific problem under consideration: The scatterer region should be subdivided into different numbers of subregions, and computed data from the various algorithms for different partitioning schemes compared for the property of interest [52–54].

The refractive index of soot at visible frequencies has been measured by a variety of experimental techniques, and has been found to be dependent on the source materials [55]. We conclude with calculations of τ/α and τ_{DB}/α for $\epsilon_r = 2.40 + 2.38i$, corresponding to a complex refractive index of $1.7 + 0.7i$, in Fig. 6. It is not difficult to gather from this figure that conclusions drawn in the previous paragraphs of this section apply to light scattering by soot agglomerates.

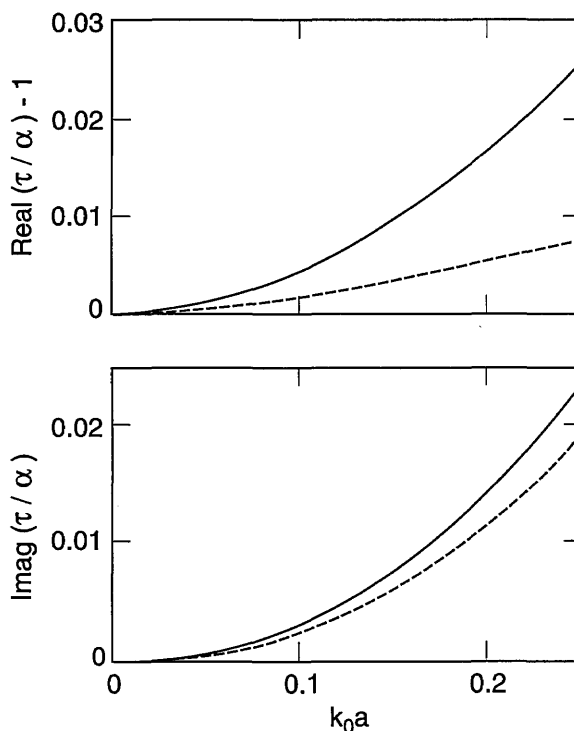


Fig. 6. Same as Fig. 2, but $\epsilon_r = 2.40 + 2.38i$.

10. Appendix A. The Volume Integral Equation for the Electric Field

The free space Green's function $\mathbf{G}(\mathbf{x}, \mathbf{x}')$ satisfies the dyadic differential equation

$$\nabla \times \nabla \times \mathbf{G}(\mathbf{x}, \mathbf{x}') - k_0^2 \mathbf{G}(\mathbf{x}, \mathbf{x}') = \mathbf{I} \delta(\mathbf{x} - \mathbf{x}'), \quad (\text{A1-1})$$

where $\delta(\mathbf{x} - \mathbf{x}')$ is the Dirac delta function. Since $J(\mathbf{x}')$ is not a function of \mathbf{x} , it follows that $\nabla \times [\mathbf{G}(\mathbf{x}, \mathbf{x}') \cdot J(\mathbf{x}')] = [\nabla \times \mathbf{G}(\mathbf{x}, \mathbf{x}') \cdot J(\mathbf{x}')] \cdot J(\mathbf{x}')$; hence,

$$\nabla \times \nabla \times [\mathbf{G}(\mathbf{x}, \mathbf{x}') \cdot J(\mathbf{x}')] - k_0^2 [\mathbf{G}(\mathbf{x}, \mathbf{x}') \cdot J(\mathbf{x}')] = \mathbf{I} \cdot J(\mathbf{x}') \delta(\mathbf{x} - \mathbf{x}'). \quad (\text{A1-2})$$

We multiply both sides of this equation by $i\omega\mu_0$ and integrate over all \mathbf{x}' to get

$$(\nabla \times \nabla \times \mathbf{I} - k_0^2 \mathbf{I}) \cdot \iiint_{|\mathbf{x}'| \leq \infty} d^3\mathbf{x}' [i\omega\mu_0 \mathbf{G}(\mathbf{x}, \mathbf{x}') \cdot J(\mathbf{x}')] = i\omega\mu_0 \iiint_{|\mathbf{x}'| \leq \infty} d^3\mathbf{x}' J(\mathbf{x}') \delta(\mathbf{x} - \mathbf{x}'), \quad (\text{A1-3})$$

whence,

$$(\nabla \times \nabla \times \mathbf{I} - k_0^2 \mathbf{I}) \cdot \iiint_{|\mathbf{x}'| \leq \infty} d^3\mathbf{x}' [i\omega\mu_0 \mathbf{G}(\mathbf{x}, \mathbf{x}') \cdot J(\mathbf{x}')] = i\omega\mu_0 J(\mathbf{x}). \quad (\text{A1-4})$$

Now by comparing Eqs. (7) and (A1-4), it is not too arduous to convince ourselves that

$$E(\mathbf{x}) = i\omega\mu_0 \iiint_{|\mathbf{x}'| \leq \infty} d^3\mathbf{x}' [\mathbf{G}(\mathbf{x}, \mathbf{x}') \cdot J(\mathbf{x}')]; \quad 0 \leq |\mathbf{x}| \leq \infty. \quad (\text{A1-5})$$

Remembering that for the present purposes $J(\mathbf{x})$ is null everywhere except in V_{int} , we next obtain

$$E(\mathbf{x}) = i\omega\mu_0 \iiint_{V_{\text{int}}} d^3\mathbf{x}' [\mathbf{G}(\mathbf{x}, \mathbf{x}') \cdot J(\mathbf{x}')]; \quad \mathbf{x} \in V_{\text{int}} + V_{\text{ext}}. \quad (\text{A1-6})$$

The solution of every linear differential equation can be divided into two parts: the *particular solution*

that depends on the *forcing function*, $J(\mathbf{x})$ being the forcing function here, and the *complementary function* that holds when the forcing function is identically zero everywhere. The right side of Eq. (A1-6) is the particular solution of Eq. (7), which has the complementary function $E_{\text{inc}}(\mathbf{x})$ satisfying

$$\nabla \times \nabla \times E_{\text{inc}}(\mathbf{x}) - k_0^2 E_{\text{inc}}(\mathbf{x}) = \mathbf{0}; \quad \mathbf{x} \in V_{\text{int}} + V_{\text{ext}}. \quad (\text{A1-7})$$

Hence, the complete solution of Eq. (7) is

$$E(\mathbf{x}) = E_{\text{inc}}(\mathbf{x}) + i\omega\mu_0 \iiint_{V_{\text{int}}} d^3\mathbf{x}' [\mathbf{G}(\mathbf{x}, \mathbf{x}') \cdot J(\mathbf{x}')]; \quad \mathbf{x} \in V_{\text{int}} + V_{\text{ext}}, \quad (\text{A1-8})$$

which can be easily re-expressed as Eq. (8a).

11. Appendix B. The Self-Integral

The integral under consideration is given as

$$a(\mathbf{x}_0) = \iiint_V d^3\mathbf{x}' \mathbf{G}(\mathbf{x}_0, \mathbf{x}') \cdot \mathbf{b}(\mathbf{x}'), \quad (\text{A2-1})$$

where V is the region bounded by the surface S , as shown in Fig. 7, $\mathbf{G}(\mathbf{x}, \mathbf{x}')$ is given by Eq. (8c), and the point \mathbf{x}_0 lies inside V . Because $\mathbf{G}(\mathbf{x}, \mathbf{x}')$ is of the order $1/|\mathbf{x} - \mathbf{x}'|^3$ for $|\mathbf{x} - \mathbf{x}'| \cong 0$, and becomes singular at $\mathbf{x} = \mathbf{x}'$, this integral has to be carefully treated.

As shown by Fikioris [56], we can transform Eq. (A2-1) to

$$a(\mathbf{x}_0) = \iiint_{V-V_0} d^3\mathbf{x}' [\mathbf{G}(\mathbf{x}_0, \mathbf{x}') \cdot \mathbf{b}(\mathbf{x}')] + \iiint_{V_0} d^3\mathbf{x}' [\mathbf{G}(\mathbf{x}_0, \mathbf{x}') \cdot \mathbf{b}(\mathbf{x}') - \mathbf{G}_s(\mathbf{x}_0, \mathbf{x}') \cdot \mathbf{b}(\mathbf{x}_0)] - (1/k_0^2) \iint_{S_0} d^2\mathbf{x}' u_n' [(x' - x_0)/4\pi|x' - x_0|^3] \cdot \mathbf{b}(\mathbf{x}_0), \quad (\text{A2-2})$$

where

$$\mathbf{G}_s(\mathbf{x}, \mathbf{x}') = (1/k_0^2) \nabla \nabla [1/4\pi|\mathbf{x} - \mathbf{x}'|] \quad (\text{A2-3})$$

is an auxiliary dyadic related to the Green's function for Poisson's equation [10]; V_0 is an exclusionary region bounded by the surface S_0 , as shown in Fig. 7; u_n is the unit normal to S_0 , pointing away from V_0 , at the point $x' \in S_0$. The exclusionary region V_0 should be small but not necessarily infinitesimal, and it must be wholly contained within V . Moreover, there is no requirement that S_0 be a miniature copy of S .

The use of the long-wavelength approximation $b(x) \cong b(x_0)$ for all $x \in V$ reduces Eq. (A2-2) to

$$a(x_0) \cong \iint \iint_{V-V_0} d^3x' [\mathbf{G}(x_0, x') \cdot b(x_0)] + \iint \iint_{V_0} d^3x' \{[\mathbf{G}(x_0, x') - \mathbf{G}_s(x_0, x')] \cdot b(x_0)\} - (1/k_0^2) \iint \iint_{S_0} d^2x' u_n' [(x' - x_0)/4\pi|x' - x_0|^3] \cdot b(x_0). \quad (\text{A2-4})$$

Since V is electrically small, but V_0 need not be infinitesimal, we set $V = V_0$ and $S = S_0$ to have

$$a(x_0) \cong [\mathbf{M} - (1/k_0^2) \mathbf{L}] \cdot b(x_0), \quad (\text{A2-5a})$$

where

$$\mathbf{M} = \iint \iint_V d^3x' [\mathbf{G}(x_0, x') - \mathbf{G}_s(x_0, x')], \quad (\text{A2-5b})$$

$$\mathbf{L} = \iint \iint_S d^2x' u_n' [(x' - x_0)/4\pi|x' - x_0|^3]. \quad (\text{A2-5c})$$

The evaluation of \mathbf{M} can be accomplished numerically for regions of different shapes using the coordinate-free (i.e., non-indices) representations [24, Chap. 9]

$$\mathbf{G}(x, x') = [(1 - u_x u_x) + (i/k_0 |X|)(1 + i/k_0 |X|)(1 - 3 u_x u_x)] [\exp(ik_0 |x - x'|)/4\pi |x - x'|]; \quad |X| \neq 0, \quad (\text{A2-6a})$$

$$\mathbf{G}_s(x, x') = (i/k_0 |X|)^2 (1 - 3 u_x u_x) / 4\pi |X|; \quad |X| \neq 0, \quad (\text{A2-6b})$$

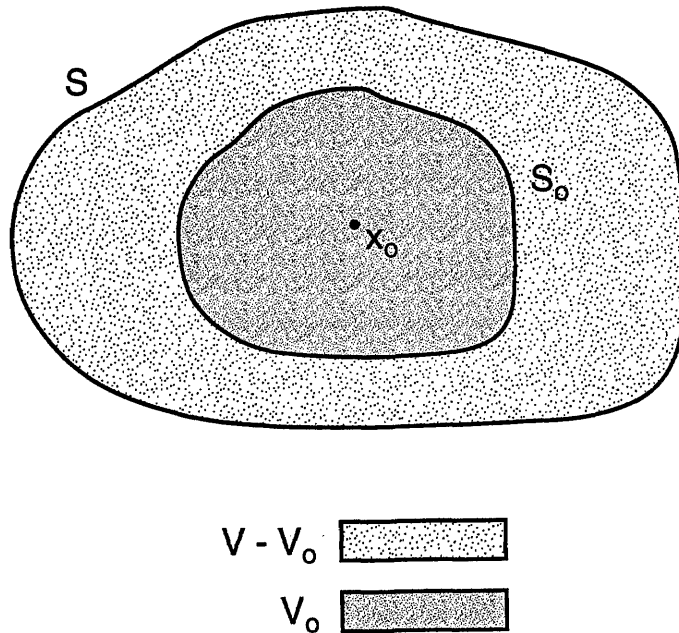


Fig. 7. For the evaluation of the integral in Eq. (A2-1) when $x_0 \in V$ and $x' \in V$.

where $\mathbf{X} = \mathbf{x} - \mathbf{x}'$ and $\mathbf{u}_X = \mathbf{X}/|\mathbf{X}|$. The evaluation of the depolarization dyadic \mathbf{L} is equally easy on a digital computer, and analytical expressions for \mathbf{L} are available for the quite general ellipsoidal shapes [57].

If V is extremely small in electrical size, the simplification

$$\mathbf{a}(\mathbf{x}_0) \cong (1/k_0^2) \mathbf{L} \cdot \mathbf{b}(\mathbf{x}_0) \quad (\text{A2-7})$$

is permissible and leads to the weak forms of the MOM and the CDM.

12. Appendix C: The Self-Dyadics for Spherical and Cubical Regions

Let the region V in Appendix B be a sphere with radius a and center at \mathbf{x}_0 . Without loss of generality due to the translational invariance of the right sides of Eqs. (A2-6a,b), we set $\mathbf{x}_0 = \theta$. Furthermore, we set $\mathbf{x}' = r' (u_1 \sin\theta' \cos\phi' + u_2 \sin\theta' \sin\phi' + u_3 \cos\theta')$, where $|\mathbf{x}'| = r'$, (u_1, u_2, u_3) is the triad of cartesian unit vectors, while (r', θ', ϕ') represent the corresponding spherical coordinate system located at the center of the sphere. Hence,

$$\iiint_V d^3\mathbf{x}' \{ \cdot \} \cong \int_0^a dr' r'^2 \int_0^\pi d\theta' \sin\theta' \int_0^{2\pi} d\phi' \{ \cdot \},$$

$$\iint_S d^2\mathbf{x}' \{ \cdot \} \cong a^2 \int_0^\pi d\theta' \sin\theta' \int_0^{2\pi} d\phi' \{ \cdot \}.$$

Now,

$$\int_0^\pi d\theta' \sin\theta' \int_0^{2\pi} d\phi' \mathbf{u}_X \mathbf{u}_X =$$

$$\int_0^\pi d\theta' \sin\theta' \int_0^{2\pi} d\phi' \{ (u_1 \sin\theta' \cos\phi' +$$

$$u_2 \sin\theta' \sin\phi' + u_3 \cos\theta') (u_1 \sin\theta' \cos\phi' + u_2$$

$$\sin\theta' \sin\phi' + u_3 \cos\theta') \} =$$

$$\pi \int_0^\pi d\theta' \sin\theta' \{ (u_1 u_1 + u_2 u_2) \sin^2\theta + 2u_3 u_3 \cos^2\theta \} =$$

$$(4\pi/3) (u_1 u_1 + u_2 u_2 + u_3 u_3) = (4\pi/3) \mathbf{I}, \quad (\text{A3-1})$$

and

$$\int_0^\pi d\theta' \sin\theta' \int_0^{2\pi} d\phi' \mathbf{I} = 4\pi \mathbf{I} \quad (\text{A3-2})$$

likewise. It follows that

$$\mathbf{M}|_{\text{sphere}} = \int_0^a dr' r'^2 \int_0^\pi d\theta' \sin\theta' \int_0^{2\pi} d\phi'$$

$$\{ [\mathbf{G}(\theta, \mathbf{x}') - \mathbf{G}_r(\theta, \mathbf{x}')] \}$$

$$= \int_0^a dr' r'^2 [(2\mathbf{I}/3) \exp(ik_0 r')/r']$$

$$= \mathbf{I} (2/3k_0^2) [(1 - ik_0 a) \exp(ik_0 a) - 1]. \quad (\text{A3-3})$$

In order to evaluate \mathbf{L} for a spherical region, we note that $\mathbf{u}_n' = \mathbf{x}'/|\mathbf{x}'|$ where $\mathbf{x}' \in S$; ergo, $|\mathbf{x}'| = a$, and

$$\mathbf{L}|_{\text{sphere}} = a^2 \int_0^\pi d\theta' \sin\theta' \int_0^{2\pi} d\phi'$$

$$\{ \mathbf{u}_n' \mathbf{x}' / 4\pi a^3 \} = (1/4\pi)$$

$$\int_0^\pi d\theta' \sin\theta' \int_0^{2\pi} d\phi' \{ (u_1 \sin\theta' \cos\phi' +$$

$$u_2 \sin\theta' \sin\phi' + u_3 \cos\theta') (u_1 \sin\theta' \cos\phi' +$$

$$u_2 \sin\theta' \sin\phi' + u_3 \cos\theta') \}$$

$$= (1/4\pi) (4\pi/3) \mathbf{I} = (1/3) \mathbf{I}, \quad (\text{A3-4})$$

after using Eq. (A3-1).

If the region V in Appendix B were to be a cube of side b , we would get

$$\mathbf{L}|_{\text{cube}} = (1/3) \mathbf{I}, \quad (\text{A3-5})$$

the same as that for a sphere. No expression exists for the dyadic \mathbf{M} for a cube in closed form; however, it is commonplace in MOM practice to use the value for an equivoluminal sphere. Thus,

$$\mathbf{M}|_{\text{cube}} \cong \mathbf{I} (2/3k_0^2) \{ [1 - ik_0 b (3/4\pi)^{1/3}]$$

$$\exp[ik_0 b (3/4)^{1/3}] - 1 \}, \quad (\text{A3-6})$$

because $[(3/4\pi)^{1/3} b]$ is the radius of a sphere having the same volume as the cube of side b .

Acknowledgments

One of the authors (George W. Mulholland) was supported in part by the Pennsylvania State University Particulate Materials Center while on sabbatical leave at Pennsylvania State University. The authors thank Dr. Egon Marx (NIST), Prof. Dike Ezekoye (University of Texas at Austin), and Prof. W. S. Weiglhofer (University of Glasgow) for their constructive comments and criticisms. Thanks are also due to the external reviewers whose comments helped improve this tutorial paper.

13. References

- [1] H. Massoudi, C. H. Durney, and C. C. Johnson, Long-wavelength electromagnetic power-absorption in ellipsoidal models of man and animals, *IEEE Trans. Microwave Theory Tech.* **25**, 47–52 (1977).
- [2] G. I. Rowlandson, and P. W. Barber, Absorption of higher-frequency RF energy by biological models: Calculations based on geometrical optics, *Radio Sci.* **14** (6S), 43–50 (1977).
- [3] V. V. Varadan, A. Lakhtakia, and V. K. Varadan, Comments on recent criticism of the T-matrix method, *J. Acoust. Soc. Amer.* **84**, 2280–2284 (1988).
- [4] R. F. Harrington, *Field Computation by Moment Methods*, McGraw-Hill Book Publishing Company, New York (1968).
- [5] D. E. Livesay, and K. M. Chen, Electromagnetic fields induced inside arbitrarily shaped dielectric bodies, *IEEE Trans. Microwave Theory Tech.* **22**, 1273–1280 (1974).
- [6] J. J. H. Wang, *Generalized Moment Methods in Electromagnetics*, John Wiley and Sons, New York (1991).
- [7] E. M. Purcell, and C. R. Pennypacker, Scattering and absorption of light by nonspherical dielectric grains, *Astrophys. J.* **186**, 705–714 (1973).
- [8] A. Lakhtakia, General theory of the Purcell-Pennypacker scattering approach, and its extension to bianisotropic scatterers, *Astrophys. J.* **394**, 494–499 (1992).
- [9] A. Lakhtakia, Macroscopic theory of the coupled dipole approximation method, *Opt. Commun.* **79**, 1–5 (1990).
- [10] A. Lakhtakia, Strong and weak forms of the method of moments and the coupled dipole method for scattering of time-harmonic electromagnetic fields, *Int. J. Mod. Phys. C* **3**, 583–603 (1992); errata: **4**, 721–722 (1993).
- [11] M. V. Berry, and I. C. Percival, Optics of fractal clusters such as smoke, *Optica Acta* **33**, 577–591 (1986).
- [12] R. D. Mountain, and G. W. Mulholland, Light scattering from simulated smoke agglomerates, *Langmuir* **4**, 1321–1326 (1988).
- [13] J. Nelson, Test of a mean field theory for the optics of fractal clusters, *J. Mod. Opt.* **36**, 1031–1057 (1989).
- [14] S. B. Singham, and C. F. Bohren, Scattering of unpolarized and polarized light by particle aggregates of different size and fractal dimension, *Langmuir* **9**, 1431–1435 (1993).
- [15] M. F. Iskander, H. Y. Chen, and J. E. Penner, Optical branching and absorption by branched chains of aerosol, *Appl. Opt.* **28**, 3083–3091 (1989).
- [16] J. C. Ku, and K. H. Shim, A comparison of solutions for light scattering and absorption by agglomerated or arbitrarily-shaped particles, *J. Quant. Spectrosc. Radiat. Transfer* **47**, 201–220 (1992).
- [17] A. Lakhtakia, Towards classifying elementary microstructures in thin films by their scattering responses, *Int. J. Infrared Millim. Waves* **13**, 869–886 (1992); errata: **14**, 663 (1993).
- [18] J. I. Hage, and J. M. Greenberg, A model for the optical property of porous grains, *Astrophys. J.* **361**, 251–259 (1990).
- [19] J. C. Ku, Comparisons of coupled-dipole solutions and dipole refractive indices for light scattering and absorption by arbitrarily shaped or agglomerated particles, *J. Opt. Soc. Amer. A* **10**, 336–342 (1993).
- [20] R. F. Harrington, *Time-Harmonic Electromagnetic Fields*, McGraw-Hill Book Publishing Company, New York (1961).
- [21] D. S. Jones, Low frequency electromagnetic radiation, *J. Inst. Maths. Applics.* **23**, 421–447 (1979).
- [22] J. van Bladel, *Electromagnetic Fields*, Hemisphere, Washington, DC (1985).
- [23] F. I. Fedorov, *Theory of Gyrotropy* (in Russian), Nauka i Tekhnika, Minsk (1976).
- [24] H. C. Chen, *Theory of Electromagnetic Waves*, McGraw-Hill Book Publishing Company, New York (1983).
- [25] I. V. Lindell, *Elements of Dyadic Algebra and Its Application in Electromagnetics*, Radio Laboratory Report S 126, Helsinki University of Technology (1981).
- [26] P. Boulanger, and M. Hayes, Electromagnetic plane waves in anisotropic media: An approach using bivectors, *Philos. Trans. Roy. Soc. Lond. A* **330**, 335–393 (1990).
- [27] L. Brand, *Vector and Tensor Analysis*, John Wiley and Sons, New York (1947).
- [28] V. V. Varadan, A. Lakhtakia, and V. K. Varadan, eds., *Field Representations and Introduction to Scattering*, North-Holland, Amsterdam (1991).
- [29] J. van Bladel, Some remarks on Green's dyadic for infinite space, *IRE Trans. Antennas Propagat.* **9**, 563–566 (1961).
- [30] W. Weiglhofer, Delta-function identities and electromagnetic field singularities, *Amer. J. Phys.* **57**, 455–456 (1989).
- [31] A. D. Yaghjian, Electric dyadic Green's functions in the source region, *Proc. IEEE* **68**, 248–263 (1980).
- [32] J. J. H. Wang, A unified and consistent view on the singularities of the electric dyadic Green's function in the source region, *IEEE Trans. Antennas Propagat.* **30**, 463–468 (1982).
- [33] E. K. Miller, L. Medgyesi-Mitschang, and E. H. Newman, eds., *Computational Electromagnetics: Frequency-Domain Method of Moments*, IEEE Press, New York (1991).
- [34] D. S. Jones, Numerical methods for antenna problems, *Proc. Inst. Elec. Eng.* **121**, 573–582 (1974).
- [35] K. M. Chen, and B. S. Guru, Internal EM field and absorbed power density in human torsos induced by 1–500-MHz EM waves, *IEEE Trans. Microwave Theory Tech.* **25** 746–756 (1977).
- [36] M. J. Hagmann, O. P. Gandhi, and C. H. Durney, Upper bound for cell size for moment method solutions, *IEEE Trans. Microwave Theory Tech.* **25**, 831–832 (1977).

- [37] C. Athanasiadis, Low-frequency electromagnetic scattering by a multi-layered scatterer, *Quart. J. Mech. Appl. Math.* **44**, 55–67 (1991).
- [38] B. Carnahan, H. A. Luther, and J. O. Wilkes, *Applied Numerical Methods*, John Wiley and Sons, New York (1969).
- [39] G. Strang, *Introduction to Applied Mathematics*, Wellesley-Cambridge Press, Wellesley, MA (1986) Chap. 5.
- [40] T. K. Sarkar, ed., *Application of Conjugate Gradient Method to Electromagnetics and Signal Analysis*, Elsevier, New York (1991).
- [41] We define $g(x) = \text{Tend}_{x \rightarrow \infty} f(x)$ as a function that replicates the asymptotic behavior of $f(x)$ as $x \rightarrow \infty$, “Tend” standing in for “tendency;” $\lim_{x \rightarrow \infty} [g(x)/f(x)] = 1$.
- [42] J. W. Goodman, *Introduction to Fourier Optics*, McGraw-Hill Book Publishing Company, New York (1968) Chap. 3.
- [43] S. B. Singham, Intrinsic optical activity in light scattering from an arbitrary particle, *Chem. Phys. Lett.* **130**, 139–144 (1986).
- [44] V. K. Varadan, A. Lakhtakia, and V. V. Varadan, Scattering by beaded helices: Anisotropy and chirality, *J. Wave Mater. Interact.* **2**, 153–160 (1987).
- [45] G. H. Goedecke, and S. G. O’Brien, Scattering by irregular inhomogeneous particles via the digitized Green’s function algorithm, *Appl. Opt.* **27**, 2431–2438 (1988).
- [46] C. F. Bohren, and D. R. Huffman, *Absorption and Scattering of Light by Small Particles*, John Wiley and Sons, New York (1983).
- [47] Chronological propriety demands that Mossotti’s name be placed before that of Clausius; see: M. T. Prinkey, A. Lakhtakia, and B. Shanker, On the extended Maxwell Garnett and the extended Bruggeman approaches for dielectric indielectric composites, *Optik* (1993; in press).
- [48] B. T. Draine, The discrete dipole approximation and its application to interstellar graphite grains, *Astrophys. J.* **33**, 848–872 (1988).
- [49] C. H. Papas, *Theory of Electromagnetic Wave Propagation*, Dover Publications, New York (1988) Chap. 4.
- [50] W. T. Doyle, Optical properties of a suspension of metal spheres, *Phys. Rev. B* **39**, 9852–9858 (1989).
- [51] C. E. Dungey, and C. F. Bohren, Light scattering by non-spherical particles: a refinement to the coupled-dipole method, *J. Opt. Soc. Am. A* **8**, 81–87 (1991).
- [52] H. Massoudi, C. H. Durney, and M. F. Iskander, Limitations of the cubical block model of man in calculating SAR distributions, *IEEE Trans. Microwave Theory Tech.* **32**, 746–752 (1984).
- [53] V. V. Varadan, A. Lakhtakia, and V. K. Varadan, Scattering by three-dimensional anisotropic scatterers, *IEEE Trans. Antennas Propagat.* **37**, 800–802 (1989).
- [54] R. A. West, Optical properties of aggregate particles whose outer diameter is comparable to the wavelength, *Appl. Opt.* **30**, 5316–5323 (1991).
- [55] I. Colbeck, E. J. Hardman, and R. M. Harrison, Optical and dynamical properties of fractal clusters of carbonaceous smoke, *J. Aerosol Sci.* **20**, 765–774 (1989).
- [56] J. G. Fikioris, Electromagnetic field inside a current-carrying region, *J. Math. Phys.* **6**, 1617–1620 (1965).
- [57] A. Lakhtakia, Polarizability dyadics of small chiral ellipsoids, *Chem. Phys. Lett.* **174**, 583–586 (1990).

About the authors: Akhlesh Lakhtakia is Associate Professor of Engineering Science and Mechanics at the Pennsylvania State University. George W. Mulholland is Research Chemist and Group Leader, Smoke Dynamics Research Group at NIST. The National Institute of Standards and Technology is an agency of the Technology Administration, U.S. Department of Commerce.

Wavelengths and Energy Levels of Neutral Kr⁸⁴ and Level Shifts in All Kr Even Isotopes

Volume 98

Number 6

November–December 1993

Victor Kaufman

National Institute of Standards and Technology,
Gaithersburg, MD 20899-0001

Interferometrically-measured wavelengths of 109 lines of neutral Kr⁸⁴ are compared with those of Kr⁸⁶. Sixty energy levels of neutral Kr⁸⁴ derived from those wavelengths and 25 Kr⁸⁶-Kr⁸⁴ isotope shifts previously measured are given along with their shifts from the energy levels of Kr⁸⁶. Twenty levels of each of Kr⁸², Kr⁸⁰, and Kr⁷⁸ are also evaluated using isotope-shift information in the literature. The differences between the experimentally observed shifts and the normal mass shift leave

large negative residuals which are accounted for by ionization energy differences and by the specific mass shift. It appears that the volume effect causes only a very small, if any, energy level shift.

Key words: energy levels; interferometry; isotope shift; krypton; wavelengths.

Accepted: September 21, 1993

1. Introduction

In 1969, Kaufman and Humphreys [1] determined a set of 45 even-parity and 66 odd-parity levels of neutral Kr⁸⁶ based upon interferometrically-determined wavelengths of that isotope of krypton. The energies relative to the ground level, based on the vacuum-ultraviolet observations of Petersson [2], had an absolute uncertainty of $\pm 0.15 \text{ cm}^{-1}$, although their relative uncertainties were much smaller. (All uncertainties in this paper are one standard deviation estimates unless otherwise stated.) Trickl et al. [3], in 1989, measured the values of the resonance lines of Kr⁸⁶ from four of the $J=1$ levels of the $4p^55s$, $6s$, and $7s$ configurations with an average uncertainty of 1 part in 10^7 . Their results led to a subtraction of $(0.0679 \pm 0.0061) \text{ cm}^{-1}$ from the values given by Kaufman and Humphreys [1]. This correction was incorporated in the compilation of the energy levels by Sugar and Musgrove [4].

2. Wavelengths of Neutral Kr⁸⁴

At the same time that the author made interferometric wavelength measurements of the Kr⁸⁶ transitions, he also did the same for a number of lines of Kr⁸⁴ between 4264 \AA and 6906 \AA . The pure isotope lamps were of the hot cathode type devised by Kösters and Engelhard at the Physikalisch-Technische Bundesanstalt (PTB). They were operated in the manner recommended by the International Commission of Weights and Measures [5].

During the summer of 1967, the author was given the opportunity to spend some time with C. J. Humphreys at the Naval Weapons Center Corona Laboratories, Corona, CA. With the cooperation of Dr. Humphreys and his staff, measurements were made on Kr⁸⁴ wavelengths between 7589 \AA and 9754 \AA . The orange line of Kr⁸⁶ at 6057 \AA , as emitted from a microwave-excited

electrodeless discharge lamp maintained in a bath of nitrogen at its triple-point temperature, was used as the wavelength standard. The Kr^{84} spectrum was observed from a similarly cooled, microwave-excited electrodeless lamp. Both lamps were viewed along the capillary. Interferometer spacers of 50 mm, 80 mm, and 100 mm were used, but final corrections for dispersion of phase change were taken from the more extensive data of C. J. Humphreys.

The 109 interferometrically measured vacuum wavelengths of Kr^{84} are given in the first column of Table 1. Also included in the table are the wavelength uncertainties in parentheses (in units of the last digit) and wavenumbers of the Kr^{84} lines, the Kr^{86} wavelengths and wavenumbers for those same 109 lines from Ref. [1], the classification of each transition and the wavenumber difference between the two isotopes. The wavelength uncertainties are the rms deviations in the set of measurements for each line.

Table 1. Interferometrically measured vacuum wavelengths of Kr^{84} and differences from those of Kr^{86}

Wavelength (Å)		Wavenumber (cm^{-1})		Classification		$\Delta\nu_{\text{diff}}^b$	Previous measurements ^c	
Kr^{84}	Kr^{86}	Kr^{84}	Kr^{86}	Odd level	Even level			
4264.4856(3) ^a	.48475	23449.4871	.4918	(² P _{1/2})5s	² [1/2] ₀ – (² P _{3/2})8p	2[1/2] ₀	4.7	
4275.17220(10)	.17148	23390.8707	.8746	(² P _{3/2})5s	² [3/2] ₂ – (² P _{3/2})6p	² [3/2] ₂	3.9(5)	3.93(8) ^d
4284.17248(10)	.17172	23341.7306	.7348	(² P _{3/2})5s	² [3/2] ₂ – (² P _{3/2})6p	² [3/2] ₁	4.2	
4287.69293(10)	.69212	23322.5657	.5701	(² P _{1/2})5s	² [1/2] ₀ – (² P _{1/2})6p	² [1/2] ₁	4.4	
4301.69626(10)	.69545	23246.6436	.6480	(² P _{1/2})5s	² [1/2] ₀ – (² P _{1/2})6p	² [3/2] ₁	4.4	
4319.7658(3)	.76561	23149.4032	.4042	(² P _{3/2})5s	² [3/2] ₂ – (² P _{3/2})6p	² [5/2] ₂	1.0	
4320.7942(3)	.79361	23143.8933	.8965	(² P _{3/2})5s	² [3/2] ₂ – (² P _{3/2})6p	² [5/2] ₃	3.2(1.6)	3.90(8) ^d 3.86(3) ^e
4352.58282(10)	.58189	22974.8644	.8693	(² P _{1/2})5s	² [1/2] ₀ – (² P _{1/2})6p	² [1/2] ₀	4.9	
4363.86767(10)	.86695	22915.4520	.4558	(² P _{3/2})5s	² [3/2] ₂ – (² P _{3/2})6p	² [1/2] ₁	3.8(5)	3.84(7) ^d
4377.35124(10)	.35027	22844.8654	.8705	(² P _{3/2})5s	² [3/2] ₁ – (² P _{3/2})6p	² [1/2] ₀	5.1(5)	4.90(8) ^d
4401.20227(10)	.20109	22721.0643	.0704	(² P _{1/2})5s	² [1/2] ₀ – (² P _{1/2})6p	² [3/2] ₂	6.1	
4411.6068(2)	.60581	22667.4780	.4831	(² P _{1/2})5s	² [1/2] ₀ – (² P _{1/2})6p	² [1/2] ₁	5.1	
4420.0022(3)	.00126	22624.4231	.4279	(² P _{1/2})5s	² [1/2] ₀ – (² P _{3/2})5f	² [3/2] ₂	4.8	
4426.43265(10)	.43162	22591.5558	.5610	(² P _{1/2})5s	² [1/2] ₀ – (² P _{1/2})6p	² [3/2] ₁	5.2	
4455.16765(10)	.16670	22445.8444	.8492	(² P _{3/2})5s	² [3/2] ₁ – (² P _{3/2})6p	² [3/2] ₂	4.8	
4464.94273(10)	.94163	22396.7038	.7094	(² P _{3/2})5s	² [3/2] ₁ – (² P _{3/2})6p	² [3/2] ₁	5.6(5)	4.83(7) ^d
4503.61721(10)	.61621	22204.3738	.3787	(² P _{3/2})5s	² [3/2] ₁ – (² P _{3/2})6p	² [5/2] ₂	4.9(5)	4.76(8) ^d
5217.2701(3)	.2695	19167.1119	.1141	(² P _{3/2})5p	² [1/2] ₁ – (² P _{3/2})8d	² [1/2] ₀	2.2	
5229.63279(10)	.63192	19121.8015	.8047	(² P _{3/2})5p	² [1/2] ₁ – (² P _{3/2})8d	² [1/2] ₀	3.2	
5281.3038(2)	.30263	18934.7186	.7226	(² P _{3/2})5p	² [1/2] ₁ – (² P _{1/2})5d	² [3/2] ₂	4.0	
5336.2389(3)	.23880	18739.7907	.7910	(² P _{3/2})5p	² [5/2] ₂ – (² P _{3/2})9d	² [7/2] ₃	0.3	
5340.6034(2)	.60296	18724.4760	.4775	(² P _{3/2})5p	² [5/2] ₃ – (² P _{3/2})9d	² [7/2] ₃	1.5	
5381.1325(2)	.13155	18583.4487	.4520	(² P _{3/2})5p	² [1/2] ₁ – (² P _{3/2})9s	² [3/2] ₂	3.3	
5492.46155(10)	.46062	18206.7729	.7760	(² P _{3/2})5p	² [1/2] ₁ – (² P _{3/2})7d	² [3/2] ₂	3.1	
5502.23831(10)	.23721	18174.4218	.4255	(² P _{3/2})5p	² [1/2] ₁ – (² P _{3/2})7d	² [1/2] ₀	3.7	
5505.5344(3)	.5339	18163.5410	.5427	(² P _{3/2})5p	² [5/2] ₂ – (² P _{3/2})8d	² [7/2] ₃	1.7	
5505.8596(3)	.8591	18162.4682	.4699	(² P _{3/2})5p	² [1/2] ₁ – (² P _{3/2})7d	² [1/2] ₀	1.7	
5518.1990(4)	.19756	18121.8546	.8593	(² P _{1/2})5s	² [1/2] ₀ – (² P _{3/2})6p	² [3/2] ₁	4.7	
5522.04373(10)	.04304	18109.2373	.2395	(² P _{3/2})5p	² [5/2] ₃ – (² P _{3/2})8d	² [7/2] ₃	2.2	
5563.76997(10)	.76905	17973.4246	.4276	(² P _{3/2})5s	² [3/2] ₂ – (² P _{1/2})5p	² [3/2] ₂	3.0(3)	2.88(5) ^f 2.86(3) ^g
5571.83623(10)	.83525	17947.4048	.4079	(² P _{3/2})5s	² [3/2] ₂ – (² P _{1/2})5p	² [1/2] ₁	3.1(3)	2.85(10) ^f 2.87(3) ^g 2.85(2) ^{h,i}
5581.93678(10)	.93533	17914.9288	.9335	(² P _{1/2})5s	² [1/2] ₀ – (² P _{3/2})6p	² [1/2] ₀	4.7	
5613.3678(3)	.3669	17814.6175	.6203	(² P _{3/2})5p	² [5/2] ₂ – (² P _{1/2})5d	² [5/2] ₂	2.8	
5651.12975(10)	.12861	17695.5767	.5803	(² P _{1/2})5s	² [1/2] ₀ – (² P _{3/2})6p	² [1/2] ₁	3.6(3)	3.33(20) ^f
5674.0250(2)	.02398	17624.1733	.1765	(² P _{3/2})5s	² [3/2] ₂ – (² P _{1/2})5p	² [3/2] ₁	3.2	
5703.7524(3)	.7513	17532.3179	.3212	(² P _{3/2})5p	² [3/2] ₁ – (² P _{3/2})8d	² [5/2] ₂	3.3	
5709.0964(2)	.09462	17515.9067	.9122	(² P _{1/2})5s	² [1/2] ₀ – (² P _{3/2})6p	² [3/2] ₂	5.5	
5723.4644(4)	.46398	17471.9354	.9366	(² P _{3/2})5p	² [5/2] ₂ – (² P _{3/2})9s	² [3/2] ₀	1.2	
5728.1764(4)	.17554	17457.5629	.5656	(² P _{3/2})5p	² [5/2] ₃ – (² P _{3/2})9s	² [3/2] ₂	2.7	
5764.4937(4)	.4927	17347.5773	.5803	(² P _{3/2})5p	² [3/2] ₂ – (² P _{3/2})8d	² [7/2] ₃	3.0	
5785.4977(4)	.49685	17284.5977	.6002	(² P _{3/2})5p	² [5/2] ₃ – (² P _{3/2})7d	² [5/2] ₃	2.5	
5807.15097(10)	.14992	17220.1481	.1513	(² P _{3/2})5p	² [5/2] ₂ – (² P _{3/2})7d	² [5/2] ₂	3.2	
5821.7315(2)	.73068	17177.0203	.0227	(² P _{3/2})5p	² [5/2] ₃ – (² P _{3/2})7d	² [7/2] ₃	2.4	

Table 1. Interferometrically measured vacuum wavelengths of Kr⁸⁴1 and differences from those of Kr⁸⁶1 – Continued

Wavelength (Å)		Wavenumber (cm ⁻¹)		Classification		$\Delta\nu_{\text{diff}}^b$	Previous measurements ^c	
Kr ⁸⁴	Kr ⁸⁶	Kr ⁸⁴	Kr ⁸⁶	Odd level	Even level			
5826.1333(2)	.13246	17164.0426	.0451	(² P _{3/2})5p	² [5/2] ₂ – (² P _{3/2})7d	² [7/2] ₃	2.5	
5834.47363(10)	.47251	17139.5067	.5100	(² P _{3/2})5p	² [5/2] ₃ – (² P _{3/2})7d	² [7/2] ₃	3.3	
5854.4974(3)	.49603	17080.8855	.8895	(² P _{3/2})5p	² [5/2] ₃ – (² P _{3/2})7d	² [3/2] ₂	4.0	
5868.37627(10)	.37472	17040.4888	.4933	(² P _{1/2})5s	² [1/2] ₁ ^o – (² P _{3/2})6p	² [1/2] ₁	4.5	
5872.54320(10)	.54160	17028.3975	.4022	(² P _{3/2})5s	² [3/2] ₁ ^o – (² P _{1/2})5p	² [3/2] ₂	4.7(3)	3.77(5) ^d 3.94(20) ⁱ
5881.52997(10)	.52867	17002.3787	.3825	(² P _{3/2})5s	² [3/2] ₁ ^o – (² P _{1/2})5p	² [1/2] ₁	3.8	
5889.3185(2)	.31753	16979.8933	.8961	(² P _{3/2})5p	² [3/2] ₂ – (² P _{1/2})5d	² [3/2] ₂	2.8	
5947.09957(10)	.09902	16814.9194	.9210	(² P _{3/2})5p	² [3/2] ₁ – (² P _{3/2})9s	² [3/2] ₁	1.6	
5979.30154(10)	.30061	16724.3614	.3640	(² P _{3/2})5p	² [3/2] ₁ – (² P _{3/2})7d	² [3/2] ₁	2.6	
5995.51035(10)	.50899	16679.1473	.1510	(² P _{3/2})5s	² [3/2] ₁ ^o – (² P _{1/2})5p	² [3/2] ₁	3.7	
6013.7274(2)	.72611	16628.6219	.6256	(² P _{3/2})5p	² [3/2] ₂ – (² P _{3/2})9s	² [3/2] ₂	3.7	
6013.8206(2)	.81950	16628.3644	.3674	(² P _{3/2})5p	² [1/2] ₁ – (² P _{3/2})6d	² [3/2] ₂	3.0	
6037.50529(10)	.50415	16563.1325	.1356	(² P _{3/2})5p	² [3/2] ₁ – (² P _{3/2})7d	² [5/2] ₂	3.1	
6057.80312(10)	.80211	16507.6345	.6373	(² P _{3/2})5p	² [1/2] ₁ – (² P _{3/2})6d	² [1/2] ₁	2.8	
6076.93707(10)	.93635	16455.6583	.6603	(² P _{3/2})5p	² [3/2] ₂ – (² P _{3/2})7d	² [5/2] ₃	2.0	
6084.54518(10)	.54409	16435.0822	.0851	(² P _{3/2})5p	² [1/2] ₁ – (² P _{3/2})6d	² [1/2] ₁	2.9	
6093.5139(2)	.51242	16410.8922	.8962	(² P _{3/2})5p	² [3/2] ₁ – (² P _{3/2})7d	² [3/2] ₂	4.0	
6110.0094(4)	.00882	16366.5869	.5902	(² P _{3/2})5p	² [3/2] ₁ – (² P _{3/2})7d	² [1/2] ₁	3.3	
6153.10907(10)	.10794	16251.9466	.9496	(² P _{3/2})5p	² [3/2] ₂ – (² P _{3/2})7d	² [3/2] ₂	3.0	
6165.3817(2)	.38052	16219.5959	.5991	(² P _{3/2})5p	² [3/2] ₂ – (² P _{3/2})7d	² [1/2] ₁	3.2	
6224.45490(10)	.45402	16065.6638	.6661	(² P _{3/2})5p	² [5/2] ₂ – (² P _{3/2})8s	² [3/2] ₁	2.3	
6238.07680(10)	.07589	16030.5817	.5841	(² P _{3/2})5p	² [5/2] ₃ – (² P _{3/2})8s	² [3/2] ₂	2.4	
6243.13125(10)	.13005	16017.6034	.6064	(² P _{3/2})5p	² [5/2] ₂ – (² P _{3/2})8s	² [3/2] ₂	3.0	
6348.43676(10)	.43559	15751.9093	.9122	(² P _{3/2})5p	² [5/2] ₃ – (² P _{3/2})6d	² [5/2] ₃	2.9	
6353.6716(2)	.67024	15738.9312	.9345	(² P _{3/2})5p	² [5/2] ₂ – (² P _{3/2})6d	² [5/2] ₃	3.3	
6370.0818(3)	.08059	15698.3855	.3885	(² P _{3/2})5p	² [5/2] ₃ – (² P _{3/2})6d	² [5/2] ₂	3.0	
6375.35220(10)	.35100	15685.4079	.4109	(² P _{3/2})5p	² [5/2] ₂ – (² P _{3/2})6d	² [5/2] ₂	3.0	
6411.9444(2)	.94347	15595.8932	.8955	(² P _{3/2})5p	² [1/2] ₀ – (² P _{3/2})7d	² [3/2] ₁	2.3	
6417.45257(10)	.45135	15582.5071	.5100	(² P _{3/2})5p	² [5/2] ₃ – (² P _{3/2})6d	² [7/2] ₃	2.9	
6422.80178(10)	.80048	15569.5292	.5324	(² P _{3/2})5p	² [5/2] ₂ – (² P _{3/2})6d	² [7/2] ₃	3.2	
6450.58162(10)	.58042	15502.4781	.4809	(² P _{3/2})5p	² [5/2] ₃ – (² P _{3/2})6d	² [3/2] ₂	2.8	
6458.07313(10)	.07189	15484.4948	.4978	(² P _{3/2})5p	² [5/2] ₃ – (² P _{3/2})6d	² [7/2] ₂	3.0(2)	2.80(7) ^d
6489.86196(10)	.86103	15408.6482	.6504	(² P _{3/2})5p	² [3/2] ₁ – (² P _{3/2})8s	² [3/2] ₁	1.8	
6506.70156(10)	.70024	15368.7700	.7732	(² P _{3/2})5p	² [5/2] ₂ – (² P _{3/2})6d	² [1/2] ₁	3.2	
6510.1675(3)	.16628	15360.5879	.5908	(² P _{3/2})5p	² [3/2] ₁ – (² P _{3/2})8s	² [3/2] ₂	2.9	
6538.3575(2)	.35639	15294.3610	.3636	(² P _{3/2})5p	² [3/2] ₁ – (² P _{3/2})6d	² [3/2] ₁	2.6	
6557.3451(3)	.34388	15250.0743	.0771	(² P _{3/2})5p	² [1/2] ₀ – (² P _{3/2})7d	² [1/2] ₁	2.8	
6557.50560(10)	.50442	15249.7010	.7038	(² P _{3/2})5p	² [3/2] ₂ – (² P _{3/2})8s	² [3/2] ₁	2.8	
6578.23694(10)	.23583	15201.6416	.6441	(² P _{3/2})5p	² [3/2] ₂ – (² P _{3/2})8s	² [3/2] ₂	2.5	
6654.07167(10)	.07041	15028.3924	.3952	(² P _{3/2})5p	² [3/2] ₁ – (² P _{3/2})6d	² [5/2] ₂	2.8	
6701.07916(10)	.07793	14922.9695	.9723	(² P _{3/2})5p	² [3/2] ₂ – (² P _{3/2})6d	² [5/2] ₃	2.8	
6725.2001(3)	.19896	14869.4460	.4486	(² P _{3/2})5p	² [3/2] ₂ – (² P _{3/2})6d	² [5/2] ₂	2.6	
6741.9591(3)	.95742	14832.4839	.4876	(² P _{3/2})5p	² [3/2] ₁ – (² P _{3/2})6d	² [3/2] ₂	3.7	
6797.2858(3)	.28442	14711.7545	.7575	(² P _{3/2})5p	² [3/2] ₁ – (² P _{3/2})6d	² [1/2] ₁	3.0	
6814.98902(10)	.98762	14673.5380	.5410	(² P _{3/2})5p	² [3/2] ₂ – (² P _{3/2})6d	² [3/2] ₂	3.0	
6830.9733(3)	.97210	14639.2023	.2049	(² P _{3/2})5p	² [3/2] ₁ – (² P _{3/2})6d	² [1/2] ₁	2.6	
6848.2895(3)	.28879	14602.1864	.1879	(² P _{3/2})5p	² [1/2] ₁ – (² P _{3/2})7s	² [3/2] ₁	1.5	
6871.5262(3)	.52476	14552.8078	.8108	(² P _{3/2})5p	² [3/2] ₂ – (² P _{3/2})6d	² [1/2] ₁	3.0	
6906.5836(2)	.58254	14478.9386	.9408	(² P _{3/2})5p	² [1/2] ₁ – (² P _{3/2})7s	² [3/2] ₂	2.2	
7589.5025(2)	.50024	13176.0942	.0981	(² P _{3/2})5s	² [3/2] ₁ ^o – (² P _{3/2})5p	² [1/2] ₀	3.9(4)	3.53(4) ^k
7603.6384(2)	.63663	13151.5986	.6016	(² P _{3/2})5s	² [3/2] ₂ ^o – (² P _{3/2})5p	² [3/2] ₂	3.0(4)	2.30(4) ^k
7687.3612(2)	.3590	13008.3650	.3687	(² P _{1/2})5s	² [1/2] ₁ ^o – (² P _{1/2})5p	² [1/2] ₀	3.7(3)	3.46(5) ^k
7696.6579(2)	.65631	12992.6523	.6550	(² P _{3/2})5s	² [3/2] ₂ ^o – (² P _{3/2})5p	² [3/2] ₁	2.7(2)	2.27(5) ^k
7856.9844(2)	.98253	12727.5294	.5324	(² P _{1/2})5s	² [1/2] ₁ ^o – (² P _{1/2})5p	² [1/2] ₁	3.0(3)	2.31(4) ^k
7915.6020(2)	.60014	12633.2779	.2809	(² P _{3/2})5p	² [1/2] ₁ – (² P _{3/2})5d	² [1/2] ₁	3.0	
7930.7798(2)	.77813	12609.1006	.1032	(² P _{3/2})5p	² [5/2] ₂ – (² P _{3/2})5d	² [7/2] ₃	2.6	
8061.7211(5)	.71987	12404.2991	.3010	(² P _{1/2})5s	² [1/2] ₁ ^o – (² P _{1/2})5p	² [3/2] ₁	1.9(8)	2.20(5) ^k
8115.1320(2)	.12988	12322.6585	.6617	(² P _{3/2})5s	² [3/2] ₂ ^o – (² P _{3/2})5p	² [5/2] ₃	3.2(3)	2.19(6) ^k

Table 1. Interferometrically measured vacuum wavelengths of Kr⁸⁴ and differences from those of Kr⁸⁶ – Continued

Wavelength (Å)		Wavenumber (cm ⁻¹)		Classification		$\Delta\nu_{\text{diff}}^b$	Previous measurements ^c
Kr ⁸⁴	Kr ⁸⁶	Kr ⁸⁴	Kr ⁸⁶	Odd level	Even level		
8192.3082(3)	.30538	12206.5720	.5762	(² P _{3/2})5s	² [3/2] _i – (² P _{3/2})5p	² [3/2] ₂	4.2(4) 3.35(4) ^k
8265.5140(3)	.51129	12098.4611	.4651	(² P _{1/2})5s	² [1/2] _i – (² P _{1/2})5p	² [3/2] ₂	4.0(4) 3.31(5) ^k
8283.3284(2)	.32590	12072.4418	.4454	(² P _{1/2})5s	² [1/2] _i – (² P _{1/2})5p	² [1/2] ₁	3.6(3) 3.24(5) ^k
8300.3907(3)	.38801	12047.6257	.6296	(² P _{3/2})5s	² [3/2] _i – (² P _{3/2})5p	² [3/2] ₁	3.9(4) 3.44(5) ^k
8511.2106(4)	.20763	11749.2099	.2140	(² P _{1/2})5s	² [1/2] _i – (² P _{1/2})5p	² [3/2] ₁	4.1(6) 3.27(5) ^k
8779.1607(3)	.15807	11390.6105	.6139	(² P _{3/2})5s	² [3/2] _i – (² P _{3/2})5p	² [5/2] ₂	3.4(4) 3.30(7) ^k
8931.1447(2)	.14294	11196.7730	.7752	(² P _{3/2})5s	² [3/2] _i – (² P _{3/2})5p	² [1/2] ₁	2.2
9754.4352(4)	.43235	10251.7468	.7498	(² P _{3/2})5s	² [3/2] _i – (² P _{3/2})5p	² [1/2] ₁	3.0

^a This is the uncertainty in the Kr⁸⁴ wavelength.

^b Wavenumber of the Kr⁸⁶ transition minus that of the Kr⁸⁴ transition in units of 10⁻³ cm⁻¹. The uncertainty of the last digit of the Kr⁸⁴ measurement is given in parentheses for those transitions for which direct isotope shift measurements are available.

^c In units of 10⁻³ cm⁻¹.

^d Direct (Kr⁸⁶–Kr⁸⁴) isotope shift measurement by Ref. [6]. The uncertainty of the measurement is given in parentheses.

^e Direct (Kr⁸⁶–Kr⁸⁴) isotope shift measurement by Ref. [7]. The uncertainty of the measurement is given in parentheses.

^f Direct (Kr⁸⁶–Kr⁸⁴) isotope shift measurement by Ref. [8]. The uncertainty of the measurement is given in parentheses.

^g Direct (Kr⁸⁶–Kr⁸⁴) isotope shift measurement by Ref. [9]. The uncertainty of the measurement is given in parentheses.

^h Direct (Kr⁸⁶–Kr⁸⁴) isotope shift measurement by Ref. [10]. The uncertainty of the measurement is given in parentheses.

ⁱ Direct (Kr⁸⁶–Kr⁸⁴) isotope shift measurement by Ref. [11]. The uncertainty of the measurement is given in parentheses.

^j Direct (Kr⁸⁶–Kr⁸⁴) isotope shift measurement by Ref. [12]. The uncertainty of the measurement is given in parentheses.

^k Direct (Kr⁸⁶–Kr⁸⁴) isotope shift measurement by Ref. [13]. The uncertainty of the measurement is given in parentheses.

A number of investigators [6-13] have made direct measurements of isotope shifts between Kr⁸⁶ and Kr⁸⁴. These are also given in Table 1. Direct measurements, by their very nature, are much more accurate than the difference between two completely independent measurements. This is evident in the stated uncertainties following both the differences, $\Delta\nu$, and the direct isotope separations in Table 1. However, it should be noted that there is agreement within the stated uncertainties in most cases.

3. Energy Levels of Kr⁸⁴

Trickl et al. [3] also measured the isotope shifts in the aforementioned four vacuum-ultraviolet lines for several of the isotopes of krypton, including those between Kr⁸⁶ and Kr⁸⁴. Without those measurements, it would not be possible to give separate values for the energy levels of the two isotopes relative to the ground level.

With the aid of the same iterative level-calculation program used in Ref. [1], the 109 wavenumbers of Kr⁸⁴ given in Table 1 were combined with the Kr⁸⁶–Kr⁸⁴ isotope shift measurements from Refs.

[6-13] and with the vuv values for Kr⁸⁴ from Ref. [3] to determine the Kr⁸⁴ energy-level values. Table 2 includes these newly determined values with their uncertainties (in units of the last digit) in parentheses. Also included are the Kr⁸⁶ values for these same levels from the work of Kaufman and Humphreys [1], the Kr⁸⁶–Kr⁸⁴ differences and the number of transitions to or from each Kr⁸⁴ level included in the 109 wavelength measurements.

Jackson [6,13] measured wavenumber shifts between pairs of the five stable even isotopes of krypton in fifteen 5s–5p lines, six 5s–6p lines, and one 5p–6d line. Champeau and Keller [8] did the same for two other 5s–5p transitions and one 5s–6p transition for all but the Kr⁷⁸ isotope. Further information on four of these 25 lines can be found in Refs. [7] and [9-12]. Combining these previously reported data with the vuv high resolution measurements of the isotope shifts between Kr⁸⁶ and each of Kr⁸², Kr⁸⁰, and Kr⁷⁸ given by Trickl et al. [3] for the 4p⁶–4p⁵ (²P_{1/2})5s ²[1/2]₁ transition, it is possible to evaluate a total of 20 excited levels in each of these isotopes. These values are given in Table 3. The isotope shifts of these levels with respect to those of Kr⁸⁶ are also given.

Table 2. Energy level of Kr⁸⁴I in units of cm⁻¹

Energy level value		$\Delta \nu_{\text{lev}}^a$	$\Delta \nu_{\text{nm}}$	Configuration	Level _j	N ^b
Kr ⁸⁴	Kr ⁸⁶					
0.0000(62)	.0000(62)	0.0	17.0	4s ² 4p ⁶	¹ S ₀	3
79971.7301(3)	.7321(1)	2.0	5.0	4s ² 4p ⁵ (² P _{3/2})5s	² [3/2] ₂	12
80916.7564(3)	.7575(1)	1.1	4.8		² [3/2] ₁	12
85191.6050(5)	.6075(1)	2.5	5.0	4s ² 4p ⁵ (² P _{1/2})5s	² [1/2] ₂	6
85846.6930(4)	.6945(1)	1.5	4.9		² [1/2] ₁	14
91168.5034(3)	.5073(1)	3.9	3.2	4s ² 4p ⁵ (² P _{3/2})5p	² [1/2] ₁	15
94092.8510(6)	.8557(1)	4.7	2.8		² [1/2] ₀	3
92294.3896(3)	.3938(1)	4.2	3.1	4s ² 4p ⁵ (² P _{3/2})5p	² [5/2] ₃	14
92307.3670(3)	.3714(1)	4.4	3.1		² [5/2] ₂	14
92964.3827(3)	.3871(1)	4.4	3.0	4s ² 4p ⁵ (² P _{3/2})5p	² [3/2] ₁	15
93123.3293(3)	.3337(1)	4.4	3.0		² [3/2] ₂	14
97595.9037(6)	.9086(2)	4.9	3.1	4s ² 4p ⁵ (² P _{1/2})5p	² [3/2] ₁	4
97945.1548(6)	.1597(2)	4.9	3.0		² [3/2] ₂	3
97919.1352(5)	.1400(1)	4.8	3.0	4s ² 4p ⁵ (² P _{1/2})5p	² [1/2] ₁	4
98855.0582(10)	.0632(3)	5.0	2.9		² [1/2] ₀	1
102887.1820(6)	.1878(1)	5.8	1.5	4s ² 4p ⁵ (² P _{3/2})6p	² [1/2] ₁	3
103761.6220(7)	.6280(2)	6.0	1.4		² [1/2] ₀	2
103115.6227(16)	.6286(4)	5.9	1.4	4s ² 4p ⁵ (² P _{3/2})6p	² [5/2] ₃	1
103121.1303(12)	.1362(2)	5.9	1.4		² [5/2] ₂	2
103313.4610(6)	.4669(2)	5.9	1.4	4s ² 4p ⁵ (² P _{3/2})6p	² [3/2] ₁	3
103362.6008(6)	.6067(3)	5.9	1.4		² [3/2] ₂	3
103801.7813(10)	.7882(1)	6.9	1.3	4s ² 4p ⁵ (² P _{3/2})5d	² [1/2] ₁	1
104916.4676(10)	.4746(2)	7.0	1.2	4s ² 4p ⁵ (² P _{3/2})5d	² [7/2] ₃	1
105647.4420(10)	.4482(2)	6.2	1.0	4s ² 4p ⁵ (² P _{3/2})7s	² [3/2] ₂	1
105770.6898(10)	.6953(1)	5.5	1.0		² [3/2] ₁	2
107603.5853(7)	.5924(2)	7.1	0.8	4s ² 4p ⁵ (² P _{3/2})6d	² [1/2] ₂	2
107676.1373(5)	.1446(1)	7.3	0.8		² [1/2] ₁	4
107778.8846(10)	.8916(1)	7.0	0.7	4s ² 4p ⁵ (² P _{3/2})6d	² [7/2] ₂	1
107876.8964(7)	.9038(2)	7.4	0.7		² [7/2] ₃	2
107796.8674(5)	.8747(2)	7.3	0.7	4s ² 4p ⁵ (² P _{3/2})6d	² [3/2] ₂	4
108258.7437(10)	.7507(2)	7.0	0.7		² [3/2] ₁	1
107992.7751(5)	.7823(1)	7.2	0.7	4s ² 4p ⁵ (² P _{3/2})6d	² [5/2] ₂	4
108046.2986(6)	.3060(1)	7.4	0.7		² [5/2] ₃	3
108324.9706(5)	.9779(1)	7.3	0.7	4s ² 4p ⁵ (² P _{3/2})8s	² [3/2] ₂	4
108373.0307(6)	.0375(1)	6.8	0.7		² [3/2] ₁	3
108438.2487(7)	.2555(2)	6.8	1.4	4s ² 4p ⁵ (² P _{1/2})6p	² [3/2] ₁	2
108567.7573(10)	.7650(4)	7.7	1.4		² [3/2] ₂	1
108514.1708(7)	.1776(2)	6.8	1.4	4s ² 4p ⁵ (² P _{1/2})6p	² [1/2] ₁	2
108821.5574(10)	.5639(3)	6.5	1.4		² [1/2] ₀	1
108471.1161(16)	.1225(5)	6.4	0.6	4s ² 4p ⁵ (² P _{3/2})5f	² [3/2] ₂	1
109296.1801(17)	.1863(5)	6.2	0.5	4s ² 4p ⁵ (² P _{3/2})8p	² [1/2] ₀	1
109330.9706(9)	.9773(7)	6.7	0.5	4s ² 4p ⁵ (² P _{3/2})7d	² [1/2] ₂	2
109342.9252(6)	.9328(2)	7.6	0.5		² [1/2] ₁	3
109375.2759(6)	.2833(2)	7.4	0.5	4s ² 4p ⁵ (² P _{3/2})7d	² [3/2] ₂	4
109688.7442(7)	.7511(2)	6.9	0.5		² [3/2] ₁	2

Table 2. Energy level of Kr^{84}I in units of cm^{-1} – Continued

Energy level value		$\Delta \nu_{\text{lev}}$	$\Delta \nu_{\text{nm}}$	Configuration	Level _j	N^b
Kr^{84}	Kr^{86}					
109433.8963(10)	.9038(2)	7.5	0.5	$4s^2 4p^5(^2P_{3/2}^o) 7d$	$2^7[7/2]_4^i$	1
109471.4098(7)	.4165(3)	6.7	0.5		$2^7[7/2]_3^i$	2
109527.5152(7)	.5227(2)	7.5	0.5	$4s^2 4p^5(^2P_{3/2}^o) 7d$	$2^5[5/2]_2^i$	2
109578.9874(8)	.9940(5)	6.6	0.5		$2^5[5/2]_3^i$	2
109751.9523(7)	.9593(3)	7.0	0.4	$4s^2 4p^5(^2P_{3/2}^o) 9s$	$2^3[3/2]_2^i$	3
109779.3024(8)	.3081(3)	5.7	0.4		$2^3[3/2]_1^i$	2
110103.2223(8)	.2299(5)	7.6	1.2	$4s^2 4p^5(^2P_{1/2}^o) 5d$	$2^3[3/2]_2^i$	2
110121.9845(10)	.9917(9)	7.2	1.2	$4s^2 4p^5(^2P_{1/2}^o) 5d$	$2^5[5/2]_2^i$	1
110290.3049(10)	.3120(2)	7.1	0.4	$4s^2 4p^5(^2P_{3/2}^o) 8d$	$2^2[1/2]_1^i$	1
110335.6153(12)	.6214(7)	6.1	0.4		$2^2[1/2]_0^i$	1
110403.6269(10)	.6333(2)	6.4	0.3	$4s^2 4p^5(^2P_{3/2}^o) 8d$	$2^7[7/2]_4^i$	1
110470.9073(10)	.9140(7)	6.7	0.3		$2^7[7/2]_3^i$	2
110496.7006(10)	.7083(12)	7.7	0.3	$4s^2 4p^5(^2P_{3/2}^o) 8d$	$2^5[5/2]_2^i$	1
111018.8656(10)	.8713(6)	5.7	0.3	$4s^2 4p^5(^2P_{3/2}^o) 9d$	$2^7[7/2]_4^i$	1
111047.1577(11)	.1626(13)	4.9	0.2		$2^7[7/2]_3^i$	1

^a The difference between the level values of the two isotopes is given in units of 10^{-3} cm^{-1} .

^b The number in this column indicates the number of interferometrically measured lines with transitions to or from that level.

Table 3. Energy level values of Kr^{82} , Kr^{80} , and Kr^{78} in units of cm^{-1} and their differences and normal mass shifts with respect to those of Kr^{86} in units of 10^{-3} cm^{-1}

Config.	Level	Energy level value			$\text{Kr}^{86}-\text{Kr}^{82}$		$\text{Kr}^{86}-\text{Kr}^{80}$		$\text{Kr}^{86}-\text{Kr}^{78}$	
		Kr^{82}	Kr^{80}	Kr^{78}	$\Delta \nu_{\text{lev}}$	$\Delta \nu_{\text{nm}}$	$\Delta \nu_{\text{lev}}$	$\Delta \nu_{\text{nm}}$	$\Delta \nu_{\text{lev}}$	$\Delta \nu_{\text{nm}}$
$4p^6$	$1S_0$	0.0000	.0000	.0000	0.0	34.9	0.0	53.6	0.0	73.3
$(^2P_{3/2}^o) 5s$	$2^3[3/2]_2^i$	79971.7275	.7252	.7232	4.6	10.2	6.9	15.6	8.9	21.4
$(^2P_{3/2}^o) 5s$	$2^3[3/2]_1^i$	80916.7549	.7535	.7528	2.6	9.9	4.0	15.2	4.7	20.8
$(^2P_{1/2}^o) 5s$	$2^1[1/2]_0^i$	85191.6019	.5991	.5964	5.6	10.2	8.4	15.7	11.1	21.5
$(^2P_{1/2}^o) 5s$	$2^1[1/2]_1^i$	85846.6910	.6892	.6876	3.5	10.0	5.3	15.4	6.9	21.1
$(^2P_{3/2}^o) 5p$	$2^1[1/2]_0$	94092.8460	.8408	.8361	9.7	5.8	14.9	8.9	19.6	12.2
$(^2P_{3/2}^o) 5p$	$2^5[5/2]_3$	92294.3849	.3801	.3756	8.9	6.4	13.7	9.8	18.2	13.4
$(^2P_{3/2}^o) 5p$	$2^5[5/2]_2$	92307.3623	.3573	.3527	9.1	6.4	14.1	9.8	18.7	13.4
$(^2P_{3/2}^o) 5p$	$2^3[3/2]_1$	92964.3778	.3728	.3680	9.3	6.2	14.3	9.5	19.1	13.0
$(^2P_{3/2}^o) 5p$	$2^3[3/2]_2$	93123.3244	.3195	.3147	9.3	6.1	14.2	9.4	19.0	12.9
$(^2P_{1/2}^o) 5p$	$2^3[3/2]_1$	97595.8985	.8931	.8877	10.1	6.4	15.5	9.8	20.9	13.4
$(^2P_{1/2}^o) 5p$	$2^3[3/2]_2$	97945.1495	.1440	.1388	10.2	6.3	15.7	9.7	20.9	13.2
$(^2P_{1/2}^o) 5p$	$2^1[1/2]_1$	97919.1298	.1244	.1189	10.2	6.3	15.6	9.7	21.1	13.2
$(^2P_{1/2}^o) 5p$	$2^1[1/2]_0$	98855.0528	.0471	.0416	10.4	6.0	16.1	9.2	21.6	12.6
$(^2P_{3/2}^o) 6p$	$2^1[1/2]_1$	102887.1757	.1693	.1629	12.1	3.1	18.5	4.8	24.9	6.5
$(^2P_{3/2}^o) 6p$	$2^1[1/2]_0$	103761.6158	.6088	.6025	12.2	2.8	19.2	4.3	25.5	5.9
$(^2P_{3/2}^o) 6p$	$2^5[5/2]_3$	103115.6164	.6099	.6033	12.2	3.0	18.7	4.7	25.3	6.4
$(^2P_{3/2}^o) 6p$	$2^5[5/2]_2$	103121.1243	.1174	.1112	11.9	3.0	18.8	4.6	25.0	6.4
$(^2P_{3/2}^o) 6p$	$2^3[3/2]_1$	103313.4548	.4479	.4416	12.1	3.0	19.0	4.6	25.3	6.2
$(^2P_{3/2}^o) 6p$	$2^3[3/2]_2$	103362.5944	.5877	.5811	12.3	3.0	19.0	4.5	25.6	6.2
$(^2P_{3/2}^o) 6d$	$2^7[7/2]_4^i$	107778.8771	.8693	.8616	14.5	1.6	22.3	2.4	30.0	3.3

Discussions of the two effects, the finite mass of the nucleus and the non-zero nuclear volume, which lead to the observation of isotope shifts are discussed in some detail in Refs. [3, 6 and 13]. In all of those instances, the authors point out that the difference between the experimentally observed isotope shift of a *line*, $\Delta\nu_{\text{diff}}$, and the normal mass shift, $\Delta\nu_{\text{nm}}$, is accounted for by the sum of the specific mass shift, $\Delta\nu_{\text{sm}}$, and the shift due to the volume effect, $\Delta\nu_{\text{vol}}$. We now have the opportunity to discuss the difference in the term values of the *levels* of isotopes. The term value T is defined as the binding energy of the electron, i.e., $T = IE - (\text{Level value})$. Here IE is the energy of the appropriate Kr II $4p^5 2P^{\circ}_{3/2}$ or $2P^{\circ}_{1/2}$ level with respect to the Kr I $4p^6 1S_0$ ground level, which has been taken as zero for each isotope. The normal mass shifts of the term values of levels near the ionization limit approach zero and increase with increasing term value of a level. The values of $\Delta\nu_{\text{nm}}$ for the corresponding term-value differences are given for Kr⁸⁶–Kr⁸⁴ in column 4 of Table 2 and for Kr⁸⁶–Kr⁸², Kr⁸⁶–Kr⁸⁰, and Kr⁸⁶–Kr⁷⁸ in Table 3. They show that the differences in binding energies of the $4p^6 1S_0$ ground states due only to the normal mass effect are 17.0×10^{-3} , 34.9×10^{-3} , 53.6×10^{-3} , and $73.3 \times 10^{-3} \text{ cm}^{-1}$, respectively for Kr⁸⁴, Kr⁸², Kr⁸⁰, and Kr⁷⁸ with respect to Kr⁸⁶.

For any two isotopes

$$\Delta T_{\text{exp}} = \Delta(IE) - \Delta\nu_{\text{lev}} = \Delta\nu_{\text{nm}} + \Delta\nu_{\text{sm}} + \Delta\nu_{\text{vol}} \quad (1)$$

where ΔT_{exp} is the observed shift in the term value. Thus by adding the experimentally observed isotope shift $\Delta\nu_{\text{lev}}$ and the calculated normal mass shift $\Delta\nu_{\text{nm}}$ for term values of levels relatively close to the ionization limit, where the specific mass and volume effects must be negligible, we can find values of the differences in the $4p^6 4p^5 2P^{\circ}$ ionization energies of these isotopes. The addition of columns 3 and 4 of Table 2 for Kr⁸⁶–Kr⁸⁴ and the equivalent columns in Table 3 for the other three krypton pairs, gives ionization energy differences with estimated uncertainties of $\pm 0.5 \times 10^{-3} \text{ cm}^{-1}$ of these four isotopes from Kr⁸⁶. They are 7.5×10^{-3} , 15.6×10^{-3} , 24.1×10^{-3} , and $32.4 \times 10^{-3} \text{ cm}^{-1}$, respectively for Kr⁸⁴, Kr⁸², Kr⁸⁰, and Kr⁷⁸. By definition, these are the experimental differences between the binding energies of a $4p$ electron in the ground level of these respective isotopes and the same binding energy for the Kr⁸⁶ isotope.

Table 4 gives the term value shifts due to the sum of the specific mass and volume effects as obtained by applying Eq. (1) to the $4p^6 1S_0$ and the

other twenty levels given in Table 3 and the same levels in Table 2. The estimated uncertainty of $\pm 0.6 \times 10^{-3} \text{ cm}^{-1}$ for term value shifts is due to both the estimated uncertainty of $\pm 0.5 \times 10^{-3} \text{ cm}^{-1}$ on the ionization energy differences given above and an uncertainty of about $0.2 \times 10^{-3} \text{ cm}^{-1}$ on the value of the isotope shifts.

Table 4. Term-value shifts, in units of 10^{-3} cm^{-1} , due to the sum of the specific mass and volume effects

Config.	Term	Kr ⁸⁶ –Kr ⁸⁴	Kr ⁸⁶ –Kr ⁸²	Kr ⁸⁶ –Kr ⁸⁰	Kr ⁸⁶ –Kr ⁷⁸
$4p^6$	$1S_0$	–9.5	–19.3	–29.5	–40.9
$(2P^{\circ}_{3/2})5s$	$2[3/2]_2^{\circ}$	0.5	0.8	1.6	1.9
$(2P^{\circ}_{3/2})5s$	$2[3/2]_1^{\circ}$	1.6	3.1	4.9	6.9
$(2P^{\circ}_{1/2})5s$	$2[1/2]_0^{\circ}$	0.0	–0.2	0.0	–0.2
$(2P^{\circ}_{1/2})5s$	$2[1/2]_1^{\circ}$	1.1	2.1	3.4	4.4
$(2P^{\circ}_{3/2})5p$	$2[1/2]_0$	0.0	0.1	0.3	0.6
$(2P^{\circ}_{3/2})5p$	$2[5/2]_3$	0.2	0.3	0.6	0.8
$(2P^{\circ}_{3/2})5p$	$2[5/2]_2$	0.0	0.1	0.2	0.3
$(2P^{\circ}_{3/2})5p$	$2[3/2]_1$	0.1	0.1	0.3	0.3
$(2P^{\circ}_{3/2})5p$	$2[3/2]_2$	0.1	0.2	0.5	0.5
$(2P^{\circ}_{1/2})5p$	$2[3/2]_1$	–0.5	–0.9	–1.2	–1.9
$(2P^{\circ}_{1/2})5p$	$2[3/2]_2$	–0.6	–0.9	–1.3	–1.7
$(2P^{\circ}_{1/2})5p$	$2[1/2]_1$	–0.3	–0.9	–1.2	–1.9
$(2P^{\circ}_{1/2})5p$	$2[1/2]_0$	–0.4	–0.8	–1.2	–1.8
$(2P^{\circ}_{3/2})6p$	$2[1/2]_1$	0.2	0.4	0.8	1.0
$(2P^{\circ}_{3/2})6p$	$2[1/2]_0$	0.1	0.6	0.6	1.0
$(2P^{\circ}_{3/2})6p$	$2[5/2]_3$	0.2	0.4	0.7	0.7
$(2P^{\circ}_{3/2})6p$	$2[5/2]_2$	0.2	0.7	0.7	1.0
$(2P^{\circ}_{3/2})6p$	$2[3/2]_1$	0.2	0.5	0.5	0.9
$(2P^{\circ}_{3/2})6p$	$2[3/2]_2$	0.2	0.3	0.6	0.6
$(2P^{\circ}_{3/2})6d$	$2[7/2]_3$	–0.2	–0.6	–0.6	–0.9

4. References

- [1] V. Kaufman and C. J. Humphreys, Accurate energy levels and calculated wavelengths of ⁸⁶Kr I, J. Opt. Soc. Am. **59**, 1614 (1969).
- [2] B. Petersson, Remeasured Ne I, Ar I, Kr I, and Xe I lines in the vacuum ultraviolet, Ark. Fys. **27**, 317 (1964).
- [3] T. Trickl, M. J. J. Vrakking, E. Cromwell, Y. T. Lee, and A. H. Kung, Ultrahigh-resolution (1 + 1) photoionization spectroscopy of Kr I: Hyperfine structures, isotope shifts, and lifetimes for the $n = 5, 6, 7$ $4p^5 ns$ Rydberg levels, Phys. Rev. A **39**, 2948 (1989).
- [4] J. Sugar and A. Musgrove, Energy levels of Kr I through Kr xxxvi, J. Phys. Chem. Ref. Data **20**, 859 (1991).
- [5] Procès Verbaux du C.I.P.M., October 1960. See also Trans. Intern. Astron. Union **11A**, 97 (1961).
- [6] D. A. Jackson, Isotope shifts in visible lines of the arc spectrum of krypton, J. Opt. Soc. Am. **70**, 1139 (1980).

- [7] H. Gerhardt, F. Jeschonnek, W. Makat, E. Matthias, H. Rinneberg, F. Schneider, A. Timmermann, R. Wenz, and P. J. West, Nuclear charge radii and nuclear moments of Kr and Xe isotopes by high resolution laser spectroscopy, *Hyperfine Interact.* **9**, 175 (1981).
- [8] R.-J. Champeau and J.-C. Keller, Spectroscopie laser a très haute résolution sur un jet atomique de krypton, *J. Phys. B* **11**, 391 (1978).
- [9] C. Brechignac, Measurements of isotope shift in visible lines of Kr I by saturated-absorption techniques, *J. Phys. B* **10**, 2105 (1977).
- [10] H. Gerhardt and E. Matthias, High-resolution spectrometer with a dye laser for the measurement of isotopic and isomeric shifts and hyperfine structure of radioactive isotopes, *Sov. J. Quantum Electron.* **7**, 1500 (1977).
- [11] H. Gerhardt, R. Wenz, and E. Matthias, Isotope shifts of the 557 nm transition in even krypton isotopes, *Phys. Lett.* **61A**, 377 (1977).
- [12] R.-J. Champeau and J.-C. Keller, Investigation of the line $\lambda = 587 \text{ nm}$ ($1s^4-2p^2$) of Kr I using stimulated emission in an atomic beam, *J. Phys. (Paris), Lett.* **38**, L463 (1977).
- [13] D. A. Jackson, Isotope shifts in the near infrared lines of the arc spectrum of krypton, *J. Opt. Soc. Am.* **69**, 503 (1979).

About the author: Victor Kaufman retired in 1988 from the Spectroscopy Group of the Atomic Physics Division at NIST. He had been with NIST since 1960. The National Institute of Standards and Technology is an agency of the Technology Administration, U.S. Department of Commerce.

Conference Report

THIRD INTERNATIONAL CONFERENCE ON CHEMICAL KINETICS REACTIONS IN GAS AND CONDENSED MEDIA Gaithersburg, MD July 12–16, 1993

Report prepared by

Robert E. Huie

Chemical Kinetics and Thermodynamics Division,
National Institute of Standards and Technology,
Gaithersburg, MD 20899-0001

1. Introduction

This quadrennial conference is organized to bring together leading scientists who generate and use chemical kinetic data in both the gas and condensed phases. Chemical kinetics is increasingly used as a tool for the understanding and control of complex chemical processes in a number of different areas. Many reaction types and intermediates are of key importance under widely different conditions. Nevertheless, investigators in one discipline are frequently unaware of work carried out in another area which may be related to their work, particularly if the other work is carried out in a different physical phase. This conference brings together scientists from these different disciplines

to discover areas of common interest where knowledge from one area can illuminate problems of another.

The conference was supported by the National Institute of Standards and Technology, the Environmental Protection Agency, the National Aeronautics and Space Administration, the NIST Standard Reference Data Program, the Chemical Manufacturers Association, and the Exxon Research and Engineering Company. Support was also provided in the form of special travel grants to attend this conference given by the International Science Foundation to some participants from the former Soviet Union. During the conference, the NIST Standard Reference Data Program demonstrated some of their computer databases and provided access to electronic mail for the participants.

Over two hundred scientists registered to attend the conference. They included representatives from over 20 countries. The delegates heard 44 oral presentations, including 6 invited lectures, on a wide range of subjects. Also, there were about 140 poster presentations.

2. Proceedings

The conference opened with a broad session titled Decomposition Kinetics chaired by John T. Herron of NIST. Jürgen Troe of the University of Göttingen delivered an invited talk on theoretical methods for the treatment of thermal high pressure dissociation and recombination reactions. Subsequent talks in this session and in the afternoon poster session dealt with the experimental determination of these rate constants. The afternoon session on Heterogeneous Reactions, chaired by Pedatsur Neta of NIST, started with an invited talk by Janos H. Fendler of Syracuse University on microheterogeneous systems, a topic which was new

to most of the participants. The other talks in that session were on reactions at gas-solid or gas-liquid interfaces, while various poster presentations also addressed micellar reactions.

On the second morning, the session on Theory, chaired by Wing Tsang of NIST, opened with an invited lecture by Carl F. Melius of Sandia National Laboratory in which the application of the BAC-MP4 method to the calculation of the thermochemical properties of reaction intermediates was outlined. A large number of heats of formation of reaction intermediates have been calculated in this manner. Because of a large number of requests, the Conference arranged to have a large table of these results duplicated and made available to the conferees. Subsequent talks in the morning session, and many of that day's poster presentations, expanded considerably on this theme and on other theoretical approaches to chemical kinetics. These methods are proving to be very important as guidance to experimental work and in the analysis of experimental data.

The Tuesday afternoon session, chaired by Arthur Fontijn of Rensselaer Polytechnic Institute, started with an invited talk by James C. Weisshaar of the University of Wisconsin on the reactions of gas-phase metal atoms and ions with alkenes and alkanes. The reactivity of the metal atoms and ions correlate well with the known atomic energy levels and with simple models of metal-hydrocarbon chemical bonding. Few of the participants were aware of the extent to which these studies have been carried out. The subsequent talks in the afternoon session focussed on reactions of silicone-containing radicals, as did many of the posters. A number of other poster presentations were on other aspects of the kinetics of chemical vapor deposition, which is becoming one of the important applications of chemical kinetics.

The Wednesday morning session opened with an invited presentation by Sidney W. Benson of the University of Southern California on the reaction of ethyl radicals with molecular oxygen. This session was chaired by Jai P. Mittal of the Bhabha Atomic Research Centre. Subsequent talks dealt further with the reactions of alkyl and other organic radicals with oxygen, particularly at high temperatures, as did several of the poster presentations that afternoon. In one of the papers, Dennis Bogan of Catholic University, presented results on the oscillating chemiluminescence observed from the reaction of methyl radicals with oxygen. Other papers were on the reactions of the peroxy radicals formed from the alkyl radical-oxygen reaction.

The afternoon session was the first of two, the other being Thursday afternoon, to focus on the reactions of inorganic radicals. The Wednesday afternoon session was chaired by Jeffrey W. Hudgens and the Thursday afternoon session was chaired by Stephen E. Stein, both of NIST. Many of the poster presentations also involved reactions of inorganic radicals and much of the theoretical work discussed earlier in the meeting had to do with reaction pathways in these systems.

Complex organic reactions were the theme of the Thursday morning session, chaired by Michael J. Kurylo of NIST. The session opened with an invited talk on the kinetics and mechanisms of the reactions of organic peroxy radicals by Timothy J. Wallington of Ford Motor Company. The session had a particularly strong atmospheric bent, with, for example, presentations on the reactions of the hydroxyl radical-aromatic adduct with nitrogen oxides and on the effect of water vapor on ozonolysis reactions. The atmospheric emphasis continued on Friday morning with a session on abstraction reactions of the hydroxyl radical, chaired by Robert F. Hampson of NIST. Several of these papers, and a number of the poster presentations Thursday afternoon, were on reactions of hydroxyl radicals with partially halogenated compounds being considered as replacements for the fully halogenated compounds, which are currently used as refrigerants, foam-blowing agents, solvents, and in other applications. This reaction is the major tropospheric loss mechanism for these species.

3. Conclusion

The emphasis on application in the field of chemical kinetics in general and in this conference in specific was reflected in the papers presented. The theoretical calculation of the properties of reaction intermediates are carried out because of the importance of these intermediates in practical problems; estimation techniques are developed to allow preliminary decisions to be made about industrially important chemicals; rate constant evaluations are driven by the needs of modelers; finally, the choice of reactions to be studied is frequently dictated by the immediate practical needs. Because of this, the chemical kinetics community is fragmented into small groups which interact more with their specific user community: in combustion, stratospheric chemistry, tropospheric chemistry, chemical vapor deposition, etc. This meeting provided the opportunity for

kineticists to interact with kineticists in many different areas of research and to learn the progress that has been made in measurements and techniques.

A limited number of copies of the meeting abstract book are available from the conference chairman, Robert E. Huie.

Conference Report

**DATA
ADMINISTRATION
MANAGEMENT
ASSOCIATION
SYMPOSIUM
Gaithersburg, MD
May 11–12, 1993**

Report prepared by

Judith Newton

Information Systems Engineering,
Computer Systems Laboratory,
National Institute of Standards and Technology,
Gaithersburg, MD 20899-0001

1. Introduction

Along with capital and human resources, an organization's data represents one of its fundamental assets. Data administration (DA) attempts the effective planning, organization, and management of an enterprise's data resource, with the intention of empowering the organization to achieve its mission and goals.

Reengineering the business processes, and the supporting information technology infrastructure, is a critical need for organizations. Yet despite substantial attention by business managers, technologists, and vendors of tools and methodologies, there are few obvious solutions or guidance on how to accomplish this.

The Data Administration Management Association (DAMA) is the professional organization for data administrators. An international board oversees a loose federation of local chapters in the United States, Canada, Australia, and Europe. The National Capital Region Chapter (NCR DAMA) has monthly meetings from September through April, as well as a Symposium in May.

NCR DAMA held its sixth annual Symposium at NIST on May 11–12, 1993. The theme this year was *Business Reengineering—The Competitive Edge*. Attended by over 200 Federal and private industry data administrators, the Symposium was cosponsored by NIST and NCR DAMA.

It emphasized the practices, technologies, activities, initiatives and ideas that deliver clearly visible value to the users, or "customers" of data administration. In addition to presentations by nationally recognized experts and practitioners, it included a workshop and panel discussions. Topics ranged from the keynote speech on reengineering business for the information age to the latest implementation of the Information Resource Dictionary System (IRDS) standard.

2. Speakers

The keynote speaker was Ron Shelby, of Connecticut Mutual Life Insurance Company. He has guided Connecticut Mutual through a complete redesign of its methods for handling insurance processing. The challenge of reengineering consists of moving away from the antiquated methods of mass production, assembly line, and cost-plus pricing to new assemble-to-order, flexible assembly, market-sensitive pricing practices. When a business can move from systems tracking things to systems driving events, results will be a change

from high price and high quality to low price and high quality. Electronic information systems can be the tool to accomplish these business miracles. The steps needed are: first, analyze what is really needed; rearchitect the information; reengineer processes; retool with technology; and finally, reorchestrate and realign the workplace.

Cathy Hirsh of American Management Systems addressed the need to incorporate legacy data and processes in the design for reengineering. Organizations cannot afford to throw away and redevelop systems from scratch. Legacy data can be used as a leverage point to develop migration strategies incorporating the information warehouse concept as a stepping stone along the journey to true reengineering.

Larry English of Information Impact International discussed the need for good data management and how it can support business reengineering. Data modeling provides stability and flexibility for the process. Data management can enable the paradigm shift in business areas by establishing business accountability for data and a single source of data capture. Single data maintenance applications by data type and life cycle must be in effect. Processes to support reengineering include focussing on strategic uses of data, establishing metrics, and keeping lines of communication open.

As an organization strives to improve its operations, the business leaders must determine the value of each process in terms that are meaningful to the operation. Ron Gustafson of EDS defined a value construct by which each business process may be evaluated before any automated system is designed, built, or selected to support that process. As the business leaders reengineer their organization's processes, they can establish, through this value construct, the set of fully integrated business processes needed to deliver optimal results to the enterprise. He illustrated how the value construct would be applied to a hypothetical business and discussed the potential benefits to both the business organization and to the information technology service provider.

Ron Ross of Ronald G. Ross Associates discussed modeling for enterprise-level reengineering. Resources include a set of subject-level databases, far more flexible than traditional application-area databases and therefore more suitable for reengineered processes. A tool to establish these subject-area databases, resource life-cycle analysis, determines the value chain and precedence of processes within each resource chain.

Mike Yoemans and Bunny Smith of DoD presented an overview of the Corporate Information Management (CIM) effort to integrate information systems within the Department of Defense. The process involves department-wide built business processes, shared data structures, a business modernization focus, matrix management organization, functional management of organization, architecturally driven philosophy, source data entry, common work breakdown structure, single code of accounts, data administration, life cycle program and project measures, and a standard hardware/software/communications platform.

The last speaker, John Zachman of Zachman International, presented an explication of his Information Architecture concept together with his personal view of the future of manufacturing and technology in the near future. We must change from Make-to-order and Provide-from-stock to Assemble-to-order processes. He issued a challenge for everyone in the audience to rise to meet the challenge of "The New Realities of the Information Age."

3. Panels

The following panel discussions were presented:

- Modeling Languages, Sandra K. Perez, Concept Technologies, moderator;
- DAMA/NCR Government Special Interest Group, Tom Kurihara, NIST, and Peter Aiken, DoD, moderators;
- Standards for Reengineering, Judith J. Newton, NIST, moderator;
- Functional Economic Analysis, Carla von Bernewitz, Vector Research, moderator;
- Data Administration Support for Business Process Improvement, Duane Hufford, AMS, moderator;
- Tangible Benefits of Reengineering, Cindy Walker, Software Solutions, moderator;
- Information Architecture, Raghu Chintala, Booz, Allen and Hamilton, moderator.

4. Standards and Procedures Workshop

The Working Group on Standards and Procedures has been meeting monthly during the past year. It has produced the Manual for Data Administration, NIST Special Publication 500-208. A copy of this publication was supplied to each Symposium attendee at registration. Additional copies are

available from the author of this Conference Report. This document discusses a wide range of data administration topics, including development and implementation of standards.

The Standards and Procedures workshop at this Symposium presented the draft result of the group's current effort: development of a survey to be distributed to data administrators in an effort to determine the current state of development of the art.

5. Proceedings

The proceedings of this, the Third, and the Fifth Symposia were distributed at the event. The Proceedings of the First,¹ Second,² and Fourth³ Symposia were published by NIST and copies are still available. The Seventh Annual Symposium will be held May 17-18, 1994.

¹ Judith J. Newton, and Frankie E. Spielman, eds., *Data Administration: Management and Practice, Proceedings of the First DAMA Symposium*, NIST Special Publication 500-159, National Institute of Standards and Technology, Gaithersburg, MD, October, 1988.

² Judith J. Newton, and Frankie E. Spielman, eds., *Data Administration: Standards and Techniques, Proceedings of the Second Annual DAMA Symposium*, NISTIR 90-4292, National Institute of Standards and Technology, Gaithersburg, MD, April 1990.

³ Judith J. Newton, Mary Lou Melley, and Holly Higgins, eds., *Managing Data: From Vision to Reality, Proceedings of the Fourth Annual DAMA Symposium*, NISTIR 4843, National Institute of Standards and Technology, Gaithersburg, MD, May 1992.

News Briefs

General Developments

Inquiries about News Briefs, where no contact person is identified, should be referred to the Managing Editor, Journal of Research, National Institute of Standards and Technology, Administration Building, A635, Gaithersburg, MD 20899-0001; telephone: 301/975-3572.

AGENCIES TARGET HELP FOR POLLUTION PREVENTION

With generally limited financial and technical resources, small and mid-sized manufacturers are particularly vulnerable to the increased costs that accompany strict environmental rules. Therefore, the NIST Manufacturing Extension Partnership and the Environmental Protection Agency have established a joint pilot project to help these companies apply innovative pollution prevention tools and strategies. The pilot is part of a planned multi-year program where the two agencies will assist companies in the selection of currently available technologies and techniques to reduce or eliminate pollution sources in manufacturing. Also planned is the development of pollution-prevention assessment procedures suitable for small and mid-sized manufacturers. The field work will be done through the Great Lakes Manufacturing Technology Center in Cleveland, one of seven MTCs in the MEP. The pilot program will concentrate on screw machine, metal stamping, and electroplating facilities, which are in large numbers in the Great Lakes region. For more information, contact David Gold, B115 Polymer Building, NIST, Gaithersburg, MD 20899-0001, (301) 975-5020.

NIST, ALASKA EVALUATE IMPACT OF BURNING OIL SPILLS

To state of Alaska officials, “burning the midnight oil” may soon take on a whole new meaning. Using computer modeling, NIST is helping the Alaska Department of Environmental Conservation better understand the impacts of burning spilled oil. Two main questions need to be answered: “How much smoke will be produced?” and “How far will the smoke spread?” As part of a cooperative research and development agreement, a new version of a NIST-developed computer model called LES (Large-Eddy Simulation) will predict smoke concentrations up to 30 km downwind of a simulated oil spill fire. ADEC has devised likely oil-spill scenarios to use in the program and has provided two types of Alaskan crude oil for testing. In laboratory tests, NIST will burn the oil in 1.2 m pans to get data for LES, such as the smoke production rate and the size of particulates in the smoke. NIST researchers also may develop yet another version of LES to predict the effect that land features, such as mountains, might have on smoke movement. This 3 year project will help ADEC develop guidelines officials at an oil-spill site can use to evaluate the effects of burning.

NEW LAB FOCUSES ON NOVEL MACHINE-TOOL DESIGNS

A new NIST laboratory will study applications and control strategies for innovative forms of machine tools. Initial efforts will focus on a potentially revolutionary design featuring a Stewart platform (also the basis for the floating platform in mechanical flight simulators) suspended from an octahedral support frame. Several machine-tool makers are

pursuing variations of this concept because the combination of rigid frame and six-axis machining capability promises important advantages over conventional machine-tool designs, including lower cost, greater flexibility and reliability, and higher accuracy. For example, a private company has developed a spider-shaped prototype called an octahedral-hexapod machine. Last year, the company received an Advanced Technology Program grant to help it evaluate and refine its prototype. Through a competitive bidding process, NIST intends to purchase an octahedral-hexapod machine, built to its specifications, for the new Advanced Machine Tool Structures Laboratory. NIST research will focus on developing computer-control architectures that maximize machine-tool performance and versatility, and on factors influencing the dimensional accuracy of the machining process. For more information, contact E. Clayton Teague, A117 Metrology Building, Gaithersburg, MD 20899-0001, (301) 975-3490.

SOFTWARE DESIGNED TO SAVE ENERGY AND DOLLARS

NIST has developed a set of four computer programs that can help building designers, owners, and managers evaluate costs and savings of energy conservation projects and select projects with the lowest life-cycle cost. For example, the Building Life Cycle Cost, or BLCC, program can be used to determine the most economical level of attic insulation, select the most cost-effective heating and cooling system, or evaluate the cost effectiveness of a solar heating system. Another program called DISCOUNT can evaluate individual components of a life-cycle cost problem, such as the present value of annual energy savings over 20 years. A third program, ERATES, evaluates electricity costs based on time-of-use, block-rate, and demand-rate schedules. These programs are designed to run on most IBM-PC-compatible microcomputers. No special hardware or graphics capabilities are required. The programs are available from several vendors for a nominal cost. NIST building economists also offer life-cycle cost workshops and training videos. For a brochure with more information, call the NIST Office of Applied Economics at (301) 975-6132.

CERAMIC "CHEFS" FINE-TUNE RECIPES WITH NEW OVEN

All soufflé chefs know that if you open the oven door during baking, the dish is ruined. Ceramics

developers have a similar problem. When sintering or firing ceramic powders at high temperatures, they typically must rely on trial and error to produce materials with the right properties. To overcome this drawback, NIST materials scientists have installed a unique furnace at the institute's Cold Neutron Research Facility that could help speed up research efforts. Paired with a small-angle neutron scattering instrument, the new furnace allows researchers to observe changes in the microstructure within ceramic materials in real time throughout the sintering process. Cold (slowed) neutrons are directed through a ceramic sample within the furnace, and the pattern of "scattering" produced as the neutrons re-emerge provides information about "grain sizes" and other structural features critical to the material's ultimate properties. For more information, contact Gabrielle Long, A163 Materials Building, NIST, Gaithersburg, MD 20899-0001, (301) 975-5975.

NO "SECOND GUESSING" WITH NIST TIME SERVICES GUIDE

Persons interested in time, timekeeping, and precise time and frequency measurements will want to get a new paper available from NIST. Titled Time and Frequency Services Offered by the National Institute of Standards and Technology, it describes in some detail shortwave radio stations WWV and WWVH, low-frequency radio station WWVB, satellite time services, and the Automated Computer Time Service. It also discusses two services for persons needing the most accurate time and frequency signals possible. Future trends in NIST services are discussed, including greater use of Global Positioning System satellites and optical communication technology. For a copy of this paper, contact Sarabeth Moynihan, Div. 104, NIST, Boulder, CO 80303-3328, (303) 497-3237. Ask for paper no. 37-93.

FEBRUARY MEETING TO FEATURE 1993 BALDRIGE WINNERS

"Quest for Excellence VI," Feb. 6–9, 1994, at the Washington Hilton and Towers in Washington, DC, will be the first conference to feature presentations by all of the 1993 recipients of the Malcolm Baldrige National Quality Award. The award recipients were announced in October. Chief executive officers and other team members from the winning companies will describe in detail their quality improvement strategies and results. The conference provides a unique networking opportu-

nity for people from across the country to exchange plans and ideas for quality and productivity improvements. It is being co-sponsored by NIST, the American Society for Quality Control, and the Association for Quality and Participation. For more information about "Quest for Excellence VI," call (301) 975-2036.

TWO COMPANIES RECEIVE 1993 BALDRIGE AWARD

The 18th and 19th winners of the Malcolm Baldrige National Quality Award were announced by President Clinton on Oct. 18, 1993. The companies are Eastman Chemical Co. (Kingsport, Tenn.) in the large manufacturing category and Ames Rubber Corp. (Hamburg, N.J.) in the small business category. Eastman Chemical, a division of Eastman Kodak Co., ranks as the 10th largest chemical company in the United States and 34th in the world. It manufactures and markets over 400 chemicals, fibers, and plastics for 7,000 worldwide customers—over 70 percent of whom rated Eastman their number one chemical supplier for the past 4 years. Founded in 1949, Ames Rubber produces rubber rollers for office machines and is the world's largest manufacturer of rollers for mid- to large-sized copiers. Quality improvements have saved the company and its customers more than \$3 million, an average of \$2,700 for each of its 445 employees in 1993. The two winners were honored for their world-class systems of management, employee involvement, and customer satisfaction at a ceremony in Washington, DC, in November.

NEW DENTAL MATERIAL CONTAINS NO MERCURY

A mercury-free, direct filling alternative for conventional dental amalgams is being developed at NIST in a collaborative effort between government and industry. The new restorative process uses metallic powders in a form easily applied to prepared tooth cavities with treatment procedures very similar to those in current dental practice. The National Institute of Dental Research is contributing support for the program through the American Dental Association Health Foundation's Center for Excellence. The ADAHF maintains the Paffenbarger Research Center at NIST. The restorative process, based on NIST electrochemical powder technology, was invented by a NIST scientist, and a guest scientist from Israel. The material involves the use of biocompatible metallic powders such as

silver-coated tin. These pairs of metals undergo fast diffusion or combine to form an in-situ intermetallic compound at body temperature. According to the NIST scientist, the new restorative material could be in dental offices within 3 years.

TECHNOLOGY CENTERS TO HOST SBA EXPERTS

The Department of Commerce and the Small Business Administration have agreed to establish Small Business Development Center subcenters at the seven current Manufacturing Technology Centers sponsored by Commerce's NIST. Under the agreement, NIST intends to provide the MTCs with funding—up to \$250,000 per center per year—to finance the subcenters for a 3-year trial period. SBDCs supply a wide range of financial and business planning services for small and mid-sized companies. The new subcenters will not only give MTC clients improved access to SBA programs but also will provide specialized services geared to needs of manufacturers. Specific details of each subcenter's operation will be decided by the associated MTC, working with the lead SBDC agency in that state. Following MTC practice, the SBDCs will be tailored to meet the specific needs of manufacturers in their service areas.

PANEL TO ADDRESS OPEN SYSTEMS COMPATIBILITY

Due to the incompatibility of two major computer networking protocol suites, NIST has named an interagency panel to review open systems network requirements and recommend policies on the use of networking standards by the federal government. The Panel on Federal Internetworking Requirements will consider the comparative strengths of the Internet Protocol Suite and Open Systems Interconnection specifications, two widely used, yet incompatible, protocol suites. The IPS and OSI specifications for computer communications provide many similar capabilities for interconnecting computers; local-area, wide-area, and other networks; and for routing information between computers. The panel will review the government's requirements for network features such as security, ease of use, national and international connectivity, and standards maintenance. Interoperability requirements, agency costs, and the role of protocols not in OSI or IPS specifications also will be considered. The panel is expected to issue a report in January 1994.

NEW STANDARD RANDOMLY CHOOSES COMPUTER PASSWORDS

For computer users who continue to rely on traceable passwords such as the name of a pet, a nickname or birthday, a new standard has been approved that may make their lives a bit easier. The Automated Password Generator, specified in NIST's Federal Information Processing Standards Publication 181, produces random passwords that are pronounceable, easily remembered, stored and entered into computer systems, yet are not readily susceptible to automated techniques that have been developed to search for and disclose passwords. Use of this algorithm adds an extra layer of security to protected computing resources. This standard complements the Password Usage Standard (FIPS 112), which specifies basic security criteria for the design, implementation, and use of passwords. Copies of FIPS PUB 181 will soon be available for purchase from the National Technical Information Service, Springfield, VA 22161, (703) 487-4650. For further information, contact Charles Dinkel, A216 Technology Building, NIST, Gaithersburg, MD 20899-0001, (301) 975-3367.

TWENTY-NINE GRANTS ANNOUNCED FOR ATP FOURTH ROUND

Commerce Secretary Ronald H. Brown announced on Nov. 4 the awarding of 29 grants for the fourth round of the Commerce Department's Advanced Technology Program. The NIST-administered grants are designed to accelerate the development and commercialization of promising, high-risk technologies with substantial potential for enhancing U.S. economic growth. These latest awards will help finance the multiyear R&D projects with a projected total cost of \$118 million, of which some \$60 million will be funded by the ATP. The new programs selected for funding included proposals in technology areas such as communications and information systems, biotechnology, electronics, manufacturing, and advanced materials. More than 50 companies, universities and research institutions—including more than 20 small businesses—will participate directly in work supported by these awards. Five grants went to joint ventures. Funding for the ATP program itself will rise from \$68 million in fiscal year 1993 to nearly \$200 million in FY 1994. The president's technology strategy calls for the program to grow to \$750 million by FY 1997.

LASER LIGHT USED TO FOCUS ATOMS ON SURFACES

NIST physicists have successfully demonstrated a rapid new process for fabricating infinitesimally small metallic structures. The new process, known as "atom optics," manipulates chromium atoms into precise locations on a silicon surface using laser light. This technique of focusing chromium atoms opens new avenues for creating smaller and faster electronic devices. The physicists report their discovery in the Nov. 5 issue of *Science*. NIST physicists have patterned structures by channeling chromium atoms between the peaks in a light wave. As focused by laser light waves, the chromium atoms form tiny parallel rows on a silicon surface. Each row is approximately 65 nm wide, about one-thousandth the diameter of a human hair. These rows, visible with a scanning electron microscope, are about 34 nm high and 213 nm apart. Although other scientists have used light to focus sodium atoms, the NIST experiment marks the first time this technique has been used to create durable metallic structures. For more information, contact Jabez McClelland, B206 Metrology Building, NIST, Gaithersburg, MD 20899-0001, (301) 975-3721.

"ELECTROMAGNETIC BOTTLE" TRAPS IONS FOR STUDY

An exotic form of matter was recently created when NIST physicists stripped 46 electrons from a barium atom in the institute's new Electron Beam Ion Trap—or EBIT—Facility. The EBIT Facility holds the supercharged atoms with a force field that compresses them into a tiny column at the center of a vacuum chamber. In this 2 cm long and 60 μm wide (the width of a human hair) column, a powerful electron beam rips electrons from atoms injected into the trap. Superconducting magnets help hold the atoms, now missing most or all of their electrons, inside what could be considered an "electromagnetic bottle." As the electron beam excites these highly charged ions, they absorb and emit photons. NIST physicists use the energy spectra of these emitted photons to study quantum electrodynamics, the interaction of virtual matter/anti-matter particles with ions. The EBIT Facility also can help determine how ions behave in solar flares, black holes, and nuclear explosions. Possible industrial applications include the use of exotic ion beams in micromachining surfaces and nanofabri-

cation of electronic devices. NIST's EBIT was built by and operates under a collaboration between NIST and the Naval Research Laboratory, and follows pioneering work done by a group at the Lawrence Livermore National Laboratory.

1994 BALDRIGE CRITERIA FOCUS ON BUSINESS PLANNING

This year's criteria for the Malcolm Baldrige National Quality Award highlight the importance of integrating quality and operational aspects, such as manufacturing and service delivery strategies, into overall business planning. The seven criteria categories—leadership, information and analysis, strategic quality planning, human resource development, and management, management of process quality, quality and operational results, and customer focus and satisfaction—remain basically the same. Over one million copies of the award criteria, which double as quality improvement guidebooks, are in use worldwide. The criteria are accepted widely as the definition of what constitutes world-class quality. Individual copies of the 1994 award criteria, along with the 1994 application forms and instructions, are available from NIST by calling (301) 975-2036. Multiple copies in packets of 10 can be ordered for \$29.95 plus postage and handling from the American Society for Quality Control, (800) 248-1946. ASQC's order number is T998. NIST manages the award program in conjunction with the private sector.

1994 NIUF MEETING DATES ANNOUNCED

Users and implementors interested in the Integrated Services Digital Network, which utilizes telephone lines to transmit voice, graphics and computer data simultaneously, are welcome to the 1994 meetings of the North American ISDN Users' Forum. The NIUF will meet first on Feb. 8–11, 1994, at the Hyatt Regency Tech Center in Denver, CO. Locations for the other meetings, June 20–24, 1994, and Oct. 3–7, 1994, have not been announced. The NIUF is a collaboration between NIST and industry partners who have a stake in using, implementing or providing service for ISDN. Previous meetings addressed the NIUF's participation in the National Information Infrastructure, impact on mass markets, and network interoperability. For more information, contact Dawn Hoffman, B364 Materials Building, NIST,

Gaithersburg, MD 20899-0001, (301) 975-2937, fax: (301) 926-9675.

NEW DEVICE IMPROVES MAMMOGRAPHY IMAGING

A new NIST invention, an x-ray crystal diffraction spectrometer, can help radiologists improve image quality in mammography, one of medicine's most important breast cancer screening tools. The quality of a mammogram, an x-ray image of breast tissue, is determined in part by the electrical voltage that generates x rays in a mammographic unit. A radiologic technician sets the voltage on the unit based on the thickness and tissue density of the breast. The NIST spectrometer will be used as a calibration device. When placed in the x-ray beam, the device tells whether the actual voltage agrees with the indicated voltage. The x-ray crystal diffraction spectrometer, a metal box about 46 cm in length, measures the electrical voltage over the range used in mammography more accurately than any existing method. The research was reported in the November/December 1993 issue of *Medical Physics*.

SOFTWARE HELPS PREDICT, SOLVE MOISTURE PROBLEMS

Researchers at NIST and the Virginia Polytechnic Institute and State University have developed a user-friendly computer program called MOIST that predicts moisture accumulation in walls and ceilings. Too much moisture can cause nails to pop; paint to blister; wood beams to bow, shift or decay; insulation to thermally degrade; and indoor air to develop quality problems. For example, in 1992, a courthouse in Polk County, Fla., was closed for renovations costing \$16 million—almost half of the original cost of the building. The problem: moisture trapped in the walls and ceilings allowed the growth of mold and mildew, causing a serious indoor air quality problem. With MOIST, users can define a wall, cathedral ceiling or low-slope roof construction, and then vary the type and placement of building materials. MOIST can determine whether a vapor retarder is needed and, if so, where it should be placed. It also can be used to evaluate the effect various paints, wall coverings, and climate have on moisture accumulation. Free copies of the MOIST software are available by writing to Doug Burch, B320 Building Research Building, NIST, Gaithersburg, MD 20899-0001.

**NEW "ONE-STOP" INDUSTRY GUIDE
TO NIST AVAILABLE**

A new publication describing more than 250 different research projects, grants, and industry outreach programs at NIST is now available both in print and via electronic mail. The 116-page Guide to NIST includes sections on the Advanced Technology Program; the Manufacturing Extension Partnership; all major NIST programs (with contact names, addresses, phone numbers and e-mail addresses); electronic bulletin boards and information retrieval systems; research consortia; grants; publications; mechanisms for collaborative research; facilities; and a detailed subject index. For a free printed copy, send a self-addressed mailing label to the NIST Public Affairs Division, A903 Administration Building, NIST, Gaithersburg, MD 20899-0001; or fax requests to (301) 926-1630. Full text of the report is available electronically through the Internet Gopher system. From a remote log in, type "telnetgopher.nist.gov". At the log-in prompt, type "gopher". From a gopher client, use the gopher server as "gopherserver.nist.gov" with port 70. The electronic version of the guide allows for customized searches of topics of interest.

**MEASURING ENERGY FLOWS IN A
SUPER-COLD REFRIGERATOR**

In the late 1980s, NIST developed a super-cold refrigerator with no moving parts in the cold end. Termed an orifice pulse tube refrigerator, or OPTR, it has a variety of potential uses in infrared sensor, vacuum pump, and medical technology. A recent NIST paper describes a technique allowing for the instantaneous measurements of mass flow rate, temperature, and pressure during the operation of an OPTR. The paper presents the values of enthalpy, entropy, and work fluxes at the cold end of the pulse tube evaluated from the measurements. These results will aid in improving input parameters to the analytical model developed at NIST, as well as verifying model predictions. The experimentally measured enthalpy flows and refrigeration powers within the pulse tube ranged from 60 percent to 85 percent of the ideal values from the NIST adiabatic model. For a copy of paper 40-93, contact Sarabeth Moynihan, Div. 104, NIST, Boulder, CO 80303-3328, (303) 497-3237.

**NIUF GROUP STUDIES ISDN WIRING
INSTALLATION**

Professionals who own a small business or work in a home office may dream of the productivity possible with an advanced telecommunication service like the Integrated Services Digital Network. While such services are more commonly found in large businesses, a joint government-industry group is working to remove some barriers to general use of ISDN. The North American ISDN Users' Forum formed a Wiring and Powering Working Group to develop guidelines for those who install ISDN wiring for residential and small business customers. To date, most of the practical information for installing this high-technology equipment is incomplete and targeted primarily at large businesses. The working group is trying to make it easier for customers in all market segments—not just large business—to get hooked up. The effort is supported by several major industry players, including ISDN service providers, component vendors, installers, and communication planners. The NIUF, a collaboration between NIST and industry, helps users and manufacturers to concur on ISDN applications, standards, and conformance tests. For more information about the Wiring and Powering Working Group, contact Steve Halpern, NYNEX Science & Technology, 500 Westchester Ave., Room 2G19A, White Plains, NY 10604, (914) 644-2581, email: sjh@nynexst.com (via Internet).

**EM MATERIALS MEASUREMENTS FOCUS
OF NEW REPORT**

In recent years, many industries have recognized a critical need for reliable data on electromagnetic properties of various materials. A new publication, NIST Measurement Service for Electro-magnetic Characterization of Materials (NISTIR 5006), presents an overview of special test and measurement services for characterizing dielectric and magnetic properties of materials at radio and microwave frequencies. For these services, NIST uses three automatic network analyzers that cover the frequency range from 100 kHz to 26.5 GHz. The publication describes measurements of permittivity and permeability using coaxial transmission line systems, waveguide systems, and several types of resonators.

The most widely used line system is the 7 mm coaxial airline with a frequency range from direct current (zero hertz) to about 18 GHz. The most widely used waveguide system uses X-band (WR-90) waveguide, which covers the frequency range from 8.2 GHz to 12.6 GHz. NIST's resonators are used for accurate measurements of loss tangents of low-loss materials. Also available is a software package for complex permittivity and permeability determination during transmission-line measurements. Copies of NISTIR 5006 are available from the National Technical Information Service, Springfield, VA 22161, (703) 487-4650. Order by PB 94-110186.

ATOMIC CLOCK, WEAR-RESISTANT ALLOY RECEIVE HONOR

Popular Science magazine has selected two NIST technologies, the NIST-7 atomic clock and a biocompatible alloy that resists fracture and wear, as among its "Best of What's New in 1993." The list honors what the publication considers "the year's 100 most significant new products and achievements in science and technology." Both NIST winners are featured in a special section in the December 1993 issue of the magazine. Started up in April 1993, NIST-7 is the seventh generation of atomic clocks built by NIST's Time and Frequency Division in Boulder, CO. It neither gains nor loses a second in 1 million years. The development of the new alloy—a biocompatible mixture of zirconium, palladium, and ruthenium—was announced in January 1993 at NIST's Paffenbarger Research Center in Gaithersburg, MD. Tests show that under applied stress normally large enough to produce a change in shape, the alloy undergoes internal changes that actually increase its ability to resist further deformation and wear. It is being researched as a potential material for dental and medical devices, and holds significant promise as an industrial coating where high-performance materials are required for bearing surfaces and mechanical joints.

INTERAGENCY COMMITTEE ON STANDARDS POLICY ISO 9000 CLEARINGHOUSE

NIST has issued a fact sheet, entitled "Federal ISO 9000 Related Activities," which summarizes information received by NIST on ISO 9000-related activities in the Departments of Education, Commerce, Health and Human Services, Interior, Labor, and State, as well as the Federal Trade Commission, General Services Administration,

U.S. International Trade Commission, Nuclear Regulatory Commission, Office of Management and Budget, and the U.S. Postal Service. The fact sheet also includes information on foreign government use of the ISO 9000 Standards and is the result of a recommendation by the newly formed Working Group on ISO 9000 of the Interagency Committee on Standards Policy (ICSP) that NIST should serve as the ICSP ISO 9000 clearinghouse for dissemination of information on federal agency activities related to the ISO 9000 Standard Series.

The fact sheet is available to federal agencies and others with an interest in such activities. Additional fact sheets on federal agency ISO 9000-related activities will be issued as new or revised information is received by the clearinghouse.

PATENT ISSUED ON SENSOR TO DETECT AND CLASSIFY SUBMICROMETER PARTICLES

NIST has received a patent on a solid-state sensor capable of detecting particles having dimensions down to 0.1 μm . The patent, number 5,218,211, was issued June 8. The target application is for the detection of particles in the ultra-clean environment required for the manufacture of integrated circuits. The sensor consists of a dime-sized "monolithic" array of individually addressable, photosensitive pixels connected to a hardware/software electronic subsystem. The array is activated by illumination with an electronically alterable spectrum of electromagnetic radiation. The device includes a screen patterned with apertures of different sizes and geometries designed to facilitate the extraction of particle-size distributions using neural network algorithms. To date, just over a dozen companies have made preliminary inquiries about the patent.

METHOD DEVELOPED FOR CHARACTERIZING PLANAR TRANSMISSION LINES FORMED ON LOSSY SUBSTRATES

Two NIST scientists have developed a method that should, for the first time, provide accurate determinations of the characteristic impedance of a microwave planar transmission line formed over a lossy or dispersive dielectric as substrate. Planar transmission lines are typically miniature structures and are essential components in applications such as monolithic microwave integrated circuits, printed-circuit boards, and special modules for high-performance computers. As the speed of advanced silicon digital circuits increases, microwave lines will be required for mainstream

silicon as well. The new method, known as the calibration comparison method, also determines the resistance, inductance, capacitance, and conductance per unit length of the line. That the conventional method used to estimate the characteristic impedance of lines fabricated on lossy dielectrics had problems was demonstrated by applying that method to a line formed over quartz, effectively a lossless substrate, for which the characteristic impedance can be determined as a function of frequency by other means. The plot of the real part of the characteristic impedance as a function of frequency showed values that agreed with the actual values at only a few points. The major problem in demonstrating the validity of the new method is that there is no other method to serve as a reference.

The scientists tested their method two ways. In the first test they used their method to determine the characteristic impedance of a line formed over quartz and showed good agreement with the actual values. In the second test, they fabricated four transmission lines with as near identical geometries as possible, one over gallium arsenide (effectively lossless) and the other three over silicon having differing conductivities. On applying their method, they found that the resistance and product of frequency and inductance for all four lines as a function of frequency was in good agreement, indicating that the method is consistent in determining them and that, as expected, these properties are independent of the substrate.

NIST IMAGES MAGNETIC RECORDING HEAD WITH NEW MAGNETIC-FORCE MICROSCOPE

Three NIST scientists have applied a new form of magnetic-force microscope having a non-vibrating sensing tip to image a thin-film recording head. This variation of magnetic-force microscopy, known as DC magnetic-force microscopy, provides direct correlation of magnetic fields to the pole pieces, as it simultaneously provides an atomic-force microscope image of the surface topography with the magnetic image. The magnetic force is calculated as the product of the spring constant of the cantilever probe and the deflection of the tip. The field gradient can then be determined. Since control of the separation of the probe tip from the scanned specimen is not dependent on the magnetic-force signal, the separation can be varied and, in particular, can match the flying height of a head above its magnetic media in a drive.

NIST-LED IEEE WORKING GROUP RECOGNIZED FOR DEVELOPMENT OF SURGE VOLTAGE DOCUMENT

Recently, the Power Engineering Society of the Institute of Electrical and Electronics Engineers recognized its Working Group on Surge Characterization in Low-Voltage Circuits for the development of IEEE Recommended Practice on Surge Voltages in Low-Voltage AC Power Circuits, C62.41-1991. This activity was led by a NIST scientist, who was both a major contributor to the over-100-page practice and coordinator for the efforts of the 28 member group.

Almost all who use computers have experienced a problem resulting from a power-line surge, whether the cause was a failure of equipment in a building distribution system or a close lightning strike from a summer thunderstorm. The practice addresses needs on the part of designers of equipment (such as computers) to provide an appropriate degree of surge-withstand capability in their products, on the part of users to specify appropriate surge-withstand capabilities, and on the part of test instrument suppliers and test laboratories for a limited set of well-defined test waveforms. The NIST scientist was the chief architect of the successful effort to simplify an extremely complex database on surges into the desired limited set of representative surge waveforms. The practice provides a basis for determining and designing voltage and current tests to be applied to equipment connected to power lines and discusses a variety of topics, including the origin of surge voltages, rates of occurrence and voltage levels that can be experienced in unprotected circuits, waveshapes of representative surge voltages, and the energy that surges can contain. The practice defines three categories of equipment location based on the relative position of the equipment with respect to the building service entrance. For each category, the practice provides two recommended "standard waveforms" and three suggested "additional waveforms" for surge voltage and surge current.

NIST'S LIGHT SCATTERING TAXONOMY HIGHLIGHTED IN *APPLIED OPTICS JOURNAL*

The July 1 issue of *Applied Optics* featured a collection of articles from the Optical Society's topical meeting on Surface Roughness and Scattering held in 1992. The issue's cover shows illustrative highlights from the conference and includes a taxonomy of light-scattering properties from rough surfaces

developed by NIST researchers for their article, "Regimes of Surface Roughness Measurable with Light Scattering," based on their presentation at the conference. The NIST taxonomy shows how different statistical properties of rough surfaces may be derived from light scattering depending on the ratio of the rms roughness to the wavelength of the incident light. The article also presents rules of thumb for distinguishing between the various regimes. This scheme represents a summary of previous experiments of the NIST researchers along with the work of many others in the field. Light scattering is an important technique for measuring the surface quality for a wide range of industrial components including optical elements and mechanical parts.

NIST CMM TEST DEVICE COMMERCIALIZED

The CMM interim testing standard invented at NIST has been commercialized by a major manufacturer of coordinate measuring machines (CMMs) and dimensional metrology equipment. Designed and developed by NIST scientists and engineers, the CMM interim testing standard was a joint effort between NIST, DOD, and private industry. The interim testing standard, a device employing kinematically mounted calibrated ball bars, is designed to detect faulty CMMs so that they can be removed from service before a significant problem develops. Fast and efficient, the interim testing standard can conduct a CMM system evaluation in typically 15 min. Early prototypes were field tested in quality conscious corporations through a cooperative research and development agreement with NIST.

ULTRATHIN FILM SnO₂ GAS SENSORS

Tin oxide has been used in carbon monoxide and combustible-gas sensors for many years. In these devices, sensing is achieved by monitoring the change in surface conductance when an analyte gas chemically interacts with the oxide surface. In commercially available devices, the active oxide material is in a bulk, polycrystalline form. While sensing performance in these devices is adequate for some applications, their utility is limited by slow and non-reproducible response characteristics. A major cause for these irreproducibilities in surface conductance is diffusion of oxygen atoms from the bulk to the surface. Because bulk diffusion is a relatively slow process, an undesirable, slowly drifting baseline-conductance occurs.

Scientists at NIST have been investigating alternative sensing materials and structures that would simplify the transduction process and improve sensor response characteristics. These alternatives include highly ordered, epitaxial films to address the problem of baseline drift. They theorize that by fabricating sensors using ultrathin films, films with essentially no bulk, the problems of baseline drift would be alleviated. Recently they have succeeded in producing 1.5 nm to 8.0 nm thick epitaxial tin oxide films on single crystal sapphire substrates. Conductance measurements were made while exposing the films to pressure cycles of prototypical oxidizing and reducing gases, O₂ and H₂, in an ultrahigh vacuum chamber. All the films, even for thickness down to 1.5 nm, showed sensing responses to O₂ and H₂. This result is quite remarkable because it requires that the 1.5 nm thick film, only 5 or 6 atoms thick, be electrically continuous over the 1 mm length scale of the conductance measurement. Most significant, however, is the observation from the initial studies that the 1.5 nm thick films exhibit less drift than the thicker films. This supports the original conjectures concerning the source of the drifts and the proposed approach to reducing drifts. Current research is extending the sensor response studies to higher pressure regimes and investigating the sensing response to other analyte gases such as CO and methane. These studies are an important step in the development of conductometric gas sensors that are more quantitative and reliable.

NEW COLLISIONAL PROCESS RESPONSIBLE FOR RADIATION DAMAGE IN COMPOUNDS

A specific collisional process that is due to electron-transfer collisions has been identified by a NIST scientist and guest researchers working in collaboration with researchers at the Jagellonian University in Poland. The results, obtained from electron emission spectra of ion-bombarded ionic crystals, define a new class of inelastic collisions in solids that are basic to defect production and chemical modification. In these collisions, the electron-transfer step involves lattice ions that are displaced and are no longer chemically bound. Such collision-induced electron transfers thus can change the chemical state of stable compounds, can switch interaction potentials, and can induce free-atom migration in the solid. The electron-transfer reactions are a fundamental component of radiation damage mechanisms in compound materials.

This type of collision event, identified at NIST, is the basis for the first mechanism to describe how collisions in solids can initiate electronic processes responsible for materials modification. Applications of this electron-transfer mechanism are found in chemical sputtering and plasma-assisted etching in ion track formation, and in the long-term stability problem of nuclear waste-storage materials where internal collisions can alter the chemical integrity of the material.

EIGHTH NATIONAL SYNCHROTRON RADIATION INSTRUMENTATION CONFERENCE CONVENED AT NIST GAITHERSBURG CAMPUS

The biennial National Synchrotron Radiation Instrumentation Conference was first organized by and held at NIST in 1979 and has since been hosted by each of the U.S. national synchrotron radiation facilities. The cycle has taken 14 years for the conference to return to NIST, where it was held Aug. 23–26. Growth in the field of synchrotron radiation during this period is indicated by a tripling of the number of papers presented at the conference. At the eighth meeting, first reports were made of operations of three new U.S. facilities, and progress and planning reports were made concerning several more. There were more than 200 attendees at the meeting, and 20 industrial firms exhibited equipment.

Synchrotron radiation sources cover the entire electromagnetic spectrum. They are of particular interest as sources of x-ray radiation, where they provide the practical basis for a wide range of research in biology, materials science, chemistry, and physics. Most research on applications of x rays also utilizes synchrotron radiation, such as x-ray angiography, microscopy, and lithography. NIST maintains an in-house synchrotron radiation source, the SURF II Synchrotron Ultraviolet Radiation Facility, which is a national standard for absolute radiometry in the soft x-ray spectral region, and also supports measurement and research programs in atomic, molecular, and surface physics. Scientists from several NIST laboratories also make extensive use of the higher-energy radiation from other synchrotron facilities.

DEVELOPMENT OF TUNABLE, PULSED SOLID-STATE LASERS IN THE VISIBLE

Clusters of atoms, the amorphous transition state between the gaseous, liquid, and solid states of matter, are the latest challenge to the ancient science of spectroscopy. Of particular interest is the ability to prepare individual quantum states of a cluster and then to probe the dynamics of these precisely selected states in real time. One invaluable tool is a narrow-band, tunable infrared (IR) laser that produces pulses for pumping specific rovibrational states of the cluster. NIST scientists recently have developed such a method for generating Fourier-transform-limited (0.005 cm^{-1}), high-energy (5 mJ) pulses of tunable IR light by "seeding" an optical parametric oscillator (OPO) pumped at frequency ω_3 (from a pulsed, frequency-tripled Nd:YAG) with a single-mode, continuous-wave (cw), ring dye laser. The OPO cavity is locked onto the dye laser via polarization servo-loop schemes and generates intense, spectrally narrow pulsed output both at the dye laser frequency, ω_1 , and the difference frequency, $\omega_2 = \omega_3 - \omega_1$. By replacing the "seed" dye laser with cw tunable, IR diode lasers, this difference-frequency scheme illustrates a novel method for generating tunable light pulses throughout the visible region, but based entirely on solid-state lasers.

CRADA WITH AISI FOR ON-LINE MAGNETIC MONITORING OF STEEL

To maintain quality control of coiled sheet steel, mechanical properties must be monitored throughout the entire length of the coil, with feedback to control the processing parameters. Because mechanical tests are costly and time consuming, a nondestructive method to continuously monitor the steel during production would increase product quality and reduce scrap. Toward this end, studies are being performed at NIST in cooperation with the Department of Energy, through a CRADA with the American Iron and Steel Institute (AISI). Researchers studied the effect of transducer configuration on Barkhausen signal characteristics, important for the constraints imposed by on-line measurements. They measured the mechanical and magnetic properties and the relationships between them for a set of low-carbon sheet steels, revealing good correlations between the mechanical yield strengths and the magnetic coercive fields. Cooperative work with the two steel companies is in progress to extend the relationships found and to determine their statistical validity.

MEASUREMENTS FOR CERAMIC POWDER PROCESSING

Fine powders are commonly used as starting materials for advanced ceramic components. These powders are often processed in suspensions for shape-forming prior to sintering. Measurements of key properties of suspensions have been recognized as one of the most important steps in the understanding and control of slurry-based processes for enhanced reproducibility of ceramics manufacturing. Researchers at NIST are developing electroacoustic techniques that show significant promise for slurry characterization.

The electroacoustic phenomena arise due to the reciprocal relationship between electric fields and sound waves in a suspension of charged particles. The electroacoustic analysis of suspensions constitutes the measurement of sound waves generated by the particles when an alternating electric field is applied to the suspension. The promise of electroacoustics is that the measurements can be carried out in concentrated suspensions that are inaccessible to optical techniques, and on stirred samples undergoing rapid sedimentation or exhibiting high viscosity.

The primary research focus has been on the development of measurement capabilities as applied to slurries of silicon nitride, an important structural ceramic. This research has been instrumental in improving understanding of the interfacial chemistry of silicon nitride and powder dispersion in slurries. Two industry-led workshops conducted on this topic at NIST in June 1992 and Feb. 1993 have led to a NIST/industry consortium to address issues relevant to powder processing.

COMBUSTION STUDY OF SILOXANE THROUGH CRADA WITH INDUSTRY

Siloxanes (silicon-oxygen based materials) are used as alternative transformer fluids, replacing PCBs. When most materials burn, the heat release rate increases significantly with an increase in external thermal radiant flux applied to the burning surface. This is true of wood and plastics. The burning behavior of siloxanes differs markedly from such carbon-based materials; the heat release rate for siloxanes (chain length > 15 Si-O units) does not increase significantly with an increase in external thermal radiant flux. Whereas carbon-based materials form products of incomplete combustion such as soot and carbonaceous char, siloxanes form a minimum of char but produce substantial amounts of solid amorphous silica as a major product of

combustion. It appears that this amorphous silica could play a significant role in mediating the burning behavior of siloxanes. A cooperative research and development agreement (CRADA) recently was signed between NIST and a private company to study why the above combustion behavior is observed for the combustion of siloxanes.

NIST RESEARCHERS LEAD EARTHQUAKE INVESTIGATION TO JAPAN

NIST researchers led a 12 member U.S. team investigating the damages resulting from a magnitude 7.8 earthquake, which struck northern Japan on July 12. The team consisted of structural/geotechnical, fire, and tsunami experts from NOAA, USGS, and the Earthquake Engineering Research Institute, who cooperated with researchers from counterpart agencies of the Japanese government, under the auspices of the 25-year-old U.S./Japan Panel on Wind and Seismic Effects. Direct structural damage to buildings was found to be light, with more widespread but still minor damage to roads, bridges, and rail lines, principally from soil displacements. A hotel located on the small island (Okushiri) hardest hit by the earthquake was buried by a landslide killing 10 people. A fire broke out on Okushiri eventually consuming half of the nearly 700 buildings in the village of Aonae. The most severe damage was the result of tsunami (tidal waves), which were determined by the team to have reached 31.5 m at one point on the island. Tsunami damaged nearly 1500 buildings. Total losses reported to date are 196 people dead (46 still missing) and property damage exceeding \$600 million.

SMOKE YIELD MEASUREMENTS MADE DURING INTERNATIONAL OFFSHORE EXPERIMENT

NIST was one of 25 agencies participating in experiments 40 km offshore east of St. John's, Newfoundland to evaluate in-situ burning of oil spills as a response technology. Environment Canada organized the effort as part of the process for gaining acceptance for the technology through measurement of the effects on the water and air. These experiments were the first opportunity to measure the effects of burning oil spills on the ocean. NIST scientists used instrumentation developed in ongoing studies of oil spill fires. The instruments, hung below a tethered helium-filled blimp, sampled the smoke plume from the fire to measure the smoke yield (fraction of fuel mass converted to

particulate) and the particulate size distribution. In this experiment, the blimp was positioned in the smoke plume using a small boat positioned immediately downwind of the burning oil slick, which was contained in a fire resistant boom. The measured smoke yield of 15 percent in two tests was consistent with previous measurements made in meso-scale experiments conducted by NIST in Mobile, AL. The St. Johns experiments involved 210 people, 20 vessels, three full-size helicopters, two remote-controlled helicopters, two fixed-wing aircraft, and the NIST blimp. Future experiments in U.S. waters are being discussed.

NEW PUBLICATION FOCUSES ON SECURITY ISSUES IN DATABASE LANGUAGE SQL

The Database Language SQL is a standard interface for accessing and manipulating relational databases. NIST Special Publication 800-8, Security Issues in the Database Language SQL, examines the security functionality that might be required of relational database management systems (DBMS) and compares these functions with the requirements and options of the SQL specifications. The document examines a variety of security policies that can be supported by SQL and discusses which types of functions are required by these security policies. The new publication will assist federal information technology managers in the selection of DBMSs with appropriate security functionality.

REPORT PRESENTS PROCEEDINGS OF WORKSHOP ON THE SECURITY OF NATIONAL COMPUTER NETWORKS

NISTIR 5232, Report of the NSF/NIST Workshop on NSFNET/NREN Security, July 6-7, 1992, describes the findings of a workshop co-sponsored by NIST and the National Science Foundation to address the need for improving the security of the National Science Foundation Network (NSFNET) and the National Research and Education Network (NREN). Workshop participants identified off-the-shelf security technology that could be implemented in the NSFNET, especially to control access to the supercomputers on the network.

NIST RELEASES SOFTWARE FOR ECONOMIC ANALYSIS

NIST has released version 4.0 of the Building Life-Cycle Cost (BLCC) computer program, the primary reference program for DOE's Federal Energy Management Program, and a related program,

ERATES, for calculating electricity costs using complex rate schedules. BLCC provides comprehensive economic analysis of proposed capital investments that are expected to reduce long-term operating costs of buildings or building systems, especially those related to energy conservation and renewable resources. BLCC calculates the life-cycle costs of alternative buildings or building systems and calculates net savings, adjusted internal rate of return, savings-to-investment ratio, and payback for any project alternative. Version 4.0 has a number of new features, including special provisions for evaluating DOD projects and projects requiring OMB Circular A-94 guidelines (revised 1992), a Quick Input module for simplified analyses, and SI units.

ERATES (Electricity RATES) generates time-of-use, block-rate, and demand-rate schedules and uses these to calculate monthly and annual electricity costs for buildings or building systems. The block-rate and demand-rate schedules generated by ERATES can be imported into BLCC 4.0 to calculate life-cycle electricity costs. These programs run under MS-DOS with no special hardware or software requirements. User's guides are available for both programs. A brochure with more information regarding these programs is available from NIST.

WORKSHOP FOR INDUSTRY

On Aug. 2-6, NIST held the workshop "Experiment Design for Scientists and Engineers" in Santa Clara, CA. NIST instructors presented the latest statistical experiment design techniques for improving product and process quality to engineers from industry. These engineers had research and development responsibilities and represented such industries as biomedical, computer, electronic, polymers, and electrical utilities.

The workshop covered statistical designs for studying a single parameter in the presence of many nuisance parameters, screening the important parameters from a large set of parameters, and determining optimum settings of the important parameters. Students run a series of hands-on experiments to reinforce the underlying design concepts. In addition, each student designs an experiment for a project they are working on at their own company. On the last afternoon of class, the students gave presentations on their proposed experiments and received valuable feedback from the instructors and fellow classmates.

As part of NIST's continuing effort to work more closely with industry, students were informed of opportunities to collaborate directly with NIST and were given survey forms requesting information on the type of technical problems their company faces and on how NIST can help.

The next workshop will be given in Orlando, Fla., in April 1994.

SECOND-GENERATION NIST THIN-FILM MULTIJUNCTION THERMAL CONVERTERS DEMONSTRATE PRACTICALITY OF APPROACH

NIST scientists and a scientist from a private company which has a CRADA with NIST, have completed successfully a "production" run of thin-film multijunction thermal converter chips and tested them to show that they have accuracies approaching those of the best conventional standards, with very low dc reversal errors and small ac-dc differences in the audio-frequency range. Earlier problems appear to have been solved through the introduction of new chip designs and incorporation of new fabrication procedures. This achievement demonstrates the practicality of the approach: the yield of good chips from a wafer was very high, and the yield of working mounted chips only slightly less.

These thin-film converters result from applying modern semiconductor processing technology to the fabrication of carefully patterned heater/thermocouple structures and represent a substantive improvement over the electrical performance of the present standard wire thermal converters. It is estimated that they can be produced with a cost range of \$100 to \$200 each, depending on the electrical parameters, as opposed to a corresponding range of \$150 to \$2,500 for present standards.

The electronic instrumentation industry is interested in this development, which not only will provide a new generation of improved standards, but also is likely to make practical the incorporation of film converters in instruments such as precision multimeters, with the result that their ac performance should approach their dc performance. At present there are no intrinsic ac standards. For example, all ac voltage measurements derive from standards based on either digital synthesis or thermal voltage conversion. (NIST is pursuing both approaches.) At ultimate accuracy levels, root-mean-square measurements of ac signals—either current or voltage—are made in terms of dc stan-

dards using thermal transfer techniques where resistive heating of a properly designed standard is independent of frequency and can be detected precisely. Patents for the thin-film converter have been applied for; an associated patent for integrated micropotentiometers (which are similar structures) has been allowed.

DEVICE SIMULATIONS MADE POSSIBLE BY NIST MODELS SPEED UTILIZATION OF NEW POWER SEMICONDUCTOR DEVICES

A software developer and a major semiconductor manufacturer have signed a \$3 million, 3 year agreement that will result in analog simulation models of a new device being available before devices are actually fabricated. This heralds a new approach to the design of semiconductor power devices and the systems in which they are incorporated and was made possible by the work of a NIST scientist.

Intelligent exploitation of the capabilities offered by a new semiconductor device in a practical circuit design requires that a model of the electrical behavior of the device exist. Before the NIST work, models customarily were not developed until long after the introduction of a new device. Furthermore, models did not take into account the thermal behavior of the device, a vital aspect of device performance. A device that has failed from overheating, no matter how good its electrical design and performance, is useless. Working in collaboration with the software company, the NIST scientist developed an electro-thermal model and applied it to his insulated-gate bipolar transistor (IGBT) model which the software company then incorporated into its commercial circuit simulator. As a result of the existence of the NIST models, the manufacturer was able last year to introduce a new IGBT ignition coil driver concurrently with the release by the software company of a model for the device in the simulator. The software company and the manufacturer now plan to carry the process one step further. When a customer submits a requirement for a power device, they will work together to develop a model for the device even before it has been manufactured. The customer then can carry out a preliminary design of the intended circuit based on the model and recommend changes in the design of the device to optimize it for the intended application.

COMMERCIAL SEMICONDUCTOR TEST EQUIPMENT BASED ON STANDARDS RESULTING FROM NIST WORK

Three private companies are now marketing hardware/software systems that depend on measurement procedures incorporated in formally adopted test-method standards based on research conducted at NIST. The availability of the procedures also results from NIST participation in the standardization process in both the American Society for Testing and Materials and the Electronic Industries Association/Joint Electron Device Engineering Council. Two important measurements relating to integrated-circuit reliability are electromigration characterization and time-dependent dielectric breakdown (TDDB). Electromigration is a failure mechanism which can occur as a result of high current densities in the thin-film metallization lines on an integrated-circuit microelectronic chip. Time-dependent dielectric breakdown measurements provide a means to characterize the reliability of the gate dielectric of devices fabricated in one of the most important semiconductor technologies, MOS (metal-oxide-semiconductor, used for example for semiconductor memory). All three companies market systems to evaluate both electromigration and TDDB.

NIST DEVELOPS ELECTRONIC POLICE RADAR CALIBRATOR

In order to support the possible use of cross-the-road radar for speed enforcement in the United States, the Office of Law Enforcement Standards has sponsored the development by NIST of an all-electronic Doppler radar calibrator. The calibrator operates at 24.1 GHz (K Band) and provides a radar signature that simulates accurately several types of vehicles passing through a radar beam aimed across the road. The simulated signature includes the effect of direction of vehicle travel. The capability of faithfully imitating the radar characteristics of a real vehicle is essential for interfacing with the sophisticated signal-processing circuitry in commercially available cross-the-road radar systems and for assessing the accuracy of speed measurement. The calibrator also can be used with conventional down-the-road radar speed-measuring systems that have been used widely by U.S. law enforcement agencies for some years. Since the NIST calibrator depends solely on

electronics, without mechanical moving parts, it is expected to be a low-cost device in large-scale production, and the potential market is seen to be large. The principles underlying the calibrator also could be applied to calibrate a laser-based speed-measuring system.

MODEL DEVELOPED TO EVALUATE SHIELDING EFFECTIVENESS OF AIRCRAFT SKIN STRUCTURE

NIST scientists have developed a theoretical model that is intended to help aircraft manufacturers and the Federal Aviation Administration evaluate how well an aircraft skin and related structure provides electromagnetic shielding for instruments and components within the aircraft. The model takes into account both pulsed and continuous sources of electromagnetic energy incident on the skin. Serious safety concerns have been raised with respect to the effects of high-level sources such as high-power radars and even broadcast stations on aircraft electronics. The introduction of composite primary aircraft structure and composite skins, coupled with the trend to increasing reliance on electronics for direct control of engines (full-authority digital engine control) and control surfaces (fly-by-wire) exacerbates the situation. Concerns still apply to the "conventional" electronic functions, including radar, communications, navigation, monitoring of aircraft functions, and cockpit instrumentation. At least one modern aircraft has crashed as a result of electromagnetic interference. The regulatory response has been to require that electronic equipment authorized for installation in an aircraft (and the aircraft itself) withstand fields as high as 200 V/m, which takes little or no account of any mitigation of the fields inside the aircraft as a result of aircraft structure.

If the model is successful when applied to real-world conditions, it will provide a basis for determining the levels of fields that electronic equipment for aircraft must withstand without degradation in performance. Testing to excessively high field levels is very costly. To date, NIST has carried out laboratory experiments to test the predictions of the theory, with the result that over the frequency range 1 GHz to 18 GHz, the agreement is good and the theory is considered verified. NIST now plans to test how well the model predicts the shielding effectiveness of the skin structure of an actual aircraft.

RESULTS OF INDO-U.S. COLLABORATIVE PROGRAM ON INTEGRATED OPTICS DISSEMINATED THROUGH WORKSHOP

NIST recently co-sponsored and hosted a Workshop on Computer Modeling of Optical Waveguide Components to introduce selected results of the joint Indo-U.S. Collaborative Program on Integrated Optics to the U.S. technical community. Some 20 representatives from industry, academia, and government participated in the workshop, which incorporated a hands-on laboratory that allowed them to experiment with working computer code implementing four analysis tools developed over the last 5 years through the program. These tools and salient points about each are as follows: (1) the matrix method of analysis, which includes a convenient and highly accurate method of analyzing leaky structures; (2) Galerkin's method for arbitrary geometries, which provides a convenient and highly accurate prediction of waveguide characteristics, including absorption loss when the complex refractive index is known; (3) a perturbation method, useful in analyzing rectangular core waveguides and especially useful in treating odd shapes such as a rib or a channel waveguide; and (4) the use of modified Airy functions in a WKB-like analysis and the WKB method itself. (WKB refers to the initials of three independent workers—Wentzel, Kramers, and Brillouin—who first used the approximation procedure to solve the Schroedinger wave equation in one dimension.) Lecture material and examples on this last subject were taken from an NIST Monograph.

NIST WORKS WITH MACHINE TOOL BUILDER TO IMPROVE HIGH-SPEED LINEAR MOTION PERFORMANCE

Two NIST scientists in conjunction with the Massachusetts Institute of Technology and a private company, have developed a high-speed linear motion system using porous graphite air-bearing pads and replication assembly methods. An epoxy replicant was used to reduce the need for expensive precision components by potting the air-bearing pads into position. A "zero-clearance" assembly methodology was developed to simplify construction and minimize bearing gap. This yields the maximum bearing stiffness of 13 MN/m (75,000 lb/in) compared to 4.9 MN/m (28,000 lb/in) for a typical mechanical system. The system showed superior damping properties along with significant improvements in straightness of motion, bearing stiffness, and reducing sliding friction. The use of this system

by the machine tool builder will result in a significant increase in reliability and reduction in manufacturing cost.

TOPOGRAPHY OF MULTILAYER X-RAY MIRROR

High-efficiency, totally reflective x-ray mirrors are critically dependent on the surface roughness of the mirrors. x-ray mirrors are utilized in such state-of-the-art technology applications as x-ray microscopes and telescopes, as well as soft x-ray projection lithography. Soft x-ray projection lithography might replace optical lithography for the production of integrated circuits with feature sizes below 0.2 μm . For a high-quality, near diffraction limited x-ray mirror, it is necessary to measure surface characteristics of the mirror with precision in the 0.1 nm range over spatial wavelengths from 0.1 nm to the full aperture of the mirror (about 0.1 m). NIST staff are developing measurement and calibration approaches that will span the requisite eight orders of magnitude in spatial wavelength.

The surface roughness of a multilayer mirror has recently been measured over more than four orders of magnitude of spatial wavelength using a long-range scanning tunneling microscope (STM) developed at NIST. Measurements were made over fields of view varying from $1\ \mu\text{m} \times 1\ \mu\text{m}$ to $500\ \mu\text{m} \times 500\ \mu\text{m}$. The lateral and vertical displacement transducers were calibrated at each field of view. The data were used to compute the mirror's surface power spectral density (PSD) function over the spatial wavelengths from 10 nm to 320 μm . The resulting PSD curves, the first to bridge short-wavelength measurements made with traditional STMs and longer wavelength measurements made with phase measuring interferometric microscopes, agree with published data taken at the lower and upper regions of this bandwidth.

DEFECTS IDENTIFIED IN PROTOTYPE ADVANCED MEMORY CHIP

Data from NIST have revealed an unexpected form of defect in multilayer magnetic thin films used for magneto-resistive random access memory (MRAM) chips. In a collaborative effort between NIST and a private company, MRAM films were investigated by scanning tunneling microscopy and by depth-profile analysis with x-ray photoelectron spectroscopy. A typical MRAM film is a complex multilayer structure containing various alloys and other materials such as in the prototype devices Ta/CoFe/CuAg/CoFe/ NiFeCo/SiN/silicon wafer.

The results indicated that these multilayer films were not the flat, well-ordered, layer-by-layer structures that had been envisioned. Instead, the films were highly granular with channels or crevices between grains. It was also found that some of the material from the upper layers of the multilayer stack was present in the deepest layers, indicating that the crevices allowed leakage of material downwards. The evidence for this leakage of material was verified by a NIST scientist using secondary ion mass spectrometry. Research is now under way to develop improved thin-film manufacturing techniques that will suppress the granularity and the associated channels or crevices.

FROBISHER IRON BLOOM STUDIED TO ESTABLISH PROVENANCE

Scientists at NIST have collaborated with a Smithsonian Institution summer intern in the study of a unique sample from the Smithsonian collection. The sample, labeled the Smithsonian Bloom, was donated to the Smithsonian in 1863 by Charles Hall who had explored the base camp (occupied 300 years earlier) of the 16th century English explorer Martin Frobisher, on the Kodlunarn Island in the Canadian Arctic. The sample was reputed to be connected to Frobisher's activities in mining and ironwork on this island. However, recent interpretations of the objects collected from the Frobisher site have identified a possible early Norse origin for some of these materials and an origin in northern Russia for others.

The goal of the project was to study the possibility that the lead isotopic signature for the artifact could be used in specifying its provenance. The work derives from a long-standing collaboration between the Smithsonian Institution and NIST in this field. Lead isotopic compositions vary considerably in nature, and these isotopic compositions can be measured very precisely by thermal ionization mass spectrometry. The analytical results showed useful levels of lead in the Smithsonian Bloom (2.5 parts per million) and the isotopic results were very different from catalogued lead compositions expected for samples of ore from England.

The information provided as a result of this study shows that the identification of the lead in the specimen is analytically viable and provides a means to relate the less than 20 existing blooms found in the arctic to one another in terms of provenance.

TWO NEW NIST PRECISION MEASUREMENT GRANTS AWARDED FOR FY 94

Two new \$50,000 NIST Precision Measurement Grants have been awarded for fiscal year 1994. The recipients, Mark Kasevich of Stanford University, and Ronald Walsworth of the Smithsonian Astrophysical Observatory, Harvard-Smithsonian Center for Astrophysics, were selected from an initial group of 22 candidates. NIST sponsors these grants (administered by the Fundamental Constants Data Center) to promote fundamental research in measurement science in U.S. colleges and universities and to foster contacts between NIST scientists and researchers in the academic community actively engaged in such work.

The aim of Kasevich's project, "Development of an Atom Interferometer Gyroscope for Tests of General Relativity," is to develop significantly improved atom interferometers based on slowed and cooled cesium atomic beams and to use the interferometers to construct a high-precision rotation sensor. The motivation for the work is the possibility of achieving levels of sensitivity high enough to observe general relativistic effects. The goal for the 3 year time period of the NIST grant is to demonstrate a sensitivity to rotations of better than 10^{-11} (rad/s)/Hz^{1/2}.

Walsworth's project, "Development of a Dual Noble Gas Laser for Use in a Test of Time Reversal Invariance," involves building a newly conceived device, a dual noble-gas maser consisting of cohabitating ensembles of ³He and ¹²⁹Xe atoms, each performing an active, steady-state maser oscillation. The device will be used for a 10-fold improvement test of time reversal invariance by searching for a permanent electric dipole moment (PEDM) of the ¹²⁹Xe atom. The ³He maser will serve as a precision magnetometer to control the system's magnetic field, while the ¹²⁹Xe is used to search for a PEDM.

COUNTING SINGLE ATOMIC LAYERS DURING THE GROWTH OF THIN FILMS

Molecular beam epitaxy (MBE) is a method of materials growth used to produce artificial structures with abrupt interfaces at the single atomic layer level. MBE has had great success in producing complex multilayer semiconductor structures and recently has been extended to produce multilayer metallic structures, most notably in systems exhibiting novel magnetic properties. To obtain single-layer precision, the MBE technique requires the counting of the individual atomic layers during

growth. The most common technique to count these layers has relied on reflection-high-energy-electron-diffraction (RHEED) measurements, in which the reflected electron beam intensity is monitored in real time. One typically observes cyclic oscillations in the RHEED intensity, which are interpreted as corresponding to one atomic layer per cycle. To date, little has been known about the actual physical structure corresponding to the RHEED intensity behavior, or about the exact cause of the intensity oscillation themselves. Some of the questions plaguing scientists are: Is one oscillation really one layer? Do oscillations mean the material is growing one layer at a time?

Recently, scientists at NIST, using scanning tunneling microscopy, have obtained some of the first atomic real space images of the growing surfaces of iron crystals that correspond to various RHEED intensity oscillations. These experiments, which were reported in the June 7, 1993 issue of *Physical Review Letters*, found that one oscillation does correspond to one atomic layer, but only in special circumstances do oscillations imply that material is growing one layer at a time. These measurements show in detail how the mechanisms of surface diffusion, nucleation, and growth affect the quality of the resulting thin film. As a result of the NIST work, the RHEED measurements that are used widely by MBE researchers in the magnetic and semiconductor industries to monitor thin-film growth now can be used more knowledgeably to optimize growth processes in order to control film quality.

NIST ASSISTS MANUFACTURERS OF COLOR DISPLAYS

Recent measurements in the NIST Facility for Automated Spectroradiometric Calibrations (FASCAL) aided the U.S. color display technology industry. A manufacturer of single phosphor color monitors requested that three color displays be measured for spectral distribution. Based on the measurements, NIST also computed the chromaticity coordinates of the displays.

Basic calibrations of color tubes are performed at the manufacturer using spectroradiometers, but the methods of calibration are not standardized. The measurements performed in FASCAL will serve as the basis for the corrections of the readings from the manufacturer's spectroradiometers. The manufacturer is also a member of the Electronic Industries Association committee JT-31. This committee will set up a round-robin intercom-

parison of color tubes from several manufacturers of TVs. Again the measurements performed in FASCAL will serve as the base for the intercomparison. NIST is looking at this special test to be the first of many similar color tests, particularly since the manufacturers lack the facilities to perform these unique measurements.

POWERFUL OPTICALLY PUMPED FAR-INFRARED LASER LINE DISCOVERED

A 124 μm methanol laser line that is more than four times stronger than the previous "strongest" line (a 119 μm line also in methanol) was just discovered at NIST. The experiments were performed by guest researchers and a NIST scientist. The discovery is of special interest to plasma physicists who use far-infrared radiation to measure electron densities in plasmas. It is also of interest to spectroscopists because spectroscopic sensitivity is especially high at infrared frequencies.

The new line was found using other newly discovered (at NIST) lines of the 9 μm hot bands in the NIST ribbed-tube CO_2 laser. The radiation from one of these new CO_2 lines was used to pump methanol to produce the 124 μm radiation. Twenty-five additional far-infrared lines in methanol also were discovered using the new CO_2 lines.

FIRST INTERNATIONAL COMPARISON OF PHASE-NOISE-MEASUREMENT SYSTEMS

The first international comparisons of phase-noise measurements between the United States, France, and Switzerland have been completed successfully. NIST-developed systems were demonstrated at the Fifth European Frequency and Time Forum in Neuchâtel, Switzerland by a NIST scientist. He subsequently took these systems to laboratories in France and Switzerland for comparisons with their measurement systems. Phase noise is rising in importance in the specification of equipment for telecommunications, radar, and aerospace electronics.

Comparisons were made at carrier frequencies of 5 MHz, 10 MHz, and 100 MHz at Fourier frequencies extending up to 10 percent away from the carrier. Good agreement was found at 5 MHz and 10 MHz, but some errors on the order of 5 dB were found at 100 MHz. Because the NIST measurement method provides a complete internal capability for evaluating errors, it was easy enough to trace the problem to the commercial systems used in these European labs.

**NIST ESTABLISHES TWO-WAY,
TIME-COORDINATION LINK TO EUROPE**

Three NIST scientists have completed construction and preliminary testing of a satellite Earth station that will provide for extremely accurate time and frequency comparisons between NIST and key national laboratories in Europe. The method promises an order of magnitude improvement in time-transfer accuracy, thereby providing better international time coordination. This is important in an era where atomic clock stability and accuracy is advancing rapidly. Improvements in international timekeeping should prove useful in international activities such as telecommunications and navigation.

The new NIST station can be used with both domestic and international communication satellites, and is expected to achieve a time comparison accuracy of 1 ns or better and stability of comparison in the 100 ps regime. There is substantial signal delay between the Earth station and the satellite, but proper handling of data exchanges broadcast through the satellite link in both directions results in a nearly perfect cancellation of the path-delay errors.

**COLD NEUTRON REFLECTOMETER
COMMISSIONED**

Neutron reflectivity has emerged as a very powerful tool for the investigation of surface behavior of polymers, magnetic thin films, surfactant films, and other technologically relevant thin-film materials. NIST in cooperation with a private company and the University of Minnesota has built a new state-of-the-art neutron reflectometer in the neutron guide hall at the Cold Neutron Research Facility (CNRF) at NIST. The new reflectometer—which represents the state-of-the-art—gives NIST scientists, along with industrial and university collaborators, the opportunity to play an even greater role in technologically important research on surfaces and interfaces.

The instrument operates with the sample in the horizontal geometry allowing reflectivity measurements from the liquid-air interfaces. The reflectometer can be operated with extremely high resolution at small wavevector transfers and is also capable of routinely measuring reflectivities down to and below the 10^{-6} level. Very low background

levels in the CNRF guide hall make it possible to use a linear-position-sensitive detector, which allows specular and off-specular reflection measurements simultaneously.

The new instrument has been fully operational since May 1993. A substantial improvement (by a factor of about 4) in the instrument is expected with the installation of new liquid hydrogen cold source in 1994. Demand for neutron reflectivity instrumentation time by U.S. industry and universities is rising rapidly, and the instrument is already oversubscribed by a large factor.

**SOFTWARE EVALUATION AGREEMENT
SIGNED**

A private company and NIST signed an agreement to evaluate software developed at NIST that models processing of polymer matrix composites by resin transfer molding (RTM). The private company is interested in applying RTM processing technology to the manufacture of structural aerospace components. The agreement with the private company complements existing separate agreements between NIST and the Automotive Composites Consortium and two other private companies. All industrial partners seek to lower manufacturing costs while improving the reliability of large structural parts made from lightweight polymer composites.

RTM involves injection of liquid prepolymer into a mold that contains the reinforcement fibers (preform) arranged to meet design criteria for strength and stiffness. Mold design and optimal processing parameters depend on the resistance of the preform to resin flow. Availability of credible models that simulate flow of resin through the fiber preform are critical to implementation of RTM. Scientists at NIST are developing such software as well as measurement methods for input permeability data but need cooperation with industry so that computer programs can be tested with actual part manufacture. Under the agreement, NIST will provide one of the companies with the software and instruct its personnel on the methods for making permeability measurements. The company will provide NIST with results of the simulations and comparisons to actual processing data, which will be useful in refinement of the software.

COMPANY SIGNS CRADA INVESTIGATING FRACTURE IN ENGINEERING POLYMERS

A private company signed a cooperative research and development agreement to perform research with NIST on the incubation process for fracture of engineering thermoplastics. Lifetime and durability are important aspects of engineering material performance. As the use of polymers and polymer-based composites in structural applications expands, the understanding of the physics and chemistry that determine their reliability in use becomes increasingly important. Scientists from the private company will collaborate with NIST staff in studies using small-angle x-ray scattering and positron annihilation lifetime spectroscopy. The studies seek to establish the nanoscale mechanisms that result in incubation of fracture in engineering thermoplastics. Both techniques are sensitive to changes in the local environment, and it is anticipated that the way in which this evolves during mechanical deformation will provide insight into the molecular mechanisms that lead to deterioration of material performance.

NIST AND NCMS SIGN COOPERATIVE AGREEMENT TO DEVELOP LEAD-FREE SOLDERS

A new cooperative research program has been established between the National Center for Manufacturing Sciences (NCMS) and NIST to identify environmentally safe alternatives for lead-based solder alloys currently used for electrical/electronic interconnections. In response to congressional concerns on the use of lead in manufacturing, NCMS has formed a consortium for the design and evaluation of possible candidate lead-free solder alloys that meet the manufacturing and performance requirements currently met by lead-based solders. NIST has joined with Rensselaer Polytechnic Institute, Sandia National Laboratories, the Electronic Manufacturing Production Facility, and the NCMS industrial partners, in establishing the guidelines for development of these new solder alloys.

NEW TECHNIQUES USED FOR SITING SMOKE DETECTORS

NIST has applied computational fluid dynamics modeling to the analysis of smoke flow under complex ceilings. The technique provides a more detailed look than can be achieved through much

more costly full-scale experiments. This new technique was used to examine the current siting guidelines for fire detectors and sprinklers and identified several areas where improved response could be achieved at lower cost. The technique has been verified against real-scale experimental data taken 10 years ago.

Both the fire detection and sprinkler industries are interested in the potential for this new methodology to address technical questions that have been extant for many years, in particular to reduce costs while improving life safety.

NEW FIRE SUPPRESSANTS RECOMMENDED FOR IN-FLIGHT PROTECTION OF AIRCRAFT

A NIST multilaboratory research team has identified a number of chemical compounds that can be used to replace halon 1301 (CF_3Br) for extinguishing aircraft fires while in flight. This chemical currently provides protection against fires in jet engine nacelles and other unoccupied spaces in nearly all commercial and military aircraft. Its manufacture will cease at the end of 1993 due to halon damage to stratospheric ozone. This makes the search for alternative suppressants urgent. As a result, the government agencies and the Federal Aviation Administration, through Wright-Patterson Air Force Base, have requested NIST to identify candidates that can be ready for use within 2 years.

Because of the unusual nature of the fires and the strict demands on the fire suppressant, the NIST team developed an array of new apparatus and procedures to understand the behavior of more than a dozen compounds in different aspects of the fire suppression process. Studies include thermodynamics of the chemicals in mixtures with nitrogen, dynamics of agent release, conditions leading to flame extinction, and byproducts of the suppression process. In addition, experiments were conducted to predict the long-term stability of the chemicals during storage and their compatibility with the metals and polymers used in storage containers. Environmental issues and the potential for human exposure also were investigated. The recommended chemicals, which are gaseous (at ambient conditions) halocarbons and halohydrocarbons, are to be tested in full-scale fixtures simulating portions of aircraft at Wright-Patterson Air Force Base. A final report documenting the NIST research and the rationale for the recommendations will be prepared by January 1994.

BACnet PRODUCES POSITIVE REACTION FROM INDUSTRY

NIST researchers have spent the last 5 years, in concert with industry, developing an open protocol for communication between computerized control systems for heating, ventilating, and air conditioning in buildings. While the BACnet protocol has not yet been released by the American Society of Heating, Refrigerating, and Air-Conditioning Engineers' (ASHRAE) Standards Project Committee 135 in its final version, it is in a form today that can be adopted by any manufacturer who chooses to write to it. A major air-conditioning company has just announced that they have chosen to implement BACnet at this time because industry use of an open standard is so important to building owners. Strong support from the company and others in the building automation industry is required to help deliver this needed standard to collective customers. All customers who join the company in implementing this early version of BACnet will be upgraded to the final version upon request and at no charge when it is accepted by ASHRAE.

COMPUTER SECURITY CONFERENCE ATTRACTS LARGE TURNOUT

On Sept. 20–23, NIST and the National Security Agency's National Computer Security Center (NCSC) co-sponsored the 16th National Computer Security Conference in Baltimore, MD. The theme of the conference was "Information Systems Security: User Choices." The conference attracted about 1,800 attendees from government and industry.

Of special interest was the conference session on the draft Federal Criteria for Information Technology Security and efforts toward international harmonization of criteria and evaluations for trusted products. Other sessions featured tutorials on viruses, trusted systems, networks, and system integration; research papers and recent technological developments by leading technical experts in information security; management topics such as contingency planning, risk management, and electronic crime; and recent accomplishments and lessons learned in the development and operation of systems and networks that provide security features. The closing plenary focused on "Information System Security Strategies for the Future."

RASTER GRAPHICS VALIDATION TEST SERVICE INITIATED

On Oct. 1, NIST initiated the NIST Raster Graphics Validation Test Service for a 1-year trial period. Conducted on a cost-reimbursable basis, the service tests raster files for conformance to Federal Information Processing Standard (FIPS) 150, Facsimile Coding Schemes and Coding Control Functions for Group 4 Facsimile Apparatus, and the DOD Military Specification MIL-R-28002, Requirements for Raster Graphics Representation in Binary Format. The test service analyzes implementations of ITU-T (formerly CCITT) Recommendation T.6 (Group 4) and Continuous Acquisition and Life-Cycle Support (CALS) Type I data files for conformance to the T.6 (Group 4) compression algorithm. A test report is produced, which summarizes the tests performed and describes any conformance deficiencies. Certificates issued for successful validations and registered test reports will be listed in the Validated Products List, which NIST updates and publishes quarterly. An information pack provides details of the test service and procedures for requesting validations.

NEW PUBLICATION FOCUSES ON INFORMATION RETRIEVAL TECHNIQUES

Information retrieval is the process of locating the data that best answer a user's query. Despite the growth of wide-area networks and the amount of potentially available information, many archives and information bases are not accessible to users who do not know site names and access methods. NISTIR 5243, *Towards Flexible Distributed Information Retrieval*, discusses a distributed information system being developed to make the best use of networked resources and to achieve flexible integration of existing information bases.

SECURITY OF ELECTRONIC DOCUMENTS SUBJECT OF NIST REPORT

NISTIR 5247, *Workshop on Security Procedures for the Interchange of Electronic Documents: Selected Papers and Results*, presents the findings of a workshop held at NIST Nov. 12–13, 1992. About 40 participants from government and industry attended the meeting. Co-sponsored by NIST and the Office of Management and Budget, the workshop focused on the need to devise rules for the use of security procedures in the electronic transmission of documents between organizations.

**DIGITAL SIGNATURE CERTIFICATE
MANAGEMENT WORKSHOP
RESULTS PUBLISHED**

NISTIR 5234, Report of the NIST Workshop on Digital Signature Certificate Management, Dec. 10–11, 1992, summarizes the presentations and discussions of about 40 invited participants representing the federal government, industry, standards organizations, and international interests. The workshop reviewed existing and required technologies for digital signature certification authorities and developed recommendations for certificate contents, formats, generation, distribution, and storage.

**NIST CRITICAL STABILITY CONSTANTS OF
METAL COMPLEXES DATABASE RELEASED**

Standard Reference Database 46 provides comprehensive coverage of interactions for aqueous systems of organic and inorganic ligands with protons and various metal ions. Based on the six-volume Critical Stability Constants, the data have been thoroughly evaluated with correction of errors and addition of new material. Protonation constants under specified conditions of temperature and ionic strength, heats of protonation, entropies of protonation, stability constants and related equilibrium constants, thermodynamic constants, and a complete bibliography are included for nearly 4000 ligands. For an additional 1000 ligands, the metal ions studied and bibliographic citations are included. The database is available from the Standard Reference Data Program.

**NIST FIRST-TIME MEASUREMENTS HELP
MANUFACTURER DESIGN IMPROVED
PORTABLE X-RAY UNITS**

The production rates of gaseous byproducts that result from decomposition and oxidation of compressed sulfur hexafluoride (SF_6) during exposure to x rays were measured for the first time by NIST scientists as part of a cooperative research and development agreement with a private company. An outcome of the work is that the company, a manufacturer of portable x-ray units that use SF_6 as an insulating gas, will be able to design more reliable and longer-lived instruments. The company approached NIST because it had become interested in evaluating any possible effects of x rays on the SF_6 gas, including the formation of corrosive byproducts that could be harmful to the operation of the x-ray units.

In the collaborative experiments, the company supplied and operated the x-ray unit, and NIST scientists carried out analyses of decomposed SF_6 using the gas chromatograph-mass spectrometer method they had developed previously. They found that the SF_6 oxidation byproducts from the x-ray unit were the same as those formed by corona discharge in SF_6 , including the very toxic gas S_2F_{10} and oxyfluorides of sulfur such as SOF_2 , SO_2F_2 , and SOF_4 . The formation of these species is known to be accompanied by the formation of such highly corrosive byproducts as HF and free fluorine. The experimental results from this work are to be presented at the International Symposium on Gaseous Dielectrics next year.

**LOCATING IMAGES PROJECTED BY
INTEGRATED-CIRCUIT MANUFACTURING
TOOLS TO NANOMETER-LEVEL ACCURACY**

NIST researchers have devised a method to measure the relative location of projected images of features on a test mask when the images have been projected onto a "calibrated" substrate. This development responds to industry's needs for the rapid determination at nanometer scale of the placement of images of fiducial features on a mask as projected by a lithography tool on a substrate.

One specific application is low-cost evaluation of image placement by x-ray lithography masks. NIST researchers have shown that the image locations can be determined with an accuracy of 10 nm or better; a patent on the method has been applied for.

In one implementation, partially formed test structures are first fabricated on a substrate. Each structure serves as a local ruler, and the structure positions and scales are calibrated by means of NIST's linear-scale interferometry system. Next, images of fiducial marks on a mask are projected onto the substrate. These images, known as pointers, overlay the partially formed test structure local rulers to form completed test structures. The locations of the pointers within the respective test structures are then determined electrically. These measurements, combined with the calibration of the rulers, provide the location of the pointers on the substrate. The team is now developing a two-dimensional implementation intended to provide a low-cost metrology directly traceable to a two-dimensional metric of atomic spacings of single-crystal surfaces determined through molecular measuring machine.

NIST TRANSMISSION LINE MEASUREMENT METHOD DEMONSTRATED FOR HIGH-PERMITTIVITY MATERIALS

NIST scientists have developed and evaluated a method capable of measuring permittivity for materials having high permittivities; previous methods were not capable of these measurements. The method employs a coaxial air line system having the relatively large diameter of 77 mm. The principal advantage of the method is that the relative magnitude of the error resulting from the presence of an unavoidable small air gap between inner conductor and specimen material is reduced greatly compared to the air-gap errors present in the conventionally used line, which is 7 mm in diameter. Models have been developed and are used as a basis for compensating for the air gap, but the resulting correction is not perfect. Using the new method, the NIST team was able to characterize a high-permittivity commercial ceramic having a nominal value of the real part of the complex permittivity $\epsilon' = 270$ over the frequency range 50 MHz to 1000 MHz. The team's measured value was $\epsilon' = 275$, after air-gap correction. Meaningful measurements on this material using the conventional 7 mm diameter coaxial line would have been very difficult, even if possible, with large errors. Work is currently under way to extend the method to the low-frequency range of 0.1 MHz to 50 MHz.

NIST DEMONSTRATES CAPABILITY FOR HIGH-FREQUENCY SURFACE RESISTIVITY MEASUREMENTS OF HIGH-TEMPERATURE-SUPERCONDUCTOR FILMS

NIST has carried out a preliminary measurement of the microwave surface resistivity of high-temperature-superconductor films in collaboration with a researcher from the Warsaw University of Technology. Microwave surface resistivity is a key parameter for determining if a given high-temperature-superconductor material has potential for high-frequency applications. NIST scientists performed the measurements on yttrium-barium-copper oxide (YBCO) films grown at NIST. The measurements were made with a sapphire-rod resonator developed for NIST by the Polish researcher.

The resulting value for the microwave resistivity of 6 m Ω to 8 m Ω per square at 77 K compares well with values reported by others on YBCO films at the same frequency. The resonator rod is a small

right circular cylinder that is excited at 25 GHz by microwave energy coupled into the resonator cavity through loops whose position can be moved to adjust the coupling. In operation, specimens of the material to be measured are brought into contact with the ends of the rod. For these first measurements, the cavity structure was submerged in a simple liquid-nitrogen bath; for planned future measurements on other YBCO specimens and on other high-temperature-superconductor films, a cryostat will be constructed to provide stable temperature control over the range 20 K to 120 K.

NEW METHOD TO DETECT HIGHLY EXCITED ATOMIC STATES

The creation and detection of very highly excited atomic states are important for precision spectroscopists and those studying the behavior of atoms in both strong and weak fields. A NIST scientist and a graduate student have demonstrated a new detection technique that uses an optical "dump" pulse from a visible dye laser to stimulate emission from the Rydberg state of interest to a lower valence level. Fluorescence from this lower level is then detected. This new technique has many advantages compared with earlier methods. It permits the selective interrogation of individual Rydberg states, and the ease of using optical light pulses. The Rydberg state being stimulated to the lower level is easily identified since the stimulated emission process is governed by the normal atomic selection rules and the wavelengths are well-known. The highest principal quantum number that can be unambiguously observed is limited by the "dump" laser's linewidth, not by the wavelength or energy resolution of the detection system. And while direct ionization of the Rydberg state occurs, this pathway is relatively limited in the new technique because of the strength of the stimulated emission transition. This technique has been first tested on Ca atom Rydberg states. Pulsed dye lasers were used to excite a series of 1D states with principal quantum numbers $n = 11$ to 38 by a two-step process. States with $n = 12$ and 25–38 were detected with a third pulsed dye laser tuned to the "dump" transition $4snd\ ^1D_2 \rightarrow 4s5p\ ^1P_1$. Fluorescence from the 1P state at 671 nm was observed through a monochromator. Work is in progress to use this new detection scheme for state-to-state collision studies of Rydberg states.

NIST RESEARCHERS DOCUMENT THERMAL AGING OF FOAM INSULATION

Two NIST scientists have completed a 1-year study of rigid polyisocyanurate foam thermal insulation co-blown with CCl_3F and CO_2 , documenting the decrease in insulating capability and change in other important properties due to exposure to elevated temperature and humidity. Foam insulation has been used extensively throughout the building industry. However, recent changes in the laws protecting stratospheric ozone have forced manufacturers to develop new technology to minimize and eventually eliminate chlorofluorocarbons from their foam products. The "long-term" effectiveness of these new products is not known.

In this study, the researchers exposed samples to five different combinations of elevated temperature and/or humidity and measured changes in thermal conductivity, mass, volume, and density about every 50 days over the year. After 1 yr, the thermal conductivity increased about 40 percent and density decreased about 5 percent. They determined three regimes of aging by correlating the changes in thermal conductivity with changes in density. Results were compared to another foam blown with only CCl_3F and aged under similar exposures with good agreement. This technique could be used in an accelerated aging test to characterize a production lot of foam over its lifetime. By additionally using Fourier transform infrared spectroscopy and measurements under a scanning electron microscope, they determined the mechanisms of change occurring within the foam.

ISDN FEDERAL INFORMATION PROCESSING STANDARD (FIPS) APPROVED

The Secretary of Commerce recently approved FIPS 182, Integrated Services Digital Network (ISDN), for federal agency use. Effective April 15, 1994, the standard defines the generic protocols necessary to establish transparent ISDN connections among government networks and between government and conformant common carrier networks. Providing a minimal set of bearer services, FIPS 182 is based on national and international standards and on implementation agreements developed by the NIUF.

NEW REPORT FOCUSES ON EMERGING FEATURES FOR GEOGRAPHIC INFORMATION SYSTEMS (GIS) APPLICATIONS IN DATABASE LANGUAGE STRUCTURED QUERY LANGUAGE (SQL)

NISTIR 5258, Towards SQL Database Language Extensions for Geographic Information Systems, presents a collection of papers by the GIS/SQL Working Group of NIST's GIS Standards Laboratory. The goal of the laboratory is to facilitate joint efforts in adapting information technology standards for use by the GIS community.

A GIS extension to SQL will benefit users by providing a common database language to directly perform many of the functions and operations they require. For the GIS vendor software community, the integration of SQL into GIS software will result in less effort and maintenance by vendors. NIST will continue to participate in the development of a GIS extension to SQL as the work progresses in the national and international voluntary standards arenas.

NIST MAKES POSIX CONFORMANCE TEST SUITE AVAILABLE ELECTRONICALLY

On Oct. 15, FIPS 151-2, Portable Operating System for Computing Environments (POSIX), replaced FIPS 151-1 in its entirety. A new test suite has been developed, NIST-PCTS:151-2, to evaluate POSIX products for conformance to the revised FIPS. To be more responsive to the needs of the NIST POSIX testing community, NIST has arranged to sell the test suite directly via electronic mail. The electronic version of NIST-PCTS:151-2 will be delivered to the customer usually the same day that NIST receives the paperwork.

Standard Reference Materials

STANDARD REFERENCE MATERIAL 1746—SILVER FREEZING-POINT STANDARD

The International Temperature Scale of 1990 (ITS-90) was adopted by the International Committee of Weights and Measures in 1989, in accordance with the request embodied in Resolution 7 of the 18th General Conference of Weights and Measures of 1987. The ITS-90 supersedes the

International Practical Temperature Scale of 1968 (IPTS-68) and the 1976 Provisional 0.5 K to 30 K Temperature Scale (EPT-76). The ITS-90 was implemented at NIST on Jan. 1, 1990. The change in the temperature scale affects not only technical interests involved directly in thermometry but also those involved with other reference standards, such as electrical standards sensitive to temperature.

The Standard Reference Materials Program announces the availability of SRM 1746—Silver Freezing Point Standard. The SRM is intended for use as one of the defining fixed points of the ITS-90. The certified freezing point of $(961.780 \pm 0.002)^\circ\text{C}$ is assigned to the freezing point of pure silver. The fixed point is realized as the plateau temperature (or liquidus point) of the freezing curve of slowly frozen high-purity silver. The metal is in the form of millimeter-size “shot.” Each unit is 300 g and is packaged in an atmosphere of argon.

STANDARD REFERENCE MATERIAL 1978— PARTICLE SIZE DISTRIBUTION STANDARD

The measurement of the particle size and particle size distribution properties of solid materials in particulate form is an essential requirement in the manufacture of many different kinds of products, including food, catalysts, paints, pharmaceuticals, and office copier products. A variety of mechanical equipment and optical and electronic-sensing instrumentation are used routinely to provide particle classification data. Calibration of such equipment and instruments is accomplished by use of standard test methods that have been validated using certified particle size standards.

The Standard Reference Materials Program announces the availability of Standard Reference Material (SRM) 1978—Particle Size Distribution Standard for Gravity Sedimentation. SRM 1978, consisting of a granular zirconium oxide powder of irregularly shaped particles with a mean dimension of about $1\ \mu\text{m}$, is certified for cumulative size distribution. The data required to establish the certified values were generated by NIST and four outside laboratories participating in the NIST-directed interlaboratory study using SediGraph^R Models 5000 and 5100. These instruments produce continuous size distribution plots, but for certification purposes only the values obtained at five representative cumulative percentiles (10, 25, 50, 75, and 90) are reported.

STANDARD REFERENCE MATERIALS 2590—2591 JOSEPHSON ARRAY VOLTAGE STANDARDS

The Josephson array device and the metrological system based on it are the realization of the quantum physics phenomenon that has been adopted as the basis of representations of the SI volt. This means that the Josephson array voltage standards, unlike most Standard Reference Materials (SRMs), are intrinsic standards.

The Standard Reference Materials Program announces the availability of two Josephson Array Voltage Standards, SRM 2590 (1 V) and SRM 2591 (10 V). These SRMs are superconductive integrated-circuit chips. They are certified to generate the quantum voltage levels on which the SI volt representation is based, when cooled to 4.2 K or less and irradiated with a millimeter wave input of approximately 5 mW and 15 mW, respectively, at 75 GHz. The precision of the voltages generated establishes the level of confidence that the Josephson standard is functioning correctly. Independent devices are found to generate voltages that agree to better than 2 parts in 10^{17} based on tests carried out in the same liquid helium bath; at room temperature, agreement is within a few parts in 10^{10} .

STANDARD REFERENCE MATERIAL 2137—BORON IMPLANT IN SILICON STANDARD FOR CALIBRATION OF CONCENTRATION IN A DEPTH PROFILE

Boron is an important dopant in the production of single-crystal silicon wafers for the semiconductor industry. The concentration depth profile of the implanted ion determines the electronic properties of the wafers so implanted. Secondary ion mass spectrometry (SIMS) is frequently used for determination of the depth profile. In the SIMS method, successive layers of the silicon wafer are removed by ion bombardment, and the sputtered ion species are monitored. Calibration of the instrument for SIMS measurement requires the availability of a standard with a known depth profile.

The Standard Reference Materials Program announces the availability of SRM 2137, Boron Implant in Silicon Standard, certified for the retained dose of ^{10}B atoms, determined by the neutron reaction method, neutron depth profiling. The SRM is intended for use as a SIMS calibration standard. It also can be used as a transfer standard for the calibration of working standards for ^{10}B in silicon.

Calendar

February 7–9, 1994

THE QUEST FOR EXCELLENCE VI

Location: Washington Hilton and Towers
Washington, DC

Purpose: The Quest for Excellence VI is the only conference that provides an in-depth opportunity to learn about the award-winning quality processes and results of the 1993 Baldrige Award winners—Eastman Chemical Company and Ames Rubber Corporation. Presentations will be made by the winners' CEOs and others who are transforming their companies. This conference is organized to maximize learning and networking opportunities.

Topics: Leadership, information and analysis, strategic quality planning, human resource development and management, management of process quality, quality and operational results, and customer focus and satisfaction.

Format: Plenary sessions and breakout discussion sessions.

Audience: Executive interested in quality improvement, in manufacturing, service and small business.

Sponsors: NIST, AQP (Association for Quality Participation), and ASQC (American Society for Quality Control).

Contact: Elizabeth Clark, A537 Administration Building, NIST, Gaithersburg, MD 20899-0001, (301) 975-5771.

February 8–11, 1994

NORTH AMERICAN ISDN USERS' FORUM (NIUF)

Location: Hyatt Regency Tech Center
Denver, CO

Purpose: To develop user-defined applications, implementation agreements for existing standards, and tests needed for a transparent, ubiquitous and user-driven integrated services digital network (ISDN).

Topics: ISDN and the National Information Infrastructure Initiative, ISDN Applications, NASA ACTS ISDN PRI Satellite demonstration, Clean Air Act, Transaction Processing issues, Mass market and small business issues, ISDN Wiring and Powering, Customer Premise Equipment, ISDN Order Simplification, and other related ISDN topics.

Format: Tutorials, roundtable discussions, users' and implementors' workshops, and working group meetings.

Audience: ISDN users, implementors and service providers.

Sponsors: NIST; Hosted by U.S. West.

Contact: Dawn Hoffman, B364 Materials Building, NIST, Gaithersburg, MD 20899-0001, (301) 975-2937.

February 16–17, 1994

GREEN BUILDING CONFERENCE

Location: National Institute of
Standards and Technology
Gaithersburg, MD

Purpose: To provide a forum to discuss Green Buildings which are defined as structures that minimize the input on our global, neighborhood, and internal environments during their design, construction, operation, and eventual demolition.

Topics: Green Building assessment methodologies, international and municipal Green Building programs, presentation of Green Building case studies, U.S. Green Building activities, current and future Green Building technologies.

Format: General sessions.

Audience: Architects, builders, building material manufacturers, Government agencies, and academia.

Sponsors: NIST and U.S. Green Building Council.

Contact: Hunter Fannery, B320 Technology Building, NIST, Gaithersburg, MD 20899-0001, (301) 975-5864.

February 23–24, 1994

**FEDERAL INFORMATION
SYSTEMS SECURITY EDUCATORS'
ASSOCIATION CONFERENCE**

Location: Gaithersburg Hilton
Gaithersburg, MD

Purpose: To elevate the general level of information systems security awareness and knowledge within the federal Government and federally-related workforce.

Topics: Improving security education, telecommunications threats, professionalization, IT Security Education and Training; Current Events, National Cryptographic Policy and the National Information Infrastructure-Security.

Format: General session and speak out.

Audience: Federal agencies, industry and academia.

Sponsors: NIST.

Contact: Kathie Everhart, B154 Technology Building, NIST, Gaithersburg, MD 20899-0001, (301) 975-3868.

Subject Index to Volume 98

Numbers in parenthesis after the page number are the issue numbers

- No. 1 January–February
 No. 2 March–April
 No. 3 May–June
 No. 4 July–August
 No. 5 September–October
 No. 6 November–December

A

accelerator mass spectrometry (ASM)..... 653(6)
 accuracy 241(2), 245(2)
 activation analysis 127(1)
 agglomerates 699(6)
 aging of polymers..... 523(4)
 argon 159(2)
 ash 607(5)
 atmospheric chemistry 725(6)
 atomic weight of silicon 225(2)
 attenuators 691(6)

B

beta counting..... 653(6)
 beta decay 135(1)
 bismuth copper oxide 469(4)
 borehole tiltmeter 191(2)
 boron 109(1)
 business reengineering 729(6)

C

calcium 469(4)
 calibration 447(4)
 calibration design..... 217(2)
 ceramic morphology 31(1)
 ceramics 607(5)
 CH₃O₃ 181(2)
 chemical kinetics 725(6)
 chemical vapor deposition..... 375(3)
 chlorine-36 653(6)
 classical optics..... 231(2)
 coal..... 607(5)
 coherence theory 231(2)
 coil probe 287(3)
 cold neutron beams..... 127(1)
 cold neutrons..... 1(1), 109(1)
 combustion chemistry..... 725(6)
 communications network..... 633(5)
 complex gas phase kinetics 181(2)
 composites 523(4)
 computer assurance..... 517(4)
 computer modeling 181(2)
 condensed matter spectroscopy..... 59(1)

conservation of energy 231(2)
 correlation-induced spectral changes 231(2)
 corrosion..... 607(5)
 coupled dipole method..... 699(6)
 critical dimensional measurements 203(2)
 crystal chemistry..... 469(4)
 crystallography 241(2)

D

data administration 729(6)
 data architecture 729(6)
 data modeling 729(6)
 density 355(3)
 deuterium..... 679(6)
 diamond 375(3)
 diffraction..... 47(1), 231(2), 241(2)
 diffraction line broadening 321(3)
 diffusion 71(1), 89(1)
 dimensional stability of polymers 523(4)
 dimensions 245(2)
 dipole field..... 287(3)
 discharge..... 159(2)
 dispersion curves 59(1)
 domain interfaces..... 585(5)
 domain structure 561(5)
 drift eliminating 217(2)

E

elastic accommodation 561(5)
 elastic scattering..... 15(1)
 elemental analysis 127(1)
 energy levels 717(6)
 experimental phase relations 469(4)

F

filter transmittance 691(6)
 free radicals..... 181(2), 725(6)

gaseous electronics 159(2)
 gray scale measurement 203(2)
 guide hall 1(1)

H

heterodyne detection 691(6)
 Hilbert transform 297(3)
 HO₂ 181(2)
 hydrogen 679(6)
 hydrogen in metals 71(1)
 hydrogen vibrations and
 translational diffusion 59(1)

I

impulse response 297(3)
 inelastic neutron scattering 59(1), 89(1)
 inelastic scattering 15(1), 71(1)
 information technology 729(6)
 infrared 691(6)
 Integrated Services Digital
 Network (ISDN) 633(5)
 inter-Landau level scattering 361(3)
 interfaces 47(1)
 interference 231(2)
 interference microscope 203(2)
 interferometry 717(6)
 isotope ratios 225(2)
 isotope shift 717(6)

K

krypton 717(6)

L

Laplace transform 297(3)
 lattice defects 321(3)
 least squares 181(2), 217(2)
 light scattering 699(6)
 lightwave communications 253(2)
 linear system 297(3)
 linewidth 447(4)
 liquid scintillation (LS) 653(6)
 lithium 109(1)
 lithography 415(4), 447(4)
 long-term storage 355(3)

M

macromolecules in solution 31(1)
 magnetic excitations 59(1)
 magnetic field 287(3)
 magnification 447(4)
 mass spectrometer 225(2)
 materials processing 383(3)
 measurement uncertainty 287(3)
 metal alloys 31(1)
 metallization 375(3)
 method of moments 699(6)
 metrology 217(2), 415(4)
 micrometer 203(2)
 microscope 203(2)
 microstructure 31(1)
 minimum phase 297(3)
 molecular reorientations 89(1)

N

neutron backscattering spectrometers 89(1)
 neutron capture gamma rays 127(1)
 neutron choppers 71(1)
 neutron decay 135(1)
 neutron depth profiling 109(1)
 neutron facilities 1(1)
 neutron guides 1(1)
 neutron inelastic scattering 71(1)
 neutron instrumentation 1(1)
 neutron interferometry 135(1)
 neutron lifetime 135(1)
 neutron properties 1(1)
 neutron reflectivity 47(1)
 neutron scattering 15(1)
 neutron spectrometer 59(1)
 neutron spin-echo spectrometers 89(1)
 neutron wave 135(1)
 neutrons 1(1)
 nitrogen 109(1)
 North American ISDN
 Users' Forum (NIUF) 633(5)
 nuclear analytical methods 127(1)

O

optical absorption 375(3)
 optical communications 253(2)
 optical emission 159(2)
 optical fiber geometry 203(2)
 optical fibers 203(2), 253(2)
 optical scattering 375(3)
 oxygen 109(1)

V

vibration isolation	135(1)
vibrational spectroscopy.....	71(1)
video microscope	203(2)
Voigt function.....	321(3)
volume loss.....	355(3)

W

Warren-Averbach analysis.....	321(3)
wavelengths	717(6)
Wolf shifts	231(2)

X

x ray.....	415(4)
x-ray diffraction	321(3)

Author Index to Volume 98

Numbers in parenthesis after the volume number are the issue numbers

No. 1 January–February
No. 2 March–April
No. 3 May–June
No. 4 July–August
No. 5 September–October
No. 6 November–December

A

Adams, J. W.

Characteristics of Unknown Linear Systems Deduced from Measured CW Magnitude. Ma, M. T., and Adams, J. W. **98(3)**, 297 (1993).

Ankner, J. F.

Neutron Reflectivity and Grazing Angle Diffraction. Ankner, J. F., Majkrzak, C. F., and Satija, S. K. **98(1)**, 47 (1993).

Arif, M.

Facilities for Fundamental Neutron Physics Research at the NIST Cold Neutron Research Facility. Arif, M., Dewey, M. S., Green, G. L., and Snow, W. M. **98(1)**, 135 (1993).

Arnold-McKenna, C.

Workshop on Aging, Dimensional Stability, and Durability Issues in High Technology Polymers. Arnold-McKenna, C., and McKenna, G. B. **98(4)**, 523 (1993).

B

Balzar, D.

X-Ray Diffraction Line Broadening: Modeling and Applications to High- T_c Superconductors. Balzar, D. **98(3)**, 321 (1993).

Beetz, C.

Workshop on Characterizing Diamond Films II. Feldman, A., Beetz, C., Klocek, P., and Lu, G. **98(3)**, 375 (1993).

Bendersky, L. A.

Transformation of BCC and B2 High Temperature Phases to HCP and Orthorhombic Structures in the Ti-Al-Nb System. Part I: Microstructural Predictions Based on a Subgroup Relation Between Phases. Bendersky, L. A., Roytburd, A., and Boettinger, W. J. **98(5)**, 561 (1993).

Transformation of BCC and B2 High Temperature Phases to HCP and Orthorhombic Structures in the Ti-Al-Nb System. Part II: Experimental TEM Study of Microstructures. Bendersky, L. A., and Boettinger, W. J. **98(5)**, 585 (1993).

Berk, N. F.

Outline of Neutron Scattering Formalism. Berk, N. F. **98(1)**, 15 (1993).

Boettinger, W. J.

Transformation of BCC and B2 High Temperature Phases to HCP and Orthorhombic Structures in the Ti-Al-Nb System. Part I: Microstructural Predictions Based on a Subgroup Relation Between Phases. Bendersky, L. A., Roytburd, A., and Boettinger, W. J. **98(5)**, 561 (1993).

Transformation of BCC and B2 High Temperature Phases to HCP and Orthorhombic Structures in the Ti-Al-Nb System. Part II: Experimental TEM Study of Microstructures. Bendersky, L. A., and Boettinger, W. J. **98(5)**, 585 (1993).

Braun, W.

Optimizing Complex Kinetics Experiments Using Least-Squares Methods. Fahr, A., Braun, W., and Kurylo, M. J. **98(2)**, 181 (1993).

Burton, B. P.

Phase Equilibria and Crystal Chemistry in Portions of the System SrO-CaO-Bi₂O₃-CuO, Part IV—The System CaO-Bi₂O₃-CuO. Burton, B. P., Rawn, C. J., Roth, R. S., and Hwang, N. M. **98(4)**, 469 (1993).

Butler, T. A.

Evaluation of Serum Volume Losses During Long-Term Storage. Craft, N. E., Epler, K. S., Butler, T. A., May, W. E., and Ziegler, R. G. **98(3)**, 355 (1993).

C

Cage, M. E.

Dependence of Quantized Hall Effect Break-down Voltage on Magnetic Field and Current. Cage, M. E. **98(3)**, 361 (1993).

Collé, R.

³⁶Cl/Cl Accelerator-Mass-Spectrometry Standards: Verification of Their Serial-Dilution-Solution Preparations by Radioactivity Measurements. Collé, R., and Thomas, J. W. L. **98(6)**, 653 (1993).

Copley, J. R. D.

Neutron Time-of-Flight Spectroscopy. Copley, J. R. D., and Udovic, T. J. **98(1)**, 71 (1993).

Craft, N. E.

Evaluation of Serum Volume Losses During Long-Term Storage. Craft, N. E., Epler, K. S., Butler, T. A., May, W. E., and Ziegler, R. G. **98(3)**, 355 (1993).

D

Dapkunas, S. J.

NIST-Industry Workshop on Thermal Spray Coatings Research. Dapkunas, S. J. **98(3)**, 383 (1993).

Corrosion Characteristics of Silicon Carbide and Silicon Nitride. Munro, R. G., and Dapkunas, S. J. **98(5)**, 607 (1993).

Day, G. W.

Symposium on Optical Fiber Measurements. Franzen, D. L., and Day, G. W. **98(2)**, 253 (1993).

De Bièvre, P.

A Three-Ratio Scheme for the Measurement of Isotopic Ratios of Silicon. Ku, H., Schaefer, F., Valkiers, S., and De Bièvre, P. **98(2)**, 225 (1993).

Dewey, M. S.

Facilities for Fundamental Neutron Physics Research at the NIST Cold Neutron Research Facility. Arif, M., Dewey, M. S., Green, G. L., and Snow, W. M. **98(1)**, 135 (1993).

Djurović, S.

Absolute Spatially- and Temporally-Resolved Optical Emission Measurements of rf Glow Discharges in Argon. Djurović, S., Roberts, J. R., Sobolewski, M. A., and Olthoff, J. K. **98(2)**, 159 (1993).

Doiron, T.

Drift Eliminating Designs for Non-Simultaneous Comparison Calibrations. Doiron, T. **98(2)**, 217 (1993).

Downing, R. G.

Neutron Depth Profiling: Overview and Description of NIST Facilities. Downing, R. G., Lamaze, G. P., and Langland, J. K. **98(1)**, 109 (1993).

E

Epler, K. S.

Evaluation of Serum Volume Losses During Long-Term Storage. Craft, N. E., Epler, K. S., Butler, T. A., May, W. E., and Ziegler, R. G. **98(3)**, 355 (1993).

F

Fahr, A.

Optimizing Complex Kinetics Experiments Using Least-Squares Methods. Fahr, A., Braun, W., and Kurylo, M. J. **98(2)**, 181 (1993).

Feldman, A.

Workshop on Characterizing Diamond Films II. Feldman, A., Beetz, C., Klocek, P., and Lu, G. **98(3)**, 375 (1993).

Franzen, D. L.

Symposium on Optical Fiber Measurements. Franzen, D. L., and Day, G. W. **98(2)**, 253 (1993).

Frenkel, A.

Filter Transmittance Measurements in the Infrared. Migdall, A. L., Frenkel, A., and Kelleher, D. E. **98(6)**, 691 (1993).

G**Glinka, C. J.**

Small Angle Neutron Scattering at the National Institute of Standards and Technology. Hammouda, B., Krueger, S., and Glinka, C. J. **98(1)**, 31 (1993).

Greene, G. L.

Facilities for Fundamental Neutron Physics Research at the NIST Cold Neutron Research Facility. Arif, M., Dewey, M. S., Green, G. L., and Snow, W. M. **98(1)**, 135 (1993).

Grilly, E. R.

Pressure-Volume-Temperature Relations in Liquid and Solid Tritium. Grilly, E. R. **98(6)**, 679 (1993).

H**Hale, P. D.**

Optical Fiber Geometry: Accurate Measurement of Cladding Diameter. Young, M., Hale, P. D., and Mechels, S.E. **98(2)**, 203 (1993).

Hammouda, B.

Small Angle Neutron Scattering at the National Institute of Standards and Technology. Hammouda, B., Krueger, S., and Glinka, C. J. **98(1)**, 31 (1993).

Ultra-High Resolution Inelastic Neutron Scattering. Neumann, D. A., and Hammouda, B. **98(1)**, 89 (1993).

Huie, R. E.

Third International Conference on Chemical Kinetics—Reactions in Gas and Condensed Media. Huie, R. E. **98(6)**, 725 (1993).

Hwang, N. M.

Phase Equilibria and Crystal Chemistry in Portions of the System SrO-CaO-Bi₂O₃-CuO, Part IV—The System CaO-Bi₂O₃-CuO. Burton, B. P., Rawn, C. J., Roth, R. S., and Hwang, N. M. **98(4)**, 469 (1993).

J**Jones, S. N.**

Interlaboratory Study on the Lithographically Produced Scanning Electron Microscope Magnification Standard Prototype. Postek, M. T., Vladar, A. E., Jones, S. N., and Keery, W. J. **98(4)**, 447 (1993).

K**Kaufman, V.**

Wavelengths and Energy Levels of Neutral Kr⁸⁴ and Level Shifts in All Kr Even Isotopes. Kaufman, V. **98(6)**, 717 (1993).

Keery, W. J.

X-Ray Lithography Mask Metrology: Use of Transmitted Electrons in an SEM for Linewidth Measurement. Postek, M. T., Lowney, J. R., Vladar, A. E., Keery, W. J., Marx, E., and Larrabee, R. D. **98(4)**, 415 (1993).

Interlaboratory Study on the Lithographically Produced Scanning Electron Microscope Magnification Standard Prototype. Postek, M. T., Vladar, A. E., Jones, S. N., and Keery, W. J. **98(4)**, 447 (1993).

Kelleher, D. E.

Filter Transmittance Measurements in the Infrared. Migdall, A. L., Frenkel, A., and Kelleher, D. E. **98(6)**, 691 (1993).

Klocek, P.

Workshop on Characterizing Diamond Films II. Feldman, A., Beetz, C., Klocek, P., and Lu, G. **98(3)**, 375 (1993).

Kohl, M. L.

Measuring Low Frequency Tilts. Kohl, M. L., and Levine, J. **98(2)**, 191 (1993).

Krueger, S.

Small Angle Neutron Scattering at the National Institute of Standards and Technology. Hammouda, B., Krueger, S., and Glinka, C. J. **98(1)**, 31 (1993).

Ku, H.

A Three-Ratio Scheme for the Measurement of Isotopic Ratios of Silicon. Ku, H., Schaefer, F., Valkiers, S., and De Bièvre, P. **98(2)**, 225 (1993).

Kurylo, M. J.

Optimizing Complex Kinetics Experiments Using Least-Squares Methods. Fahr, A., Braun, W., and Kurylo, M. J. **98(2)**, 181 (1993).

L**Lakhtakia, A.**

On Two Numerical Techniques for Light Scattering by Dielectric Agglomerated Structures. Lakhtakia, A., and Mulholland, G. W. **98(6)**, 699 (1993).

Lamaze, G. P.

Neutron Depth Profiling: Overview and Description of NIST Facilities. Downing, R. G., Lamaze, G. P., and Langland, J. K. **98(1)**, 109 (1993).

Langland, J. K.

Neutron Depth Profiling: Overview and Description of NIST Facilities. Downing, R. G., Lamaze, G. P., and Langland, J. K. **98(1)**, 109 (1993).

Larrabee, R. D.

X-Ray Lithography Mask Metrology: Use of Transmitted Electrons in an SEM for Linewidth Measurement. Postek, M. T., Lowney, J. R., Vladar, A. E., Keery, W. J., Marx, E., and Larrabee, R. D. **98(4)**, 415 (1993).

Lennon, E. B.

North American Integrated Services Digital Network (ISDN) Users' Forum (NIUF). Lennon, E. B. **98(2)**, 257 (1993).

COMPASS '93, Eighth Annual Conference on Computer Assurance. Wallace, D. R., and Lennon, E. B. **98(4)**, 517 (1993).

North American Integrated Services Digital Network (ISDN) Users' Forum (NIUF). Lennon, E. B. **98(5)**, 633 (1993).

Levine, J.

Measuring Low Frequency Tilts. Kohl, M. L., and Levine, J. **98(2)**, 191 (1993).

Lindstrom, R. M.

Prompt-Gamma Activation Analysis. Lindstrom, R. M. **98(1)**, 127 (1993).

Lowney, J. R.

X-Ray Lithography Mask Metrology: Use of Transmitted Electrons in an SEM for Linewidth Measurement. Postek, M. T., Lowney, J. R., Vladar, A. E., Keery, W. J., Marx, E., and Larrabee, R. D. **98(4)**, 415 (1993).

Lu, G.

Workshop on Characterizing Diamond Films II. Feldman, A., Beetz, C., Klocek, P., and Lu, G. **98(3)**, 375 (1993).

M**Ma, M. T.**

Characteristics of Unknown Linear Systems Deduced from Measured CW Magnitude. Ma, M. T., and Adams, J. W. **98(3)**, 297 (1993).

Majkrzak, C. F.

Neutron Reflectivity and Grazing Angle Diffraction. Ankner, J. F., Majkrzak, C. F., and Satija, S. K. **98(1)**, 47 (1993).

Marx, E.

X-Ray Lithography Mask Metrology: Use of Transmitted Electrons in an SEM for Linewidth Measurement. Postek, M. T., Lowney, J. R., Vladar, A. E., Keery, W. J., Marx, E., and Larrabee, R. D. **98(4)**, 415 (1993).

May, W. E.

Evaluation of Serum Volume Losses During Long-Term Storage. Craft, N. E., Epler, K. S., Butler, T. A., May, W. E., and Ziegler, R. G. **98(3)**, 355 (1993).

McKenna, G. B.

Workshop on Aging, Dimensional Stability, and Durability Issues in High Technology Polymers. Arnold-McKenna, C., and McKenna, G. B. **98(4)**, 523 (1993).

Mechels, S. E.

Optical Fiber Geometry: Accurate Measurement of Cladding Diameter. Young, M., Hale, P. D., and Mechels, S.E. **98(2)**, 203 (1993).

Mielenz, K. D.

“Wolf Shifts” and Their Physical Interpretation Under Laboratory Conditions. Mielenz, K. D. **98(2)**, 231 (1993).

Migdall, A. L.

Filter Transmittance Measurements in the Infrared. Migdall, A. L., Frenkel, A., and Kelleher, D. E. **98(6)**, 691 (1993).

Misakian, M.

Coil Probe Dimension and Uncertainties During Measurements of Nonuniform ELF Magnetic Fields. Misakian, M. **98(3)**, 287 (1993).

Mulholland, G. W.

On Two Numerical Techniques for Light Scattering by Dielectric Agglomerated Structures. Lakhtakia, A., and Mulholland, G. W. **98(6)**, 699 (1993).

Munro, R. G.

Corrosion Characteristics of Silicon Carbide and Silicon Nitride. Munro, R. G., and Dapkunas, S. J. **98(5)**, 607 (1993).

N**Neumann, D. A.**

Ultra-High Resolution Inelastic Neutron Scattering. Neumann, D. A., and Hammouda, B. **98(1)**, 89 (1993).

Newton, J.

Data Administration Management Association Symposium. Newton, J. **98(6)**, 729 (1993).

O**Olthoff, J. K.**

Absolute Spatially- and Temporally-Resolved Optical Emission Measurements of rf Glow Discharges in Argon. Djurović, S., Roberts, J. R., Sobolewski, M. A., and Olthoff, J. K. **98(2)**, 159 (1993).

P**Postek, M. T.**

X-Ray Lithography Mask Metrology: Use of Transmitted Electrons in an SEM for Linewidth Measurement. Postek, M. T., Lowney, J. R., Vldar, A. E., Keery, W. J., Marx, E., and Larrabee, R. D. **98(4)**, 415 (1993).

Interlaboratory Study on the Lithographically Produced Scanning Electron Microscope Magnification Standard Prototype. Postek, M. T., Vldar, A. E., Jones, S. N., and Keery, W. J. **98(4)**, 447 (1993).

Prask, H. J.

The NIST Cold Neutron Research Facility. Prask, H. J., Rowe, J. M., Rush, J. J., and Schröder, I. G. **98(1)**, 1 (1993).

R**Rawn, C. J.**

Phase Equilibria and Crystal Chemistry in Portions of the System SrO-CaO-Bi₂O₃-CuO, Part IV—The System CaO-Bi₂O₃-CuO. Burton, B. P., Rawn, C. J., Roth, R. S., and Hwang, N. M. **98(4)**, 469 (1993).

Roberts, J. R.

Absolute Spatially- and Temporally-Resolved Optical Emission Measurements of rf Glow Discharges in Argon. Djurović, S., Roberts, J. R., Sobolewski, M. A., and Olthoff, J. K. **98(2)**, 159 (1993).

Roth, R. S.

Phase Equilibria and Crystal Chemistry in Portions of the System SrO-CaO-Bi₂O₃-CuO, Part IV—The System CaO-Bi₂O₃-CuO. Burton, B. P., Rawn, C. J., Roth, R. S., and Hwang, N. M. **98(4)**, 469 (1993).

Rowe, J. M.

The NIST Cold Neutron Research Facility. Prask, H. J., Rowe, J. M., Rush, J. J., and Schröder, I. G. **98(1)**, 1 (1993).

Roytburd, A.

Transformation of BCC and B2 High Temperature Phases to HCP and Orthorhombic Structures in the Ti-Al-Nb System. Part I: Microstructural Predictions Based on a Subgroup Relation Between Phases. Bendersky, L. A., Roytburd, A., and Boettinger, W. J. **98(5)**, 561 (1993).

Rush, J. J.

The NIST Cold Neutron Research Facility. Prask, H. J., Rowe, J. M., Rush, J. J., and Schroder, I. G. **98(1)**, 1 (1993).

S

Satija, S. K.

Neutron Reflectivity and Grazing Angle Diffraction. Ankner, J. F., Majkrzak, C. F., and Satija, S. K. **98(1)**, 47 (1993).

Schaefer, F.

A Three-Ratio Scheme for the Measurement of Isotopic Ratios of Silicon. Ku, H., Schaefer, F., Valkiers, S., and De Bièvre, P. **98(2)**, 225 (1993).

Schröder, I. G.

The NIST Cold Neutron Research Facility. Prask, H. J., Rowe, J. M., Rush, J. J., and Schröder, I. G. **98(1)**, 1 (1993).

Snow, W. M.

Facilities for Fundamental Neutron Physics Research at the NIST Cold Neutron Research Facility. Arif, M., Dewey, M. S., Green, G. L., and Snow, W. M. **98(1)**, 135 (1993).

Sobolewski, M. A.

Absolute Spatially- and Temporally-Resolved Optical Emission Measurements of rf Glow Discharges in Argon. Djurović, S., Roberts, J. R., Sobolewski, M. A., and Olthoff, J. K. **98(2)**, 159 (1993).

Stalick, J. K.

Accuracy in Powder Diffraction II: A Report on the Second International Conference. Stalick, J. K. **98(2)**, 241 (1993).

Swyt, D. A.

Metrological Issues in Precision-Tolerance Manufacturing: A Report of a NIST Industry-Needs Workshop. Swyt, D. A. **98(2)**, 245 (1993).

T

Thomas, J. W. L.

³⁶Cl/Cl Accelerator-Mass-Spectrometry Standards: Verification of Their Serial-Dilution-Solution Preparations by Radioactivity Measurements. Collé, R., and Thomas, J. W. L. **98(6)**, 653 (1993).

Trevino, S. F.

The Triple Axis and SPINS Spectrometers. Trevino, S. F. **98(1)**, 59 (1993).

U

Udovic, T. J.

Neutron Time-of-Flight Spectroscopy. Copley, J. R. D., and Udovic, T. J. **98(1)**, 71 (1993).

V

Valkiers, S.

A Three-Ratio Scheme for the Measurement of Isotopic Ratios of Silicon. Ku, H., Schaefer, F., Valkiers, S., and De Bièvre, P. **98(2)**, 225 (1993).

Vladar, A. E.

X-Ray Lithography Mask Metrology: Use of Transmitted Electrons in an SEM for Linewidth Measurement. Postek, M. T., Lowney, J. R., Vladar, A. E., Keery, W. J., Marx, E., and Larrabee, R. D. **98(4)**, 415 (1993).

Interlaboratory Study on the Lithographically Produced Scanning Electron Microscope Magnification Standard Prototype. Postek, M. T., Vladar, A. E., Jones, S. N., and Keery, W. J. **98(4)**, 447 (1993).

W

Wallace, D. R.

COMPASS '93, Eighth Annual Conference on Computer Assurance. Wallace, D. R., and Lennon, E. B. **98(4)**, 517 (1993).

Y

Young, M.

Optical Fiber Geometry: Accurate Measurement of Cladding Diameter. Young, M., Hale, P. D., and Mechels, S.E. **98(2)**, 203 (1993).

Z

Ziegler, R. G.

Evaluation of Serum Volume Losses During Long-Term Storage. Craft, N. E., Epler, K. S., Butler, T. A., May, W. E., and Ziegler, R. G. **98(3)**, 355 (1993).